

CRANFIELD UNIVERSITY

OSAHON EHIGIATOR

INVESTIGATION OF WIRE AND ARC ADDITIVE
MANUFACTURING METHODS FOR HIGH INTEGRITY, HIGH
PRODUCTIVITY FABRICATION OF LARGE STEEL STRUCTURES

SCHOOL OF AEROSPACE, TRANSPORT AND
MANUFACTURING (SATM)
Department of Welding Engineering and Laser Processing Centre
(WELPC)

PhD Thesis
Academic Year: 2017 - 2021

Supervisor: Dr. Supriyo Ganguly

June 2021

CRANFIELD UNIVERSITY

SCHOOL OF AEROSPACE, TRANSPORT AND
MANUFACTURING (SATM)

PhD Thesis

Academic Year 2017 - 2021

OSAHON EHIGIATOR

APPLICATION OF WIRE AND ARC ADDITIVE MANUFACTURING
METHODS FOR HIGH PRODUCTIVITY, HIGH INTEGRITY
MANUFACTURE OF LARGE STEEL STRUCTURES

Supervisor: Dr. Supriyo Ganguly

June, 2021

© Cranfield University 2021. All rights reserved. No part of this
publication may be reproduced without the written permission of the
copyright owner.

PROJECT ABSTRACT

This thesis describes advances in aspects of deposition process control, mechanical performance optimisation and improved material property development, undertaken for high productivity and integrity wire and arc additive manufacture of large heavy-walled components. One key objective of this study was to undertake a fundamental study to understand the important factors at play during tandem-GMAW deposition of single bead and multi-layer wall structures, with a focus on achieving substantial improvement in deposition rate and surface quality of WAAM components. The study of the influence of key deposition parameters on the instantaneous arc characteristics and deposited bead geometry was conducted. The study found that while wire feed speed and travel speed significantly affected the arc and bead characteristic, the influence of contact tip to work distance was minimal. However, the later strongly influences the arc stability, due to its effect on the mode of metal transfer. The study also showed that consistent high quality single bead deposit is achievable when the lead wire is set about 1-2m/min lower than the trail wire and increase in total wire feed speed of tandem process above 24m/min, produced insignificant effect on bead width. Furthermore, tandem parallel wire configuration, produced the optimum surface quality and metal deposition efficiency; however, it was more susceptible to defect formation at higher travel speed, compared to tandem series wire set-up. The fundamental experience and knowledge gained through the aforementioned process study was instrumental in building a rectilinear wall structure, with excellent surface and geometrical quality and, subsequently a large skin and core part, with significant improvements in deposition rate and surface quality of the component.

Thermal cycle generation during deposition of a thick-walled WAAM structure, built using 2.25Cr 1Mo type steel composition and response of the structure to heat treatment were studied. The main focus was to improve understanding on the effect of thermal cycle on the mechanical performance of the component and develop a suitable heat treatment regime to restore an acceptable material property, without requiring the more expensive and complex austenitisation heat

treatment process. The study found that the generated thermal cycle produced microstructural heterogeneity, high hardness level, with large gradient in hardness of the multi-layered structure, in as-deposited condition. This resulted in poor impact toughness. However, the applied post deposition heat treatment parameters, was beneficial in homogenising the material, reducing the high hardness and variation in hardness, and restored the impact toughness.

Tandem GMAW modification of alloy 2.25Cr 1Mo type wire composition, (using ER90S-G wire), with ER120S-G wire, having higher nickel content, was studied to exploit the potential for compositional modification, through this manufacturing route. The mixing of the two wires was carried out to determine whether higher nickel content can improve the impact toughness and eliminate the need for PDHT. The focus was to increase the as deposited charpy impact toughness, while maintaining excellent all-round static mechanical properties. The result showed that significant increase in charpy impact toughness, in both testing direction, at -30deg C, was achieved with the modified composition, containing equal proportions of ER90S-G and ER120S-G wire materials.

Finally, laboratory sour service corrosion test was conducted to compare the corrosion performance of WAAM alloys, obtained under different processing conditions, to a similar but conventional wrought steel variant. The results showed that both the exposure temperature and time, accelerated the corrosion degradation of the materials. Also, while 2.25Cr 1Mo WAAM alloy and the wrought variant showed comparable corrosion performance, the modified WAAM alloy containing equal blend of ER90S-G and ER120S-G wire, exhibited superior corrosion performance compared to the wrought alloy, which was attributed to the higher nickel content of the former.

Keywords:

Tandem-wire, GMAW, Skin and core deposition strategy, Surface waviness, Wire composition modification, Heat treatment, ER90S-G, ER120S-G, ASTM A182 F22, Single bead geometry, multi-layer wall

ACKNOWLEDGEMENTS

I would like to acknowledge with profound gratitude, the sponsorship and funding provided by Schlumberger company, in Houston Texas, USA, that made this doctoral thesis a reality.

I would first like to express my deepest appreciation and thanks to Dr. Clint Wildash, the Welding Technical Engineering Manager, in Schlumberger, Houston Texas, for his support and efforts in securing the research funding, helping to develop the project, providing the necessary information and invaluable guidance throughout the duration of this project, as well as helping to proofread my thesis.

I would also like to acknowledge with much appreciation the crucial role played by my project supervisor, Dr Supriyo Ganguly who invested his effort in guiding me in achieving the goal. His excellent insights, invaluable guidance and assistance throughout the thesis was instrumental to helping my cope efficiently with the research work.

A special thanks to Professor Stewart Williams, for the exceptional role he played in the course of this study. As a rudder is to a ship, so his technical insight and inputs were to the success of this work.

I would like to extend my sincere thanks to all the staff at the Welding Engineering and Laser processing centre (WELPC) and my colleagues who supported me during my studies.

I want to specifically say a big thank you to Mr Flemming Nielsen, Mr Nisar Shah, Dr Goncalo Rodrigues Pardal, Dr Sonia Martins Meco, Mrs Anne Fiorucci and Mr John Thrower, for their ideas, technical and operational support they provided me and also convey my thanks to Dr Christine Kimpton, Dr Tracey Roberts and Dr Diane Johnson, for their huge assistance and support, which helped to make this work possible.

I would like to express my special and profound gratitude to my wife Peace and my adorable children, Eghosa and Etinosa, for their understanding, love, prayer, and support throughout my study. Also, I thank the rest of my family, especially

my sister Osarugue, my mum Mrs F. Ehigiator, and my uncles Air Cdre. A.U. Agbonlahor (Rtd.) and Mr F. Ehigiator, for their prayers, love and encouragement which helped me in the completion of this study.

Finally, I am immensely indebted in gratitude, praises and thanks to God Almighty for His unfailing mercy, love, favour, divine health, strength, ability, and blessings, which saw me through this study.

TABLE OF CONTENTS

PROJECT ABSTRACT	i
ACKNOWLEDGEMENTS.....	iii
LIST OF FIGURES.....	x
LIST OF TABLES	xxiii
LIST OF EQUATIONS.....	xxv
1 PROJECT INTRODUCTION	1
1.1 Background of Research	2
1.2 Why WAAM	5
1.3 Research challenges	5
1.3.1 Issues related to productivity (deposition rate) and surface quality	7
1.3.2 Successive thermal cycle generation	7
1.3.3 Lack of optimised deposition feedstock.....	8
1.4 Research questions	9
1.5 Thesis outline.....	9
2 LITERATURE REVIEW	11
2.1 Subtractive versus additive manufacturing methods.....	11
2.2 What is Additive manufacture	12
2.2.1 Benefits of Additive manufacture.....	14
2.2.2 Additive manufacturing of metallic materials	16
2.2.3 Classification of additive manufacture	17
2.2.4 AM material cost and utilisation.....	19
2.2.5 Classification of wire-feed AM processes.....	19
2.3 Wire and arc additive manufacturing (WAAM)	20
2.3.1 GMAW process in WAAM technology	22
2.4 Automation of WAAM process	24
2.4.1 Generation of deposition process parameter	25
2.4.2 Automatic WAAM path generation (Toolpath generation strategies)	
.....	28
2.5 High productivity development in WAAM process.....	40
2.5.1 High productivity arc processes	40
2.5.2 Multi-wire GMAW process.....	44
2.5.3 Comparison between Tandem and Twin Wire GMAW Processes ...	47
2.5.4 Tandem-GMAW process.....	50
2.6 Surface quality improvement	53
2.6.1 Surface quality (waviness) in WAAM structures.....	54
2.7 Skin and core deposition strategy for WAAM components	60
2.8 Thermal cycle generation and heat treatment during WAAM process	62
2.8.1 2.25Cr 1Mo steel alloy.....	63
2.8.2 Alloying additions and effect.....	63
2.8.3 Martensitic formation in 2.25Cr 1Mo alloy	66

2.8.4 CCT Curve of 2.25Cr 1Mo steel	68
2.8.5 Microstructure of 2.25Cr 1Mo weldment.....	70
2.8.6 Multi-pass weld zones	72
2.8.7 Multi-pass weld thermal cycle	74
2.8.8 Tempering heat treatment of steel weld metal	75
2.9 Tailored modification of wire composition	77
2.9.1 Weldability issues of 2.25Cr 1Mo alloy weldment	77
2.9.2 Weld metal micro-constituents	78
2.9.3 Improvement in weld metal impact toughness	82
2.9.4 Development of weld metal property	85
2.9.5 Tandem-GMAW modification of weld metal property	86
2.10 Comparative assessment of corrosion performance of WAAM and wrought alloys.....	88
2.10.1 Corrosion degradation of metallic materials	88
2.10.2 Sour corrosion.....	89
2.10.3 Types of corrosion degradation.....	89
2.10.4 Factor influencing corrosion rate	92
2.10.5 Corrosion of WAAM alloy	96
2.11 Summary of literatures and key gaps.....	98
2.12 Research aims and objectives	102
3 Experimental study of high deposition and surface quality for WAAM parts	103
3.1 Materials and equipment.....	104
3.1.1 Material	105
3.1.2 Equipment.....	105
3.2 Metallographic preparation	108
3.3 Measurement of weld bead characteristics.....	108
3.3.1 Measurement of weld bead profile	108
3.3.2 Measurement of multi-layer wall profile	109
3.3.3 Surface waviness measurement	110
3.4 High deposition rate process study	112
3.4.1 Characterisation of Tandem-GMAW single bead deposition parameters	112
3.5 Results and discussion on high deposition rate study.....	114
3.5.1 Results of effect of Tandem-GMAW primary process parameters electrical transient, bead geometry and quality	114
3.6 Characterisation of the effect of Tandem-GMAW secondary process parameters on bead geometry, surface quality and electrical transient characteristics.....	129
3.6.1 Effect of variation in WFS of lead wire(A) and trail wire(B) on the bead geometry and surface quality	130
3.6.2 Effect of torch travel direction on bead geometry and deposited surface quality	135

3.6.3	Result of effect of torch travel direction on bead surface quality	137
3.6.4	Effect of wire configuration (set-up) on heat input, bead geometry and deposited surface quality.....	139
3.7	Effect of tandem-GMAW primary and secondary process parameters on electrical transient arc characteristics	144
3.8	High speed camera visualisation of arc and weld pool	147
3.9	Multi-layer deposition process study	149
3.9.1	Determination of Tandem-GMAW lower deposition process parameter range for series and parallel configurations	150
3.9.2	Effect of CTWD, on generated heat input, bead geometry and surface quality, using tandem-GMAW parallel and series wire configurations.....	155
3.9.3	Effect of arc correction and CTWD on deposited bead quality, geometry and heat input generated, using single-wire GMAW process..	160
3.10	Multi-layer wall deposition.....	165
3.11	Experimental method for multi-layer wall deposition study	165
3.12	Results and discussion on multi-layer wall deposition study.....	167
3.12.1	Results of effect of layer numbers and deposition process, on multi-layer wall characteristics.....	167
3.12.2	Effect of TS, WFS and deposition process on surface SWav and EWW of the multi-layer walls.....	172
3.12.3	Effect of WFS, on SWav and EWW, at constant WFS/TS ratio....	176
3.12.4	Metal deposition efficiency of Single-wire and Tandem wire GMAW processes	180
3.13	Case study 1: Manufacture of a thin wall structure, using Tandem-GMAW parallel wire technique.....	182
3.13.1	Manufacturing strategy.....	182
3.13.2	Result and discussion of case study 1	183
3.14	High deposition and surface quality manufacture	186
3.15	Skin and core parameter study	187
3.15.1	Generation of process parameters for deposition of skin section .	187
3.15.2	Results of parameter study for deposition of the skin section	188
3.15.3	Generation of process parameters for deposition of core section	190
3.15.4	Results and discussion of process parameter study for core section.....	191
3.16	Case study 2: WAAM of large structural part, using skin and core deposition technique.....	194
3.16.1	Materials and consumables.....	194
3.16.2	Equipment set-up	195
3.16.3	Manufacturing procedure	195
3.17	Conclusions	201
3.17.1	Recommendations	203

4	Experimental study of thermal cycle generation and heat treatment in WAAM fabricated 2.25Cr 1Mo alloy	204
4.1	Experiment and procedures.....	204
4.1.1	Deposition Materials.....	204
4.1.2	Equipment set-up and parameters	204
4.1.3	Manufacture of test block and thermal cycle measurement	205
4.1.4	Non-destructive test on block.....	206
4.1.5	Heat treatment study	207
4.1.6	Microstructural and mechanical analysis.....	208
4.2	Results presentation	210
4.2.1	Manufactured WAAM block.....	210
4.2.2	Non-destructive test of WAAM block.....	211
4.2.3	Thermal cycle evolution during WAAM block deposition	211
4.2.4	CCT curve of deposited WAAM alloy	214
4.2.5	Post deposition heat treatment (PDHT) of WAAM block	215
4.2.6	Microstructure of as-deposited WAAM alloy.....	220
4.2.7	Microstructure of WAAM alloys after PDHT	223
4.2.8	Analysis of inclusion in the WAAM block.....	224
4.2.9	X-Ray diffraction analysis of WAAM alloy	226
4.2.10	Tensile and charpy impact toughness tests	227
4.2.11	Deterioration in charpy impact toughness	233
4.2.12	Quality of deposited WAAM block	235
4.2.13	Evolution of thermal cycle and effect on microstructure of deposited WAAM alloy	235
4.2.14	Inclusion characteristics	237
4.2.15	Effect of thermal cycle and heat treatment on deposited mechanical properties	238
4.2.16	Deterioration in charpy impact toughness	242
4.3	Conclusions	244
5	Experimental modification of alloy 2.25Cr 1Mo composition, using the Tandem-GMAW	246
5.1	Hypothesis and technical approach	246
5.2	Experimental procedure.....	247
5.2.1	Materials.....	247
5.2.2	Equipment setup	247
5.2.3	Experimental plan	249
5.2.4	Manufacture of test samples	249
5.2.5	Non-destructive examination (NDT)	250
5.2.6	Elemental analysis	250
5.2.7	Microstructure and mechanical analysis.....	251
5.3	Result presentations	254
5.3.1	Manufactured test samples	254

5.3.2 NDT result of test blocks	256
5.3.3 ICP-OES chemical analysis of WAAM alloys	256
5.3.4 Analysis of actual and theoretical composition of WAAM alloys, as a function of wire mixing proportions	257
5.3.5 Microstructural evolution of WAAM alloys	259
5.3.6 Analysis of inclusions in deposited test blocks	261
5.3.7 EDS chemical analysis of inclusions and weld metal oxygen test ..	262
5.3.8 Results of mechanical test	263
5.3.9 Fracture surface morphology of WAAM alloys	267
5.4 Discussions.....	269
5.4.1 Effect of increased nickel content on microstructure	270
5.4.2 Effect of increased Ni content on inclusion evolution	271
5.4.3 Effect on hardness	272
5.4.4 Effect on strength	273
5.4.5 Effect on impact toughness	273
5.5 Conclusions	275
6 Experimental study of corrosion performance of WAAM alloys exposed to a simulated sour service environment	277
6.1 Experimental procedure.....	277
6.1.1 Equipment set up	277
6.1.2 Test materials and compositions	278
6.1.3 Choice of test method	279
6.1.4 Sample preparation and testing	280
6.2 Results presentation	282
6.2.1 Macroscopic surface appearance of samples after test	282
6.2.2 Weight loss of WAAM samples	285
6.2.3 Effect of exposure duration	286
6.2.4 Effect of temperature.....	287
6.2.5 SEM surface morphology of corrosion samples	287
6.2.6 Analysis of corrosion product	288
6.3 Discussion	290
6.4 Conclusions	293
6.4.1 Recommendations	294
7 OVERALL CONCLUSIONS.....	295
7.1 Further suggestions for future work	296
REFERENCES.....	297
APPENDICES	329

LIST OF FIGURES

Figure 1-1 Examples of subsea assemblies used for oil extraction.....	2
Figure 1-2 Subsea Drill bit.....	3
Figure 1-3 (a) M-Jumper and subsea connector schematic diagram (b) Subsea collet connector structure diagram	3
Figure 1-4 Tandem SAW of shell ring for reactor vessel fabrication	4
Figure 1-5 Strip overlay welding of inside shell ring	4
Figure 1-6 AM revenue forecast and Year on Year Market Growth in the oil and gas industry	6
Figure 2-1 Cost comparison between AM and conventional process	12
Figure 2-2 Schematics of the basic chain for AM	12
Figure 2-3 (a) A rapid tool with conformal cooling channel built using EoS's SLS process, (b) Stress pattern of a blade captured in colour using ZCorp's 3DP, (c) Time-delivery drug produced using Therics's 3DP, (d) Functional gradient metallic objects made using OptoMec's LENS	13
Figure 2-4 Schematic of an aircraft landing gear fabricated by forging and additive manufacturing	15
Figure 2-5 (a) LBM-produced fuel nozzle of the LEAP aero engine (from GE Aviation). Integrated design built as one piece with optimised interior channels and a weight saving of approximate 25%, (b) LBM-produced Ti-6Al-4V bracket for Airbus A350 (from LZN Laser Zentrum Nord GmhH and Airbus).....	16
Figure 2-6 Comparison between the Geometric complexities and Quantity of AM technology and other manufacturing options (MIM metal injection moulding, PS-Sintering powder metallurgy sintering)	17
Figure 2-7 Illustration of an electron beam system.....	20
Figure 2-8 Illustration of a laser beam system	20

Figure 2-9 Schematic diagram of an experimental robotic WAAM system.....	21
Figure 2-10 Schematic illustrations of the (a) GMAW, (b) GTAW and (c) PAW process.....	21
Figure 2-11 Examples of WAAM parts manufactured using GMAW processes (a) 1.2 m Ti-6Al-4V wing spar built for BAE Systems, top view (courtesy BAE Systems; process: PAWWAAM); (b) high strength steel wing model for wind tunnel testing (process: Fronius CMT WAAM), (c) particular of hollow structure, (d) mild steel truncated cone (process: Fronius CMT WAAM).....	23
Figure 2-12 Intersecting stiffened panels produced by WAAM, (a and b) carbon steel, (c and d) aluminium, (e) titanium-stiffened panel, (f) Ti thick wall crossover, (g) Ti residual stress balance cruciform, (h) Ti intersections after machining.....	23
Figure 2-13 Cross section of WAAM parts showing (a) lack of fusion defect, (b) excessive remelting and loss of geometric accuracy (c) irregular geometry and poor surface quality.....	25
Figure 2-14 Various object partitioning strategies (a) Object partitioning with multiple build directions (b) Alternating build directions for symmetrical heat deposition (c) Splitting up fill layers and using different fill patterns	29
Figure 2-15 Part partitioning approach, with allocation of different tool path.....	29
Figure 2-16 Cross sections of straight and sloping thin walls, produced with a (a) constant build direction (b) a variable build direction.....	30
Figure 2-17 Wall cross sections built before and after improvement of deposition process parameter.....	31
Figure 2-18 WAAM beer mug produced using GMAW process.....	32
Figure 2-19 Enclosed structure produced using WAAM – Semicircle (left) square section (right).....	32
Figure 2-20 Cross sections of low-quality solid parts produced using thin wall offsetting technique (a) Showing lack of fusion due to inadequate heat input, but	

little loss of shape (b) showing loss of shape due to excessive heat input, but with good fusion.....	33
Figure 2-21 (a) Cross-section of solid block deposited using the boundary method (b) Schematic illustration of the boundary method (the arrows indicate the deposition paths)	34
Figure 2-22 A schematic diagram of a single layer, showing deposition of multiple beads on a substrate in flat position.....	35
Figure 2-23 Sketch of the traditional overlapping flat-top model.....	36
Figure 2-24 Schematic illustration of tangent overlapping model, TOM	37
Figure 2-25 Raster path filling.....	38
Figure 2-26 Deposition of perimeter and layer filling with the use of raster path in LENS process	38
Figure 2-27 Illustration of continuous raster filling paths	39
Figure 2-28 Occurrence of voids by continuous raster paths, near fill area edges	39
Figure 2-29 Build rate versus layer height for different AM technologies	41
Figure 2-30 Multi-wire SAW deposition system	44
Figure 2-31 Multiple-wire tandem GMAW system, showing (a) Equipment set-up (b) Detailed view of tandem touch	45
Figure 2-32 Schematics of two types of double-wire GMAW processes (a) Twin-wire (b) Tandem-wire.....	46
Figure 2-33 Schematic diagrams of heat distribution of double wire GMAW process (a) twin-wire (b) Tandem-wire.....	47
Figure 2-34 Heat source model diagram of GMAW twin wire and Tandem process.....	48

Figure 2-35 Relationship between twin wire welding and material transfer (a) Tandem (b) GMAW.....	49
Figure 2-36 Comparison of travel speeds for Single-wire and Tandem-wire GMAW applications	50
Figure 2-37 Tandem GMAW functional principle scheme showing (1) Wire-feeder units 1 and 2 (2) Wire electrodes 1 and 2 (3) LHSB HUB (synergic controller) (4) Power source 1 and 2 (5) Separate welding potential	51
Figure 2-38 Schematic diagram, showing an approximate surface and “stair stepping” effect.....	55
Figure 2-39 Surface quality of tandem-GMAW WAAM manufactured wall structure, using WFSs of (a) 7m/mins WFS (b) 9m/mins WFS.....	58
Figure 2-40 Wall structure, showing irregular geometry and poor surface quality.....	59
Figure 2-41 Schematic illustration of boundary layer technique	61
Figure 2-42 Build rate and horizontal resolution Versus layer height for different AM technologies.....	62
Figure 2-43 Effect of different alloying elements on the TTT-diagram of a Fe-0.5 at% C steel.....	64
Figure 2-44 Effect of alloying elements on Eutectoid temperature.....	65
Figure 2-45 IT and CCT diagram for steel with composition closely matching F22 steel. Composition: [0.15% C – 0.36% Mn – 0.44% Si – 0.020% S – 0.022% P – 0.09% Ni – 2.24% Cr – 0.85% Mo – 0,23% Cu – 0.097% Al – 0.01% Ti; Grain size: 10, Austenitised at 975°C for 30mins]	67
Figure 2-46 CCT diagram for 2.25Cr-1Mo by S��ferian.....	69
Figure 2-47 CCT diagram for 2.25Cr-1Mo by Lundin, Kruse and Pendley.....	69
Figure 2-48 Optical image of P22 etched with 2% Nital.....	71

Figure 2-49 Illustrations of microstructures in HAZ of multi-pass weld metal as a, function of maximum temperatures of successive thermal cycles.....	73
Figure 2-50 Hardness change in iron-carbon martensite tempered for 1 hour as a function of tempering temperature.....	76
Figure 2-51 Schematic illustration of a weld metal cooling curve and a hypothetical continuous cooling transformation diagram showing different phase transformation that may occur as the weld metal cools to room temperature.....	79
Figure 2-52 Nature of Acicular ferrite in weld metal.....	80
Figure 2-53 Effect of oxygen content on the mechanical properties of weld metal	82
Figure 2-54 Effect of Ni content on Charpy impact toughness of as-deposited weld metals at two levels of Mn content, (a) 0.5wt% and (b) 1.6%wt%. Note that Ni is innocuous at low level of Mn but harmful at high level of Mn.....	85
Figure 3-1 Illustration of Tandem-GMAW torch set-up.....	106
Figure 3-2 Equipment setup.....	106
Figure 3-3 Transverse cross-sectional macrograph of single bead deposit, illustrating the measured bead outputs.....	109
Figure 3-4 Definition of WH, EWH, WW, EWW, MDE and SW.....	110
Figure 3-5 Surface waviness performed using a Talysurf surface profiler.....	111
Figure 3-6 Effect of WFS and CTWD on average voltage (V), current (I) and instantenous power (kJ mm^{-1}) outputs: (a) $I_{\text{Wire (A)}}$ (b) $I_{\text{Wire (B)}}$ (c) $V_{\text{Wire (A)}}$ (d) $V_{\text{Wire (B)}}$ (d) $H.I_{\text{Wire (A)}}$ (e) $H.I_{\text{Wire (B)}}$	116
Figure 3-7 Effect of WFS on (a) BW (b) BH (c) BP and (d) BA.....	118
Figure 3-8 Effect of TS on (a) BW (b) BH (c) BP and (d) BA.....	121
Figure 3-9 Effect of CTWD on (a) Bead width (b) bead height(c) Bead penetration (d) Bead angle.....	122

Figure 3-10 Effect of Preheat temperature on (a) Bead width (b) Bead Height (c) Bead penetration (d) Bead angle.....	124
Figure 3-11 Cross sections of single bead deposited using Tandem wire, showing effect of TS on weldment surface quality, using 22.5mm CTWD, at (a) Low (b) Medium and (c) High WFS.....	126
Figure 3-12 Surface appearance of Tandem-GMAW deposited weld beads...	128
Figure 3-13 Effect of variation in WFS of lead wire (A) and trail (B), on deposited bead geometry (a) H.I (b) BW (c) BH (d) BP (e) BA.....	132
Figure 3-14 Surface quality of single pass beads and transverse cross sections obtained by varying the WFS between the lead wire wire (A) and trail wire (B)..	134
Figure 3-15 illustration of torch travel directions relative to the lead wire (A) and trail wire (B).....	135
Figure 3-16 Effect of torch travel direction on deposited (a) BW (b) BH, (c) BP and (d) BA.....	137
Figure 3-17 Effect of torch travel directions on surface quality of deposited bead.....	138
Figure 3-18 Effect of torch travel directions on transverse cross sections of the deposited bead.....	138
Figure 3-19 Illustration of tandem-GMAW wire configurations (a) Series (b) Parallel.....	140
Figure 3-20 Effects of Tandem-GMAW parallel and series wire orientations, on deposited bead geometries (a) H.I (b) BW (c) BH (d) BP (e) BA.....	141
Figure 3-21 Weld bead surface and transverse cross sections obtained, showing effects of tandem-GMAW series and parallel wires configuration.....	142
Figure 3-22 Tandem-GMAW weld pool visualisation, with wires configured in (a) Series and (b) Parallel, to each other.....	143

Figure 3-23 Effect of WFS on electrical transient, voltage (left plot) and current (right plot) when (a) Lead wire WFS > Trail wire WFS (b) Trail wire WFS > Lead wire WFS.....	146
Figure 3-24 Weld pool behaviour using WFS of 5m/mins on each wire, TS of 20mm/s and 25mm CTWD.....	147
Figure 3-25 Weld pool behaviour, using WFS of 10m/mins on each wire, TS of 20mm/s and 20mm CTWD.....	148
Figure 3-26 Weld pool behaviour, using WFS of 10m/mins on each wire, TS of 20mm/s and 20mm CTWD.....	148
Figure 3-27 Surface appearance of bead profiles deposited with lead and trail wires WFSs of (a) (3.5 and 3.5) m/mins and (b) (5 and 5) m/mins	152
Figure 3-28 Macrographs of etched samples, deposited using WFS of 4.5m/mins, showing undercut defect formation, using Tandem-GMAW wire configurations of (a) Parallel (b) Series.....	154
Figure 3-29 Effect of CTWD, on generated heat input using tandem-GMAW series and parallel wire configurations.....	156
Figure 3-30 Effect of change in CTWD of series and parallel wires configuration on lead and trail arc characteristics (a) current (b) voltage (c) heat input.....	157
Figure 3-31 Weld bead surface appearances produced at different CTWD, and TS of 10mm/s, using Tandem-wire (a) Parallel configuration and (b) Series configuration.....	159
Figure 3-32 Examples of weld bead appearance produced using single-wire GMAW, with (a) without the use of arc and pulse correction (b) with use of arc and pulse correction.....	160
Figure 3-33 Effect of TS and CTWD on (a) Heat input (b) BW, and (c) BH, using SW-GMAW process.....	162

Figure 3-34 Morphology of weld bead surfaces produced using single-wire GMAW, with WFS= 6m/mins, TS = 7mm/s, and CTWD of (a) 18mm and (b) 21mm.....	163
Figure 3-35 Experimental set-up.....	166
Figure 3-36 Schematic representation of the multi-layer wall deposition method.....	166
Figure 3-37 Influence of layer number and deposition processes on relative height increment, at 7m/min WFS, and WFS/TS of (a) 23.5 and (b) 16.7.....	168
Figure 3-38 Influence of deposition process on EWW and Swav and MDE in a ten layer high wall of ten layers high, at 7m/min WFS.....	170
Figure 3-39 Effect of WFS/TS ratio on MWW and EWW of multi-layer walls, deposited using Single-wire GMAW, Tandem-wire (series) and Tandem-wire (parallel) processes, at WFS of (a) 7m/mins and (b) 10m/mins.....	171
Figure 3-40 Effect of TS on (a) SWav and (b) EWW, at a constant WFS of 7m/mins.....	173
Figure 3-41 Cross-sectional macrographs of wall, showing effect of TS on EWW and SWav at 7m/mins WFS, for (a) Tandem-wire (Series) (b) Tandem-wire (Parallel) (c) Single-wire GMAW.....	174
Figure 3-42 Effect of TS on SWav and EWW, at a constant WFS of 10m/mins.....	175
Figure 3-43 Influence of TS on SWav and EWW of walls, deposited using (a)Tandem-wire, series set up (b) Tandem-wire, parallel set-up, at 10m/mins WFS.....	176
Figure 3-44 Effect of WFS and deposition process on SWav of walls deposited at a constant WFS/TS of 23.5.....	177
Figure 3-45 Effect of WFS and deposition process on EWW and surface quality of walls deposited at constant WFS/TS of 23.5, using tandem, (a) series wire configuration, and (b) parallel wire configuration.....	178

Figure 3-46 Influence of WFS on SWav, at a lower WFS/TS of 16.7, using Tandem-wire (series and parallel) setups	179
Figure 3-47 Transverse cross-sections of walls, showing effect of WFS, at a constant WFS/TS ratio of 16.7, for (a) Tandem-wire, series set up and (b) Tandem-wire parallel set up.....	179
Figure 3-48 Relationship between MDE and EWW, for (a) SW-GMAW, Tandem-wire (series) and Tandem-wire (parallel) processes, using 7m/mins WFS (b) Tandem-wire (series) and Tandem-wire (parallel), using 10m/mins WFS.....	181
Figure 3-49 Experiment set-up.....	182
Figure 3-50 Illustration of bi-directional parallel tool path strategy utilised in building the demonstration WAAM wall.....	183
Figure 3-51 Surface appearance of wall structure built using tandem-wire (parallel wire configuration, with dimensions 250 mm × 55 mm × 9.5mm (a) Front view (b) side view. Note the excellent surface finish and straightness of the WAAM part.....	184
Figure 3-52 Surface appearance of WAAM structures built using tandem-GMAW series wire setup (a) Thin wall, deposited using ER120S-G and ER70S-G on each wire (b) Thick block, deposited using ER120S-G on both wires.....	185
Figure 3-53 illustration of skin and core deposition technique.....	186
Figure 3-54 Interaction effects of single-wire GMAW process parameters on measured bead responses, presented using (a) Linear and (b) contour plots...	189
Figure 3-55 Cross sectional macrographs of deposited bead, produced using Tandem-GMAW (series wire) configuration.....	191
Figure 3-56 Effect of process parameters on bead width for core section.....	192
Figure 3-57 Effect of process parameters on bead height for core section.....	193

Figure 3-58 Interaction effect of Tandem-GMAW (series wires) configuration process parameters, on deposition rate, shown using (a) Linear and (b) Contour plots.....	193
Figure 3-59 Equipment set-up, used for building the skin and core part (Substrate bolted to support table).....	195
Figure 3-60 Deposition tool path strategy, showing combination of Parallel beads and wide oscillation beads, for depositing the skin and core sections respectively.....	197
Figure 3-61 First layer of skin and core deposits, showing the tool path directions.....	197
Figure 3-62 Skin and core structures, built (a) without external trailing shield (b) with external argon gas trailing shield.....	198
Figure 3-63 Surface morphology of large WAAM block deposited using skin and core deposition strategy, measuring 220mm x 90mm x 55mm in dimension....	199
Figure 4-1 (a) Equipment set-up (b) AMV 5000 weld data loggers.....	205
Figure 4-2 Illustration of WAAM test block, showing deposition strategy and thermal cycle measurement procedure.....	206
Figure 4-3 Heat treatment furnace used in this study.....	208
Figure 4-4 Mechanical test matrix.....	208
Figure 4-5 WAAM deposited block (a) First two layers (b) Completed block (21-layer).....	210
Figure 4-6 Machined WAAM block, measuring (320 x 210 x 75) mm.....	211
Figure 4-7 Dye penetrant test on WAAM block.....	211
Figure 4-8 Thermal cycle measured during deposition of WAAM block.....	212
Figure 4-9 Cooling rates (from 800 to 500°C) obtained during deposition of WAAM block.....	214

Figure 4-10 Superimposition of experimental cooling rates on CCT curve of a similar 2.25Cr 1Mo alloy	215
Figure 4-11 Extraction of individual sub-block sub-segments, from the deposited WAAM block (measuring 210x75x25)	216
Figure 4-12 Micro-hardness measurement method.....	217
Figure 4-13 Hardness survey taken along the built height of the WAAM block, in (a) as-deposited, and (b) PDHT conditions	218
Figure 4-14 Comparing the effect of PDHT parameters, with respect to as-deposited sample. Error bars indicate variations in hardness value.....	219
Figure 4-15 illustration of microstructure analysis on WAAM block samples...	220
Figure 4-16 Microstructure of WAAM block sampled along the deposited height (lower and higher magnifications)	221
Figure 4-17 High magnification, SEM-EDS image of WAAM block sample, showing heterogenous dispersion of microstructural phases.....	222
Figure 4-18 Le’Pera etched microstructures of WAAM 2.25Cr 1Mo alloy (in as-deposited and heat-treated conditions)	223
Figure 4-19 Distribution of inclusions in the deposited block.....	224
Figure 4-20 WAAM sample showing (a) Distribution of inclusion (b) EDS chemical analysis spectra.....	226
Figure 4-21 XRD spectral of ER90S-G WAAM weldment in as-deposited and heat-treated conditions, showing the retained austenite {111} planes, and ferritic {110} planes.....	227
Figure 4-22 Average charpy impact tests obtained at -60°C.....	230
Figure 4-23 Charpy impact fractured samples (a) As-deposited (b) PDHT	231
Figure 4-24 SEM images of charpy v-notch impact samples in as-deposited condition and heat-treated at 50°C/hr heating/cooling rate.....	232

Figure 4-25 Microstructure of charpy v-notch samples, in as-deposited condition and PDHT at a heating/cooling rate of 50°C/hr.....	233
Figure 4-26 Charpy impact fracture WAAM sample G, obtained from: (a) bottom section of block, showing ruptured and irregularly shaped particles (b) top section of block, showing unruptured and spherical particles.....	234
Figure 5-1 Tandem GMAW set-up.....	248
Figure 5-2 Tandem WAAM: Wire setup and travel directions.....	248
Figure 5-3 Procedure for depositing the test blocks.....	250
Figure 5-4 Chemical and microstructure and mechanical test plan of deposited block.....	251
Figure 5-5 Micro-hardness test method.....	252
Figure 5-6 Instron 5500R tensile testing set-up, showing the test sample gripped in-between the fixed and movable machine jaws and laser extensometer illumination line.....	253
Figure 5-7 Appearance of tandem-GMAW deposited test block. (a) Before and (b) After wire brush cleaning.....	254
Figure 5-8 X-ray radiograph image of WAAM test block, showing sound internal structure of the weld metal.....	256
Figure 5-9 Plots of actual tested and calculated elemental content of WAAM alloys, as a function of ER120S-G and ER90S-G base wire compositions.....	258
Figure 5-10 Micrographs sections of Le’Pera etched WAAM alloys showing combination of different microstructure including, Martensite (MA), Bainite, (B) Grain boundary ferrite (GBF), Ferrite with side plate (FSP), Acicular ferrite (AF).....	260
Figure 5-11 Inclusion characteristics (a) Distribution in unetched WAAM samples (b) Morphology of inclusion in a charpy fracture sample and EDS analysis of inclusion chemical composition	262

Figure 5-12 Weld metal oxygen content analysed by combustion method.....	263
Figure 5-13 Average Hardness of deposited WAAM alloys and wrought 2.25Cr 1Mo steel metal.....	264
Figure 5-14 Plot of tensile test results of the deposited WAAM alloys.....	265
Figure 5-15 Influence of composition modification on sub-zero temperature Charpy impact toughness performance of WAAM alloys.....	267
Figure 5-16 Charpy impact fracture morphology of different WAAM samples, in as deposited condition, as a proportion of ER120S-G composition.....	268
Figure 6-1 Equipment and set up showing (a) Mass flow controller (b) Glass cell bottles immersed in a temperature-controlled water bath (c) ph meter, and (d) H ₂ S gas monitor.....	278
Figure 6-2 Appearance of test bottle content before and after test.....	282
Figure 6-3 Surface appearance of samples after exposure to corrosion.....	284
Figure 6-4 Comparative evaluation of WAAM weight loss after (a) 24hrs and (b) 72hrs test duration.....	285
Figure 6-5 Effect of exposure duration on corrosion weigh loss.....	286
Figure 6-6 Effect of exposure temperatures on corrosion average weight loss.....	287
Figure 6-7 SEM macrographs of corrosion samples.....	288
Figure 6-8 X-Ray diffraction analysis of corrosion product film (a) Obtained after 24hrs (b) after 72hrs.....	289

LIST OF TABLES

Table 2-1 Comparison of the basic characteristics between powder-feed/-bed and wire-feed process.....	18
Table 2-2 Comparison between Powder feed and Wire feed AM technology.....	18
Table 2-3 Arc mode combinations possible with Tandem-GMAW process.....	52
Table 2-4 Typical composition range of 2.25Cr 1Mo steel alloy.....	63
Table 2-5 Schlumberger material specification (MS-011513) for forgings.....	100
Table 3-1 Material compositions of (a) Steel substrate (b) Deposition wire.....	105
Table 3-2 Process parameters and range used for high deposition study.....	113
Table 3-3 Pre-set parameters used to study effect of variation in WFS of lead wire (A) and trail wire (B), when (a) WFS wire(A) > WFS wire(B) and (b) WFS wire (A) < WFS wire (B).....	131
Table 3-4 Pre-set conditions applied in the study of effect of torch travel directions relative to lead wire (A) and trail wire (B).....	136
Table 3-5 Pre-set conditions used to study the effect of wire configurations.....	140
Table 3-6 Tandem-GMAW parameter range for (a) Parallel wire setup (b) Series wire setup.....	150
Table 3-7 Pre-set deposition conditions utilised for investigating the effect of change in CTWD for Tandem-GMAW parallel and series wire configurations.....	155
Table 3-8. Pre-set deposition conditions utilised in the study of CTWD and TS for Single-wire GMAW process.....	161
Table 3-9 Pre-set condition used to study multi-layer wall deposition.....	167
Table 3-10 Effect of deposition process and WFS/TS on average layer height (aLH) and standard deviation of Layer height (SdLH), using 10-layer high walls and WFS/TS of 23.3 and 16.7.....	169
Table 3-11 Deposition condition utilised in building the demonstration wall.....	183

Table 3-12 Single-wire GMAW process parameters used to study bead parameters optimisation for depositing the skin section.....	188
Table 3-13 Tandem-GMAW, series wire parameters used to study bead parameters optimisation for depositing the core section.....	190
Table 3-14 Bead output range of tandem-GMAW (Series wire) and single-wire GMAW processes, for single layer deposits. The intervals represent minimum and maximum achievable dimensions for WFS/TS ratios of (15 – 25) and (8 – 18) respectively.....	194
Table 3-15 Parameter utilised in building the demonstration wall.....	196
Table 4-1 Composition of substrate and deposition wire.....	204
Table 4-2 Deposition parameters for building the WAAM test block.....	205
Table 4-3 Post deposition heat treatment (PDHT) matrix.....	207
Table 4-4 Characteristics of oxide inclusions in the deposited weld block.....	225
Table 4-5 Tensile test results of block samples in as-deposited and PDHT conditions.....	228
Table 5-1 Chemical compositions of tandem deposition wires and substrate.....	247
Table 5-2 Composition modification plan adopted in this study.....	249
Table 5-3 Preset tandem-GMAW parameters utilised for this study and measured arc characteristics obtained during deposition, using 10mm/s TS. Note (1) and (2) represent the two tandem-GMAW power sources.....	255
Table 5-4 Results of ICP-OES tests conducted on deposited WAAM alloys, showing percentage indicating proportion of ER120S-G, and balance is ER90S-G.....	257
Table 5-5 Analysis of inclusion in deposited WAAM alloys.....	261
Table 5-6 Hardness of modified compositions, as a proportion of ER120S-G in the WAAM alloys and wrought 2.25Cr 1Mo steel metal.....	264
Table 6-1 Experimental matrix and test parameters for corrosion study.....	278
Table 6-2 Samples utilised for corrosion tests.....	279
Table 6-3 Chemical composition of test samples.....	279
Table 6-4 EDS analysis of corrosion samples, in wt %.....	290

LIST OF EQUATIONS

(2-1)	35
(2-2)	43
(2-3)	67
(2-4)	68
(2-5)	81
(2-6)	81
(2-7)	83
(2-8)	90
(2-9)	90
(3-1)	107
(3-2)	107
(3-3)	107
(3-4)	107
(3-5)	109
(3-6)	111
(3-7)	113
(3-8)	116
(3-9)	120
(5-1)	248
(5-2)	249
(5-3)	251
(6-1)	281
(6-2)	281

LIST OF ABBREVIATIONS

3DP	3D printing
AF	Acicular ferrite
AISI	American Iron and Steel Institute
AIP	Average instantaneous power
aLH	Average Layer height
AM	Additive manufacture
ANOVA	Analysis of variance
AR	Aspect ratio
ASME	American society of mechanical engineers
ASTM	American Society for Testing and Materials
AWS	America welding society
BA	Bead angle
BH	Bead height
BR	Burn-off rate
BTF	Buy-to-fly
BW	Bead width
CGHAZ	Coarse grain heat affected zone
CMT	Cold metal transfer
CO ₂	Carbon dioxide
CR	Corrosion rate
CS	Cross sectional
CTWD	Contact tip to work distance
DLD	Direct Laser Deposition
DLF	Directed light fabrication (DLF)
DMLS	Direct metal laser sintering
DWF-PAM	Double-wire feed and plasma arc additive manufacturing

EAC	Environmentally assisted cracking
EBFF	Electron beam freeform fabrication
EBM	Electron beam melting
EDS	Energy dispersive spectrometer
EPDC	Electron positive direct current
EWH	Effective wall height
EWV	Effective wall width
FeS	Iron sulphide
FGHAZ	Fine-grain heat affected zone
FWHM	Full width at half maximum
GB	Grain boundary
GMAW	Gas metal arc welding
GTAW	Gas tungsten arc welding
NaCl	Sodium chloride
NaOH	Sodium hydroxide
NDT	Non-destructive testing
HAZ	Heat affected zone
HCl	Hydrogen chloride
H. I	Heat input
H ₂ S	Hydrogen sulphide
H _{THP}	Higher temperatures and pressure
ICCHAZ	Intercritical coarse-grain heat affected zone
ICP-OES	Inductive coupled plasma optical emission spectrometer
ISO	International Organization for Standardization
JIP	Joint industrial project
LC	Laser consolidation (LC)
LENS	Laser engineering net shaping (LENS)

LOM	Laminated object manufacturing
MAG	Metal active gas
MDE	Metal deposition efficiency
MIG	Metal inert gas
MLMB	Multi-layer multi-bead
MS	Material specification
MWW	Maximum wall width
NACE	National Society of Corrosion Engineers
ODPP	One-droplet-per pulse
OFAT	One-factor-at-a-time
PAGB	Prior austenite the grain boundaries
PAW	Plasma arc welding
PB	Powder bed
PD	Penetration depth
PDHT	Post deposition heat treatment
PWHT	Post weld heat treatment
RSM	Response surface methodology
SAW	Submerged arc welding
SdLH	Standard deviation of average layer height
SEM	Scanning electron microscopy
SiC	Silicon carbide
SLM	Selective Laser melting
SLS	Selective laser sintering
SMAW	Shielded metal arc welding
SSC	Sulphide stress corrosion
SW	Single wire
SWav	Average surface waviness

SWF-PAM	Single-wire plasma arc process
TEM	Transition electron microscope
TS	Travel speed
TTT	Time temperature transformation
UC	Ultrasonic consolidation
UNS	Unified numbering system
WAAM	Wire and arc additive manufacture
WELPC	Welding Engineering and Laser Processing Centre
WFS	Wire feed speed
WH	Wall height
WM	Weld metal
WW	Wall width
YS	Yield strength

1 PROJECT INTRODUCTION

This dissertation is one of a two-part project, partly funded by Schlumberger, the world's largest oil services company, headquartered in Houston Texas, USA. This work was carried out in collaboration between the Schlumberger welding research department, in the USA and the department of Welding Engineering and Laser Processing Centre (WELPC), Cranfield University, UK.

The broad focus of the project was to provide Schlumberger, and in particular one of its divisions OneSubsea, the theoretical and technological capabilities, to enable the company to leverage WAAM technology for the manufacture of selected component(s) used in the oil and gas environment. The study was conducted in two complimentary parts. The first part which involved PhD research project, was tasked with undertaking required fundamental experimental studies and analysis; while the second part, a Joint Industrial Project (JIP), was responsible amongst others, for developing an appropriate WAAM digital methodology for actualising the fabrication of prototype component(s), such as a drilling bit.

The research project was structured into four phases.

- The first phase included investigation of WAAM process parameters and conditions, with a view to simultaneously achieve improved productivity and surface quality of the as-deposited structure.
- The second phase investigated the performance of a large metallic WAAM structure, fabricated by using ER90S-G wire. Such large components are traditionally manufactured from forgings.
- The third phase involved a study to carefully mix and modify the composition of different welding consumable wires, with a focus to achieve improved as-deposited material properties.
- In the fourth part of the study, the corrosion performance of the various WAAM steel materials, produced under different processing conditions were investigated, with a view to understanding how they compare, under a laboratory simulated sour oil and gas environment.

1.1 Background of Research

Traditionally, heavy-walled components utilised for marine, oil and gas (Petrochemical or Subsea) applications are fabricated by subtractive manufacturing methods applied to forgings. These forgings are commonly derived from ASTM A182 2.25Cr-1Mo steel, a type of Cr-Mo steel material, used due to its outstanding through thickness hardenability and strength to withstand high pressures (Deng, D. and Kiyoshima, S., 2007), high weldability, machinability (Choi, D. H. et al., 2012). Additionally, they exhibit relatively good resistance to corrosion, excellent toughness and are relatively low in cost. (Lima, W. F. *et al.*, 2017)

2.25Cr-1Mo alloy material such as ASTM A182 F22 forgings are usually supplied in the quenched and tempered condition. They are utilised for example to manufacture pressure components such as valve bodies and spool bodies (Elrefaey, A. *et al.*, 2018; Javadi, Y. et al., 2017; Queguineur, A. et al., 2018; Deng, D. and Kiyoshima, S. 2007), (which are components in Subsea assemblies such as Christmas trees), Figures 1-1 (OneSubsea, 2020), while near equivalent steel grades such as ASTM 4130 are used for oil and gas drill bits Figures 1-2. (Schlumberger, 2020).

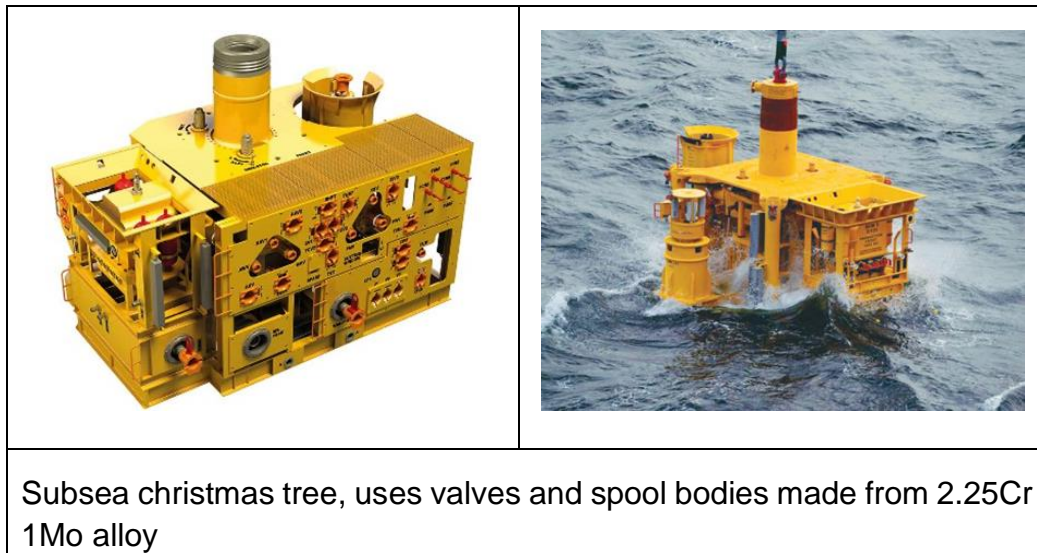
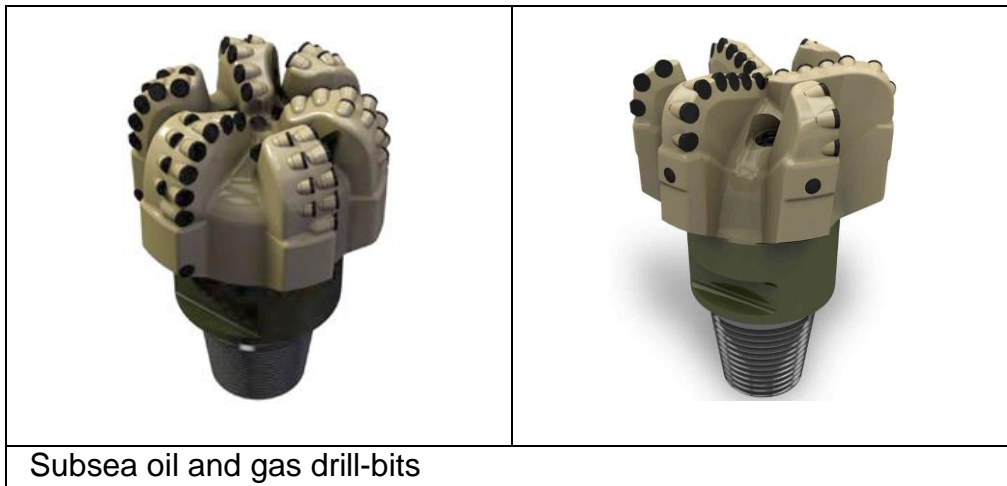


Figure 1-1 Examples of subsea assemblies used for oil extraction (OneSubsea, 2020)



Subsea oil and gas drill-bits

Figure 1-2 Subsea Drill bit (Schlumberger, 2020)

2.25Cr-1Mo alloys are used because, they possess outstanding strength at higher temperatures and pressure (HTHP) (Deng, D. and Kiyoshima, S. 2007; Choi, D. H. et al., 2012), (where HTHP refer to a bottom hole pressure in excess of 1000 bar (15,000 psi) and 177°C (350°F), Sridhar, N. et al. (2018). Additionally, they exhibit excellent corrosion resistance, excellent toughness and have lower cost (Lima, W. F. et al., 2017). They could also find application in other marine components such as subsea collet connectors, shown in Figure 1-3(a), which consists of parts including Upper hub, Lower hub, and Claw made from F22 forgings, as shown in Figure 1-3(b) (Zhang, K. *et al.*, 2016).

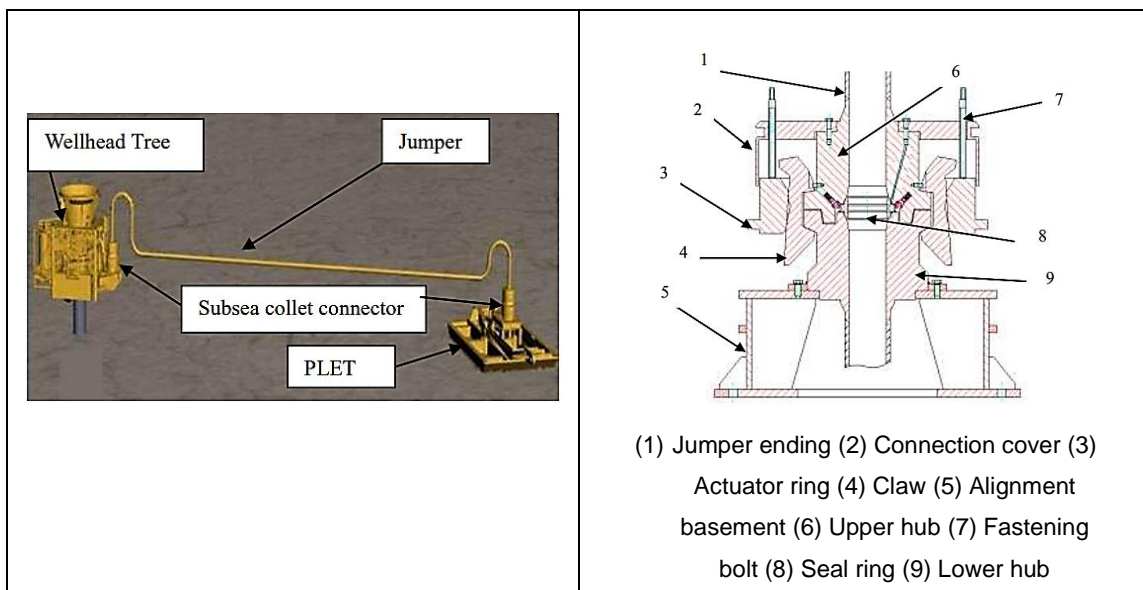


Figure 1-3 (a) M-Jumper and subsea connector schematic diagram (b) Subsea collet connector structure diagram. Zhang, K. *et al.* (2016)

Other examples of components manufactured using ASTM A182 F22 forgings are subsea connector riser joints, (Ortolani, M. and Novelli, P, 2013). Petrochemical reactor vessels, shown in Figures 1-4 and Figure 1-5, are also manufactured using A182 2.25Cr-1Mo steel material. (Takauchi, H. et al., 2017)

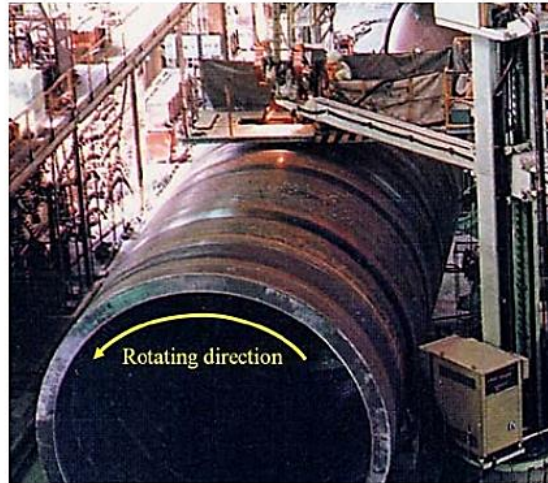


Figure 1-4 Tandem SAW of shell ring for reactor vessel fabrication (Takauchi, H. et al., 2017)

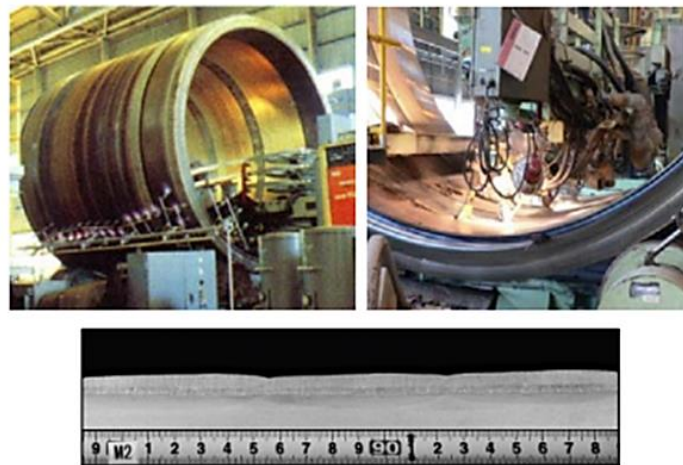


Figure 1-5 Strip overlay welding of inside shell ring (Takauchi, H. et al; 2017)

The forgings typically undergo welding/cladding, pre- and post-heat treatments, etc. before obtaining the final product geometry. However, the subtractive manufacturing method can be associated with high lead time, low design flexibility, high tooling costs, machining challenges and higher material wastage.

It can also have relatively high inventory and manufacturing costs, as well as low manufacturing efficiency.

1.2 Why WAAM

Wire and Arc additive manufacturing (WAAM) is a variant of AM which builds a part by using a heat source to melt and fuse solid feed wires (Ghasri-Khouzani, M. et al., 2017). Its acceptance in the oil and gas industry has occurred at a much slower pace compared to the aerospace or medical sectors. (Sireesha, M. et al., 2018; Burns and Wangenheim, 2019).

However, there has been a recent quest in the oil and gas industry to source, develop and utilise more cost-efficient manufacturing technologies. This quest has partly been driven by the need to drive down the ever-increasing costs of production, and to improve the sustainability of manufacturing processes. Therefore, WAAM technology has been hailed as a viable alternative due to its important industrial attractiveness, including the ability to shorten manufacturing lead times, increase design flexibility and provide overall manufacturing efficiency, beneficial for the oil and gas industry (Sireesha, M. et al., 2018; Burns M, and Wangenheim C., 2019; DebRoy, T. et al., 2018).

Furthermore, AM can potentially be quickly deployed and also potentially scalable. Savings associated with storage of parts can be achieved as components can be manufactured as the need arise. This decreases inventory of spares and generally reduces lead times for replacing essential parts (DebRoy, T. et al., 2018; Sireesha, M. et al., 2018; Burns M, and Wangenheim C., 2019).

1.3 Research challenges

The market share of AM in the oil & gas sector is expected to increase above \$60 billion worldwide by 2030, its growth rate is slowly adjusting and consolidating, as shown in Figure 1-6, hence, it is projected this growth will be substantially higher in the next few years, which will make AM a sustainable technology as it matures (Vendra, L. and Achanta, A., 2020).

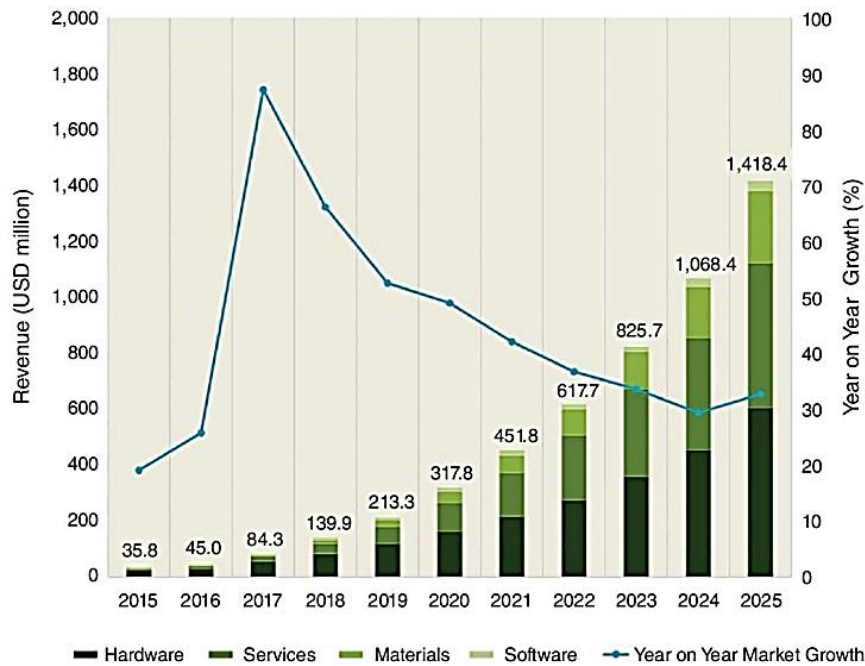


Figure 1-6 AM revenue forecast and Year on Year Market Growth in the oil and gas industry (Vendra, L. and Achanta, A., 2020)

This progress could be driven by advances in AM materials and technologies and the need to introduce new business models. (Thompson, M. K. *et al.*, 2016). In view of these projections, the need for increased participation from industrial stakeholders and research organisations, in advancing this technology for oil and gas applications cannot be overemphasised.

The integrity and reliability of steel components fabricated using AM process, is highly dependent on the microstructure and mechanical properties of the deposited material (Koseki, T., 2005). Although WAAM technology possess numerous potential technological advantages as earlier explained, it is however still saddled with some materials and processing challenges. The challenges currently limit its broad application and economic competitiveness, for example in the manufacture of large heavy-walled oil and gas components. These challenges are described as follows:

1.3.1 Issues related to productivity (deposition rate) and surface quality

Lower productivity issues could be a significant challenge of AM technology, because it plays a major role in influencing the unit cost of manufacturing. Also, it forms part of the business driver towards cost justification for adopting the AM technology in place of conventional manufacturing techniques. As the productivity of AM technology increases, the cost advantage associated with increased throughput would make this process more justifiable (Baumers *et al.*, 2016).

The WAAM process utilises a heat source to melt and deposit the filler metal. The actual technique and processing parameters largely determine the deposited bead sizes and consequently the size of the built parts (DebRoy, T. *et al.*, 2018). Hence, increasing productivity, through higher filler metal deposition rates leads to increase in the heat generated. This is a critical challenge as the generated heat can cause the warping and deformations of the deposited part, resulting in poor geometrical tolerance and potential untimely failure (Klingbeil, N. W. *et al.*, 2002; Mughal, M. P. *et al.*, 2005; Alimardani, M. *et al.*, 2007)

Increased deposition rate could lead to high heat generation and cause significant increases in surface waviness of the part, which potentially require high machining costs to correct the dimensional tolerance of the part. This could limit the commercial competitiveness of the WAAM technology (DebRoy, T. *et al.*, 2018). Therefore, development of a robust WAAM strategy which maximises productivity and surface quality of parts, would significantly benefit this technology.

1.3.2 Successive thermal cycle generation

The generation of localised repeated cycles of melting and solidification, owing to the characteristic layer-by-layer deposition of WAAM materials, leads to microstructure variation in the built part (Yan, F. *et al.*, 2017).

The complex heterogenous microstructure developed, owing to the successive thermal cycle generations, could cause significant variations in mechanical properties of the deposited part (Song, H. Y. *et al.*, 2014). This leads to poor

charpy impact toughness and diminish the integrity of the WAAM part (Pandey, C. *et al.*, 2019). Hence investigation of this metallurgical challenge is critical to deploying the WAAM components for oil and gas applications, especially those requiring exposure to harsh service environments (DebRoy, T. *et al.*, 2018).

1.3.3 Lack of optimised deposition feedstock

The feedstock materials used for producing the finished part is critical to the WAAM process, because it determines the properties of a component and influences its performance when deployed in service (Sun, C. *et al.*, 2021).

Typical commercially available low alloy steel wire materials used for WAAM applications are originally designed for welding applications. The wires have relatively lean alloying chemistry and solidify at faster rates. Regrettably, the as-deposited steel wire feedstocks do not possess a combination of excellent strength and toughness (Zhang, T. *et al.*, 2015), making them less suitable for WAAM application.

The unique material development and processing challenges still limits the amount of WAAM specific low alloys steel wires that have been produced for commercial application (Zhang, T. *et al.*, 2015). Knowledge of the material properties developed during WAAM deposition is essential, prior to the large-scale use for manufacturing critical load bearing components (Sames, W. J. *et al.*, 2016). The development of specially tailored alloy compositions adapted for WAAM processes, which can produce improved as-deposited compositions, metallurgy and mechanical properties, will be a game changer for the AM technology.

1.4 Research questions

The two pertinent questions this study seek to address are as follows:

- The ideal way of building parts through WAAM technique, is to limit deposition rate to about 3kg/hr for steel, to enhance the surface and dimensional quality. But how can deposition rate be maximised, while achieving high tolerance and surface quality of the manufactured part?
- Alloy 2.25Cr 1Mo steels are typically used in manufacturing heavy-walled component in marine oil and gas industry, through subtractive manufacturing techniques. But can the use of WAAM technology achieve the minimum material specification demanded for these components? and how does their corrosion performance compare, when exposed to a sour service environment?

1.5 Thesis outline

The thesis comprises of seven chapters including this project introductory chapter.

Chapter 2 on literature review, begins with a brief comparison of subtractive and additive manufacturing processes. An overview of the additive manufacturing technology, with a particular attention to wire and arc additive manufacturing process was then given. Automation of WAAM process, including parameter generation, path planning strategy, thin and thick block building are then discussed,

A review of productivity and surface quality issues associated with the WAAM process was presented, followed by description of high energy multi-wire GMAW process, as well as skin and core deposition strategy, were presented as a technique to maximise both productivity and surface quality characteristics of WAAM part.

An overview of 2.25Cr 1Mo alloy composition, with a particular focus on the microstructure of the deposited weldment, was presented. The review highlighted some of weldability issues of the alloy and use of heat treatment in improving the weldment property. The section then discusses a method for improving the as-

deposited property of weldment, through mixing different wire compositions to obtain a modified composition. Some studies by other authors utilising this technique, with tandem-wire GMAW process in actualising this technique were reviewed.

Furthermore, corrosion of steel materials in the oil and gas environment was discussed, with reference to the corrosion types, including sour corrosion and factors influencing corrosion. Some studies conducted by other authors on corrosion of WAAM alloys was presented. Finally, a summary of the literature and research gap based on the review was presented

Chapter 3 presented process parametric studies on high productivity and surface quality, utilising tandem-wire and single-wire GMAW processes. This then culminates in reporting of the manufacture of a thin rectilinear wall structure and a relatively large skin and core part. ER120S-G wire was utilised for this study.

Chapter 4 investigates the generation of thermal cycles and application of post processing heat treatment during WAAM of a large steel block. Microstructure and mechanical tests were conducted to characterise the performance of the WAAM block, with respect to a given minimum requirement.

Chapter 5 presents experimental modification of alloy 2.25Cr 1Mo type wire composition, using ER120S-G wire compositions, containing a higher nickel content, with a view to improving the properties, particularly, the low temperature charpy impact toughness. Microstructure and mechanical tests were also performed to characterise the performance of the modified composition, with respect to a base or starting compositions.

In chapter 6, assessment of the corrosion performance between different WAAM alloys obtained under different processing conditions and a similar wrought counterpart was presented. The experimental procedures deployed in the investigations are described and the effect of some environmental conditions on the corrosion performance of the alloys were determined.

Chapter 7 provides a summary of the overall conclusions from the research studies and suggest other possible areas for additional research.

2 LITERATURE REVIEW

2.1 Subtractive versus additive manufacturing methods

Traditional industrial fabrication of components, such as in the marine oil and gas industry generally use large, forged materials (Queguineur, A. et al., 2018), which undergo subtractive processes to obtain the finished product (Almeida, P.M.S. and Williams, S., 2010). Challenges associated with lead time occur as a result of the need to design and manufacture the required tools, the size of forged materials and limitations imposed by the technology. Problems with high material wastage also exists (Queguineur, A. et al., 2018; Almeida, P.M.S. and Williams, S, 2010), and defects such as shrinkage cavities, oxide notches, etc., can often occur in the forged products, which could lead to enormous and extensive repairs or outright rejection of parts (Queguineur, A. et al., 2018).

Unlike the subtractive method of manufacturing, which achieves the desired geometry by removing surplus materials from a large forging feedstock, Additive Manufacturing (AM) technology builds near-net-shape parts in a layer-by-layer fashion (Ghasri-Khouzani, M. et al., 2017).

AM technology, nevertheless, has some challenges including deficiency in its manufacturing precision, low fatigue performance of components, trade-offs, or challenges in maximising both cost and efficiency (Ding, D. et al., 2015a).

The low production rate of WAAM is a challenge in manufacturing large batch-sized components (Hirtler, M. et al., 2020). Cost savings of over 30% are achievable compared to conventional subtractive processes; however, AM is presently more profitable for small volume production of parts, because of its high recurring costs, associated with high raw material cost. Figure 2-1 (Zadi-Maad, A. et al., 2018).

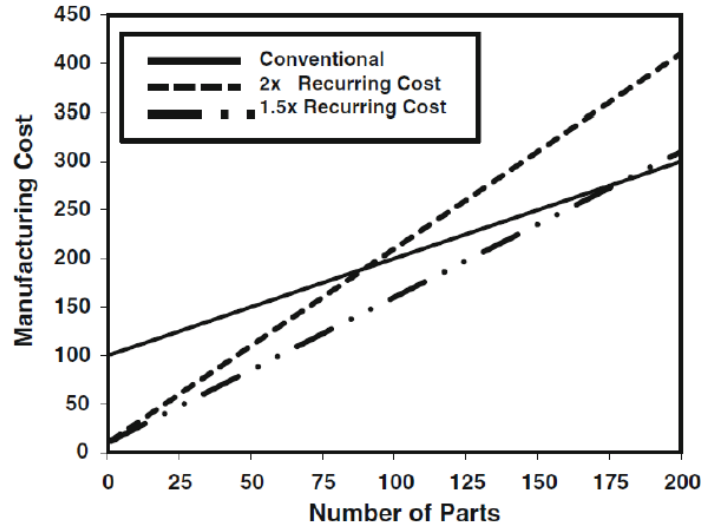


Figure 2-1 Cost comparison between AM and conventional process. (Zadi-Maad, A. et al., 2018)

In addition, metallurgical dissimilarities exist between components manufactured by forging and AM techniques. Hence, the inherent anisotropy in mechanical properties, microstructural heterogeneity and defects peculiar to AM processes certainly needs addressing for critical applications, especially those structure that will be exposed to harsh environments (DebRoy, T. et al., 2018).

2.2 What is Additive manufacture

Additive manufacture (AM) technology is a relatively novel method of fabrication (Yan, F. et al., 2017; Ghasri-Khouzani, M. et al., 2017), that have transformed manufacturing from 'negative' to 'positive', addition of material, since its inception in 1987 when the first rapid prototyping machine was pioneered by 3D Systems, in the US (Hascoet, J. Y., et al., 2014; Herzog, D. et al., 2016).

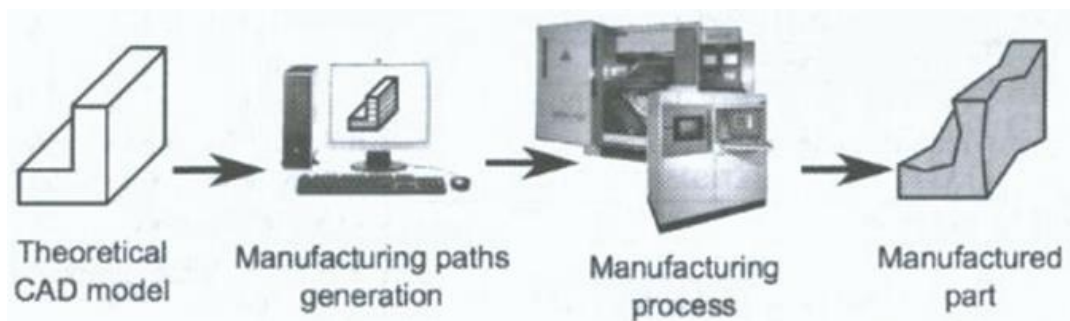


Figure 2-2 Schematics of the basic chain for AM (Hascoet, J. Y., et al., 2014)

The purpose was to enable wholly functional parts to be built directly, using real materials and digital models of the parts, unlike rapid prototyping which produced non-functional parts. This has now led to a whole new array of possible designs, in combination with shapes and multi-material components, impossible or difficult with traditional methods (Hascoet, J. Y., et al., 2014; Herzog, D. et al., 2016).

Hence, AM has matured from mere rapid prototyping to rapid manufacturing of parts, thus requiring not only huge process knowledge itself, but also knowledge of the effect of process parameters, on generated microstructure and consequently, properties of the produced parts (Hascoet, J. Y., et al., 2014; Herzog, D. et al., 2016).

Advancement in AM of various metals has enabled the discovery of several niche application, through concerted R&D and industrial collaborations, where it has found applications for example, in repair of parts, manufacture of biomedical implants, aerospace structures and high-temperature components (Sames, W. J. et al., 2016).

Some illustrations of mixed applications of AM technology, which ranged from integrating a cooling channel in a component, to producing a part with functional gradient properties, are shown in Figure 2-3.

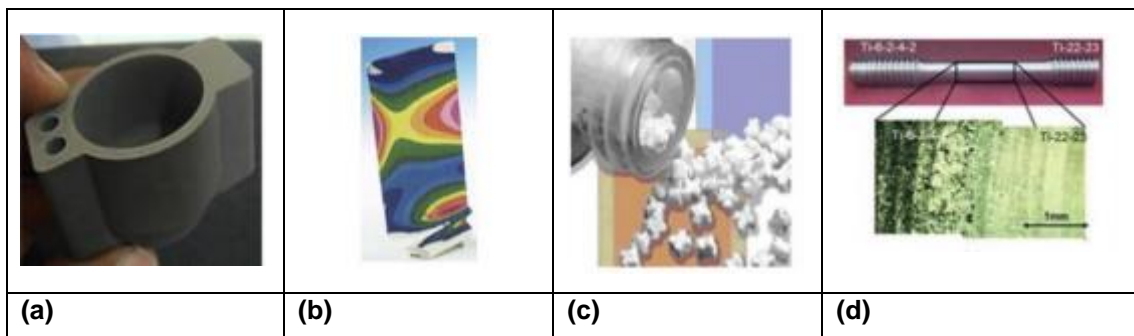


Figure 2-3 (a) A rapid tool with conformal cooling channel built using EoS’s SLS process, (b) Stress pattern of a blade captured in colour using ZCorp’s 3DP, (c) Time-delivery drug produced using Therics’s 3DP, (d) Functional gradient metallic objects made using OptoMec’s LENS (Karunakaran, K. et al., 2012)

2.2.1 Benefits of Additive manufacture

Additive manufacture (AM) technology has found significant attractiveness as an industrial technology employed in manufacturing processes (Yan, F. et al., 2017; Ghasri-Khouzani, M. et al., 2017; Herzog, D. et al., 2016). One reason is because of the possibility of manufacturing intricate near-net-shape components by consecutive deposition of multiple layers-upon-layers of materials (Yan, F. et al., 2017; Ghasri-Khouzani, M. et al., 2017; Herzog, D. et al., 2016.), which ordinarily would be impossible or challenging with the use of orthodox subtractive method of manufacturing (Brandl, E. et al., 2010).

Compared to the traditional manufacturing method by machining, AM has proven to have a high potential for efficiently speeding up the development of products, for example, reducing production lead time in the manufacture of extremely complicated, interconnected shapes (Brandl, E. et al., 2010; Ghasri-Khouzani, M. et al., 2017). It also has the potential to reduce manufacturing costs by minimising wastage of materials, owing to increased material utilisation; while ensuring excellent performance of the final product (Williams, S.W. et al., 2016) (Brandl, E. et al., 2010). Scrap reduction by AM leads to reduced impact on the environment and increased financial gain (Sireesha, M. et al., 2018).

It can potentially enable unrivalled design flexibilities and associated weight savings, for example, complex geometrical assemblies originally made of several sub-assemblies, (e.g., flanged pairs) can be manufactured as a single unit (Williams, S. W. et al., 2016).

An example of a technical challenge associated with the subtractive process is the manufacture of an aircraft landing gear which consists of intricate “budlike” structures, traditionally shaped through forging, Figure 2-4

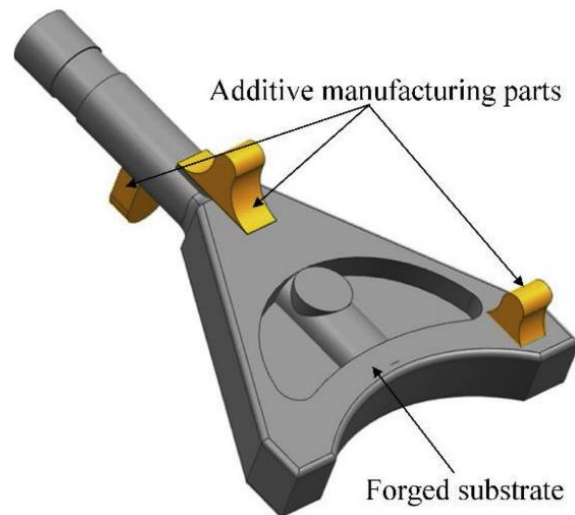


Figure 2-4 Schematic of an aircraft landing gear fabricated by forging and additive manufacturing (Liu, X. et al., 2020)

The grey section indicated in Figure 2-1 is fabricated by forging, while the more complex parts indicated in yellow can be fabricated using the AM method. The high flexibility and material utilisation associated with the use of AM makes the fabrication of the budlike features easier and less expensive than forging (Liu, X. et al., 2020).

Some examples of products traditionally machined from forging, but manufactured using AM technology include- A fuel nozzle of the LEAP aero engine, shown in Figure 2-5(a) and Ti-6Al-4V bracket for Airbus A350 shown in Figure 2-5(b) (Herzog, D. et al., 2016).



(a)



(b)

Figure 2-5 (a) LBM-produced fuel nozzle of the LEAP aero engine (from GE Aviation). Integrated design built as one piece with optimised interior channels and a weight saving of approximate 25%, (b) LBM-produced Ti-6Al-4V bracket for Airbus A350 (from LZN Laser Zentrum Nord GmbH and Airbus), with topology optimised bionic design resulting in approximately 30% weight saving compared to conventional milled bracket. Three brackets with support structures on a build plate after LBM process (left) and finished part (right) (Herzog, M. et al., 2016).

2.2.2 Additive manufacturing of metallic materials

A basic metallic AM system uses a heat source, metallic feedstock and a computer driven motion system that guides the deposition and fusion of the feedstock in predetermined locations, using a digital model of the component. (Herzog, D. et al., 2016)

The competitiveness of AM for metallic component fabrication, in comparison to other traditional technology is dependent on the geometrical complexity and production quantity. As indicated in Figure 2-6, the competitive edge of AM can be increased when employed in manufacturing metallic components with low, medium and high complexity at relatively lower production volumes, compared to other manufacturing methods (Ding, D. et al., 2015a).

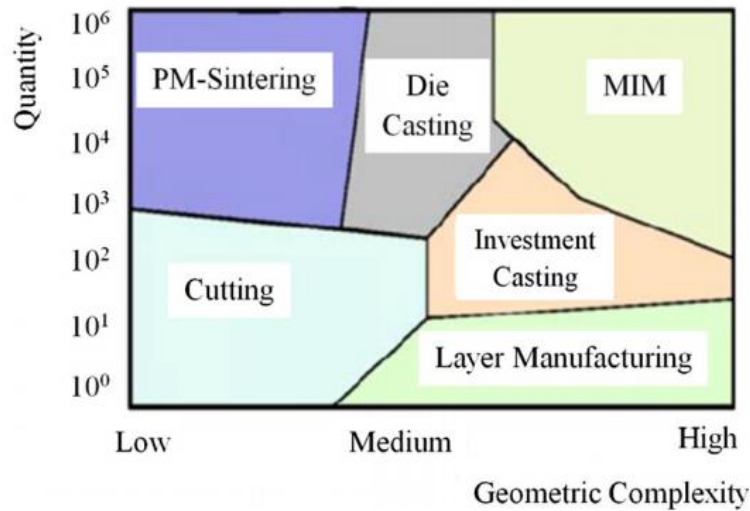


Figure 2-6 Comparison between the Geometric complexities and Quantity of AM technology and other manufacturing options (Metal injection moulding, MIM, PS-Sintering powder metallurgy sintering) (Ding, D. *et al.*, 2015a)

2.2.3 Classification of additive manufacture

Numerous variants of AM techniques have evolved in the last three decades, with valuable results (Ghasri-Khouzani, M. *et al.*, 2017). Considering how additive material is supplied, common AM technologies can be categorised as either a powder-feed/powder-bed or a wire-feed process. The bulk of AM research have predominantly been devoted to areas of powder-feed/-bed AM, with laser or electron beam system generally used as the energy source (Ding, D. *et al.*, 2015a).

A comparison of the basic characteristics between powder-feed/-bed and wire-feed process is given in Table 2-1 (Ding, D. *et al.*, 2015a).

Table 2-1 Comparison of the basic characteristics between powder-feed/-bed and wire-feed process (Ding, D. *et al.*, 2015)

Additive materials	Processes	Layer thickness (um)	Deposition rate (g/min)	Dimensional accuracy (mm)	Surface roughness (um)
Powder	LC	N/A	1 – 3	±0.025 – ±0.069	1 – 2
	SLM	20 – 100	N/A	±0.04	9 – 10
	SLS	75	≈0.1	±0.05	14 – 16
	DLF	200	10	±0.13	≈20
Wire	WAAM	≈1500	12	±0.2	200
	EBF	N/A	Up to 330	Low	High

Table 2-1, shows that powder-feed/-bed system can fabricate parts with higher geometrical tolerance, compared to wire feed process. Nevertheless, powder-feed/-bed technology have very low deposition rates.

Table 2-2 shows a comparison between Powder feed and Wire feed AM technology. The material usage efficiency of wire-feed AM is higher, reaching almost a 100 % of the wire material used in depositing the component and the deposition rate is much greater, reaching almost 2500 cm³ /h (330 g/min for stainless steel), compared to powder feed AM (Ding, D. *et al.*, 2015a).

Table 2-2 Comparison between Powder feed and Wire feed AM technology (Ding, D. *et al.*, 2015)

Characteristics	Powder feed system	Wire feed systems
Cost	High	Medium
Quantity	Variable	High (Ti, Fe, Ni), Variable Al
Deposition rate	0.1 – 0.2 kg/hr	Several kg/hr
Feeding	Complicated, unless side-fed (in case of powder feed)	Easy, well established industrial process
Material Efficiency	Typically, 40 – 60%	100%
Complexity	High	Low to medium
Safety issues	Yes – especially Ti/Al	No
Recycling	Possible with processing	Not required

In view of these differences, certain trade-offs between the requirement for high deposition rate and high geometrical tolerance is necessary in choosing the type

of AM processes desired for a given application or component (Ding, D. *et al.*, 2015a).

2.2.4 AM material cost and utilisation

Welding wire is a cheap form of feedstock, compared to powder feedstock. The price depends on the type of material, composition, and nominal diameter. The price of steel varies between £2 /kg and £15 /kg, aluminium is between £6 /kg and £100 /kg, while Ti–6Al–4V range between £100 /kg and £250 /kg. In addition, the use of wires prevents several challenges associated with powder feedstock, including the control of particle size or distribution, which influences the process performance. Importantly, the possibility of contamination is low in wire feedstock compared to powder, because immediately following deposition, the wire is completely molten and becomes part of the final component (Williams, S. W. *et al.* 2016). The use of commercially available inexpensive welding wire potentially makes wire-feed AM technology economically viable (Haden *et al.*, 2017).

2.2.5 Classification of wire-feed AM processes

With respect to the source of energy employed in deposition of the metal, Wire-AM can be classified as- laser based, arc welding-based and electron beam-based processes.

Laser has the lowest energy efficiency (2–5) % of the trio, followed by electron beam (EB) with energy efficiency of (15–20 %), but EB requires a high vacuum environment. In comparison, the energy efficiency of arc welding processes for example gas metal arc welding (GMAW) or gas tungsten arc welding (GTAW) processes can reach as much as 90 % under certain conditions. Furthermore, traditional arc welding equipment is relatively lower in costs, compared to laser or electron beam equipment (Ding, D. *et al.*, 2015a).

Figure 2-7 illustrates the electron and laser beam systems.

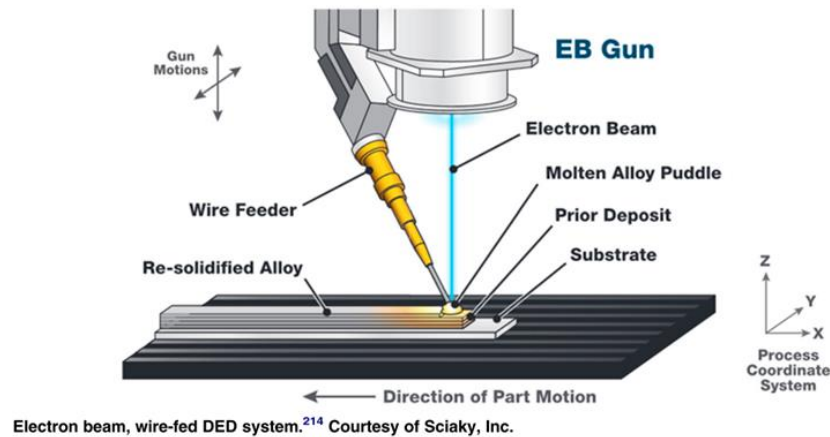


Figure 2-7 Illustration of an electron beam system (Sames, W.J. et al., 2016)

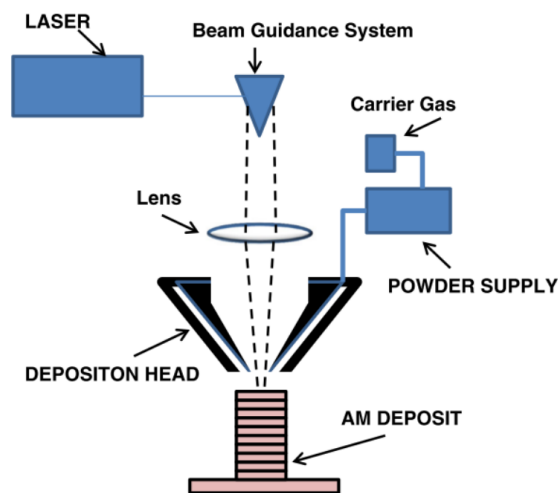


Figure 2-8 Illustration of a laser beam system (Herzog, D. et al., 2016)

2.3 Wire and arc additive manufacturing (WAAM)

Wire and arc additive manufacturing (WAAM) is a unique variant of wire-feed AM (Li et al., 2018), which has continued to gain wide acceptance as a suitable and efficient technology for the rapid manufacturing of engineering parts for several applications (Ding, D., et al., 2015b; Yan, F. et al., 2017; Herzog, D. et al. 2016).

WAAM employs a combination of electric arc heat source and wire as feedstock and incorporate hardware which currently use standard, off-the-shelf welding equipment: including welding power source, torches and wire feeding systems. A robotic system or computer numerical controlled gantries can be used to provide the required motion (Williams, S.W. et al., 2016).

A typical diagram of a robotic WAAM system (GMAW-based) is presented in Fig. 2-9 (Ding, D. *et al.*, 2015b).

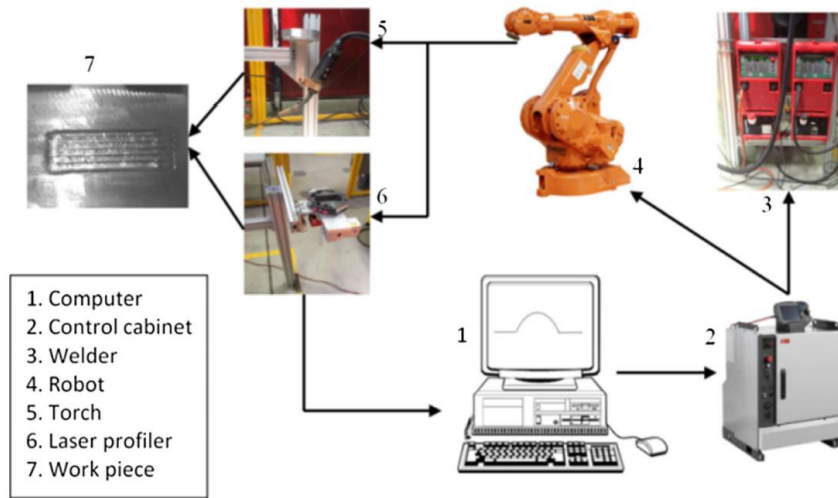


Figure 2-9 Schematic diagram of an experimental robotic WAAM system

A number of studies have been conducted on WAAM process, using gas metal arc welding (GMAW), gas tungsten arc welding (GTAW) or plasma arc welding (PAW) as a heat source (Ding, D. *et al.*, 2015a). Figure 2-10 shows schematic illustrations of the GMAW, GTAW and PAW processes.

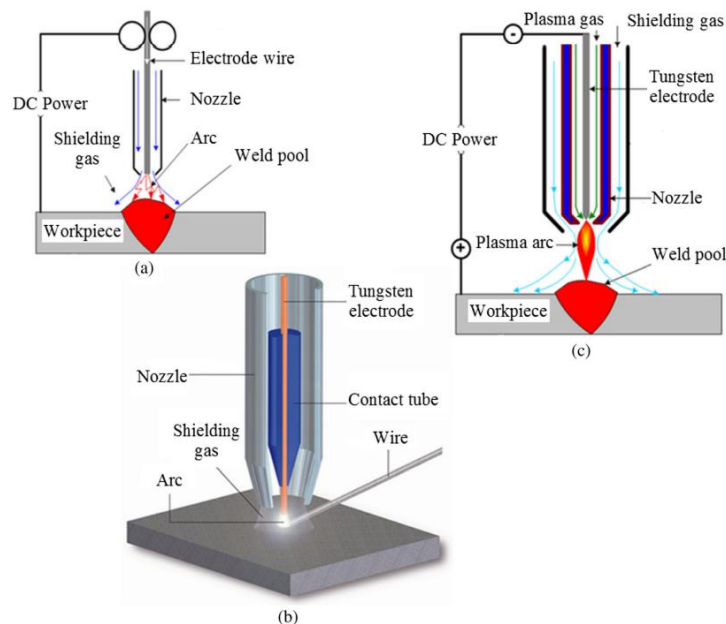


Figure 2-10 Schematic illustrations of the (a) GMAW, (b) GTAW and (c) PAW process. (Ding, D. *et al.*, 2015a)

2.3.1 GMAW process in WAAM technology

In the GMAW welding process an electric arc is formed between a consumable wire electrode and the metallic workpiece. The wire is typically positioned vertically to the substrate. Four principal methods of metal transfer exist in the GMAW process which includes- Short-circuit, spray and pulsed-spray, globular, and dip transfer. With each possessing a distinctive characteristic (Ding, D. *et al.*, 2015a). Short circuit metal transfer occurs when the metal wire is in contact with the weld pool. Spray transfer of metal occurs through clusters of small droplets with sizes equal to or less than the wire diameter, while globular transfer of metal occurs through large droplets with the size four times larger than the wire diameter. Dip transfer occurs at low current levels, with recurring short-circuits occurring between the metal wire and melt pool. It is usually utilised in welding thin sheet materials, and in AM processes, owing to its high deposition rate and low heat input generated (Ding, D. *et al.*, 2015a).

When possible, MIG (Metal Inert Gas) welding, also known as MAG (Metal Active Gas) and in the USA as GMAW (Gas Metal Arc Welding), is the process of choice for WAAM, and is commonly used for depositing a number of ferrous and non-ferrous materials. The coaxiality of the consumable wire electrode, with the welding torch enables continuous feeding into the arc from a coil, resulting in easier tool path automation. (Williams, S. W. *et al.*, 2016; Shoeb, M., 2013; & Kamble, A. G. and Rao, R. V., 2013).

GMAW processes possess satisfactory deposition rate, such that the manufacture of large-scale components can be realised in reasonable times. Figures 2-11(b-d) and 2-12 show examples of WAAM parts manufactured using the GMAW processes. Figure 2-11(a) was produced using Plasma arc process.

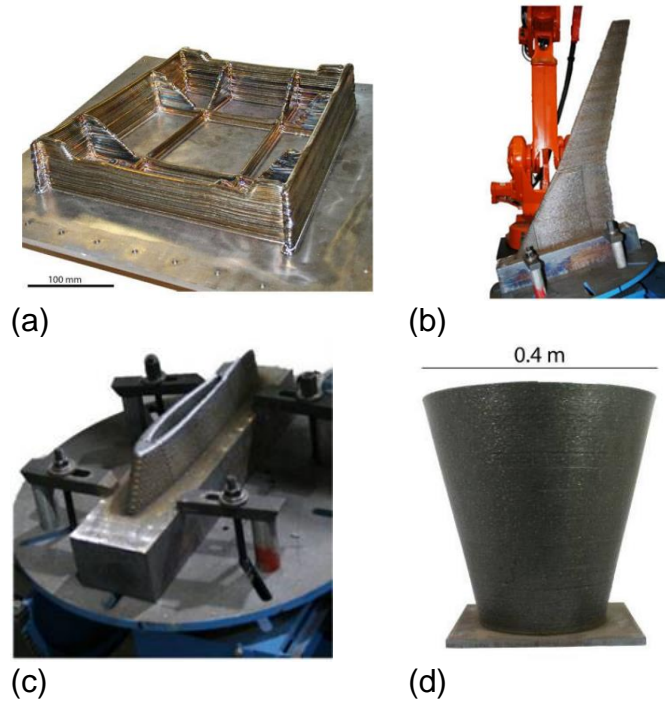


Figure 2-11 Examples of parts produced using WAAM technology (a) 1.2 m Ti-6Al-4V wing spar built for BAE Systems, top view (courtesy BAE Systems; process: PAWWAAM); (b) high strength steel wing model for wind tunnel testing (process: Fronius CMT WAAM), (c) particular of hollow structure, (d) mild steel truncated cone (process: Fronius CMT WAAM) Williams, S.W. *et al.* (2016).

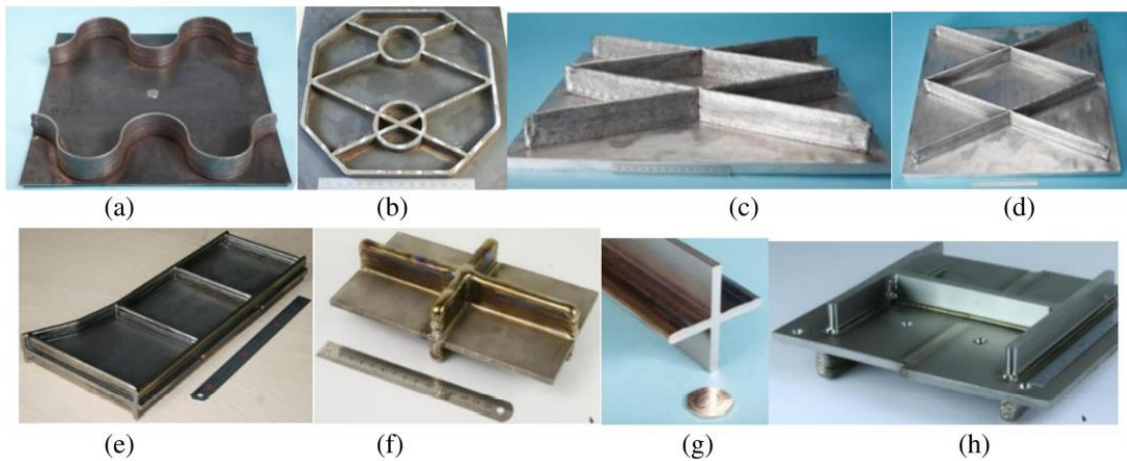


Figure 2-12 Intersecting stiffened panels produced by WAAM, (a and b) carbon steel, (c and d) aluminium, (e) titanium-stiffened panel, (f) Ti thick wall crossover, (g) Ti residual stress balance cruciform, (h) Ti intersections after machining (Ding, D. *et al.*, 2015a)

2.4 Automation of WAAM process

The automation of WAAM processes requires a suitable combination of deposition parameters and tool path trajectory that the robot can fully understand to realise the part.

The geometry of the WAAM part influences the generation of the weld path and deposition parameter required to build it. These activities can be highly complex because of the several complex and interacting phenomena occurring during deposition of the part, all of which influence the microstructural and mechanical properties, and well as the geometrical and surface quality of the finished part. (Kovacevic, R., 1999).

The tool paths utilised to build a part affect the geometry, regularity, and smoothness of each single weld bead, and contribute to the occurrence of weld defects. The presence of defects can lead to poor mechanical property of the part

The heating and cooling cycles at different sections of the part is also influenced by the geometry and thermal characteristics of the weld paths. Consequently, the prevailing thermal condition in the part influences the amount of remelting experienced by previously deposited weldment and fusion characteristics with subsequently deposited metals (Kovacevic, R., 1999).

Some examples of parts produced using inadequate GMAW deposition parameters are shown in Figures 2-13 (Kovacevic, R., 1999).

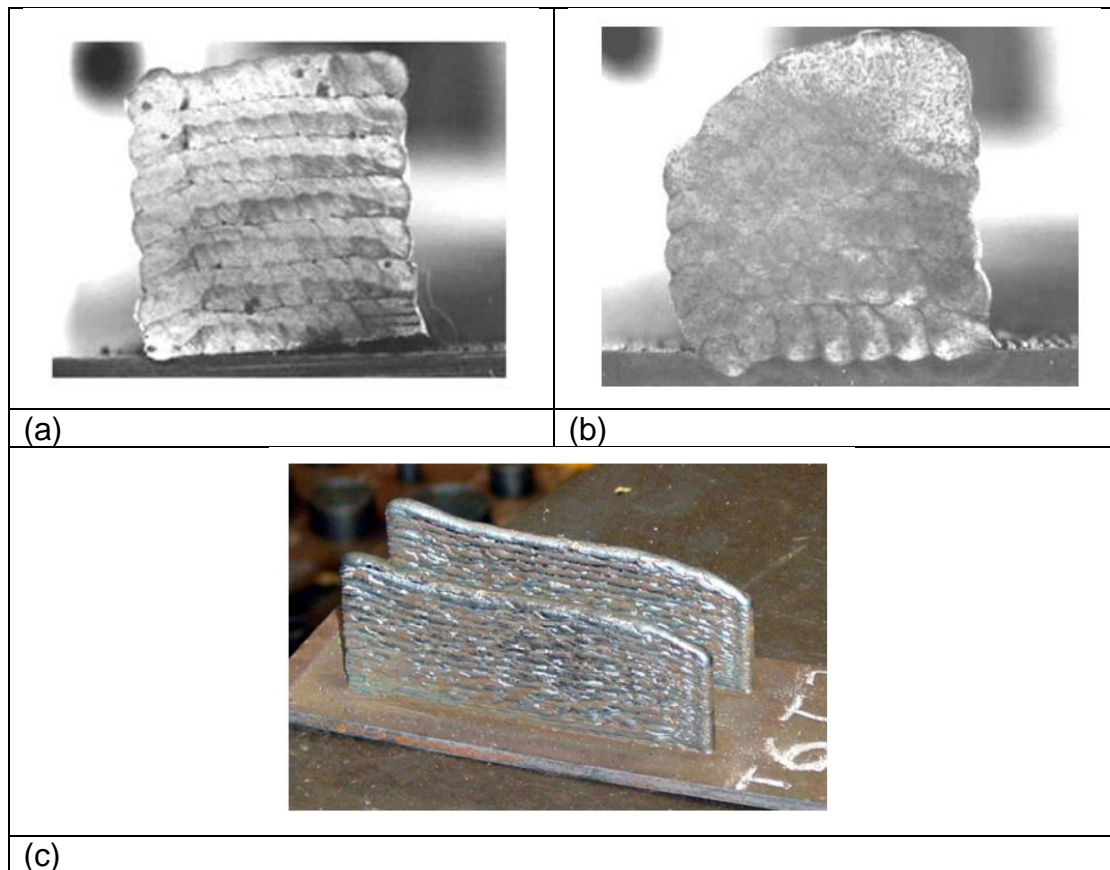


Figure 2-13 Cross section of WAAM parts showing (a) lack of fusion defect, (b) excessive remelting and loss of geometric accuracy (c) irregular geometry and poor surface quality. (Kovacevic, R., 1999)

2.4.1 Generation of deposition process parameter

The most common problem faced in WAAM fabrication is the optimization of the process parameters because welding involves interaction of several parameters, and each of them significantly affect the quality of the deposited weldment. (Mistry, J. P., 2016).

Previously, it was common practice to select suitable deposition parameters and settings, based on established practices or through a trial-and-error approach. However, this approach to selecting optimal parameter levels consistently, were tedious and time-consuming.

Nowadays, the increased reliance on automation and/or robotic arc welding systems have been a driver in efforts to predicting and enhancing understanding of the influence of the deposition process parameters on the geometry of the

deposited beads. Hence, developing models to relate the deposition parameters to the bead responses is highly required to improve efficiency of the welding process, as well as deposited weld quality (Almeida, P. M. S., 2012).

Currently, the trend in the fabrication industries is the automation of welding processes, to attain increased production rates and high precision. Hence, a robust method for selecting process parameters and stringent control over weld bead shape is important in welding automation because the mechanical strength of a weldment is dependent on the weld bead shape and dimensions, apart from the weld metal composition (Shoeb, M., 2013; Mistry, J. P., 2016). Therefore, it is vital to establish a relationship between the deposition process parameters and weld bead geometry, to assess and control the weld bead quality (Mistry, J. P., 2016).

Statistical technique such as regression analysis have commonly been utilised to determine the interrelationships between deposition process parameters and the geometrical bead responses. Other welding optimisation techniques which focused on statistical experimental design (DoE) and mathematical approaches were also created in recent times, enabling ideal weld deposition conditions to be defined. They include factorial design, Taguchi, multiple linear regression, and response surface methodology, which provide the ability to vary all deposition parameters together and investigate all possible combinations of parameters settings, as opposed to the one-factor-at-a-time approach (Montgomery, D.C., 2017).

In view of the aforementioned, a number of researchers and experts over the years, have made efforts to explore the effects of different deposition parameters and conditions on the formation and characteristic of deposited weld bead (Yao, P. *et al.*, 2020).

Shoeb, M. *et al.* (2013) for example investigated the effects of some process parameters, such as welding speed, voltage, and gas flow rate on the weld bead geometry, including penetration, width, and height. The result of the study showed that at higher welding speed, the bead width and height decreased in size due to decreased in the weld pool volume and metal deposition rate, and

welding speed showed no significant effect on penetration. Likewise, the gas flow rate had no significant effect on penetration for the parameters, under the experimental conditions utilised (Shoeb, M. et al., 2013).

Martina, F. et al. (2012) adopted a D-Optimal to predict the main geometrical features of Ti-6Al-4V multi-layer deposits, using transferred plasma welding and wire deposition (PWD) process parameters. The input parameters selected included WFS, TS, and welding current, whereas the output parameters measured were layer height, total wall width and effective wall width. ANOVA was utilised to carry out statistical significance tests. Contour plots were then used to graphically present the important main effects of interactions between the deposition parameters and measured responses.

Vedrtnam, A. et al. (2018), utilised response surface methodology (RSM) to design the experiment and to develop relationships for predicting the hardness and geometry of the weld bead. The effects of variation in open circuit voltage, current, welding speed, and nozzle-to-plate distance; on bead width, bead height, and hardness were investigated and analysed. Later, analysis of variance (ANOVA) was performed to further analysis and validate the experiment. The results may be used for predicting the weld bead quality, selecting optimum process parameters quality, and optimizing the welding process. The result showed that increase in voltage, increased the bead width but decreased the bead height. Whereas the increase in current produced an increase in bead height and no change in bead width. Increase in welding speed caused a decrease in bead width and height decrease. Increase in the nozzle-to-plate distance, produced a decrease in bead width, but the bead height increased. They further found that predictions from the mathematical model was in fair agreement with the experimental results (Vedrtnam A. et al., 2018).

From the foregoing review, investigation on the effects of deposition process parameters on bead geometry, is very important to ensure proper selection of optimised input process parameters. This is because, achievement of good weld bead geometry is crucial in providing the required mechanical and geometrical

quality of the final part, as well providing enhanced productivity and total cost efficiency (Kamble, A. G. and Rao, R. V, 2013).

It is vital to note that some of the studies in mathematical modelling used to forecast bead geometries have been limited to traditional welding fabrications, rather than WAAM. Additionally, majority of the studies have been based on single wire-GMAW process; but process development studies for multi-wire GMAW process, such as tandem-GMAW process is still not extensively explored.

2.4.2 Automatic WAAM path generation (Toolpath generation strategies)

According to Sarma, R. (2000), "the geometric and functional properties of the product are dependent on the trajectory of the tool" and "the trajectory dictates the accuracy of the product and the time taken to manufacture it" (Sarma, R., 2000). Various weld path and build process design strategies have been studied in the literature, and some will be briefly described in the preceding sections.

2.4.2.1 Object partitioning

The part to be built could first be partitioned into sections and any cross-sectional layers that are to be filled can also be partitioned into sub-sections. Also, the manufacture of parts may require complex shapes to be divided into separate build processes. These could be because some part geometries are much better built-in certain build directions, or because occasionally it is impossible to build-up a complex object in one build direction (Siminski, M., 2003).

Sometimes it could be beneficial to alternate between the build processes of several sub-components. For instance, where sub-components are distributed symmetrically around the part, it could be advantageous to build them all simultaneously by frequently swapping between the parts. This could aid in a more symmetrical dissipation of heat and could eliminate the need to wait for a particular weld layer to cool down, thereby reducing build time.

After slicing the part into fill layers, the different sections could then be filled with separate fill patterns. This may be necessary for parts with complex cross-sections (Siminski, M., 2003).

Ramaswami, K., (1997), proposed various part partitioning strategies as illustrated in Figure 2-14.

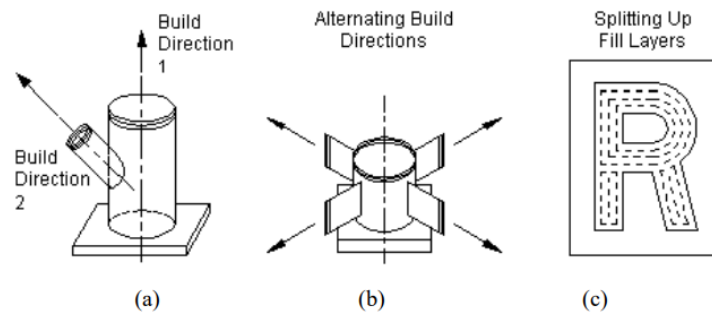


Figure 2-14 Various object partitioning strategies (a) Object partitioning with multiple build directions (b) Alternating build directions for symmetrical heat deposition (c) Splitting up fill layers and using different fill patterns

Also, an example of part partitioning approach, in which a CAD model of the part is sectioned into three parts, in accordance with the wall thickness, with different tool paths allotted to the individual sections is shown in Figure 2-15.

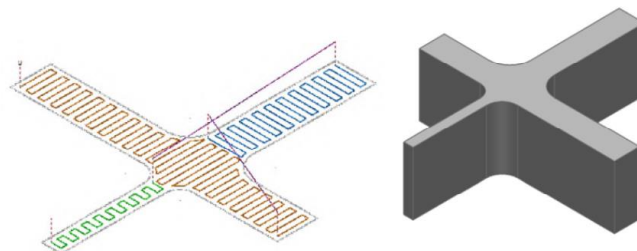


Figure 2-15 Part partitioning approach, with allocation of different tool path

2.4.2.2 Thin wall building

Thin wall building in WAAM relates to the building of walls of weld metal one weld bead thick in width, by depositing single welds on top of each other. Parts with thin cross-sections are deposited using thin wall building strategy if the thickness of the part is within the appropriate range. Thin walls are also used in (thick) solids wall building where high surface quality of the outer sections are required. Thin walls may be vertical, horizontal, or inclined and are usually produced using a fixed or varying direction of build and torch orientation, as shown in Figure 2-16 (Jacono, S. F., 1999).

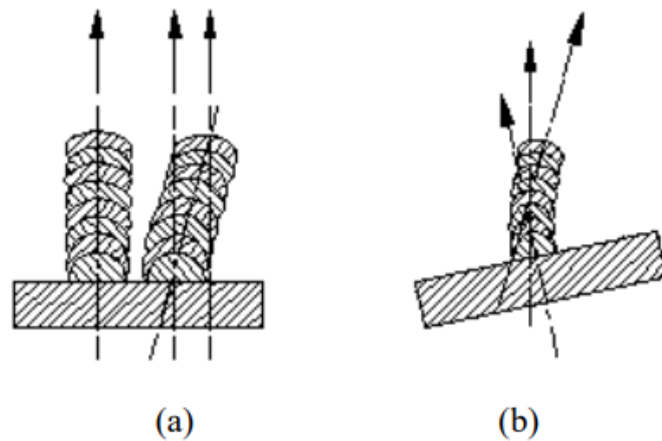


Figure 2-16 Cross sections of straight and sloping thin walls, produced with a (a) constant build direction (b) a variable build direction (Jacono, S. F., 1999).

Dickens P. M., et al. (1992) did some investigations to select parameters for thin wall building using GMAW. He observed that the shape and dimensions of the weld beads were important because they influence the range of wall thicknesses produced, as well as the walls surface quality. He performed some weld deposition trials and investigated the response of the thin walls to various changes in weld parameters, with a view to improving the quality of the thin wall and enabling the development of weld parameter database. Consequently, it led to improvement in the build walls as shown in Figure 2-17. He however noted that further studies were needed particularly regarding on how the deposition of multiple layers effects the dimensions of the weld bead.

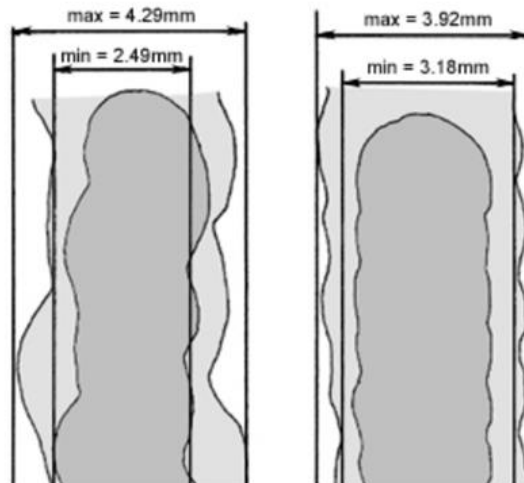


Figure 2-17 Wall cross sections built before and after improvement of deposition process parameter (Dickens P. M., et al., 1992).

Thin wall building by robotic GMAW have also been researched by some authors including Spencer, J.D. and Dickens, P.M. (1995); Spencer, J.D. et al. (1998) and Zhang, Y. M., et al. (2002).

Spencer, J.D. and Dickens, P.M. (1995), reported that thin walls of between 3mm and 6mm in thickness were easily produced, using 1mm diameter filler wire. However, when attempting to produce walls thicker than 6mm, Spencer found that excessive heat input was generated, leading to deterioration in bead profiles, due to inadequate cooling rates. As a result, they suggested that walls thicker than 6mm would require the use of multiple weld beads (Spencer and Dickens, 1995).

Ribeiro, F. (1998b) studied the effects of weld deposition parameter on thin wall building and observed that highly optimised weld parameters and consistent weld beads are critical. He investigated several aspects of weld path design strategy for thin wall building and developed an automatic 3D part slicing and weld deposition parameter generation system, complete with automatic weld parameter prediction. Figure 2-18 shows the thin-walled part produced by Ribeiro, F. (1998b).



Figure 2-18 WAAM beer mug produced using GMAW process. Ribeiro, F. (1998b)

Furthermore, Kazanas, P. et al. (2012), explored the capability of WAAM to create parts using aluminium and carbon mild steel. He also considered the effects of process parameters on the wall quality and transferred the knowledge gained to build enclosed structures. Some of the enclosed parts produced are displayed in the Figure 2-19.

The semi-circular part was built by initially utilising two quarter circles and then joining them in the middle, while the hollow square box was built by initially building vertical walls, followed by bridging the overhang wall.

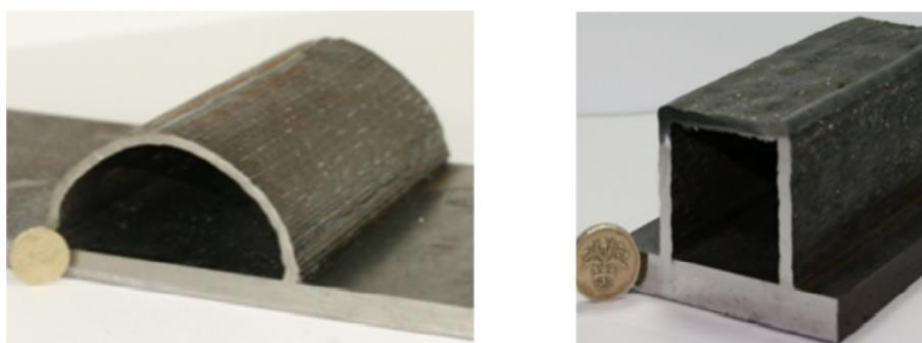


Figure 2-19 Enclosed structure produced using WAAM – Semicircle (left) square section (right). Kazanas, P. et al. (2012)

2.4.2.3 Solid wall building

Solid wall building in WAAM refers to the deposition of parts whose cross-sections are too thick to be produced by single thin wall. If any region of an object has a cross-section that is thicker than the maximum wall thickness producible with thin wall building, that section of the object needs to be deposited using solids wall building technique. Such thicker cross sections require larger areas to be filled with weld metal, hence, requiring the use of some sort of layer filling technique (Siminski, M.R., 2002b).

Studies carried out by authors including (De Boer, F.G., et al., 2000; Jacono, S. F., 1999; Spencer, J.D. and Dickens, P.M., 1995; and Spencer, J. D. et al., 1998), found that solid WAAM parts cannot be produced by simply depositing multiple thin walls side by side. This is because doing so leads to lack of fusion because the thin wall welds do not generate enough heat input to penetrate the surrounding substrate. They also showed that increasing the heat input in an effort to improve the fusion characteristics deteriorated the shape and surface quality of the part. An example of lack of fusion defects formed with mild steel material, due to insufficient GMAW heat input is depicted in Figure 2-20.

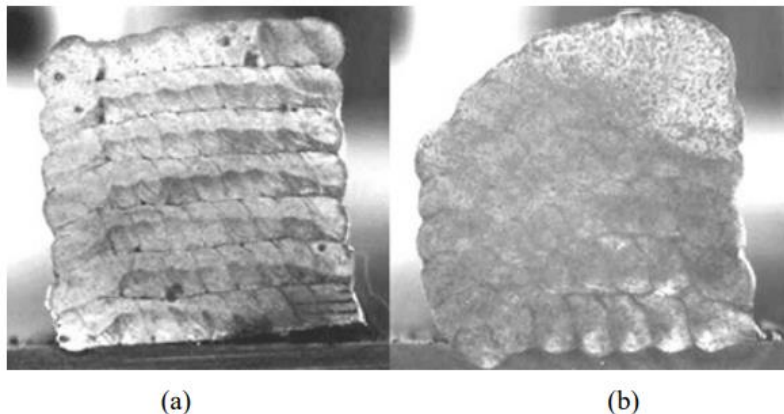


Figure 2-20 Cross sections of low-quality solid parts produced using thin wall offsetting technique (a) Showing lack of fusion due to inadequate heat input, but little loss of shape (b) showing loss of shape due to excessive heat input, but with good fusion. Jacono, S. F. (1999)

Thus, using layer filling to build solid WAAM parts, requires higher heat input welds compared to those suitable for building thin walls. Hence, if a part requires smooth outer walls, it should be built using separate thin walls deposited around the perimeter of the fill layers. In other words, an outer boundary should be produced using deposition parameters suitable for thin wall building, while the interior section could then be filled using a different parameter appropriate for larger weld deposits.

This approach is termed "boundary method" and was successfully demonstrated by (De Boer, F. G. et al., 2000; Jacono, S. F., 1999; Spencer, J.D. and Dickens, P.M., 1995; and Spencer, J. D. et al., 1998 and Zhang, Y. M. et al., 2002).

Zhang, Y. M. et al. (2002) noted that the boundary approach is necessary to maximise the dimensional quality of the built part.

Figure 2-21 shows the cross-section of a solid part produced by Jacono, using the boundary method.

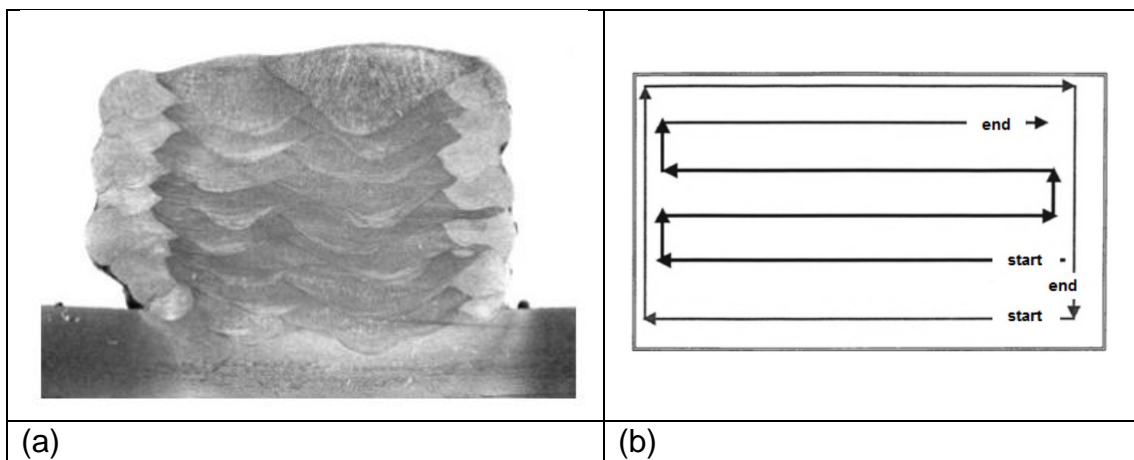


Figure 2-21 (a) Cross-section of solid block deposited using the boundary method (b) Schematic illustration of the boundary method (the arrows indicate the deposition paths) (Jacono, S. F., 1999)

2.4.2.4 Weld bead overlapping

Typically, WAAM fabricated consists of several layers with constant or different thicknesses overlapping each other base on a predefined overlapping strategy (Zhang, Y. et al., 2003).

WAAM fabricated parts can be classified as (i) thin-walled parts and (ii) multi-layer multi-bead (MLMB) parts, depending on the number of weld beads in a single layer. The layers of a thin-walled part contain only one weld bead, while the layers of an MLMB part contain multiple beads which overlap each other. A single layer illustration of deposition of a MLMB components is shown in Figure 2-22 (Li, Y. et al., 2018)

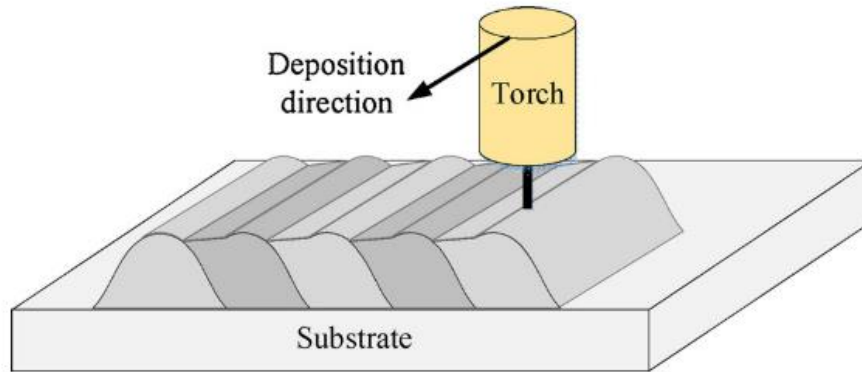


Figure 2-22 A schematic diagram of a single layer, showing deposition of multiple beads on a substrate in flat position

The interactions between adjacent beads in the layers play an important role in the process of forming and shaping the MLMB parts. If a constant step-over distance is applied between adjacent weld beads, the width of the layer is calculated using the equation (2-1) Li, Y. *et al.* (2018).

$$W_l = aw_b(n - 1) + w_b \quad (2-1)$$

where: n is the number of weld beads in the layer and $n \geq 2$, a is the step-over rate, W_l is the width of a layer, and w_b is the width of an elementary bead (EB) in the layer.

Though many mathematical models were proposed for handling the process of beads overlapping, there is no overall or generic solution available in the literature yet (Li, Y. *et al.*, 2018).

To produce flat surfaces during part deposition, Cao, Y. *et al.* (2011) deposited weld beads next to each other and concluded that the optimal value of

overlapping coefficient, that is the centre distance between the beads should be 63.66 % of the width of single bead (Cao, Y. et al., 2011).

Suryakumar, S. et al. (2011) considered the weld bead shape as a parabola in describing the distribution of overlapped material. Figure 2-23 depicts the area of valley and overlapped material. They explained that at a given centre distance 'd', the area of the valley is equal to the overlapping area. They estimated the centre distance between two adjacent beads as 66.66% width of a single bead. From observation of the deposited weld beads, they noted that it was not practicable to produce a completely flat overlapped surface (Suryakumar, S. et al., 2011).

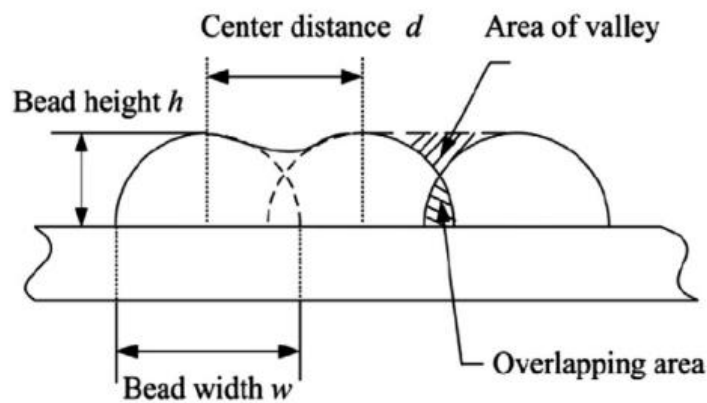


Figure 2-23 Sketch of the traditional overlapping flat-top model.

Studies were recently conducted by researchers from the University of Wollongong, to develop a new method for overlapping the beads, which they termed Tangent Overlapping Model (TOM). They stated that an optimum centre to centre distance between adjacent beads should be 73.8% width of the single bead. They also considered the weld bead shape as a parabola, Ding et al. (2015b). The top of the valley was drawn as a straight-line tangent to the adjacent bead 'Bead 2', as shown in Figure 2-24.

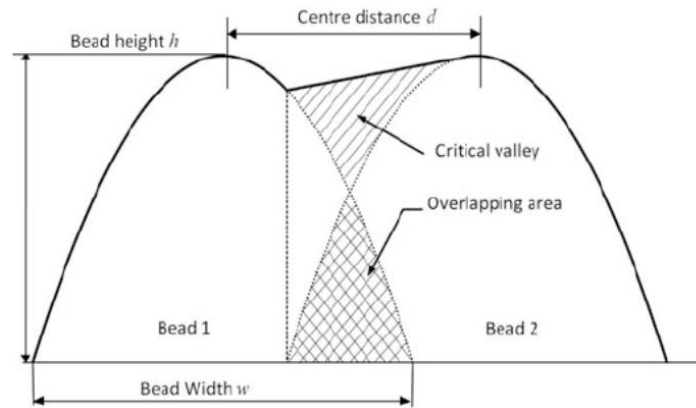


Figure 2-24 Schematic illustration of tangent overlapping model, TOM (Ding et al., 2015b)

They explained that a change in centre distance d , changes the area of valley. At a given value of centre distance d^* , the overlapping area becomes equal to the valley area, which they referred to as critical valley. The surface smoothness of the bead is maximum at this value of centre distance and was established as 73.8% width of the single bead. It should be noted that although the part they produced showed good flat surfaces, inspection of the overlapping areas for defects was not reported.

2.4.2.5 Solid block filling strategies

After a solid block have been sliced into layers, the tool paths need to be designed for the torch to follow in filling the layers. There are three basic categories of tool path filling-in patterns for layers that have been identified in literature. These include raster fill, contour, and spiral fill.

A summary description of different tool path filling-in patterns and their pros and cons, provided by Ding, D, et al. (2014) is presented in Appendix A. The raster path filling pattern will be employed in this study and is described as follows.

2.4.2.5.1 Raster path filling patterns

Raster paths are weld paths comprising of regularly spaced parallel weld deposits covering a 2D area of a part to be filled and could form a "staircase" or "zigzag" pattern. Figure 2-25 illustrates the raster fill path for filling-in a square cross-section, where 'w' denotes the gap between the parallel lines

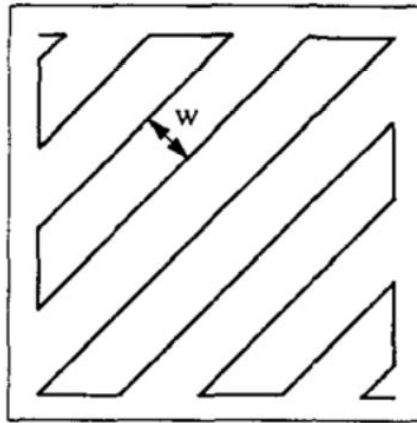


Figure 2-25 Raster path filling (Siminski, M.R. et al., 2002b)

Several variations of raster paths are possible and raster path design variables that have been identified includes – discrete or continuous.

A study by Hensinger, D. M. et al. (2000) demonstrated the use of raster paths for filling-in a solid part, using the LENS process. After depositing the outer boundary of each layer, the interior layers were filled in using a raster path pattern, as illustrated in Figure 2.26. This method is termed discrete raster paths.



Figure 2-26 Deposition of perimeter and layer filling with the use of raster path in LENS process (Hensinger, D. M. et al., 2000)

Kulkarni, P. and Dutta, D. (1999) also utilised raster paths in FDM process and evaluated the effect of the process. The raster path used in their study incorporated linking sections which connected the end of one raster path to the start of the next, ensuring the complete fill layer was covered using one unbroken

path that zig-zags across the layer as illustrated in Figure 2.27. This is an example of "continuous" raster paths (Kulkarni, P. & Dutta, D., 1999).

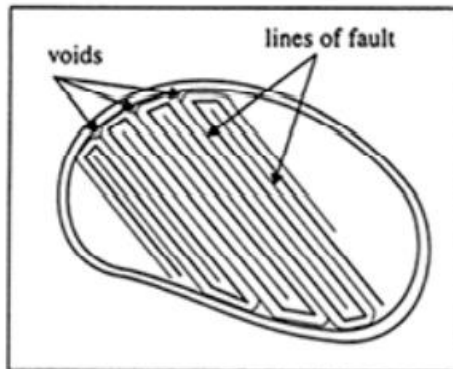


Figure 2-27 Illustration of continuous raster filling paths (Kulkarni, P. and Dutta, D., 1999)

Kulkarni and Dutta observed that a major problem with continuous raster paths involves the creation of unfilled voids near the edges of the fill areas (Kulkarni, P. and Dutta, D., 1999). This can be seen in Figure 2-28. They observed that the smallest voids are formed when the raster paths meet the edge of a fill area at 90°. They also noted that to reduce unfilled voids, there is the need to minimise the number of corners or changes in direction of deposition paths.

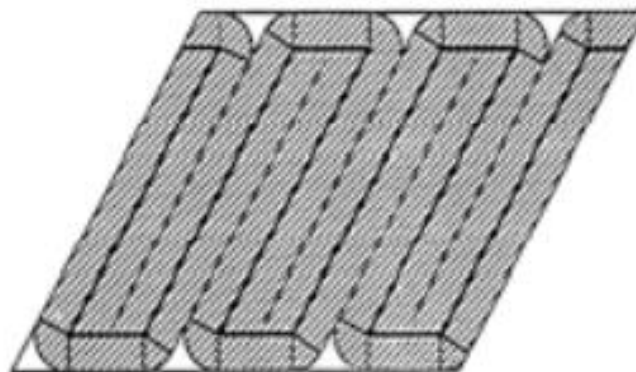


Figure 2-28 Occurrence of voids by continuous raster paths, near fill area edges (Kulkarni, P. and Dutta, D. (1999))

2.5 High productivity development in WAAM process

The quest to achieve greater productivity rates in the use of WAAM technology, especially for the fabrication of large or heavy-walled structural components have continued to be the subject of several research efforts. The desire is driven partly by the need to maximise WAAM manufacturing lead time and throughput, to compete with the levels of productivity associated with subtractive manufacturing methods (Hirtler, M. et al., 2020).

This is important because the productivity of WAAM technology is a major factor determining the unit cost of the manufactured components and equally contributes to the cost justification for adopting the WAAM technology in place of conventional manufacturing methods. As the productivity of WAAM technology increases, the cost advantage associated with increased throughput can be successfully realised (Baumers, M. et al., 2016).

Zadi-Maad, A. et al. (2018) remarked that WAAM technology is currently more beneficial for small volume production of parts. Hence, there is no doubt that achieving increased deposition rates in WAAM fabrication would significantly encourage increased utilisation of the technology for large volume production of large-sized parts, enabling enhanced economy of scale. Zadi-Maad, A. et al, (2018)

2.5.1 High productivity arc processes

Gas metal arc welding process (GMAW) is a common arc-welding process used in industries owing to its higher deposition rates and economic efficiency. The typical deposition rates of GMAW process varies from 1 kg/h to 4 kg/h for aluminium and steel respectively, and several components can be manufactured within a working day.

It is possible to achieve higher deposition rate of up to 10kg/h, but this then leads to unintended deterioration in the quality of the part, owing to the high heat generated. Because of this, enormous machining efforts in addition to deposition of significantly higher amount of more material, could subsequently be required to compensate for the required tolerance. Ultimately the process becomes less

able to compete with traditional subtracting technology and hence, commercially less attractive.

As a result, the general option is to maintain the deposition rate at medium levels of about 1 kg/h for titanium and aluminium, and 3 kg/h for steel, to always guarantee a BTF ratio of 1.5 and maximise manufacturing cost savings (Williams, S.W. *et al.*, 2016).

It is hypothesised that the deposition (build) rate currently possible with WAAM process, Figure 2-29, could be increased using multiple point GMAW heat source, in conjunction with an optimised deposition tool path strategy, which could prevent or minimises the unfavourable deterioration in the integrity and quality of the built part (Rodriguez N. *et al.*, 2018).

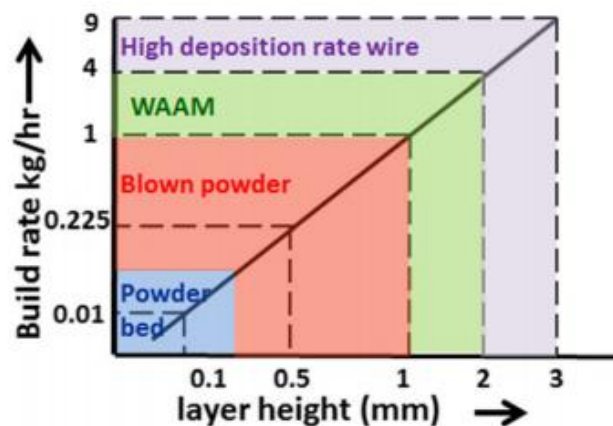


Figure 2-29 Build rate versus layer height for different AM technologies [adapted from Rodriguez, N. *et al.* (2018)]

Several welding studies have been conducted to develop and introduce variants of GMAW processes, to increase productivity (Rodriguez N. *et al.*, 2018) and improve manufacturing process efficiency (Lockett, H. *et al.*, 2017), in the fabrication of structural parts. Multiple-wire welding is one such technique that came into existence to increase productivity Ueyama, T. *et al.* (2005a; 2005b; 2005c), which could also be utilised to increase productivity in the fabrication of medium to large sized WAAM parts.

Yuehai F. *et al.* (2018), for example, utilised a double-wire feed and plasma arc additive manufacturing process (DWF-PAM), to achieve high productivity

efficiency in the fabrication of Cr-Ni stainless steel components. The study reported that the deposition rate of (DWF-PAM) was 1.06 times higher than the single-wire plasma arc process (SWF-PAM). They also reported that the DWF-PAM process produced superior bead appearance, microstructure, and mechanical properties in comparison to the part fabricated using (SWF-PAM). This was attributed to the large number of completely grown equiaxed ferrite grains produced by the DWF-PAM process. Yuehai, F. *et al.* (2018)

Shi, J. *et al.* (2019) investigated the use of an innovative multi-node trajectory planning strategy, in combination with higher efficiency Tandem-GMAW process, to efficiently fabricate grid structural panels (Shi, J. *et al.*, 2019). The author concluded that Tandem-GMAW process was successfully utilised to fabricate the grid stiffened panels, leading to significant reduction in production time, energy and material requirements. Additionally, the number of interruptions (stops/starts), during the fabrication was minimised. Shi, J. *et al.* (2019)

Tandem-wire GMAW process was employed by Queguineur, A. *et al.* (2018), to investigate the possibility of manufacturing large-sized components using CMT process. The authors specifically evaluated the implication of process parameters on the manufacturing lead time, metallurgical and mechanical properties, during WAAM fabrication of austenitic stainless (AISI 316L) steel and Cu-Al alloy parts for naval applications. The study showed that the WAAM manufacturing time was comparable to that of a similar industrial manufacturing process. The mechanical performance of fabricated AISI 316L material was comparable to the counterpart forged alloy, underscoring the capability to integrate the WAAM technique into the production of austenitic stainless-steel parts for naval application. However, the part produced using the Cu-Al alloy showed a slight reduction in mechanical performance. This was attributed to the evolution of large columnar grain structure because of low cooling rate. The low cooling rates was the effect of high deposition rates and multiple thermal cycles associated with the deposition process. Queguineur, A. *et al.* (2018)

A comparative study of single-wire and Tandem-wire GMAW processes in the fabrication of Q690 steel, was conducted by Fang *et al.* They reported that the

welding speed, deposition rate, manufacturing efficiency and quality of the deposited weld were noticeably improved using Tandem-wire processes, compared to the single-wire counterpart. They also observed that the heat input of Tandem-GMAW was about 23.4% lower than the SW-GMAW, and consequently, the travel speed and deposited weld bead quality were clearly enhanced (Fang, C. fu *et al.*, 2012).

The authors also observed that the Tandem-GMAW process generated a push-pull pulsed current characteristics, which produced unique droplets transfer, heat flow distribution and arc interaction between the two wires that were totally different from those observed in the twin-wire GMAW process. The push-pull effect triggered a strong oscillation of the weld pool which resulted in the refinement of the weld metal and HAZ microstructures. This led to a lower heat input and consequently lower welding distortions. In addition, a narrow HAZ and enhanced mechanical properties, including the tensile strength, impact energy and hardness of the joint produced by Tandem-GMAW increased by 5%, 17% and 18.5% respectively compared to twin-wire GMAW. (Fang, C. fu *et al.*, 2012)

The energy efficiency of tandem-GMAW process was also highlighted by Sproesser, G. et al. (2016), when comparing the energy consumed by different GMAW processes, using their electrical deposition efficiencies as the key performance indicator. The electrical deposition efficiency was calculated using equation (2-2).

$$EDE = (WFS/P_w) \times p \times A_w \text{ (in g/kWh)} \quad (2-2)$$

Where:

P_w = Process power, A_w = wire cross sectional area and p = calculated arithmetic mean of the instantaneous power (Sproesser, G. et al., 2016).

The study found that the energy consumed, and welding time achieved when a 30mm thick plate was joined using Tandem-GMAW process, was 23% and 55% respectively lower, compared to using Single-wire GMAW. (Sproesser, G. et al., 2016)

This study proposes to investigate the multi-wire GMAW deposition process, such as Tandem-wire process to improve productivity in the fabrication of structures. Hence the subsequent sections will be devoted to multi-wire GMAW processes.

2.5.2 Multi-wire GMAW process

Multi-wire GMAW process, such as Tandem-GMAW, is an advanced form of traditional GMAW process, and is among the successful high deposition techniques utilised today (Goecke, S. *et al.*, 2001). It uses two or more deposition wires at the same time and could be easily incorporated with an existing production line, at relatively low cost (Zhou, K. and Yao, P., 2019).

Figures 2-30 and 2-31 show examples of multi-wire systems, utilising submerged arc (SAW) and Tandem GMAW deposition processes respectively.

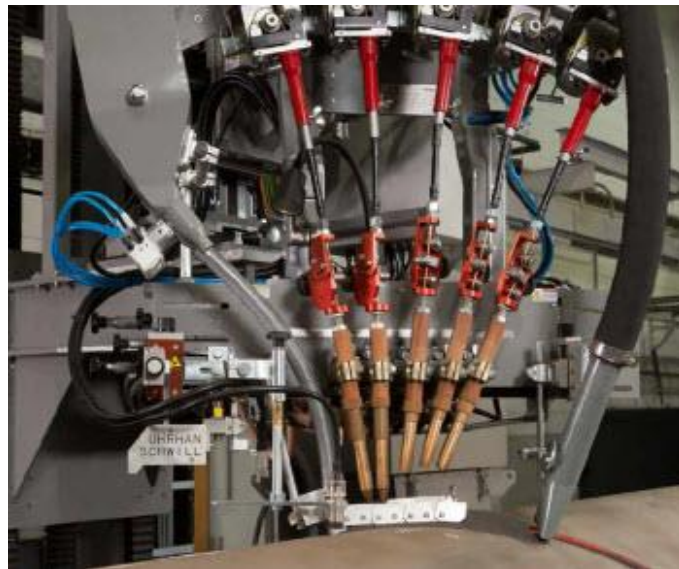


Figure 2-30 Multi-wire SAW deposition system. Lincoln electric (2020)

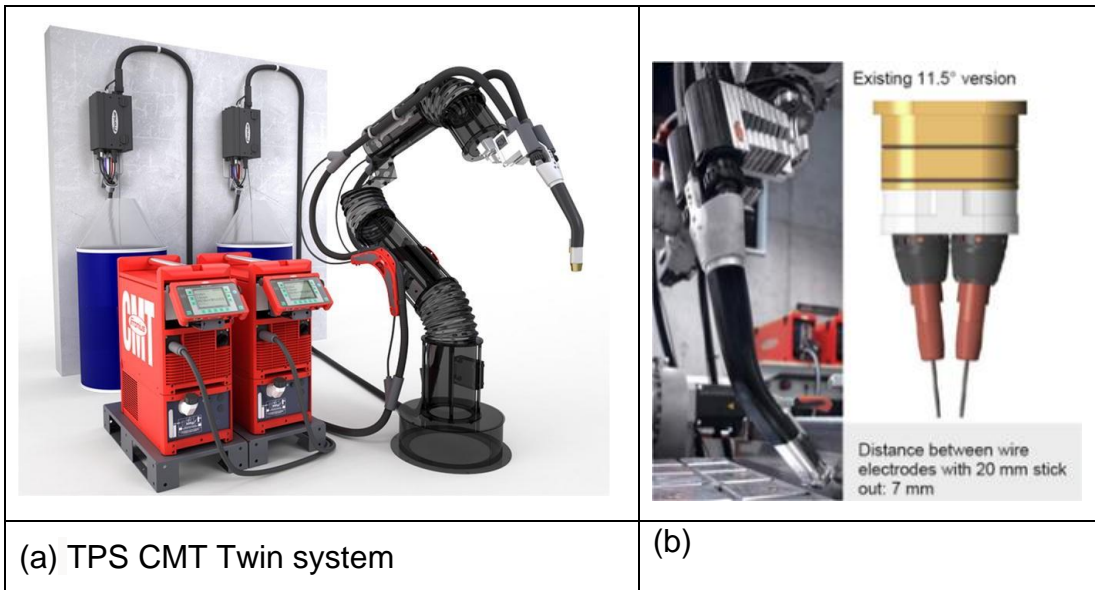


Figure 2-31 Multiple-wire tandem GMAW system, showing (a) Equipment set-up (b) Detailed view of tandem touch (Queguineur, A. *et al.*, 2020)

The use of a multi-wire GMAW process represents a fundamental commercial attractiveness to the WAAM technology, due to its ability to achieve high deposition rates at about 1.5 to 5 times, compared to the conventional single-wire GMAW process, and even achieving it at a relatively lower heat input (Huang, P. F. *et al.*, 2012).

2.5.2.1 Double-wire GMAW process

Application of high-efficiency energy process for structural fabrication, in the welding industry, continues to attract significant research interest and one innovative technique for actualising high efficiency weld deposition is by use of double-wire GMAW process (Wu, K. *et al.*, 2020).

Double-wire GMAW is a variant of multi-wire GMAW process (Wu, K. *et al.*, 2020), which feed two wires (Goecke, S. *et al.*, 2001; Wu, K. *et al.*, 2020). It can be classified based on several principles (Goecke, S. *et al.*, 2001) and includes the following-

- Twin wire (one wire feeding unit) – This system feeds two wires from the same wire feed unit. The same potential exists between both wires, and are powered by the same power source

- Twin welding (two wire feeding unit) – Two different wire feeder units feed each wire. Both wires are connected to the same power source or to two similar power sources, having the same potential, at the same output frequency, electrical current and wire feed speed. Also, the wires are housed in the same contact tube and are not electrically isolated. (Goecke, S. et al., 2001; Zhou, K. and Yao, P., 2019), Figure 2-32(a).
- Tandem welding (two wire feeders and two power sources) – This incorporates two separate wire feed units, which feeds two wires connected to two separate power sources. The wires are isolated electrically from each other in the welding torch; they can have different potentials and deposition parameters and can be set independently of each other. (Goecke, S. et al., 2001; Zhou, K. and Yao, P., 2019), Figure 2-32(b).

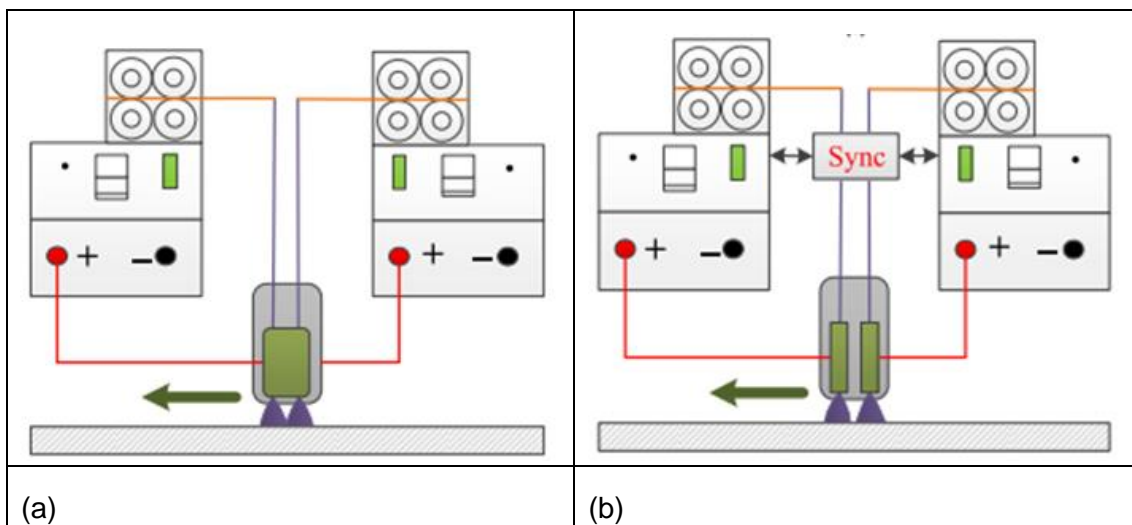


Figure 2-32 Schematics of two types of double-wire GMAW processes (a) Twin-wire (b) Tandem-wire. (Zhou, K. and Yao, P., 2019)

The process operational window of multi-wire MIG/MAG processes is smaller than that of traditional SW- MIG/MAG process. It is therefore imperative that the entire multi-wire MIG/MAG equipment installation, including the welding equipment fixtures, wire feed support etc., are precisely set-up to ensure smooth deposition process. (Goecke, S. et al., 2001). A comparison of tandem and twin wire GMAW process will reviewed briefly in the following sections.

2.5.3 Comparison between Tandem and Twin Wire GMAW Processes

Tandem-wire and twin-wire processes are GMAW multi-wire processes which utilise two separate welding power sources, nevertheless, significant difference exists between them in terms of the process characteristics namely - heat generation, metal transfer and arc interference. (Fang, C. fu *et al.*, 2012)

2.5.3.1 Heat distribution and arc heating effect in double-wire process

The quality of deposited weld metal is directly affected by the heat distribution and weld pool activity during deposition and significant difference exists between the heat distributions in Tandem and twin-wire GMAW processes as illustrated in Figure 2-33 below. (Fang, C. fu *et al.*, 2012)

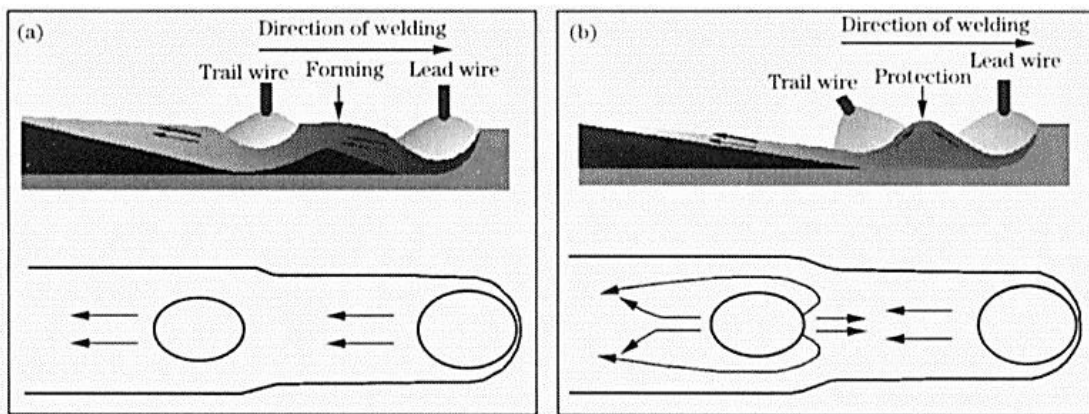


Figure 2-33 Schematic diagrams of heat distribution of double wire GMAW process (a) twin-wire (b) Tandem-wire

In twin-wire GMAW process, no significant interaction exists between the two arcs and weld pools due to the relatively larger distance separating the arcs. Hence the weld pool beneath the trail wire has no substantial effect on the weld pool underneath the lead wire, see Figure 2-33(a), (Fang, C. fu *et al.*, 2012).

In tandem-wire GMAW process, the formation of a single weld pool by the two arcs occurs at a given inter-arc angle. Interaction occurs between the two arcs as illustrated in Figure 2-33(b). The lead arc melts and penetrates the substrate, it also controls the front portion of the weld pool and flow of the molten metal, whereas the trail arc heat and pours its contents in the rear portion of the weld pool, combining its energy. This effect causes the molten pool to remain longer

at a higher temperature resulting in a complete microstructural change. This could act to minimise solute alloy segregation from rapid solidification, leading to increased ductility and enhanced microstructure and mechanical performance of the deposit. (Fang, C. fu *et al.*, 2012)

Generally, the heat input utilised during GMAW deposition is aimed at obtaining sound and acceptable bead profiles. As the travel speed increases, the heat input required by the Tandem-GMAW process to produce acceptable bead geometry was observed to be 25% less than that required by twin-wire GMAW, even at a faster travel speed. This results in lower distortion and reduced HAZ width of the joint. (Fang, C. fu *et al.*, 2012)

In addition, the push-pull method of metal transfer during T-GMAW stimulates strong mixing of molten metal underneath the arc and plasma flow force, helping to promote uniform nucleation of fine microstructures. (Fang, C. fu *et al.*, 2012)

2.5.3.2 Heat input model in double-wire process

An illustration of the heat input process of tandem and twin wire-GMAW welding process is shown in Figure 2-34. In twin wire-GMAW process, the two welding wires are independently heated by two different power sources to produce two separate arcs and two weld pools. The distance between the two arcs is L and their energies are simultaneously discharged into the pool. (Fang, C. fu *et al.*, 2012)

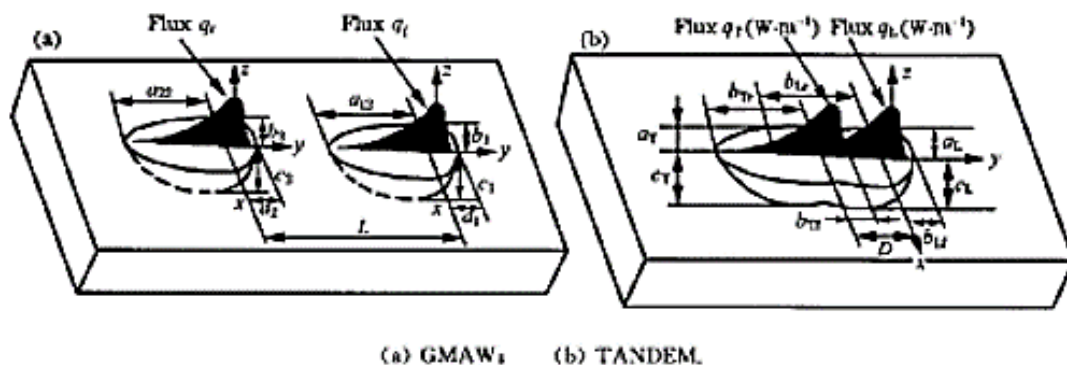


Figure 2-34 Heat source model diagram of GMAW twin wire and Tandem process

However, Tandem-GMAW process utilise two arcs but produces a single weld pool and the formation of the single weld pool by the two arcs occur at a given

distance, D (Fang, C. fu *et al.*, 2012). The two arcs discharged their energies into the single weld pool in a push and pull manner. This technique keeps the trail wire in its base period while the lead wire is at its peak cycle and vice-versa. Heating of the two arcs occur by coupling effect. The coupling heat generates significant heat energy, leading to increased deposition rate.

2.5.3.3 Metal transfer process in double-wire process

In Tandem GMAW system, the lead and trail welding power sources generate pulsed current which transfers metal and heat input in a manner akin to push-pull technique, Figure 2-35(a). In the first half of pulsed cycle, the lead wire generates a higher current, melts, and transfer metal; while the trail wire produces a relatively low current to keep the arc burning, with no metal transfer taking place. The other half of the pulsed cycle is totally different, in that the lead wire induces a lower current, while the trail wire performs the metal transfer. The lead arc in Tandem GMAW process produces a higher level of energy and controls the penetration, while the trail arc produces a lower energy and controls the bead appearance, which effectively refines the grain structure and improve the quality of deposited weld metal (Fang, C. fu *et al.*, 2012).

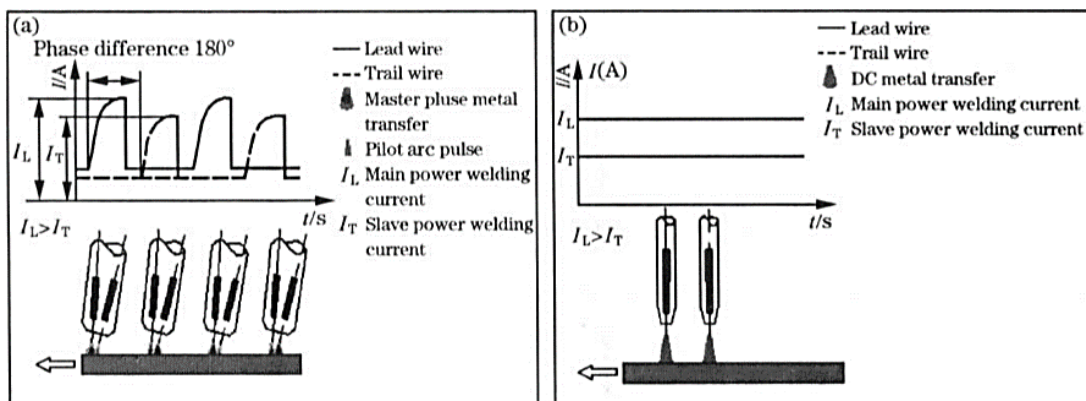


Figure 2-35 Relationship between twin wire welding and material transfer (a) Tandem (b) GMAW (Fang, C. fu *et al.*, 2012)

However, in twin-wire GMAW, the lead and trail welding power sources produce direct current and simultaneously produce and transfer weld metal into two different weld pools. Therefore, twin wire-GMAW process is comparable to two

individual GMAW processes and the heat input and mode of metal transfer is equivalent to the traditional SW-GMAW, Figure 2-35(b). (Fang, C. fu *et al.*, 2012)

2.5.4 Tandem-GMAW process

The tandem-GMAW process is a relatively novel form of WAAM technique and has the potential to produce substantially higher deposition rates and excellent weld quality, compared to the conventional SW-GMAW deposition process (Huang, P. F. *et al.*, 2012; Ge, J. *et al.*, 2018). This is because, the arrangement allows the arc pressure to remain the same, hence the wire feed speed can be doubled along with the deposition rate (Li, K. H. and Zhang, Y.M, 2008).

Figure 2-36 shows a comparison of travel speeds between Single-wire and the Tandem-wire process for different fabrication applications (Goecke. S. *et al.*, 2001).

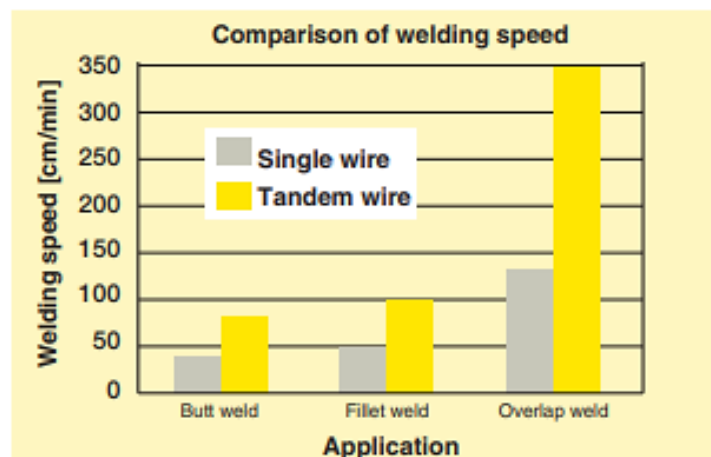


Figure 2-36 Comparison of travel speeds for Single-wire and Tandem-wire GMAW applications (Goecke, S. *et al.*, 2001).

The tandem-GMAW process simultaneously feed and melt two independent wires into one weld pool (Fang, C. fu *et al.*, 2012; Huang, P. F. *et al.*, 2012).

The arcs in tandem-GMAW process are heated by coupling effect. The push-pull pulsed current changes the arc shape, reduces the arc force which acts between the two arcs, and cancels the magnetic blows (Fang, C. fu *et al.*, 2012). The deposition travel speed can be significantly increased, leading to relatively lower

heat input and excellent weld bead appearance (Fang. C. fu *et al.*, 2012; Huang, P.F. et al., 2012).

2.5.4.1 Tandem-GMAW power source configuration

The two power sources of the tandem-GMAW process can each be set up to function as a master and slave. They are synchronised to communicate with each other by means of a synergy arc controller or (local high-speed bus - LHSB), which could adjust the power source characteristics to obtain suitable deposition parameters in the two arcs. Processes including electric arc start, are synchronised to begin at the same time, or with a start delay if required. (Huang, P.F. et al., 2012; Queguineur, A. et al., 2020). Figure 2-37.

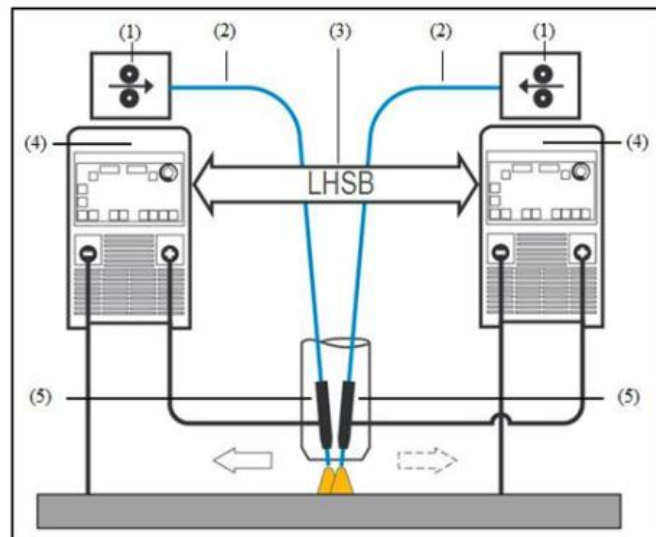


Figure 2-37 Tandem GMAW functional principle scheme showing (1) Wire-feeder units 1 and 2 (2) Wire electrodes 1 and 2 (3) LHSB HUB (synergic controller) (4) Power source 1 and 2 (5) Separate welding potential (Queguineur, A et al., 2020)

The deposition parameters can be set independently for the Tandem system. The inter-wire distance is relatively small, which allows the two wires to be fed into the same weld pool. For efficient welding application, different parameters can be set for the two wires. This is so because the leading wire does the heavy work of heating the wire and the substrate to form the molten pool, while the trailing wire fills the groove and at the same time smoothen the weld surface with minimum spatter (Goecke, S. *et al.*, 2001).

In fact, the tandem-GMAW process can be regarded as two independent traditional GMAW systems, which enables the doubling of deposition rates, without causing a corresponding increase in the arc pressure (Zhou, K. and Yao, P., 2019).

2.5.4.2 Tandem-GMAW arc modes

It is an established fact that suitable control of metal droplets transfer is necessary to obtain a smooth and stable metal deposition process. The tandem-GMAW process is quite unique in that all the metal transfer modes namely, dip (short arc), spray arc and pulsed arc; can be applied in different combinations.

Table 2-3 shows the various arc mode combinations possible with the Tandem-GMAW system, consisting of two power sources referred to as a master and slave (Goecke, S. *et al.*, 2001).

Table 2-3 Arc mode combinations possible with Tandem-GMAW process (Goecke, S. *et al.*, 2001).

Arc mode settings	Power Source	
	A – Master	B – Slave
Synchronised (same pulse frequency)	Pulsed	Pulsed
Non-Synchronised	Pulsed	Pulsed
Mixed	Pulsed	Short arc
Mixed	Pulsed	Spray arc
Mixed	Spray arc	Short arc

Metal transfer in GMAW processes have largely been studied by several authors. Ding, X. *et al.* (2013) utilised simulation and applied the fluid dynamics and electromagnetic theories to study metal transfer in SW-GMAW and T-GMAW. They utilised high speed photography to visualised and capture the actual process of metal transfer. The result of the simulation showed that while the metal droplets transferred axially in the SW-GMAW, they transferred non-axially in the T-GMAW. This difference was attributed mainly to the influence of electromagnetic force occurring between the arcs. As the welding current (WFS) increased, the surface tension coefficient of the molten metal decreases, leading to increased electromagnetic force. This accelerates the transfer of molten metal during the process (Ding, X. *et al.*, 2013).

The electromagnetic attraction phenomenon occurs because current flows in the same direction in both wires in proximity, which could cause the two arcs to offset towards each other. The interference of the two arcs can lead to process instability and poor weld quality (Wu, K. *et al.*, 2020). Despite the high deposition capability of multi-wire heat source like tandem-GMAW, this could challenge the efficiency of the process; hence the need for a robust tandem-GMAW process study and parameter development.

2.6 Surface quality improvement

The primary challenge of conventional GMAW welding processes, is the fact that to increase the deposition rate, the wire feed speed (and welding current), applied during deposition must increase. This potentially subjects the workpiece to higher temperatures leading to significant distortion and reduction in surface quality of the part. Consequently, the necessity for additional machining or reworked operation, to correct the distortions and poor surface quality occasioned by the high thermal energy, could potentially increase the manufacturing costs (Ribeiro, R. A. *et al.*, 2015).

DebRoy, T. *et al.* (2018), also noted that deposition rate is one factor which influences the surface quality of WAAM parts and suggested that a suitable selection of both wire feed speed and travel speed is important in achieving acceptable surface quality. (DebRoy, T. *et al.*, 2018)

Hence, despite the productivity benefits of WAAM technology, it is nevertheless still saddled with this significant process challenges, which relates to the poor surface quality of the manufactured part. This is a consequence of the high “stair-stepping” effect, resulting from high thermal energy, arc pressure and fluidity of molten metal associated with the deposition process (DebRoy, T. *et al.*, 2018).

Because of this, the achievement of high surface quality and geometrical tolerance of parts, mostly with the use of a high energy multi-wire GMAW process, such as Tandem-GMAW, is still very inadequate. This currently limits its wide industrial application and economic competitiveness, mostly in the manufacture of large sized WAAM components. Therefore, to enhance the

surface quality of parts produced using Tandem-GMAW process, it is essential to understand the factors which influence the physical processes that produce the associated surface waviness (Yacob, S. et al., 2015).

2.6.1 Surface quality (waviness) in WAAM structures

Achieving high deposition rate of 1.5 to 5 times, by use of tandem-GMAW process, compared to conventional SW GMAW process (Huang, P. F. et al., 2012), is beneficial for economy of scale of WAAM technology. However, this benefit comes at a cost to the surface and dimensional quality of the built part, owing to the excess thermal energy generated during deposition of the part.

As the deposition rate of any process increases, so does the surface waviness and roughness, which tend to scale with the layer height in AM. The surface quality of a finished part is an essential consideration for several engineering components produced via WAAM, since they are intended to be used in the as-built condition for net shape applications (DebRoy, T. et al., 2018). But the surfaces of WAAM built parts are generally not continuous, as they contain irregular interphases between the recent and previously deposited material, which can act as an initiation point for cracks like defects (DebRoy, T. et al., 2018; Martina, F. et al., 2010), which can be detrimental to the fatigue properties of the WAAM part (Gockel, J. et al., 2019).

Numerous factors influence the surface quality of WAAM components, however the “staircase effect” (see Figure 2-38), is one of the primary factors affecting the surface quality, which result from the layer-by-layer deposition of the parts (Gockel, J. et al., 2019).

The “staircase” effect occurs because of the approximate construction of surfaces using deposition layers with a particular layer thickness. It produces dimensional errors (defined by the cusp height, Ref. Figure 2-38), normal to the deposition or build direction. For a particular part surface, the larger the layer thickness, the greater the dimensional error produced in the part. The cumulative effect of the dimensional misalignment leads to a longer build time, material wastage,

deterioration of surface quality and time-consuming post processing (Singh, P. and Dutta, D., 2003).

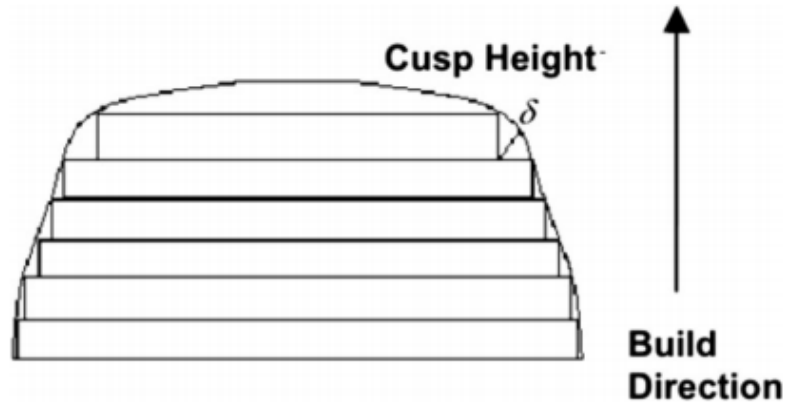


Figure 2-38 Schematic diagram, showing an approximate surface and “stair stepping” effect (Singh, P. and Dutta, D., 2003).

In terms of the WAAM process, the surface waviness or roughness of a part is determined by the deposition parameters including WFS, travel speed, layer height, interpass temperature and deposition strategy or tool path strategy (Gockel, J. *et al.*, 2019).

Therefore, the characteristic surface finish that can be achieved from a WAAM part manufactured using Tandem-GMAW process is a critical determinant of the performance of the technology. This is because premature failure from stress concentration due to surface-initiated cracks, could affect the structural integrity of the part (Hu, S. *et al.*, 2018; Tian, Y. *et al.*, 2017). The stresses developed can cause warping and deformation of the structure, leading to poor surface quality and dimensional inaccuracy of the final parts (Charles *et al.*, 2019).

Furthermore, the necessity for time-consuming post-process machining operation to correct the poor surface quality of the as-deposited part, could negate the cost competitiveness of the technology (Hu, S. *et al.*, 2018; Tian, Y. *et al.*, 2017).

Studies on surface quality of parts built via arc-additive manufacture (AM) processes, have received much fewer research efforts than the counterpart energy beam-AM processes. In comparison to Direct Laser Deposition (DLD), it is harder to realise high surface finish and geometrical accuracy with the Tandem WAAM process, due to the relatively high arc energy, arc pressure, as well as high fluidity of the molten pool. Nevertheless, much higher material deposition rates are possible with Tandem-WAAM, and the equipment costs are also relatively lower and hence worthy of consideration (Ge, J. *et al.*, 2018).

A study evaluating the influence of process parameters on surface quality (roughness) in Selective laser melting of steel powder material was undertaken by Tian *et al.* They highlighted that suitable combination of scan power and speed was critical to achieving the desired surface finish and noted that too high a scan power could increase surface roughness, due to spattering of the powder arising from high energy intensity of the weld pool. Relatively lower levels of scan speed, which gives sufficient time for the redistribution, wetting and flattening of the melt pool, was in general preferred for achieving better surface finish (Tian, Y. *et al.*, 2017).

Strano, G. *et al.* (2013), conducted a study to predict and model the surface roughness in Selective Laser Melting (SLM) deposition. They stated that the parameters which determined the surface roughness included the build orientation and thickness of deposited layer. They concluded that smaller layer thickness gives lower surface roughness. They acknowledged the role of the “stair-step” effect in the characteristic roughness produced by the parallel edges on the deposited surface (Strano, G. *et al.*, 2013).

Past studies on surface quality characterisation of WAAM parts, deposited using GMAW processes are very limited, and the few existing ones have only focused on the use of single-wire GMAW process. Kazanas, P. *et al.* (2012) utilised a Fronius CMT GMAW process to investigate the surface quality of deposited wall structures. They reported that travel speed is the main factor which determined the surface quality obtained in the manufacture of inclined and horizontal WAAM wall features. The high surface waviness of the wall was attributed to the humping

defect occasioned by the backward flow momentum of molten metal at high travel speed, in conjunction with gravitational effect on the horizontal walls. They further explained that the observed poor surface waviness was also caused by lower current levels applied, at lower wfs/ts ratio. The low temperature which resulted, led to poor fluidity and fusion characteristic between the layers, giving rise to a larger distance between the peaks and valleys of the deposit beads (Kazanas *et al.*, 2012).

The above conclusion is somewhat contrary to the findings by Yacob, S. *et al.* (2015) who investigated the effects of GMAW-CMT parameters on surface roughness. They concluded that the surface roughness decreased with increase in welding speed and substrate thickness but increased with increase in contact tip to work distance (Yacob, S. *et al.*, 2015).

Xiong, J. *et al.* (2018), recently investigated the effects of process parameters on surface roughness for GMAW single-wire WAAM deposition of thin wall structures and summarised that lower inter-layer temperatures were beneficial for improving the surface roughness of the part. At a constant wire feed speed to travel speed ratio (wfs/ts), surface roughness increased with increase in wire feed speed. They concluded that a suitable combination of lower wire feed speed and lower travel speed was most effective in enhancing the as-deposited surface finish of the built wall parts (Xiong, J. *et al.*, 2018).

A recent Tandem-GMAW high productivity study by (Martina, F. *et al.*, 2019), conducted to deposit single layer walls showed significant deterioration in surface quality and dimensional tolerance of the wall. This was attributed to excessive heat accumulation, from the use of a high wfs/ts ratio. Further adjustments of the deposition parameters enabled the deposition of a wall structure, howbeit with poor surface quality, as shown in Figure 2-39 (Martina, F. *et al.*, 2019).

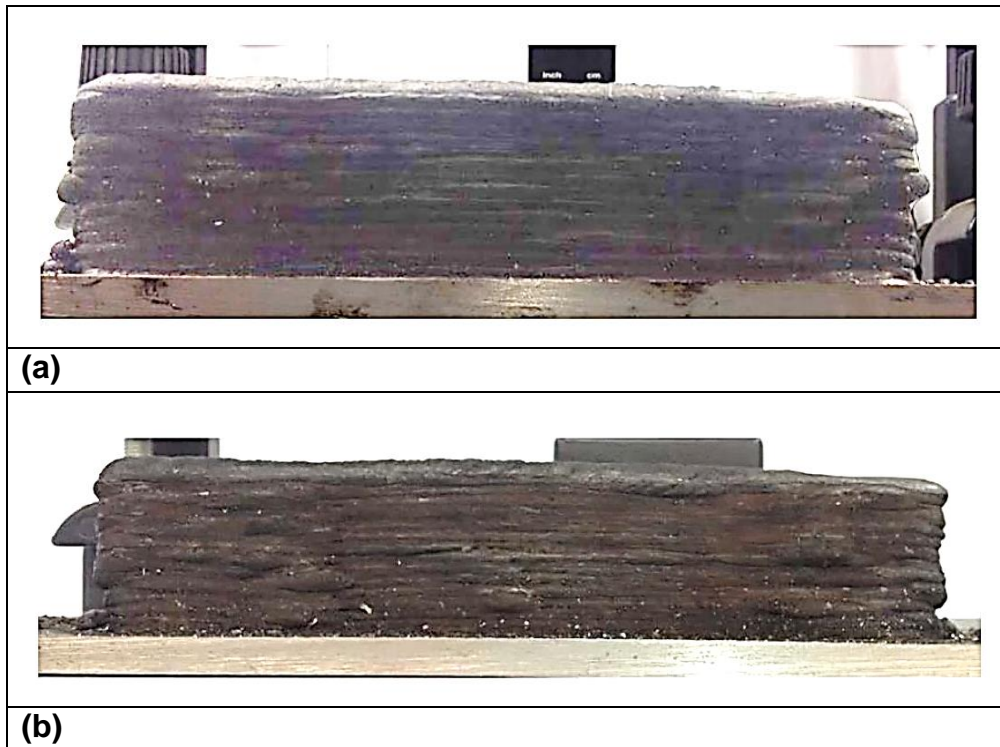


Figure 2-39 Surface quality of tandem-GMAW WAAM manufactured wall structure, using WFSs of (a) 7m/mins WFS (b) 9m/mins WFS (Martina, F. *et al.*, 2019).

Apart from the process parameter, the poor surface quality was significantly caused by the unavoidable “staircase effect”, from the layer-by-layer bead deposition. This was accentuated by the larger layer height deposit which was the result of the use of the tandem-GMAW process, compared to the traditional SW-GMAW setup (Xiong, J. *et al.*, 2018). The study however reported acceptable hardness and microstructure in the tested samples (Martina, F. *et al.*, 2019).

Figure 2-40 also show an overview of a wall structure, with poor geometrical and surface quality, deposited using high deposition rate parameters (Kovacevic, R., 1999).

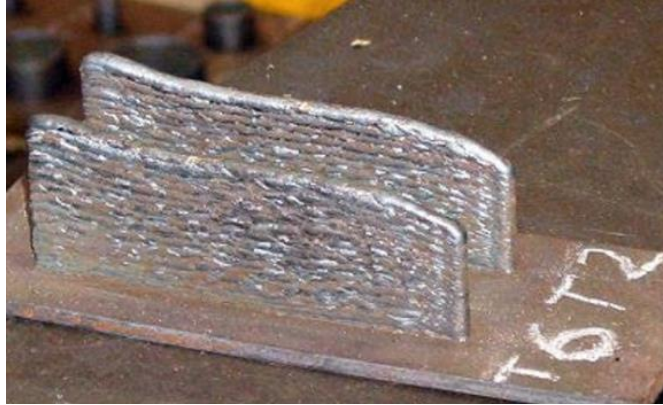


Figure 2-40 Wall structure, showing irregular geometry and poor surface quality. (Kovacevic, R.,1999)

Sanaei, N. and Fatemi, A. (2020) noted that post deposition processing methods such as machining, blasting, shot peening, and vibratory grinding are typically employed for improving the surface quality of AM parts (Sanaei, N. and Fatemi, A., 2020). This is to obtain the required dimensional and technical specification, because the as-deposited surface quality of WAAM parts is not sufficient in meeting the general industrial application requirements (Mahesh, M. et al., 2004).

Several researchers have lauded the development of a hybrid rapid manufacturing system because it enabled the simultaneous layer-by-layer deposition and machining of WAAM features, to actualise enhanced surface finish and a functional integrity of the part (Pandey, P. M. et al., 2003; Simoni, F. et al., 2019). For example, Shrestha, R. et al. (2019), reported that the tensile properties of Ti-6Al-4 V manufactured part, using the electron beam power bed fusion (EB-PBF) process, increased significantly with reduction in surface roughness. They found that elongation to failure increased by almost twice; also, the yield and ultimate tensile strengths increased by approximately 15%, when the surface roughness of the specimen was reduced from 38.9– 10.9 μm (Shrestha, R. et al., 2019).

In view of the above discussion, the consensus among several authors is that the applied process parameters (especially relating to high deposition rate), have a significant influence on the characteristic deposited bead profiles and consequently the resulting surface quality (Yacob, S. et al., 2015; DebRoy, T. et

al., 2018). Hence, it is considered imperative to achieve a suitable trade-off between actualising a higher deposition rate and the potential technical necessity to perform significant costly and time-consuming post deposition machining associated with the WAAM process. This is important for the economic justification of the technology (Hu, S. et al., 2018; Tian, Y. *et al.*, 2017).

Most of the available literature has been mainly focused of energy beam-AM, while very limited studies have been devoted to single-wire WAAM processes. Interestingly, this review has found no previous research work dedicated to characterizing the surface and dimensional quality of Tandem-WAAM deposited metallic structures.

This study therefore seeks to utilise tandem-GMAW process in combination with an innovative skin and core deposition strategy, that can be applied to manufacture of large WAAM structures, with the aim to maximise deposition rates, while ensuring high surface and dimensional quality, as well as acceptable property, of the fabricated part. This could be a game changer and increase interest in the wide deployment of WAAM technology, particularly for manufacturing heavy wall components.

2.7 Skin and core deposition strategy for WAAM components

Both the increase in deposition rate and decrease in surface waviness or macro roughness can contribute to decreasing the cost of producing WAAM components. Nevertheless, increase in deposition rate is usually accompanied with higher part distortions (owing to the higher heat input), and a deterioration in surface quality of parts, and consequently leading to higher buy-to-fly ratios, requiring more machining time and raw material.

This is essentially why it was recently concluded that increasing the deposition rate of Ti6 4V above 1 kg/h will not provide any significant economic benefits in automated WAAM cells, and that maintaining the deposition rates of steel at a medium level of approximately 3 kg/h, will result in a buy-to-fly ratio of less than 1.5, thereby maximizing cost savings (Williams, S.W. et al., 2016).

But, if the deposition rate could be increased, while maintaining the same buy-to-fly ratio and surface waviness, it would provide a significant decrease in WAAM manufacturing costs. This would also be accompanied with a reduction in manufacturing time and increase the capacity utilization and productivity of the WAAM process (Rodriguez, N. *et al.*, 2018).

To simultaneously maximise deposition rate and surface quality of a WAAM part, using Tandem-wire process, the “boundary” technique, referred to as skin and core deposition technique, was investigated in this study, in which a WAAM part is partitioned into two sections, an outer “Skin” and inner “Core” sections, as illustrated in Figure 2-41.

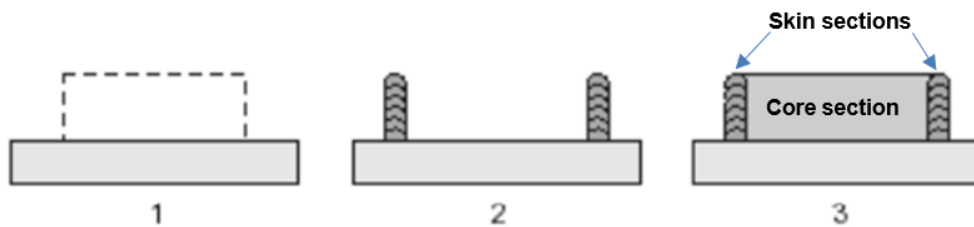


Figure 2-41 Schematic illustration of boundary layer technique (Cooper, 1999)

This technique allows different deposition parameters to be specified for each portion. The core does not have strict requirement for surface or dimensional quality; hence its deposition rate can be maximised within the limit of the process parameter and deposition stability. On the other hand, the skin can be built at a lower deposition rate to maximise the dimensional and surface quality, while ensuring adequate fusion performance (Poprawe, R. *et al.*, 2015).

The reference chart in Figure 2-42, shows a comparison of typical build rates and process resolutions presently achievable with powder bed fusion additive manufacturing, blown powder-directed energy deposition, WAAM and high building rate wire-based AM processes such as EBAM and Rapid Plasma Deposition (Rodriguez, N. *et al.*, 2018). It indicates that build rate depends on the square of the layer height, while both resolution and surface waviness changes linearly with layer height. It is anticipated that this build rate and surface quality currently achievable with high deposition WAAM processes, could be increased using the skin and core technique.

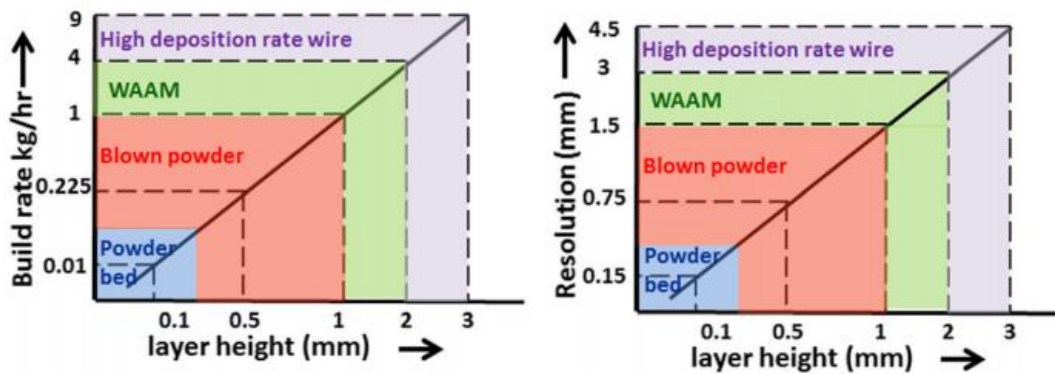


Figure 2-42 Build rate and horizontal resolution Versus layer height for different AM technologies. Rodriguez, N. *et al.* (2018)

2.8 Thermal cycle generation and heat treatment during WAAM process

The conventional manufacturing processes for alloy 2.25Cr 1Mo, utilises the subtractive technique from forgings (Queguineur, A. *et al.*, 2018; Deng and Kiyoshima, 2007) and several other processing routes to obtain the required finished product (Almeida, P.M.S. and Williams, S., 2010).

Recently there has been significant interest to manufacture 2.25Cr 1Mo steel components via WAAM for use for example in subsea oil and gas applications. However, before the extensive use, its inherent properties including microstructural phase formations, as well as mechanical performance need to be thoroughly evaluated.

Little or no study have been reported on WAAM fabricated heavy-walled component using 2.25Cr 1Mo alloy. However, numerous literatures exist for welding fabrication of wrought 2.25Cr 1Mo alloys. Many of these studies for example have typically reported that the material cannot be used in the as-fabricated condition, unless heat treated. (Javadi, Y. *et al.*, 2017; Elrefaey, A. *et al.*, 2018). This is because of the need to temper the hard and brittle HAZ microstructures which develops during welding fabrication, (Javadi, Y. *et al.*, 2017). The heat treatment helps to restore its toughness which is critical to the safe operation and integrity of the products (Elrefaey, A. *et al.*, 2018), amongst other benefits.

Another critical issue concerning the use of 2.25Cr-1Mo materials for marine subsea applications is the potential for its exposure to sour environment during production activities. In this environment, failure from hydrogen sulphide (H₂S) stress corrosion cracking can occur when a susceptible microstructure is present. A suitable hardness level of the material is crucial in mitigating its susceptibility to premature failure. Hence, the National Society of Corrosion Engineers (NACE) and the International Organization for Standardization (ISO) have set a standard which limits the hardness of the HAZ and weld metal. The standard specifies a maximum HAZ hardness of 22 HRC (or 250 HV10) under certain environmental conditions (Elrefaey, A. *et al.*, 2018).

To successfully utilise 2.25Cr 1Mo alloy material in the production of WAAM components intended for marine subsea oil and gas application, an investigation of the microstructural and mechanical performance of the weldment made through this method is imperative.

2.8.1 2.25Cr 1Mo steel alloy

The range of typical composition of the alloy given by ASME SA335-P22 is presented in Table 2-4 (Bhadeshia, H.K.D.H., 1992).

Table 2-4 Typical composition range of 2.25Cr 1Mo steel alloy

ASTM	UNS Equivalent	C≤	Mn	P≤	S≤	Si≤	Cr	Mo
P22	K21590	0.05~0.15	0.30~0.60	0.025	0.025	0.5	1.90~2.60	0.87~1.13

2.8.2 Alloying additions and effect

The presence of alloying elements in steel determines the metallurgical phases, as well as the mechanical performance of the material. Carbon increases the strength of the material. When present in sufficient amount, it forms carbides with Iron as well as other elements. This impacts precipitation strengthening and creep resistance on the material. Nevertheless, excess amount of carbon leads to poor weldability of the material (Olsen, D.L. and North, T.H., 1992).

Nickel, manganese, and copper are austenite stabilizers which lower the eutectoid transformation temperature. But molybdenum and chromium suppress

the transformation of austenite, by raising the eutectoid transformation temperature (A_1). Hence, they effectively stabilize the ferrite phase (Grong, O. & Matlock, D. K., 1986; Sidney H. Avner, 1974; Olsen, D.L. and North, T.H., 1992).

Chromium and molybdenum cause delay to the ferrite-pearlite reaction in 2.25Cr 1Mo steel because of their higher proportions, compared to other alloying elements. This increases the hardenability of the steel material (Bhadeshia H.K.D.H. and Honeycombe R.W.K., 2006)

The time temperature transformation (TTT) diagram in Figure 2-43, shows the separation of ferrite-pearlite and bainite reactions when molybdenum was added (Bhadeshia H.K.D.H. and Honeycombe R.W.K., 2006).

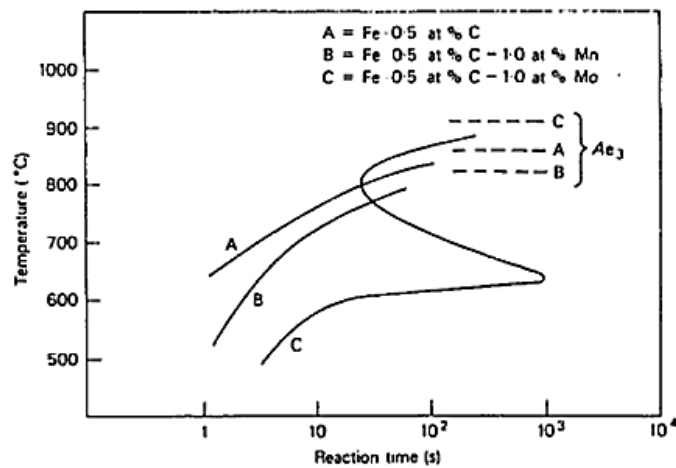


Figure 2-43 Effect of different alloying elements on the TTT-diagram of a Fe-0.5 at% C steel.

The effect of molybdenum in suppressing the γ/α -reaction is indicated by the “bay” between the bainite and ferrite fields in curve C. The dashed lines show the ferrite stabilizing properties of molybdenum, since increased molybdenum content increases the A_{c3} temperature (Bhadeshia H.K.D.H. and Honeycombe R.W.K., 2006).

The effect of alloying elements on eutectoid temperature is illustrated in Figure 2-44.

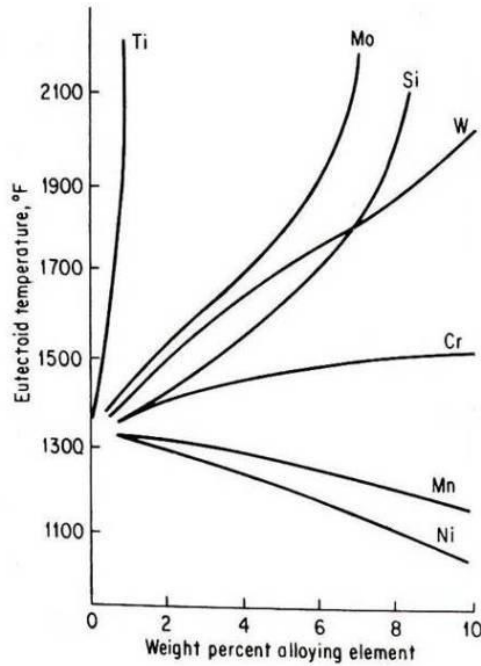


Figure 2-44 Effect of alloying elements on Eutectoid temperature (Sidney H. Avner, 1974).

Molybdenum and chromium both promote the formation of bainite preferentially to acicular ferrite (Bose-Filho, W. W. et al., 2007). They like many other alloying elements, increases tensile strength and hardness by solid solution strengthening; and, through precipitation of harder phases such as carbides (Jorge, J. C. F. et al., 2001).

Chromium could promote formation of acicular ferrite (AF) under certain conditions, it however can also decrease the impact toughness of weld metal due to evolution of high-volume fractions of martensite-austenite (M-A) microphases in single pass weld deposits, and increased formation of martensite (MA) in the reheated regions of multi-pass weld deposits. Their presence within the notch of charpy impact specimen leads to premature failure (Avazkonandeh-Gharavol, M. H., et al., 2009; Jorge, J. C. F. et al., 2001).

Manganese and silicon play an important role in the deoxidising process of weld metal and are constituent parts of oxide inclusions. Manganese is mainly added as an austenite stabilizer, increasing the strength and hardenability of the steel. It is however a weaker deoxidizer compared to silicon (Sindo Kou, 2003).

Manganese and nickel have a strong influence on hardenability and increase the volume fraction of acicular ferrite preferentially to allotriomorphic ferrite (Bose-Filho, W. W. et al., 2007).

Nickel can be increased to improve the weld metal toughness in as-deposited condition. Higher nickel content could decrease resistance of the material to tempering, by suppressing the A1 transformation temperature, and favouring formation of higher temperature microstructures. However, it is important to understand whether adverse effect on the strength of the deposited weldment can result from increased nickel content (DuPont, J. N., 2017). Other studies have found that the beneficial effect of Nickel depends on the presence of other alloying elements (Bhole, S. D. *et al.*, 2006).

2.8.3 Martensitic formation in 2.25Cr 1Mo alloy

Martensite develops when austenite is cooled rapidly enough to miss the bainite nose (Figure 2-45). It is a hard and brittle compound. The reaction is dubbed shear transformation as it occurs without diffusion of Carbon and is accompanied by a change in volume or shape within the transformed area. Since the formation of martensite occur in a diffusion-less manner, the reaction causes entrapment of carbon atoms within the interstitial lattice and induces strain in the lattice. The martensite develops in the form of thin plates or laths, to decrease the strain energy induced from the surrounding materials (Bhadeshia H.K.D.H. and Honeycombe R.W.K., 2006).

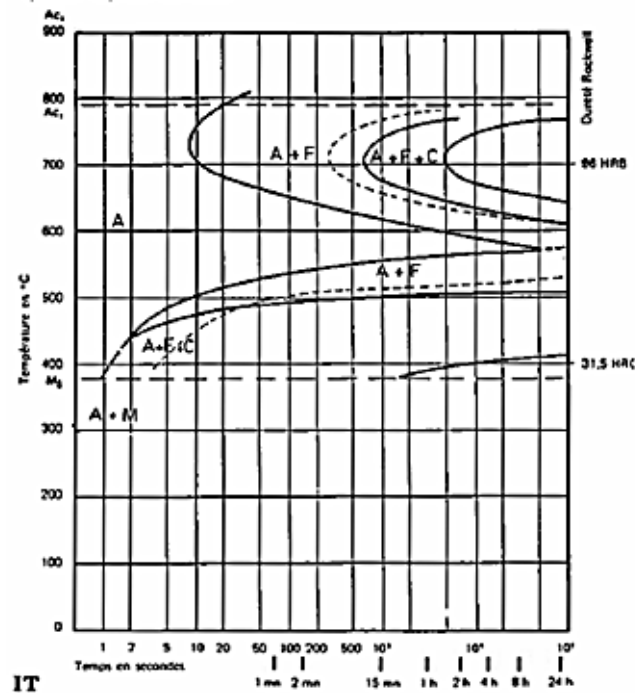


Figure 2-45 IT and CCT diagram for steel with composition closely matching F22 steel. Composition: [0.15% C – 0.36% Mn – 0.44% Si – 0.020% S – 0.022% P – 0.09% Ni – 2.24% Cr – 0.85% Mo – 0.23% Cu – 0.097% Al – 0.01% Ti; Grain size: 10, Austenitised at 975°C for 30mins] (Bhadeshia H.K.D.H. and Honeycombe R.W.K., 2006).

In low or medium carbon steel, the microstructure in martensite is present as laths, however, in high carbon steel, they occur as plates. The martensitic laths in low carbon steel are fine structures, they nucleate in the grain boundaries and can extend through the whole prior austenite grain. The substructure of the individual lath consists of high dislocation density (Speich G.R. and Leslie W.C., 1972).

The empirical formula for determining the Martensitic Start (Ms) temperature with respect to steels with compositions up to 0.6% C, 5.4% Mo and 4.6% Cr., was developed by Andrews (Andrews, K.W., 1965) and is given in equation (2-3) as follows:

$$Ms = (539 - 423C - 30.4Mn - 12.1Cr - 17.1Ni - 7.5Mo) \text{ } ^\circ\text{C} \quad (2-3)$$

2.8.4 CCT Curve of 2.25Cr 1Mo steel

Continuous cooling transformation (CCT) diagram is a plot of transformation temperature against time.

The transformation temperature between 800 and 500 °C ($t_{8/5}$) (Krauss, G., 1980), is regarded as most crucial with regards to the development of steel property as the metal cools down during welding (Krauss, G., 1980; Grong, O. & Matlock, D. K., 1986).

For a three-dimensional flow of heat, (involving thick volume of weld deposits), the net heat input is roughly proportional to $\Delta t_{8/5}$.

$$\Delta t_{8/5} \approx 5hE \quad (2-4)$$

Where h is the efficiency of the arc and E is the overall heat input in (kJ/mm)

Also, $\Delta t_{8/5}$ is influenced by the mode of heat flow (which differs between a thin and thick plate) and is a function of both the preheating temperature and heat input (Grong, O. & Matlock, D. K., 1986).

The prior austenite grain size, bainitic ferrite volume fraction and M/A constituent increased as the cooling time increases, whereas the amount of martensite decrease (Shi, Y. and Han, Z., 2008).

The CCT diagram for 2.25Cr-1Mo type alloys are shown below as provided by S  f  rian (S  f  rian, D. and Bishop, E.E.,1962), Figure 2-46 and Lundin, Kruse and Pendley, Figure 2-47 (Lundin, C. D., et al.,1982).

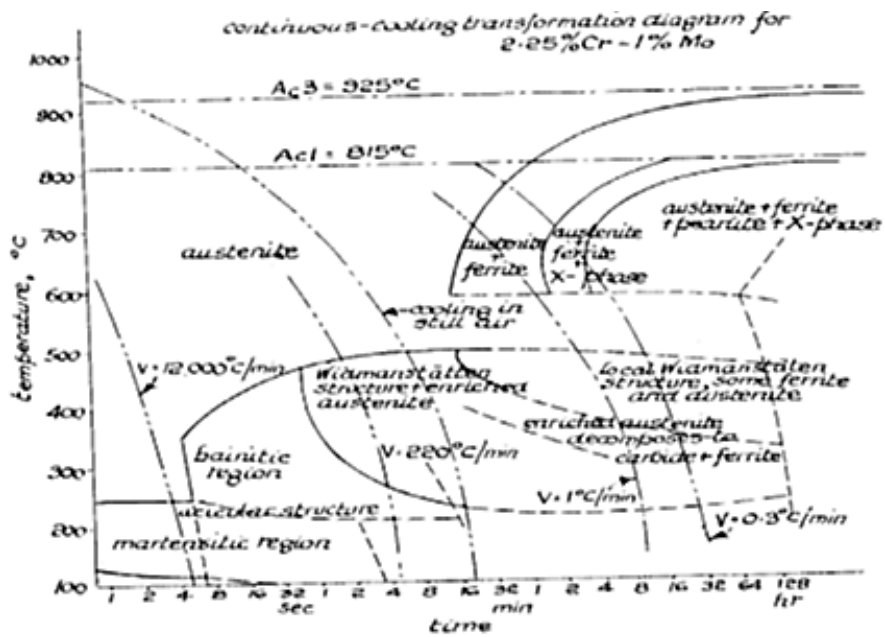


Figure 2-46 CCT diagram for 2.25Cr-1Mo by S  f  rian (S  f  rian, D. and Bishop, E.E.,1962).

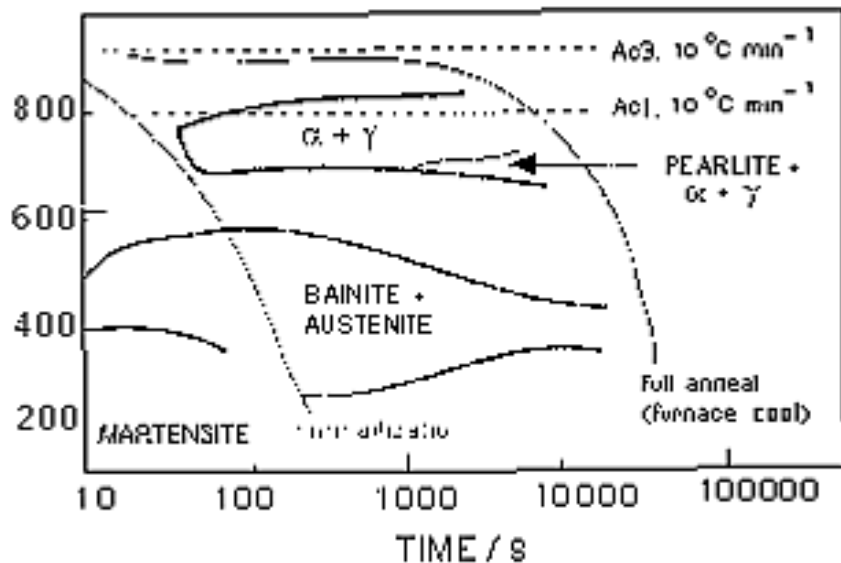


Figure 2-47 CCT diagram for 2.25Cr-1Mo by Lundin, Kruse and Pendley (Lundin, C. D., et al.,1982).

During the fusion welding of steel, phase transformation begins in the steel material from the austenitic phase, above the Ac3 temperature. At this temperature, grain growth can occur at higher temperatures resulting in coarse grain heat affected zone (CGHAZ) or recrystallisation resulting in evolution of

fine-grain heat affected zones (FGHAZ). In between the Ac3 and Ac1 temperature range, the material exists in a dual phase of austinite and ferrite, termed Intercritical HAZ region (Rodrigues, T. A. *et al.*, 2019). Tempering of the steel material occurs below the Ac1 temperature.

2.8.5 Microstructure of 2.25Cr 1Mo weldment

The Weld metal microstructure in 2.25Cr-1Mo have been studied by a number of authors including Hans-Olof *et al.*, who termed the microstructure they observed as granular bainite. This is because of how it appeared under the microscope. TEM analysis of the microstructures showed that they consisted of bainitic ferrite and retained austenite (Andrén, H. O., Cai, G. and Svensson, L. E., 1995). They also reported that a heterogeneous and non-equilibrium phase such as δ -ferrite is expected to form, due to the fast solidification rate of 2.25Cr 1Mo weldment and inclusions are often precipitated in the microstructure. The dominant precipitate after post weld heat treatment (PWHT) was $M_{23}C_6$. At about 530°C cementite (M_3C) was precipitated, 600°C precipitated M_2C , while above 660°C produced $M_{23}C_6$ precipitates. Further analysis found that the M_2C precipitates consisted of a mixture of Mo-Cr carbides (Andrén, H. O., Cai, G. and Svensson, L. E., 1995).

In a multi-pass weld, the HAZ microstructure of 2.25Cr-1Mo, near the fusion line has been termed by Baas, Pickles and Prince to be primarily 'tempered bainite' (Choi, D. H. *et al.*, 2012). It was found that the microstructure consisted of 'relatively large bainitic packets', with a small fraction of ferritic zones and tempered martensite. At a farther distance from the fusion line, the microstructure in the intercritical zone was observed as untransformed ferrite and tempered martensite. Furthermore, Peddle and Pickles designated the HAZ microstructure after a traditional weld cycle as lower bainite with a fraction of martensite (Peddle B. E. & Pickles C. A., 2001).

Studies by (Arivazhagan, B. and Vasudevan, M., 2015) observed that the as-deposited microstructure in A-TIG welding of 2.25Cr-1Mo (P22) steel consisted of a bainitic microstructure with small patches of proeutectoid ferrite. A combination of fine and coarse lath structures was distributed throughout the

bainite packets, and several precipitates were observed within the ferrite matrix. $M_{23}C_6$, M_7C_3 and M_6C were the three carbides observed in the weldment, Figure 2-48 (Arivazhagan, B. and Vasudevan, M, 2015). The “M” signifies metallic elements such as Cr, Mo, V, and Fe (Wu, K. et al., 2020).

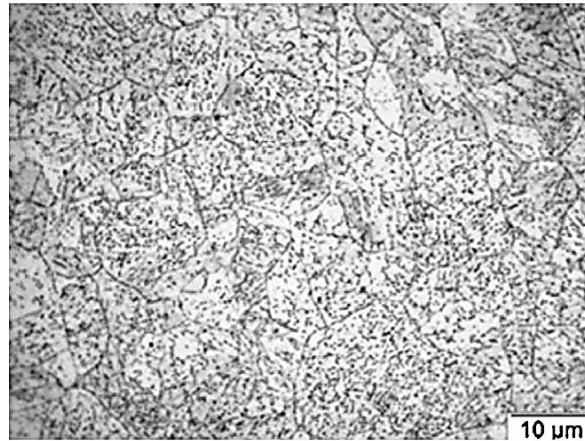


Figure 2-48 Optical image of P22 etched with 2% Nital (Arivazhagan, B. and Vasudevan, M, 2015).

EDS analysis after PWHT showed the presence of the more stable $M_{23}C_6$ precipitates. The precipitates became nearly spherical in shape after PWHT, and coarsens with increase in PWHT temperature, resulting in increased toughness (Arivazhagan, B. and Vasudevan, M, 2015).

A study on the microstructure and charpy impact toughness of a 2.25Cr-1Mo-0.25V Steel Weld Metal conducted by (Wu, K. et al., 2020), reported that the microstructure of the as-deposited metal consisted of bainitic ferrite, blocky martensite islands, and retained austenite (M-A constituents). The slender M-A constituents were distributed in the prior austenite grain boundary. Transformation of the microstructure to ferrite and carbide precipitates occurred after PWHT and carbides were distributed in the ferrite grain boundaries (Wu, K. et al., 2020).

Elrefaey, A. *et al.* (2018) evaluated the effect of heat input on toughness in the weld metal and 2.25Cr-1Mo-LAS forging interface. They reported that the as-deposited microstructure was mainly composed of approximately 90% coarse bainite and small grains of ferrite. They also observed that the microstructures in

the weld regions were tempered to some extent due to the thermal cycles associated with successive weld depositions and attributed the observed decrease in hardness to increased precipitate coarsening and decrease in dislocation densities. The presence of inclusions transformed the charpy impact toughness morphology to cleavage fracture and coarse columnar grains were attributed to the low fracture toughness of the weld metal observed (Elrefaey, A. *et al.*, 2018).

Inclusions have been long recognised to be beneficial in the control of weld metal microstructure and toughness. This is because they produce two opposite effects- including providing nuclei sites for the nucleation of acicular ferrite and initiation of ductile and/or cleavage fracture (Bose-Filho, W. W., *et al.*, 2007; Avazkonandeh-Gharavol, M. H., *et al.*, 2009). The effect is dependent on their sizes and compositions (Avazkonandeh-Gharavol, M. H., *et al.*, 2009).

Certain types of inclusions are thought to be more effective in nucleating intragranular ferrite and it is assumed that the occurrence of potent inclusions could be indicated by the presence of large volume fraction of acicular ferrite. Inclusions in steel weld metal typically consists of oxide rich cores (Koseki, T., 2005).

2.8.6 Multi-pass weld zones

During multi-pass weld deposition, an HAZ area of weld metal is subject to an effect of successive thermal cycles and, consequently, the creation of metallographic structures characterised by various mechanical (strength and plasticity-related) properties takes place. In addition, tempered structures are formed in some areas within the HAZ. As far as plastic properties and especially impact strength is concerned, the most unfavourable HAZ area is CGHAZ (i.e., Coarse Grain Heat Affected Zone). Subsequent thermal cycles reheat portions of the CGHAZ to intercritical temperatures from the range of AC1 and AC3 giving rise to coarse grain structure known as ICCGHAZ (i.e., Intercritically Reheated Coarse Grained HAZ).

The different zones of a weld metal HAZ are illustrated as shown in Figure 2-49. (Łomozik, Mirosław and Edmund, Tasak, 2006)

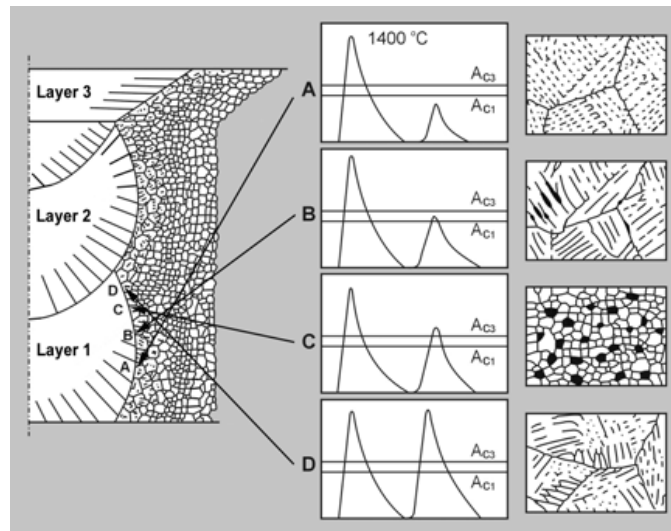


Figure 2-49 Illustrations of microstructures in HAZ of multi-pass weld metal as a function of maximum temperatures of successive thermal cycles (Łomozik, Mirosław and Edmund, Tasak, 2006).

- A- The areas within the HAZ reheated by the thermal cycle of the maximum temperature below the AC1 temperature. This zone is characterised by a coarse grain structure and is termed SRCGHAZ (i.e., Sub-critically Reheated CGHAZ).
- B- The reheated coarse grain HAZ areas is referred to as ICCGHAZ. Here, the maximum temperature of subsequent thermal cycle is contained within the AC1 and AC3 temperature ranger
- C- Fine grain HAZ zone referred to as FGHAZ. This zone experiences maximum temperature due to successive thermal cycle which is higher than the temperature value of AC3.
- D- The coarse grain HAZ area, is associated with successive thermal cycles where the temperature exceeds 1150°C.

2.8.7 Multi-pass weld thermal cycle

Additive manufacturing such as the WAAM process, has some similarity to multi-pass weld deposition. Despite its numerous benefits, one concern during the process is that the weld metal experiences multiple thermal cycles of melting and solidification, due to the layer-by-layer wire deposition technique (Yan, F. et al., 2017; Bai, J. Y. et al., 2016).

The repeated melting and solidification of materials during WAAM deposition process, far exceeds those from traditional forging of similar materials and significantly influence the microstructure and phases formed in the material (Sun, C. et al., 2018). As a result of this, metallurgical dissimilarities exist between components manufactured by traditional forging and WAAM process (DebRoy, T. et al., 2018; Bai, J.Y. et al., 2016). The dissimilarities also depend on the cooling rates and alloying content (DebRoy, T. et al., 2018).

Yan, F. et al. (2017), reported that repeated thermal cycles result in the formation of microstructures which varies within the deposited parts, as well as promoting anisotropy in mechanical properties and defects which are peculiar to AM processes (Yan, F. et al., 2017).

Complex thermal gradients are experienced in the reheated regions of the part as successive layers are deposited (Ge, J. et al., 2018), which can alter the material properties of the end products (Grong, O. & Matlock, D. K., 1986).

Additionally, the magnitude of the local residual stresses during the deposition can be as high as $\frac{3}{4}$ of the material yield strength, which could lead to poor dimensional tolerance of the built part. Therefore, additional post-processing such as by heat treatment is typically required to correct any dimensional inaccuracies (Zadi-Maad, A. et al., 2018). Post deposition heat treatment (PDHT) is commonly performed to counteract the undesirable microstructural changes which develops in material, from welding thermal cycle and improve its mechanical performance (Grong, O. & Matlock, D. K., 1986; Shi, Y. and Han, Z., 2008). PDHT has been shown as a suitable method for achieving equilibrium, enhanced microstructure, and grain structure of WAAM materials. (Yan, F. et al., 2017; Sun, C. et al., 2018; Seow C. E. et al., 2019).

PWHT of 2.25Cr 1Mo steel weld is a common requirement during welding fabrication which is performed to relieve residual stresses, reduce the hardness, and restore toughness of the weldment (Javadi, Y. *et al.*, 2017; Elrefaey, A. *et al.*, 2018).

2.8.8 Tempering heat treatment of steel weld metal

The transformation of metastable phases into highly stable forms could occur with the application of heat. Tempering is the process by which a quenched material is transformed to improve its toughness and ductility, by application of heat energy (Krauss, G., 1980). The steel is heated to below the lower critical temperature (A_{c1}) and then cooled at any desired rate (Kalyankar, V. D. and Chudasama, G., 2018). After tempering, the microstructures formed will attain a more stable condition (Krauss, G., 1980).

Martensitic microstructure is hard and brittle, but when tempered correctly can possess an excellent combination of strength and toughness achievable in low carbon steel. Tempering of martensite is one of the main essential operations in contemporary steel making process. Combining several heat treatment time and temperature parameters can produce desirable mechanical properties. But temperature has the most significant effect on tempering (Hollomon, J.H. and Jaffe, L.D., 1945).

During tempering, precipitates of finely dispersed carbides in a matrix of ferrite initially appear in the microstructure. The hardness of the tempered martensite reduces with a corresponding increase in its toughness (Aleksander, R. S., 2012).

The initial reduction in hardness during tempering is commonly attributed to carbon segregation and precipitation as well as disappearance of tetragonality. This is followed by dislocation annihilation which begins above 300°C as illustrated in Figure 2.8 (Speich, G.R., 1969).

As the tempering progresses, coarsening of the carbide precipitates continues, and the hardness reduces further (Krauss, G., 1980). Coarsening and spheroidization of cementite occurs as temperature increase between 300°C to 700°C. As the temperature approaches 700°C, ferrite begins to form by

recrystallization (Bhadeshia H.K.D.H. and Honeycombe R.W.K., 2006). The increase in temperature consequently causes the formation of larger iron carbide grain size, thereby increasing the softening and ductility of the steel material (Kalyankar, V. D. and Chudasama, G., 2018).

Disintegration of possible retained austenite also occurs, but does not cause softening, particularly not in low carbon steel such as F22 (2.25Cr 1Mo), which contains insignificant level of retained austenite (Baltazar Hernandez, V.H., et al., 2011).

When the tempering is prolonged Ostwald ripening of cementite particles will occur, which was also reported by (Speich, G.R., 1969; Krauss, G., 1980; Bhadeshia H.K.D.H. and Honeycombe R.W.K., 2006). A common result of the processes is reduction in strength, with associated increase in the toughness of the steel.

Figure 2-50 shows the variation of hardness with tempering temperature for steels with varied carbon content tempered for 1 hr (Speich, G.R., 1969). It shows that hardness reduces when tempering temperature is increased and a higher carbon content increases resistance to tempering.

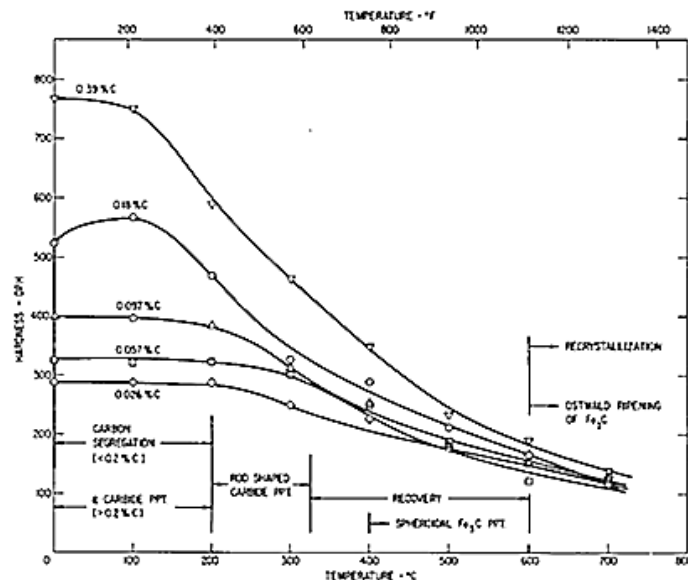


Figure 2-50 Hardness change in iron-carbon martensite tempered for 1 hour as a function of tempering temperature (Speich, G.R., 1969).

Precipitation of carbides occurs during tempering. Also, loss of possible tetragonality and release of lattice stresses occurs. The carbides which precipitate can function or act to pin the sites (grains) as the recovery of martensite laths occur (Bai, J. Y. et al., 2016).

2.9 Tailored modification of wire composition

High strength and toughness are desirable properties for weldments required in the fabrication of oil and gas components and filler wire chemical composition has the most significant influence on the microstructure and mechanical characteristics of weld metals (Gouda, M. et al., 2005; Haerian, A, 2009; Avazkonandeh-Gharavol, M. H. et al., 2009), and consequently performance of the final components (Sames, W. J. et al., 2016).

In recent times, efforts have been geared towards the synthesis of new materials for additive manufacture processes. An important consideration in designing alloy materials for WAAM manufacture is the ability of the alloy to cope with the high thermal variation as it solidifies and to facilitate the control and formation of desirable microstructure, grain orientation and in situ phase precipitates. (Sames, W. J. et al., 2016). Understandably, the developmental efforts have mainly been focussed on those alloys utilised in high end industries (such as nickel-based super alloys and titanium alloys) Sames, W. J. et al., 2016. It is however important to increase efforts in the knowledge, design, and development of low alloy steel materials suitable for WAAM fabrication. This is essential to boost large scale use of the technology in the manufacture of critical load bearing components such as required for marine oil and gas applications (Haden, C. V. et al., 2017).

2.9.1 Weldability issues of 2.25Cr 1Mo alloy weldment

Alloy 2.25Cr-1Mo steel material loses its pristine properties during deposition, leading to high hardness and poor toughness within the HAZ and reheated regions of multi-pass weld metal (Choi, D. H. et al., 2012).

The presence of relatively high amount of Cr and Mo raises the A1 temperature (Eutectoid temperature) imparting high hardenability on 2.25Cr 1Mo weldments. The alloy forms a heterogenous microstructures typically consisting of high

proportion of martensitic microstructure, as well as fractions of bainite and retained austenite, depending on the cooling rate (Deng, D. et al., 2013).

The as-deposited martensitic microstructure in 2.25Cr 1Mo alloy is hard and brittle, and significantly contributes to the deterioration in mechanical properties, especially impact toughness of the weld metal. As a result, post weld heat treatment (PWHT) is essentially performed to homogenise and soften the hard microstructures formed in the reheated zones of the deposited weld metal. PWHT leads to improvement in strength, hardness, and toughness of the weld metal, (Deng, D. and Kiyoshima, S., 2007; Zhang, L. *et al.*, 2015; Javadi, Y. et al., 2017), as well as relieves detrimental residual stresses generated in the fabricated part (Deng, D. and Kiyoshima, S., 2007; Elrefaey, A. et al., 2018).

The additional post processing of WAAM parts by heat treatment can lead to substantial increase in manufacturing lead time, costs and add further complexities to the WAAM process. This could potentially make the WAAM technology commercially less attractive.

Therefore, the development of optimised wire compositions, or new alloys suitable for WAAM deposition, that can adequately meet the required as-deposited material property, would provide a significant technological impact.

Although enormous research effort is needed to achieve this, it is however desirable to provide a broader variety of suitable deposition wire compositions and increase the robustness of WAAM materials for marine applications. Novel alloys will also be useful for new industries and new components; and alloys specifically suited for WAAM process would have the potential to outperform the capability of conventional wrought materials (Sames W. J. et al., 2016).

2.9.2 Weld metal micro-constituents

Microstructures have the most significant influence among the factors that affect toughness and strength of weld metal. In addition, grain size, phase structure, number of inclusions and solute elements also play important role (Zhang, L. *et al.*, 2015; Setiyanto, N. A. et al., 2019).

Microstructures of high strength filler metals with alloying additions of Ni, Mn, Cr and Mo contain a combination Acicular ferrite (AF), Bainite (B), and low carbon martensite (MA). The relative amount of these different phases is mainly dependent on the chemical composition of the wire and thermal cycle prevailing during deposition (Aglan, H. A. *et al.*, 2013).

Acicular ferrite (AF) microstructure is mostly desired in weld metal. This is because it can effectively produce excellent mix of strength and toughness and is able to repel the formation and propagation of cracks. This is due to its fine grain size, consisting of “high dislocation grains density, large-angle grain boundaries, and exceptional fine interlocking structures. (Zhang, T. *et al.*, 2015)., Zhang, L. *et al.*, 2015).

The high-temperature phase changes which takes place in a steel weld metal, with respect to the complete microstructural formation, is summarised in Figure 2-51 (Babu, S. S., 2004). The formation of acicular ferrite is illustrated as shown.

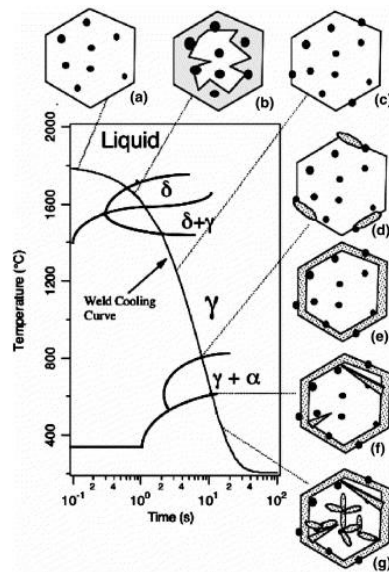


Figure 2-51 Schematic illustration of a weld metal cooling curve and a hypothetical continuous cooling transformation diagram showing different phase transformation that may occur as the weld metal cools to room temperature (Babu, S. S., 2004).

A conventional weld microstructure consisting of acicular ferrite (α_a) is shown in Figure 2-52. The structure is generally described as a “basket-weave structure”.

Figure 2-52(a) shows the optical microstructure illustrating the interlocking nature of acicular ferrite (α_a), in the presence of other ferritic microstructures including Widmanstätten ferrite (α_w) and allotriomorphic ferrite (α) (Babu, S. S., 2004).

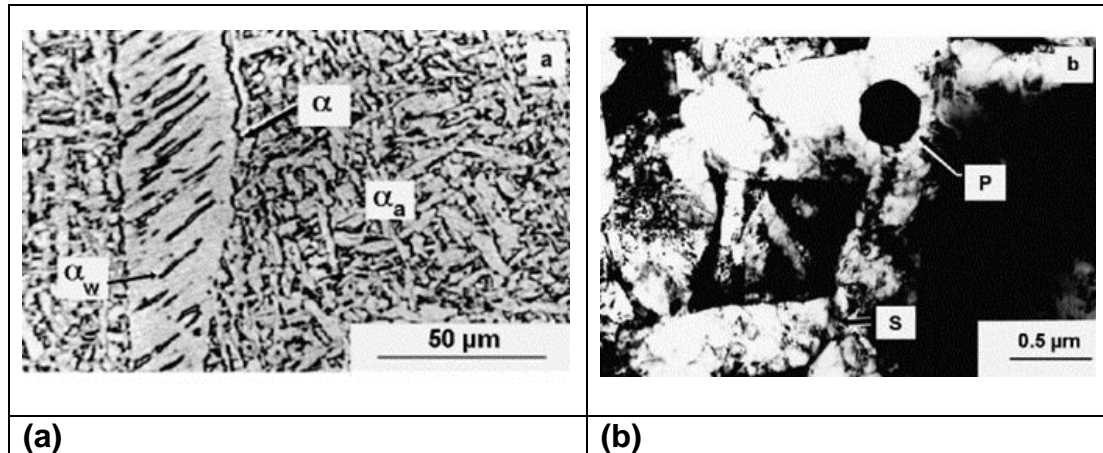


Figure 2-52 Nature of Acicular ferrite in weld metal (Babu, S. S., 2004)

Transmission electron microscope (TEM) analyses of the microstructure shows primary plates (marked as P) nucleated on the inclusions and the secondary ferrite plates (marked as S) formed on previously existing ferrite plates, Figure 2-52(b).

As earlier noted, one method by which the weld metal toughness is strengthened, is related to the frenzied arrangement of lenticular ferrite plates within an austenite grain. The nucleation of acicular ferrite on oxide inclusions promotes this sort of arrangement (Babu, S. S., 2004).

Inclusions have been recognised to be important in the control of weld metal microstructure and toughness. This is because they produce two opposite effects- including providing nuclei sites for the nucleation of acicular ferrite and initiation of ductile and/or cleavage fracture (Avazkonandeh-Gharavol et al., 2009; Bose-Filho, W. W. et al., 2007). The effect is dependent on their size, distribution, number density and compositions (Avazkonandeh-Gharavol et al., 2009). Because AF nucleation is linked to non-metallic inclusions, the properties of a weld metal can be controlled and improved by modifying the inclusion characteristics (Zhang, L. et al., 2015; Schnitzer, R. et al., 2017).

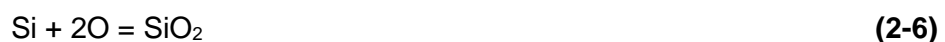
Certain types of oxide inclusions are thought to be more effective in nucleating intragranular ferrite and it is assumed that the occurrence of potent inclusions could be indicated by the presence large volume of fraction of acicular ferrite. Inclusions in steel weld metal typically consists of oxide rich cores (Koseki T., 2005).

The study by Pamnani, R. *et al.* (2016), found that the impact toughness of a weldment produced using submerged arc welding (SAW) was lower in comparison to those of shielded metal arc welding (SMAW) and fluxed core arc welding (FCAW). The low impact toughness of the SAW weld metal was attributed to the higher number density of inclusions formed (Pamnani, R. *et al.*, 2016).

A similar observation was reported where it was found that the mechanical property of weld metal deposited using GMAW process with 100% argon shielding gas, was superior to that obtained using 98%Ar/2%O₂, which was attributed to the lower number density of oxide inclusion formed in the former (Barrick, E. J. and Dupont, J. N., 2020).

2.9.2.1 Weld metal oxygen

During GMAW process, the weld metal is enriched with oxygen from a variety of sources including from the atmosphere, use of shielding gas containing O₂ or CO₂, and reaction of the slag and metal in the weld pool. Oxygen or CO₂ are normally added as a constituent of argon shielding gas for arc stabilisation, reduction of spatter and to prevent the deposited metal from flowing out of the fusion line. However, oxygen can react with the elements in the weld metal, and alter their normal functions, reduce the hardenability, and produce inclusions. Oxidation of the alloying elements result in formation of oxides which either form slag or remain as constituent part of the weld metal inclusion particles. The oxidation of Mn and Si under the high arc heat can be represented by the expressions in equations (2-5) and (2-6) (Sindo Kou, 2003).



Excessive oxidation of the elements in the weld metal can lead to substantial loss of alloying elements, which goes into the slag, thereby deteriorating the mechanical properties of the weld metal. Significant loss of Mn can also occur by evaporation, because of its high vapour pressure (Sindo Kou, 2003). Figure 2-53 illustrate the effect of oxygen content on the mechanical property of deposited weld metal.

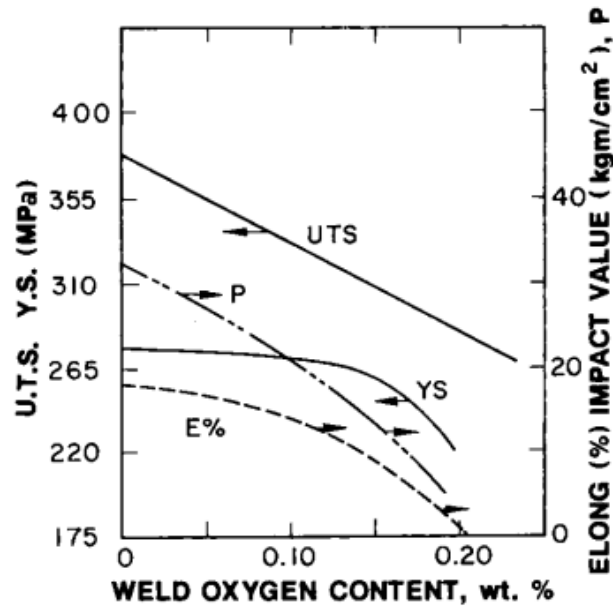


Figure 2-53 Effect of oxygen content on the mechanical properties of weld metal (Sindo Kou, 2003).

Under some situations however, the inclusions particles formed in the weld metal can provide favourable site for the nucleation of acicular ferrite, which helps to improve the toughness of the weld metal (Sindo Kou, 2003).

2.9.3 Improvement in weld metal impact toughness

Nickel is widely recognised as important in enhancing the strength and toughness of weld metal (Wang, Z. Q. et al., 2018), due to its contribution in the formation of acicular ferrite (Setiyanto, N. A. et al., 2019). The maximum toughness of weld metal with increased Ni content, has been shown to be related to the maximum volume fraction of acicular ferrite. This is a result of its fine grain size, with the individual laths separated by high angle grain boundaries (Yang, L. et al., 2015).

The improvement in mechanical strength of weld metal, has been attributed to the ability of nickel to form solid solution and increased hardenability in the material (Wang, Z. Q. et al., 2018). As a strong austenite grain stabilizer, Ni lowers the transformation temperature of ferrite, increasing the formation of pearlite (Wang, Z. Q. et al., 2018; Sun, Y. et al., 2012), and can also decrease the bainite start and bainite finish temperature in steel (Huang G. et al., 2018).

A study showed that a 1% increase in nickel content lowered the transformation temperature of ferrite by 15°C. It was reported that a certain increase in the amount of Ni can inhibit the evolution of coarse grain boundary ferrite (GBF), and promote acicular ferrite microstructure, leading to improved mechanical property of the weld metal (Wang, Z. Q. et al., 2018) which is achieved through grain refinement.

The yield strength of weld metal and grain size can be related according to Hall-Patch expression in equation (2-7), which shows that yield strength of the weld metal can be increased by formation of smaller grain sizes. (34)

$$\sigma_y = \sigma_o + k_y d^{-1/2} \quad (2-7)$$

where σ_o and k_y are constant for the deposited weld metal and d is the average grain diameter.

The improvement in weld metal toughness have been a focus of several investigations. A study of effects of small additions of Ni on the microstructure of weld metal, found that the deposited samples predominately contained bainite, and small fractions of AF and M-A constituents. Changes were observed in the size, density, and area fractions of M-A constituents as the nickel content was increased. The mean length and area percentage of M-A constituents decreased with increase in nickel content, leading to improvement in impact toughness property (Huang G. et al., 2018).

Pamnani, R. et al. (2016) studied the effect of addition of nickel and summarised that the nickel content of the weld metal was directly related to the sub-zero impact toughness of the welded joints. The toughness was influenced by the

chemical composition, proportion of acicular ferrite, inclusions, as well as the weld metal grain size (Pamnani, R. *et al.*, 2016).

Another report which investigated the effects of nickel on low-temperature impact strength and corrosion resistance of high-ductility ductile iron, alloyed with 0–1.8 wt% Ni was presented by Yufu *et al.* They showed that the weld metal low temperature impact toughness increased significantly with increase in the nickel content and reached a maximum value at 0.71wt% Ni. A further increase in wt% of nickel above this value, produced a decrease in impact toughness (Sun, Y. *et al.*, 2012).

A similar observation was reported by, Nova *et al.*, who found that impact toughness increased when Ni content was increased from 0wt % to 1wt%. But a further increase in Ni content to 1.5 wt%, resulted in a reduction in impact toughness, which was attributed to the evolution of hard phases and coarse grain structure (Setiyanto, N. A. *et al.*, 2019).

There is no consensus on the precise weld metal Ni content that can guarantee improvement in charpy impact toughness. Though increase in nickel can greatly increase weld metal toughness, nevertheless, it is contingent on the presence of other alloying elements (Setiyanto, N. A. *et al.*, 2019; Wang, Z. Q. *et al.*, 2018).

The combination of nickel with a high amount of Mn, can affect the mechanical property of the material in a complex way, leading to preferential formation of martensitic microstructure, which is prone to propagation of intragranular brittle crack (Setiyanto, N. A. *et al.*, 2019).

Wang *et al.* reported that the critical content of nickel was influenced by the content of Mn and a significant decrease in sub-zero temperature impact toughness could occur when nickel exceeded the critical content. They explained that increased formation of acicular ferrite could occur with increase in nickel content when the content of Mn was lower than 1.0wt%. But the weld metal toughness deteriorated when the Mn content was above 1.4wt% and Ni content above 2.25wt% (Wang, Z. Q. *et al.*, 2018). Hence quantifying the precise effect of nickel in weld metal is complicated.

This observation had earlier been reported by Kang et al., who found that at a low amount of Mn, increased addition of Ni produced increased hardness, as well as impact toughness. However, at a higher amount of Mn, increase in the Ni content led to decrease in impact toughness as shown in Figures 2-54. (Kang, B. Y. et al., 2000).

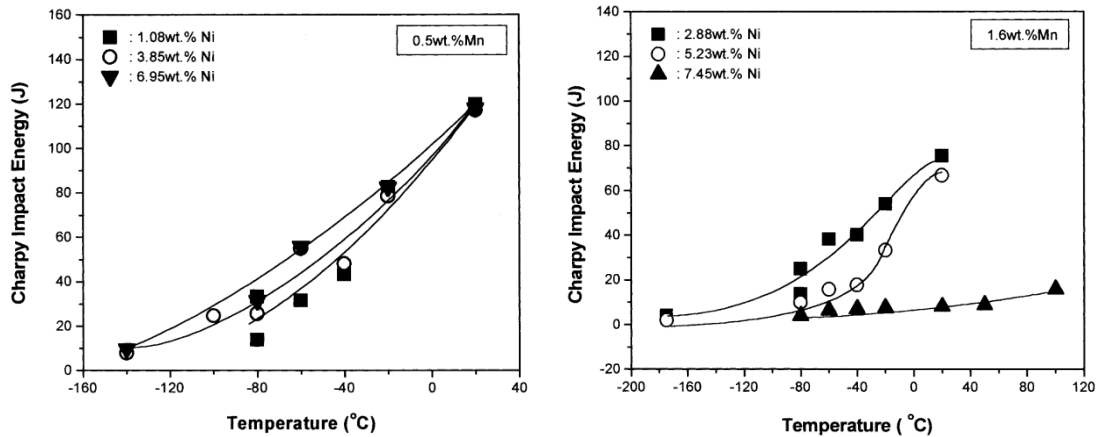


Figure 2-54 Effect of Ni content on Charpy impact toughness of as-deposited weld metals at two levels of Mn content, (a) 0.5wt% and (b) 1.6%wt%. Note that Ni is innocuous at low level of Mn but harmful at high level of Mn (Kang, B. Y. et al., 2000).

The reduction in impact toughness was due to evolution of predominantly martensitic microstructure, which lead to the propagation of intergranular brittle crack (Kang, B. Y. et al., 2000).

It is also a common knowledge that nickel content is limited to a maximum of 1wt%, for some applications in the oil and gas industry, because of its potential to produce lower resistance to crack propagation (Setiyanto, N. A. et al., 2019).

2.9.4 Development of weld metal property

Development of improved weld metal property, especially low temperature toughness has traditionally been achieved by two main techniques. One method involves using different flux compositions, while the second approach involves changing the composition of the weld metal by use of new filler metal or adding powdered metal to the molten weld metal (Bhole, S. D. et al., 2006).

Mechanical properties such as hardness and tensile strength can be influenced to a small extent through control of process parameters namely current, layer thickness, and travel speed etc. But a more significant control of property is possible by feeding two different wire compositions, into the same melt pool, by means of Tandem-GMAW process (Suryakumar S. and Somashekara M. A., 2013).

Therefore, the use of tandem-GMAW technique to combine two different wire compositions in the same weld pool, could present a new paradigm in the synthesis of new or improved low alloy WAAM wire compositions. The composition can be tailored to enhance the as-deposited Charpy impact toughness property, which is highly desirable in fabricating large WAAM components for marine oil and gas applications

2.9.5 Tandem-GMAW modification of weld metal property

The capability of WAAM to simultaneously deposit both material and geometry in-situ, presents a possibility to create tailored metallurgy, microstructure, and material properties. For example, specific material compositions can be created by alternating commercially available wire materials using single-wire GMAW process (Thompson, M. K. et al., 2016), or by feeding two different wire compositions simultaneously and mixing them in same weld pool, using Tandem-GMAW process (Somashekara, M. A. and Suryakumar, S., 2017).

Tandem-GMAW is a variant of conventional GMAW process which utilises two power sources to melt and deposit two electrically insulated wires in a single weld pool. The process has been recognised for its ability to achieve greater productivity compared to conventional single-wire GMAW process (Somashekara, M. A. and Suryakumar, S., 2017; Chen, D., et al., 2015; Groetelaars, P. J., 2009; Motta, M. F. et al., 2007; Wu, K. et al., 2019).

Tandem GMAW technique have been utilised by some authors to mix different commercially available wire compositions, to produce target microstructure with improvement in specific material property. The use of tandem-WAAM process to modify material composition has typically been focused on Functionally Graded

Material Objects (FGM) (Zhang, B. et al., 2018), in which the deposited material composition and microstructures are progressively varied within the entire built object (Suryakumar S. and Somashekara M. A., 2013). For example, Somashekara et al. demonstrated the potential to modify WAAM metal composition by utilising twin-wire GMAW process. They controlled the deposition wire feed speed of two dissimilar low alloy steel wires designated ER70S-6 and ER110S-G. The process produced a variation in composition within the deposit and resulted in a part having a blend of hardness properties. (Somashekara, M. A. and Suryakumar, S., 2017)

Gu et al. successfully utilised tandem-GMAW and WAAM technique to design new WAAM alloy compositions, in which they investigated the cracking susceptibility of WAAM manufactured Al-Cu-Mg alloys. Al-Cu and Al-Mg wires were mixed in the study, using the tandem-GMAW process. The work produced a suitable range of Cu and Mg composition which promoted isothermal ternary eutectic reaction. The final composition that was developed effectively reduced susceptibility of the material to solidification cracking during deposition (Gu, J. et al., 2018).

A recent study by Motta et al. investigated in-situ alloy composition development by utilising the tandem-GMAW process to deposit ferritic steel (AWS A5.18 ER80S-D2) and Austenitic stainless steel (AWS A5.9 ER 307) materials. This resulted in the creation of a novel martensitic alloy composition with high hardness and acceptable mechanical properties. The study further investigated the mixing of N06625 (AWS ER NiCrMo-3) and UNS N10276 (AWS ER NiCrMo-4) alloys, containing similar amounts of chromium and molybdenum elements respectively, as a reference alloy, designated UNS N06686 alloy. The reference alloy was superior in corrosion performance compared to the two baseline alloys but was more expensive (Motta, M.F. et al., 2020).

The result of the experiment revealed that the corrosion resistance of the intermediary alloy developed by insitu mixing was superior to that of the starting materials (N06625 and UNS N10276 alloys), and comparable to the performance of reference UNS N06686 alloy (Motta, M. F. et al., 2020).

The review therefore demonstrated the potential to create novel alloys for practical industrial application, using the tandem-GMAW process.

2.10 Comparative assessment of corrosion performance of WAAM and wrought alloys

Marine oil and gas environments such as sour gas, salt water and arctic represents some of the most challenging and harsh conditions WAAM manufactured components could be exposed to while in service (Iannuzzi, M. et al., 2017; Grover, H. S. et al., 2017).

2.10.1 Corrosion degradation of metallic materials

Corrosion of structures in marine environments has continued to remain a significant challenge, which greatly affects the integrity of the structures and shortens their service life. Marine sea water environments present an avenue by which low alloy steel materials are attacked by general corrosion, localised corrosion, and environmentally assisted cracking (EAC) (Iannuzzi, M. et al., 2017; Grover, H. S. et al., 2017). Corrosion in sea water environment can lead to pitting and stress corrosion cracking of metallic materials (Grover H. S. et al., 2017). The corrosion degradation of oil and gas structural components could culminate in costly equipment and human disaster. (Iannuzzi, M. et al., 2017)

General corrosion is the “uniform loss of material from all environment-wetted surfaces of a component”. The corrosion of the surface causes the component to reduce in thickness. This is a critical challenge, for pressure vessels or load bearing equipment, because their structural functionality diminishes as the thickness reduces (Gibson Applied Technology and Engineering, 2013).

The occurrence of H₂S in combination with CO₂ results in the formation of FeS film instead of FeCO₃. Formation of FeS product film can occur at low temperature because the precipitation of FeS occurs much more readily compared to FeCO₃. When the corrosion product film does not give adequate protection to the steel, localised corrosion at higher corrosion rates could occur and its most detrimental to oil and gas structures (Iannuzzi, M. et al., 2017).

Two theories are typically propounded for the occurrence of localized corrosion in H₂S containing environments. One is related to the presence of elemental sulphur, and the other is associated with the conductive iron sulphide scales that form in the corrosion product film, including pyrite and pyrrhotite. These mechanisms lead to propagation of galvanic corrosion attack (Esmaeely, S. N. et al., 2017).

Corrosion of marine components occurs in many ways. But corrosion from CO₂ (sweet corrosion), and H₂S corrosion (sour corrosion) are among the most common forms of material degradation that have affected numerous oilfield equipment made from carbon and low alloy steels (Kermani, B. et al., 2006). CO₂ have been generally attributed to these corrosions, but the presence of H₂S had further increased the aggressiveness of these geologic environments, increasing the frequency of aqueous corrosion of the materials. (Gao, S. *et al.*, 2017; Kermani, B. et al., 2006)

2.10.2 Sour corrosion

Sour corrosion is a type of aqueous corrosion caused by carbon dioxide (CO₂) in the presence of hydrogen sulphide (H₂S). H₂S is an acidic gas, just as CO₂ which is present everywhere, it turns water acidic and increase the corrosion of steel. Conversely, H₂S forms iron sulphide scale when it reacts with steel. The scale which forms on the surface of the metal can act as a protective barrier, preventing further corrosion of the metal material. The competitive interaction between corrosion process and scale formation influences the corrosion rate of the steel (Sun, W. and Nešić, S., 2009).

2.10.3 Types of corrosion degradation

CO₂ and H₂S are acidic gases which can form a corrosive solution with water and lead to a significant degradation of marine structures. The corrosive tendency of the two acidic gases is unique in nature and has attracted a lot of attention from the industry (Smith, S. N. and Ling, S., 2014). Corrosion degradation from the gases can occur either individually or in combination.

2.10.3.1 CO₂ corrosion

Typically, CO₂ occurs in hydrocarbon formation. It can cause severe corrosion attack when present with H₂S. Its corrosive tendency increases significantly when in contact with other aqueous medium, (such as sea water, NaCl), particularly when the corrosion attack is localised (Kermani, M.B. and Morshed A., 2003); ISO 15156-1, 2020). The corrosion is relatively simple and could produce only one type of iron carbonate corrosion product (Smith, S. N. and Ling, S., 2014).

FeCO₃ corrosion product can form from CO₂ corrosion and the corrosion scale could offer either a protective or non-protective film on the surface of the metal, depending on the prevailing environmental condition (Hunnik, E. V. et al., 1996)

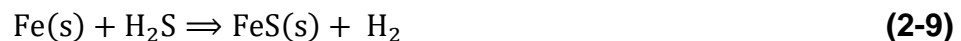
The corrosion by CO₂ occurs by electrochemical reaction and the complete reaction is given as shown in equation (2-8):



2.10.3.2 H₂S Corrosion

H₂S produces a weak acid when it dissolves in water. Its corrosive tendency is like that of CO₂. The corrosion occurs by localised corrosion or general corrosion, which is dependent on the characteristics and type of the precipitated corrosion products (Kermani, B. et al., 2006).

Corrosion by H₂S involves a direct heterogeneous chemical reaction, which leads to formation of a solid and adherent scale such as mackinawite on the steel surface. The complete reaction can be given by the expression in equation (2-9): (Sun, W. and Netic, S., 2007).



The ability of the film to provide protection depends on the type of scale formed, the kinetics of its formation, its stability, and its effect at decreasing corrosion (Kermani, B. et al., 2006). The rate at which the scale is formed and damaged determines the amount of scale retained on the surface of the steel (Smith, S. N. and Ling, S., 2014).

A turbulent flow could cause the breakdown of the FeS film and lead to significant corrosion like that which occur when FeCO₃ film breakdown during CO₂ corrosion (Kermani, M.B. and Morshed A., 2003).

2.10.3.3 Mixed CO₂/H₂S Corrosion

In mixed CO₂/H₂S corrosion, it is a common knowledge that iron sulphide film can precipitate on the surface of the steel, leading to a significant change in the corrosion rate (Smith, S. N. and Ling, S., 2014). Iron carbonate (FeCO₃) can also form alongside iron sulphide (FeS) scale, on steel surfaces exposed to CO₂/H₂S environments. The composition of the scale depends on the brine solution, the solubility of the individual iron carbonate and iron sulphide, and more so on the competitive interaction associated with the formation mechanism of both scales (Hunnik, E. V. et al., 1996; Gray L.G.S, et al., 1990; Nesic S. and Lee K.L.J., 2002).

Unlike the relatively less complex iron carbonate that are formed in pure CO₂ corrosion, several types of iron sulphides scale precipitates could be generated in a CO₂/H₂S environment. This could include amorphous ferrous sulphide, mackinawite, cubic ferrous sulphide, smythite, greigite, pyrrhotite, troilite, and pyrite. The first corrosion product to form on the surface of steel is Mackinawite, and the reaction occurs directly on the steel surface. (Smith, S. N. and Ling, S., 2014)

Mackinawite is thermodynamically the least stable form of FeS, and ultimately changes to more stable forms including pyrrhotite and pyrite. Poorly formed layer of mackinawite film can cause discontinuities leading to initiation of localized corrosion in the layer. This condition enables the entry of corrosive elements like hydrogen ion (H⁺) into the steel surface, by reduction reaction. Concurrently, Fe²⁺ readily vacates and diffuse out from the steel lattice. Hence the corrosion progresses unrestricted within the material (Esmaeely, S. N. and Nešić, S., 2019).

Pyrrhotite is among the most plentiful iron sulphides found within the earth crust and is also among the commonest corrosion products formed during aqueous corrosion of H₂S environment on steel. Non-uniform or disrupted FeS corrosion product layers, potentially leads to localised corrosion, which spreads through the

discontinuity by galvanic coupling between the conductive FeS corrosion product film and the underlying steel near to it (Esmaeely, S. N. and Nešić, S., 2019).

Iron carbide are also formed as by-product which remains after the corrosion of the steel. The films are non-protective, they are electrically conductive and very porous. The presence of the film can exacerbate the corrosion process (Wang H.B, et al., 2001).

Low concentration of H₂S can influence the corrosion tendency of CO₂ in several ways. It can either enhance CO₂ corrosion by supporting anodic dissolution through adsorption of sulphide and effect on the pH; or conversely, it can decrease sweet corrosion through the formation of protective sulphide film (Kermani, B. et al., 2006).

Therefore, in general, the presence of H₂S in CO₂ containing environment can lead to an-

- Increase in the corrosion tendency by-
 - o Promoting localised corrosion at a higher rate than the localised or general corrosion associated with CO₂. It could also precipitate less protective FeS corrosion product, in place of iron carbonate corrosion products
- Decrease in the corrosion tendency through the precipitation of FeS corrosion product layer by-
 - o Displacing less protective iron carbonate layers
 - o Precipitating both iron sulphide and iron carbonate protective films (Kermani, B. et al., 2006).

2.10.4 Factor influencing corrosion rate

Several environmental, physical, and metallurgical factors influence the corrosion rates of CO₂, H₂S and CO₂/H₂S gas. The factors are interrelated and act together. The corrosion rate can be significantly altered by a slight change in any one of the factors (Iannuzzi, M. et al., 2017; Kermani, M.B. and Morshed A., 2003). They include the following:

- Gas content

The presence of CO₂ can cause a decrease in the corrosion rate, when conditions are favourable for the formation of iron carbonate (FeCO₃) corrosion films, which provide a thick protective layer on the steel surface. A condition of high temperature and high pH promotes the formation of iron carbonate film and severe corrosion degradation can occur when the corrosion products do not form on the steel surface (Iannuzzi, M. et al., 2017).

Several experiments conducted to study the influence of H₂S gas concentration on the formation of mackinawite scale showed that increase in H₂S concentration increased the corrosion rate and the scale retention rate also increased with the increased H₂S gas concentration. But the corrosion rate is generally higher than the scale retention rate.

- Effect of temperature

Several studies evaluating low temperature corrosion, that is corrosion occurring at temperatures lower than 80°C have been conducted. (Tang, J. et al., 2010; Bonis, M., 2009) and substantial advancement have been achieved in clarifying the mechanisms by which the corrosion generally occurs. Initially, the corrosion rate of the steel increases as the temperature increases, and temperature greatly influences the formation of corrosion product when favourable conditions exist (Gao, S. et al., 2017). Porous and non-protective mackinawite scales are formed on the surface of the steel at temperature of 25°C. However, at 80°C, thick and protective layers of corrosion products are formed on the material, consisting of mackinawite and pyrrhotite scale. Both the corrosion rate of the material and the rate at which the corrosion products are formed can be accelerated by temperature (Gao, S. et al., 2017).

Corrosion behaviour of steel material in sour environment have also been studied at elevated temperature of between 80 and 200°C. It was found that initially, the corrosion rate increases with temperature, so does the rate of formation of corrosion products. But subsequently, the corrosion decreases as an equilibrium state is reached, due to the formation of passive layers of corrosion products on the surface of the materials. At every test temperature, Iron oxide scale typically

formed as the primary constitute of the corrosion product. The corrosion products consisted of two different layers, the first was an inner layer of iron oxide, (assumed to be Fe_3O_4), and an outer layer with the main constituents identified to be mackinawite, troilite, pyrrhotite and pyrite, forming at temperatures of 80°C , 120°C , 160°C and 200°C respectively. The pH value in all the tests was observed to rise from 4.00 and exceeded 5.40, hence presenting a suitable condition for increased formation of iron sulphide (Gao, S. *et al.*, 2017).

- Exposure duration

During $\text{CO}_2/\text{H}_2\text{S}$ corrosion, it was observed that the corrosion rate increased initially, but then it reduced drastically at longer test duration. This resulted from the protective iron sulphide films that formed on the surface of the steel over time (Smith, S. N. and Ling, S., 2014). A comparison of the effect of time was also made, using a 1-hour and 24-hour corrosion duration. It was evident that iron sulphide scale built up over time and provided increased protection on the material. This is however dependent on other prevailing factors. (Smith, S. N. and Ling, S., 2014)

- Effect of flow

The mackinawite FeS corrosion product can form a protective layer when the fluid flow does not dislodge it. However, in a condition of high or turbulent flow the FeS layer becomes less protective, when the layers are dislodged by the stream of flowing fluid (Kermani, B. *et al.*, 2006). This loss of the larger proportion of FeS scale to the solution is attributed to the hydrodynamic stresses induced on the scales by the flow. (Sun, W. and Netic, S., 2007)

A corrosion review by Bonis *et al.*, focussed on the effect of sour corrosion on material weight loss. It concluded that the primary factor determining whether a corrosion is termed as severe, intermediate, or negligible was the flow of the gas (i.e., whether it is low or stagnant flow (Bonis, M., 2009).

An evaluation of the effect of flow rate on corrosion rate was also conducted by Wei *et al.*, showed a clear increase in corrosion rate, which was more severe when

the material was exposed for a short period of time. When the duration was longer in the flowing conditions, significant reduction in the corrosion rates was observed. This was attributed to increased build-up of the protective iron sulphide scale (Sun, W. and Netic, S., 2007). Conversely, under certain circumstance, flow could significantly increase general corrosion and high flow rates could lead to severe localised corrosion (Smith, S. N. and Ling, S., 2014).

- Effect of pH

pH is a measure of the H⁺ concentration in the solutions, a major constituent which contribute to the cathodic reaction of CO₂ process. It has been shown from experimental as well as computational studies that corrosion rate changes considerably with pH. The solubility of iron carbonate decreases at higher pH, leading to increased precipitation of protective corrosion layer, and hence decreasing the corrosion rate. pH can increase the rate of corrosion at low H₂S partial pressure (Smith, S. N. and Ling, S., 2014).

- Effect of Chlorides

The presence of Chlorides can significantly increase corrosion rate, due to their ability to break down the FeS protective film and trigger sour localised/pitting corrosion (Sun, W. and Nešić, S., 2009). The increase in corrosion rate from chloride is also attributed to increased conductivity and galvanic interaction between chloride ions and the protective FeS layer (Kermani, B. et al., 2006; Esmaeely, S. N. and Nešić, S., 2019).

- Effect of microstructure

There is limited data on the actual effect of metal surfaces and steel microstructure on the corrosion behaviour of H₂S-CO₂ corrosion. A comparison of the relative sulphide stress corrosion (SSC) cracking resistance was made between UNS S17400 stainless steel, produced using powder bed fusion AM and welded wrought parts of the same alloy, in accordance with NACE TM0177 Method A.

The chemistry, microstructure, mechanical properties, and electrochemical performance of these materials were studied to explain the observed results and to determine the suitability of AM parts for sour service. The result of the SSC tests of AM specimens aligned along the build direction, failed within 24 hours with both the “High H₂S” and “Low H₂S” concentrations, in contrast to the wrought/welded specimens tested in the same chloride and H₂S concentrations.

Several multiple factors were given as contributory to the poor performance of the AM specimen in the sour environment, which included the presence of inclusions, precipitates, intra-layer defects, porosity, the material condition and heat treatment and specific AM microstructure. Discontinuities were also observed in the polished AM surfaces. Ultimately, it was suggested that the poor performance was probably because of inhomogeneities and scale/defects which resulted from the fabrication (Kovacs, W. *et al.*, 2017)

2.10.5 Corrosion of WAAM alloy

Low alloy steel represents some of the most reliable and versatile engineering materials widely used for oil and gas applications. Their excellent properties make them the material of choice. Despite their excellent performance, they can still be subjected to severe damage in H₂S containing environment, such as environmentally assisted cracking. (Iannuzzi, M. *et al.*, 2017)

2.25Cr 1Mo type alloy is a widely used low alloy steel in manufacturing oil and gas equipment, for example forged connectors, which are used to connect riser joints, Ortolani *et al.*, (2013). A critical issue with the materials for marine applications is the potential for its exposure to sour environment during production activities. In this environment, failure from hydrogen sulphide (H₂S) stress corrosion cracking can occur when a susceptible microstructure is present.

Suitable strength and hardness level of the material is crucial in mitigating its susceptibility to premature failure. Hence, the National Society of Corrosion Engineers (NACE) and the International Organization for Standardization (ISO) have set a standard which requires weld metal hardness not to exceed a

maximum of 22 HRC (or 250 HV) under certain environmental conditions (Elrefaey, A. et al., 2018).

Components manufactured using WAAM possess a different metallurgical characteristic, compared to those manufactured through machining of wrought materials (Bai, J. Y. et al., 2016). This is primary due to the repeated rapid heating and solidification and deposition thermal cycle generated during the WAAM process. This significantly influences the unique microstructure and phases formed in the WAAM material (Sander, G. et al., 2018; Sun, Y. et al., 2018).

In general, the corrosion performance of AM materials can be influenced by these unique microstructural constituents, which could typically include heterogenous structures consisting of hard martensitic phases, dendritic growth, large grain structures, solute segregation, and dislocation networks. Metallurgical defects such as porosity, hot cracking, gas porosity, lack of fusion defect, surface roughness, residual stress could also develop within the build (Sander, G. et al., 2018).

These metallurgical formations could potentially modify the electrochemical properties of alloys produced by WAAM technique (Sander, G. et al., 2018), and make it more susceptible to degradation in a sour service environment.

A review of some studies on the corrosion performance of materials deposited via Laser and Electron beam-based AM was presented by Sander, G. et al. (2018). Titanium and high alloyed steel were mostly the materials studied and an aqueous NaCl (sweet) environment was typically used. The conclusion from vast majority of the study found that, the corrosion performance of AM-prepared alloys was affected and was not similar in performance to the wrought counterparts. There were some beneficial outcomes of the AM processes, in some cases, including improved resistance to pitting in austenitic stainless steels, while Ti alloys manufactured through AM was in general affected minimally. However, there are several instances where detrimental effects, due to AM process were observed, with high inconsistency in findings, such as with the use of Al-Si alloys (Sander, G. et al., 2018).

A study of the corrosion performance of additive manufactured Ti-6Al-4V alloy part showed that the corrosion of the part in the as-deposited condition was significantly higher than that of the wrought alloy. The increased corrosion was attributed to the presence of non-equilibrium phases. However, after the part was suitably heat treated at 800°C for 2 h, the corrosion performance increased commensurately to that of the wrought alloy. The enhanced corrosion resistance was attributed to stress relieving of the martensitic phase and precipitation of BCC phase of β Ti-6Al-4V (Hemmasian, E. A. et al., 2019).

Extensive studies on the corrosion behaviour of wrought low alloy steel exposed to sour service oil and gas environments have been carried out by many authors, but very little or no work have been conducted on the corrosion behaviour of WAAM deposited low alloy steel materials. Therefore, it is necessary to ensure that WAAM materials developed for fabricated marine components possess sufficient resistance to corrosion damage when used in sour corrosion environments (Arai, Y. et al., 2012).

2.11 Summary of literatures and key gaps

The beneficial effect of utilising AM technology for heavy wall component manufacture, compared to the subtractive manufacturing technique, especially in the oil and gas industry have been well reviewed. Although the findings outline the potential manufacturing cost and production efficiency benefits of AM technology, but a few challenges relating to product throughput, quality and material properties still limit its wide scale utilisation, for the manufacture of large sized components. A WAAM process that can provide substantial increase in productivity, without adversely compromising the surface quality of the manufactured part, could change this position.

A review of parameters generation and tool path techniques have showed that the choice of a particular deposition process or strategy, is dependent on the size, shape, and surface quality desired for the component.

Tandem-wire process for example, can provide improved productivity, but the potential deterioration in surface quality is an issue. The use of two wires in close

proximity could add further complexity to the WAAM process, both in terms of optimum parameter settings, because the process parameter window of tandem-wire is smaller compared to SW-GMAW process (Goecke, S. et al., 2001). and from practical deposition perspective, because the manipulation of the two wires could present challenges when building WAAM part with complex geometries, consisting of rounded features, such as corners and intersections.

Several studies on tandem process have mainly focused on arc interruption, metal transfer phenomenal (Wu, K. et al., 2020; Ding, X. et al. (2013), and productivity improvement (Somasekara, M. A. and Suryakumar, S., 2017; Chen, D., et al., 2015; Groetelaars, P. J., 2009; Motta, M. F. et al., 2007; Wu, K. et al., 2019). The primary process parameter including WFS, and TS are typically studied, while limited work on secondary parameters such as wire configuration have been conducted. However, no literature investigating the simultaneous improvement in productivity and surface quality, using the tandem-wire skin and core technique was found. Additionally, investigations of effect of tandem GMAW secondary process parameters including variations in WFS of lead and trail wires and torch travel directions was not found in literature, to the best of the author's knowledge.

The study on 2.25Cr 1Mo steel composition used in welding fabrication application, found that the as-deposited material does not typically meet the engineering properties requirement, owing mainly to formation of heterogenous microstructure, consisting of hard martensitic structures.

Several literatures have reported on the residual stress generation (Dean Deng et al., 2013), microstructure and mechanical performance of welded and heat treated 2.25Cr 1Mo steel material (Hans-Olof Andren et al., 1995; B.E. Peddle & C.A. Pickles., 2001). However, to increase the utilisation of equivalent 2.25Cr-1Mo alloy composition for WAAM manufacture of oil and gas component, it is critical to understand the characteristic microstructural and mechanical performance of the WAAM alloy.

This work partly sets out to investigate two primary material processing factors important for the manufacturing of large 2.25Cr 1Mo WAAM steel components for marine applications, including-

- Thermal cycle generation, which is crucial to the microstructure development and hence the resulting mechanical performance of the component, and
- Secondly, the effect of heat treatment on the mechanical performance, especially the low temperature charpy impact toughness will be evaluated.

The study will determine whether WAAM deposited ER90S-G alloy can meet a typical Schlumberger company material design specification e.g., MS-011513, required for the manufacture of heavy-wall marine oil and gas components; as given in Table 2-5.

Table 2-5 Schlumberger material specification (MS-011513) for forgings

Material specification – ASTM A182 F22 (e.g., MS-011513)		
Properties	Transverse direction	Longitudinal direction
0.2%YS (MPa/ksi) min	517/75	517/75
UTS (MPa/ksi) min	655/95	655/95
Elongation (%) min	18	18
Charpy (J) min/avg. @ -29°C	32/42	32/42
Charpy (J) min/avg. @ -29°C	32/42	32/42
Hardness (Rockwell C) Max	16 – 22	16 – 22
Hardness (Vickers) Max	201 – 250	201 – 250
Fracture toughness (-29/-46) °C	200 – 400 MPam ^{1/2}	+2.0 mm CTOD

The available 2.25Cr 1Mo deposition wire variants are not optimised for WAAM process. Its relatively high cooling rate, coupled with the numerous localised depositions of weld metal layers during manufacture, leads to significantly higher multiple thermal cycles generation, compared to traditional welding fabrication. Consequently, this led to poor mechanical properties, especially charpy impact toughness in the reheated zones of 2.25Cr 1Mo weldment through, formation of hard heterogonous microstructures

Post-processing heat treatment is typically used to improve the as-deposited properties of the 2.25Cr 1Mo weldments, but this potentially leads to higher manufacturing lead time, costs, and process complexity. The review also

demonstrated the potential to create novel alloys with improved properties, for practical industrial application, by mixing different wire compositions, using the tandem-GMAW process (Gu, J. et al., 2018; Motta, M.F. et al., 2020). However, such studies utilising wire mixing technique to improve the as-deposited properties of 2.25Cr 1Mo weldments, by mixing ER90S-G and ER120S-G wire compositions, was not found in literatures. Hence, the optimum alloy composition resulting from mixing both wires have not been reported.

Extensive studies on the corrosion behaviour of wrought low alloy steel exposed to sour service oil and gas environments have been carried out by many authors, but very little or no work have been conducted on the sour service corrosion behaviour of WAAM deposited low alloy steel. Some literatures have indicated that WAAM alloys could lack in corrosion performance compared to the wrought variants. Therefore, it is necessary to ensure that WAAM materials intended for fabricating marine components possess sufficient resistance to corrosion damage when used in sour gas environment.

The relative sour service corrosion behaviour of different low alloy steel materials deposited by WAAM technique, will be investigated using the weight loss/gain method. The corrosion performance of the alloys will also be compared with that of an equivalent but wrought ASTM A182 F22 alloy exposed to the same environment.

Finally, the reviews have shown the potential of WAAM to become a significant technology disruptor, capable of shortening production lead time from months to weeks and improving manufacturing efficiencies, but its limitations need to be adequately addressed before the full impact of the technology could be realised.

2.12 Research aims and objectives

This study has aimed to investigate and understand different key aspects of WAAM, for fabrication of large marine structures. The specific objectives of the study are as follows:

1. Investigate the effects of Tandem-GMAW process parameters and conditions on electrical transient and geometrical characteristics of single beads and multi-layer wall deposits.
2. Evaluate a novel build strategy and optimisation parameters for high productivity and surface quality deposition of relatively large WAAM structures.
3. Deposit and evaluate the influence of thermal-cycle and post deposition heat treatment (PDHT) on the performance of a large WAAM structure, deposited using single-wire GMAW process and ER90S-G filler wire.
4. Perform controlled tandem-GMAW mixing of selected filler wires available off the shelf, to tailor the composition to improve mechanical properties. Evaluate the effect on the properties of the resulting WAAM compositions.
5. Evaluate the corrosion performance of different WAAM weldments produced under different processing conditions and compare with the wrought variant used in existing oil and gas components.

3 Experimental study of high deposition and surface quality for WAAM parts

This study presents the investigation conducted on various aspects of Tandem-WAAM process parameters and conditions, with a focus on maximising the productivity and as-deposited dimensional tolerance and surface quality. It is expected that the outcome will provide additional technical knowledge, relating to the use of Tandem-WAAM processes, as well as aid in boosting manufacturing cost efficiency, through reduction in production lead time, enhanced material utilisation and increased sustainability.

In approaching this study, experiments will be conducted to investigate important primary and secondary deposition process parameters in four stages.

1. The first stage will investigate the influence of the Tandem-GMAW primary parameters of:
 - i. WFS
 - ii. TS
 - iii. Contact tip to work distance (CTWD)
 - iv. Interpass temperature,

on the transient arc characteristics, bead geometry and surface quality. This experiment will utilise higher parameters settings, to maximise deposition rates.

2. The second stage will investigate the effect of Tandem-GMAW primary and secondary parameters including:
 - i. Variations in WFS of lead and trail wires
 - ii. Wire configurations, and
 - iii. Torch travel direction,

on bead geometry and surface quality.

3. The third study will investigate the effect of multi-layer primary and secondary process parameters, including-
 - i. WFS
 - ii. TS

iii. Tandem-GMAW wire configurations

on the multi-layer wall responses including -

- Effective wall width (EWW)
- Average Layer height (aLH)
- Metal deposition efficiency (MDE) and
- Average surface waviness (SWav)

Single-wire GMAW and Tandem-wire GMAW processes will be utilised in this stage of the study, Also, this stage of the experiment will utilise lower parameters settings, to maximise the surface and dimensional quality of the WAAM part.

4. In the fourth investigation, the study will apply the knowledge gained from the previous stages, in a WAAM case study, to build a component, utilising the skin and core deposition strategy,

A series of process parameter studies for single-pass bead and multi-layer wall deposits conducted and described in this chapter, which formed the basis for skin and core process study studies.

To effectively maximise the deposition rates (productivity) of the Tandem-GMAW process, it is essential to evaluate the influence of both primary and secondary parameters, on the process stability, deposited bead geometry and quality. This is essential as they affect the integrity and manufacturing costs of the final part.

In the initial study, a sequenced methodical approach was used to evaluate the effect of tandem-GMAW primary parameters and secondary process conditions, on the arc characteristics and measured bead responses.

3.1 Materials and equipment

This section reports on the substrate material and typical dimensions, the deposition wire, as well as the equipment used in this study.

3.1.1 Material

The experiments were conducted using rolled S355 (or C-Mn) structural steel substrate of different dimensions, per EN 10025 – Hot rolled products of structural steels and degreased with acetone prior to deposition. The deposition wire used was low alloy steel designated, ER120S-G of diameter 1.2 mm per AWS A5.28. The nominal chemical compositions of the wire and substrate in wt%, are given in Table 3-1.

Table 3-1 Material compositions of (a) Steel substrate (b) Deposition wire

(a) Substrate (S355)												
C	Si	Mn	P	S	Cu	Cr	Ni	Mo	Ti	V	Al	Zr
0.20	0.55	1.60	0.025	0.025	0.55	-	0.05	-	-	-	-	-

(b) Deposition Wire (ER120S-G)												
C	Si	Mn	P	S	Cu	Cr	Ni	Mo	Ti	V	Al	Zr
0.09	0.72	1.87	0.011	0.01	0.07	0.32	1.82	0.51	<0.01	0.01	0.01	0.01

Unless otherwise stated, the dimensions of the substrate used in this study was 300 x 250 x 12.5 mm. The shielding gas used was argon-spec shield, comprising 92%Ar + 8%CO₂ mixture and supplied at a flow rate of 30l/min.

ER120S-G wire was selected in this investigation because it is proposed for the wire modification experiment study. It is comparable in strength to ER90S-G.

3.1.2 Equipment

The Tandem-GMAW system used comprised two Fronius TransSynergic 4000, Time Twin Digital MIG/MAG power sources, with a direct current polarity and equipped with two Fronius A-4600 Wels push-pull wire feeders. Power source (A) is the Leading Arc, which also controls the power characteristics of the Trailing arc, via power source (B).

Figure 3-1 shows a schematic illustration of the tandem torch set-up. The leading current is generated by the master power source, in wire A; while the trailing current is supplied by the slave power source, to wire B.

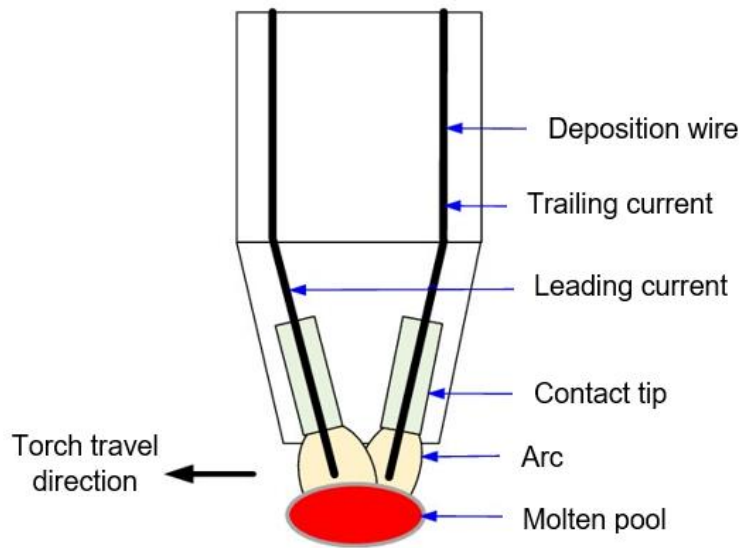


Figure 3-1 Illustration of Tandem-GMAW torch set-up

The torch manipulation was performed with a 6-axis ABB robot, which was electrically linked to the power sources. Figure 3-2 shows the equipment set-up. Temperature was measured during deposition using a K-type contact thermometer.

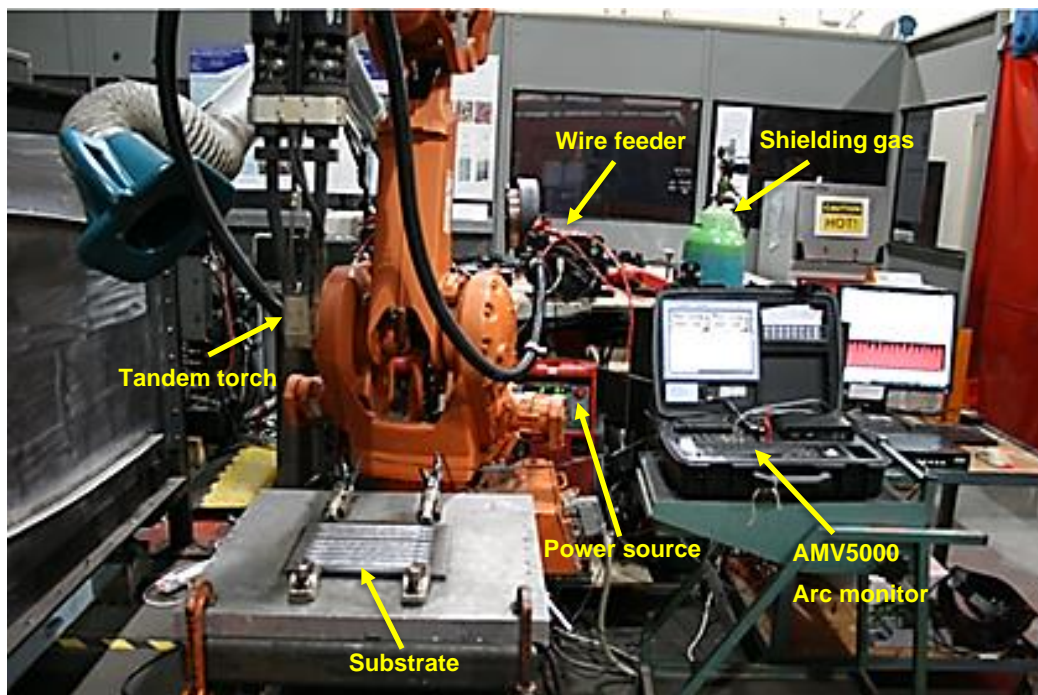


Figure 3-2 Equipment setup

The instantaneous arc current and voltage characteristics were acquired and recorded using an AMV5000 weld data logger, at a sampling rate of 25 kHz. Figure 3-2 shows the AMV5000 data acquisition system that was used.

The heat input per unit length of weld is given by the expression in equation (3-1).

$$H.I = \eta \frac{I \times V}{TS \times 1000} (KJ/mm) \quad (3-1)$$

Where:

I is the average arc current (A); V is the average arc voltage (volts), TS is the deposition travel speed (mm/s). The arc efficiency, η was taken as 1, throughout this study (Om, H. and Pandey, S., 2013; Gu, J. et al., 2018).

The total heat input per unit length of weld generated by lead wire A and trail wire B, is given by equation (3-2).

$$H.I_{total} = H.I_{wire(A)} + H.I_{wire(B)} \quad (3-2)$$

The instantaneous arc power (AIP) can be calculated using the expression in equation (3-3).

$$AIP = \frac{I \times V}{1000} (kW) \quad (3-3)$$

Where:

The total instantaneous arc power generated by wire A and wire B, is given by equation (3-4).

$$AIP_{total} = AIP_{wire(A)} + AIP_{wire(B)} \quad (3-4)$$

3.2 Metallographic preparation

Cross-sections of single pass and multi-layer specimens for geometrical analysis were extracted from the mid-section of the deposit and prepared by standard metallographic method. The specimens were cold mounted and ground using 240, 320, 1200, 2500 grits SiC papers, and then polished to a 9µm finish. This was followed by etching with 2% Nital solution to reveal the macroscopic details. Macrograph images of the etched specimens were obtained by optical microscopy, as well as with a digital camera for the various analysis. Geometrical measurements of the deposited specimens were performed using Axio vision image analysis software.

3.3 Measurement of weld bead characteristics

A desirable condition in high productivity WAAM deposition is the achievement of suitable single bead dimensions and consequently multi-layer profiles, which will reduce manufacturing lead time, while providing acceptable material properties, as well as providing high surface and geometrical quality. Geometrical features are central in evaluating the deposited bead quality and are generally dependent on the input parameters. Therefore, a critical evaluation of the characteristics of the weld bead geometrical features, with respect to the processing parameters is vital to developing fit for purpose WAAM structures.

Preparation of single-bead and multi-pass deposits were conducted prior to measurement and analysis of the cross-sections, as described in section 3.2.

3.3.1 Measurement of weld bead profile

The single bead geometries measured included bead width (BW), bead height (BH), bead penetration (BP) and bead contact angle (BA), as illustrated in Figure 3-3. The BA measurements were performed on both sides of the bead profile, and the average value was used for analysis.

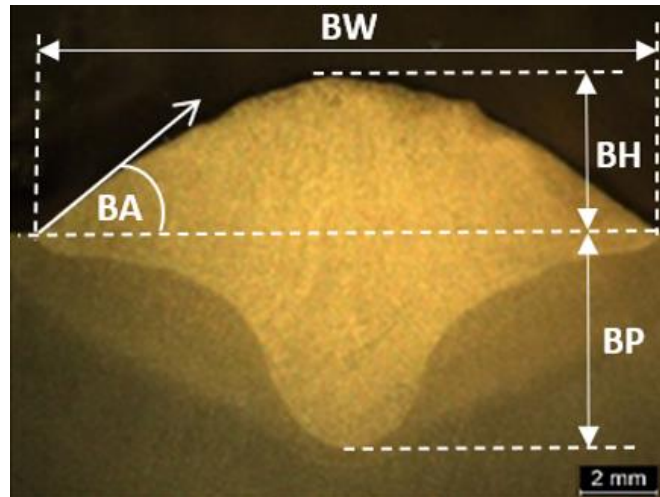


Figure 3-3 Transverse cross-sectional macrograph of single bead deposit, illustrating the measured bead outputs

3.3.2 Measurement of multi-layer wall profile

Measurement and analysis of the multi-layer wall cross sections were made on a ten (10) layer high wall deposit. The output parameters used to study the geometry and surface quality of the WAAM wall structures, deposited using Tandem-wire and single-wire GMAW processes include - Wall height (WH), which refers to the maximum built height, Average Layer Height (aLH), which is the average of the height of all the individual beads deposited to achieve the maximum wall height, Effective wall width (EWW), which relates to the maximum constant wall width realised, after the walls have been machined to net shape, Metal deposition Efficiency (MDE) represented by equation (3-5), which is a measure of the material utilisation factor. It indicates the quantity of excess materials machined away to achieve the required net geometry and dimensions of the part. The transverse macrograph section in Figure 3-4 illustrates the measured multi-layer wall responses.

$$MDE = \frac{Area\ A}{Area(A + 2B + C)} \% \quad (3-5)$$

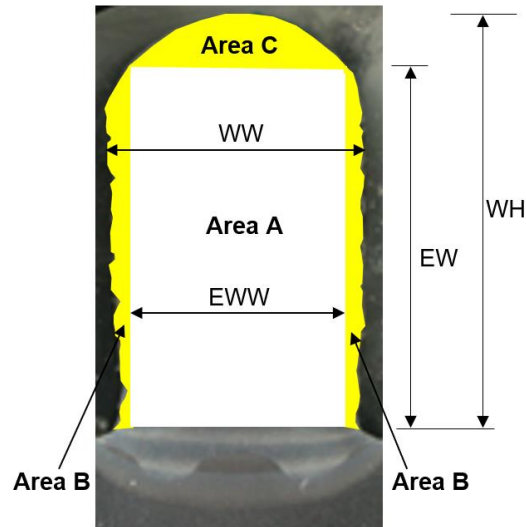


Figure 3-4 Definition of WH, EWH, WW, EWW, MDE and SW

Surface waviness (SW_{av}) gives an average measure of the surface quality of the as-built multi-layer parts. It is defined as the average maximum peak-to-valley distances measured from a profile from a specific area on the built wall.

The dimensional stability or built consistency of the wall was characterised in terms of the standard deviation from the average layer height, which is an indication of the level of variations between the Layer heights (LH) of each deposited bead. This has implications for the stability of the deposition process, due to effect of CTWD.

3.3.3 Surface waviness measurement

Compared with roughness, waviness relates to the more widely spaced variations of the surface texture and is a key parameter in assessing the quality of the final product. Though the same measurement precision depth is required, it is usually conducted along a longer profile of between 4 to 12.5 mm (Frade, M. et al., 2013).

Contact and non-contact techniques are the two main methods for relating material surfaces to the physical effect applied in their measurement. The contact measurement method was employed in this study and involved dragging a stylus tip across the lateral wall surface.

One of the typical waviness parameters utilised is the arithmetic average surface waviness (SWav), which refers to the deviation of waviness from the mean line. (Al-Quzweny, M. B. et al., 2016).

The arithmetical average surface waviness of the vertical wall surfaces can be calculated using equation (3-6); where $f(x)$ is the surface profile and l denotes the evaluated length (Lalehpour, A. and Barari, A., 2018).

$$SWav = \frac{1}{l} \int_0^l |f(x)| dx \quad (3-6)$$

The surface waviness (SWav), of the deposited wall samples were measured using a Taylor Hobson 'Form Talysurf - L120' profilometer, equipped with a Ruby ball stylus of 500 microns radius. The profile readings were captured and recorded using the in-built Taylor Hobson Ultra 6.1.5.33 software. Figure 3-5 shows a setup of the Talysurf profiler during surface waviness measurement.

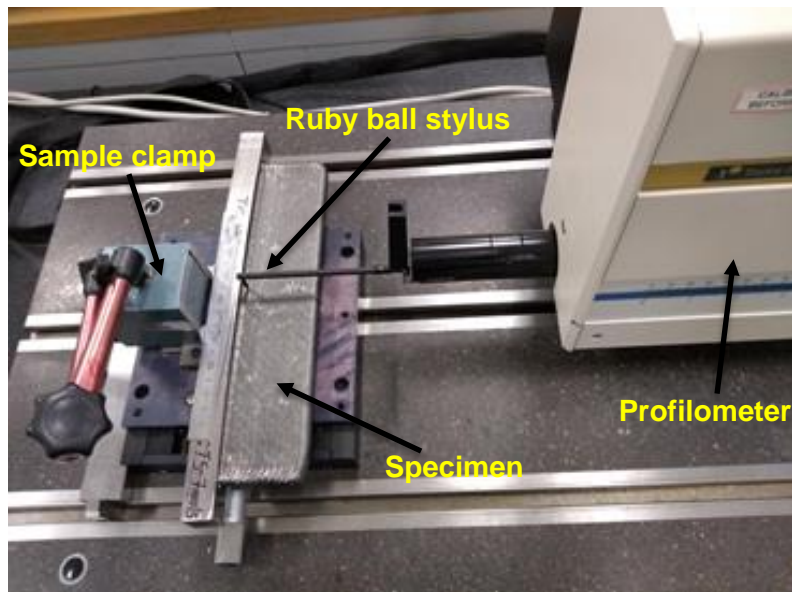


Figure 3-5 Surface waviness performed using a Talysurf surface profiler

The surface profile measurements were taken at five locations on the samples, spaced 5mm apart. The length measured for the analysis was 11 mm and a measurement speed of 0.5 mm/s was used. All the measurements were

conducted in the surface laboratory room at Cranfield University, at room temperature.

3.4 High deposition rate process study

The primary rationale in this stage of the investigation was to maximise the deposition rates of Tandem-wire GMAW process, while achieving a stable deposition process and acceptable bead quality, suitable for building large WAAM structures. The practical range of WFS setting achievable from the Tandem-GMAW wire feeder utilised in this study, varied between 2.5 and 18m/min, when operated in pulsed current mode. To maximise deposition rates, the middle to high WFS parameter settings were considered.

3.4.1 Characterisation of Tandem-GMAW single bead deposition parameters

The independent process parameters which mostly influence arc stability, bead profile, formation surface quality and deposition rates in GMAW process are identified as WFS, TS and CTWD. Preheat temperature was considered as a secondary process parameter, important in terms of fusion characteristics and bead quality. Furthermore, the effect of Tandem-wire GMAW process conditions on deposited beads responses were investigated. The experimental methods are described in the following sub-headings.

3.4.1.1 Effect of Tandem-GMAW process parameters on electrical transient, deposited bead geometry and surface quality

Preliminary experimentation was conducted to select suitable high WFS and travel speed settings, using one-factor-at-a-time (OFAT) technique. Thereafter, Response Surface methodology (RSM), by Box-Behnken parametric approach, was used to systematically plan and conduct the high deposition rate experiment. The main effect plots were utilised to evaluate the effects of deposition process parameters on the measured single bead responses. Minitab-17 statistical software was used to organise the experiment and plot the results.

27 beads on plate specimen were deposited for this study, which was repeated making a total of 54 beads on plate trials. The tandem-wire experimental design

matrix, used for the high deposition rate parameter study, including the measured instantaneous arc characteristics and single bead responses, are presented in Appendix B.

The maximum WFS of the Fronius power source, in pulsed current condition is limited to 18m/mis. Preliminary deposition trials showed significant fume generation and unstable metal deposition occurring from WFS of 15m/mis. To minimise these effects, a maximum WFS of 14m/mis was utilised on each wire.

The deposition parameters and range selected for the experiment are presented in Table 3-2. The minimum and maximum input values of the parameters were coded as shown. The torch was travelled in the leading direction during this experiment.

Table 3-2 Process parameters and range used for high deposition study

Parameters	Range			
	Lower value		Higher value	
	Actual	Coded	Actual	Coded
Travel speed (TS), mm/s	13	-1	27	+1
Interpass temp (T). °C	20	-1	250	+1
Wire feed speed (WFS), m/mis	14	-1	28	+1
Contact tip to work distance (CTWD), mm	20	-1	24	+1

Note that the WFS quoted in this stage of the study is equal to the sum of both lead wire (A) and trail wire (B). i.e.

$$WFS = WFS(\text{Wire A}) + WFS(\text{Wire B}) \quad (3-7)$$

3.4.1.2 Effect of Tandem-GMAW process conditions on electrical arc characteristics, deposited bead geometry and surface quality

The second stage in the single-bead characterisation study was carried out with the focus to improve the surface quality of the deposited bead. The effect of WFS and TS, in combination with Tandem-GMAW process conditions, on arc stability, bead geometry and surface quality was investigated. The process conditions studied included-

- Variations in WFS of lead wire (A) and trail wire (B),

- Effect of torch travel directions and
- Effect of wire configurations.

3.5 Results and discussion on high deposition rate study

The results of the experiments detailed in section 3.12 are presented here. The experiment which investigated the effect of Tandem-GMAW process parameters namely- WFS, TS, CTWD and Preheat temperature, are presented first. This is followed by presentation of results on the effects of Tandem-wire secondary process conditions.

3.5.1 Results of effect of Tandem-GMAW primary process parameters electrical transient, bead geometry and quality

This section presents graphical plots of the measured mean arc current, voltage and heat input characteristics, as well as the measured bead geometries, obtained from the experimental study described in section 3.4.1. The experimental design plan used in this study and results are presented in Appendix B.

3.5.1.1 Result of effects of WFS and CTWD on transient arc characteristics

Pulsed current arc mode was applied to both wires. The effect of WFS and CTWD, on the average current ($I_{Wire(A)}$ and $I_{Wire(B)}$), voltage ($V_{Wire(A)}$ and $V_{Wire(B)}$) and heat input ($H.I_{Wire(A)}$ and $H.I_{Wire(B)}$), generated in lead wire (A) and trail wire (B) respectively, are presented in Figure 3-6.

It can be seen in Figure 3-6(a) and 3-6(b), that both $I_{Wire(A)}$ and $I_{Wire(B)}$ are strongly linearly correlated with the applied WFS. Initially, $I_{Wire(A)}$ and $I_{Wire(B)}$ increased rapidly by 51% and 50.9%, to 263A and 258A respectively, as WFS was increased from 14m/mins to 21m/mins. Thereafter, $I_{Wire(A)}$ and $I_{Wire(B)}$ increased rather slowly by 22.8% and 21.7%, to 323A and 314A respectively, with further increase in WFS from 21m/mins to 28m/mins

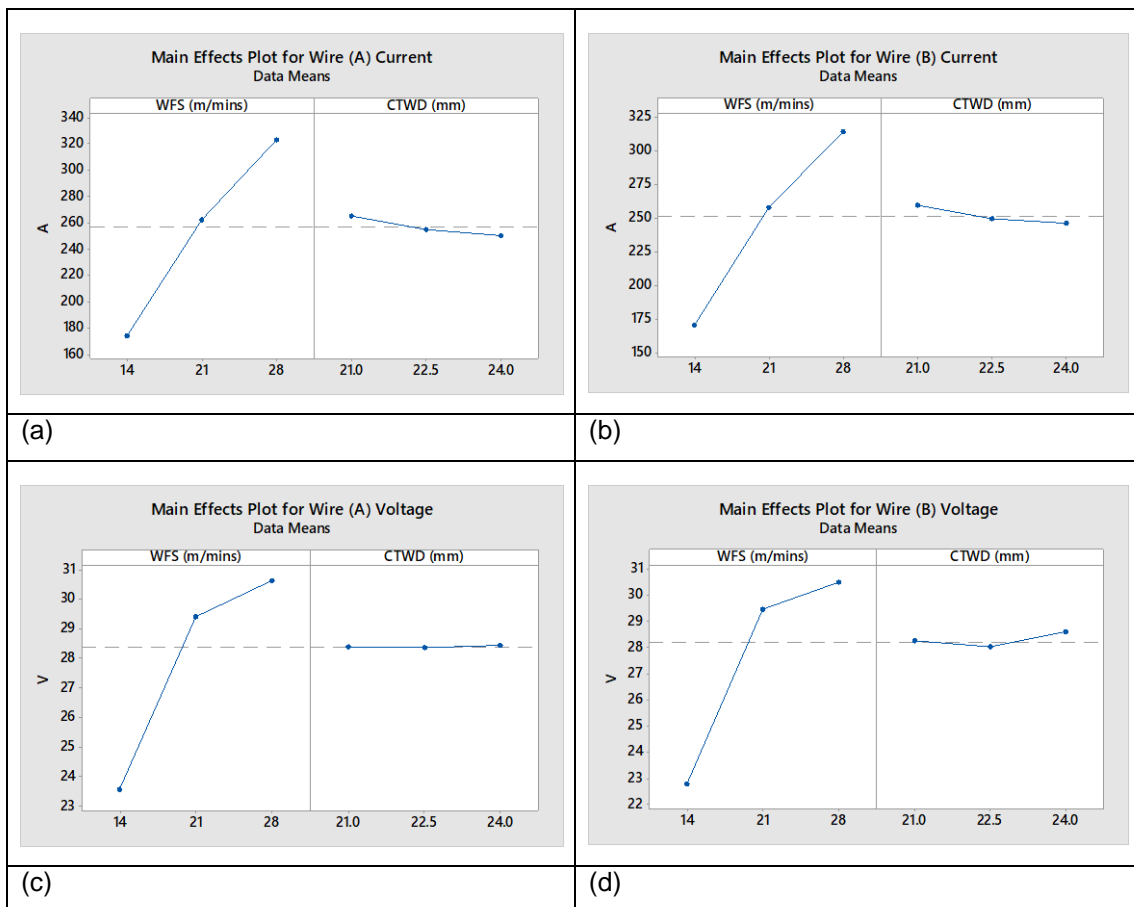
The voltage followed a similar trend as current. In Figure 3-6(c) and 3-6(d), $V_{Wire(A)}$ and $V_{Wire(B)}$, increased rapidly by 24.6% and 29.4%, to 29.4V and 29.5V

respectively, as WFS increased from 14 to 21 m/mins. Thereafter, $V_{\text{Wire (A)}}$ and $V_{\text{Wire(B)}}$ increased marginally by 4.1% and 3.1%, to 30.6V and 30.4V respectively, as WFS was further increased from 14m/mins to 28m/mins.

The marginal increase may be due to the fact that by increasing the WFS, mean current increased and caused the arc column to be more concentrated (constricted) in the centre of the weld pool, hence produced a reduction in arc voltage increase.

Figure 3-6(e) showed that heat input of wire (A), $H.I_{\text{Wire (A)}}$ increased by 138%, as WFS increased from 14m/mins to 28m/min. While Figure 3-6(f) showed that the heat input generated by Wire (B), $H.I_{\text{Wire (B)}}$ increased by 149% at a similar WFS setting.

The heat input generated in the lower to medium WFS range, was observed to be higher compared to the medium to higher WFS setting.



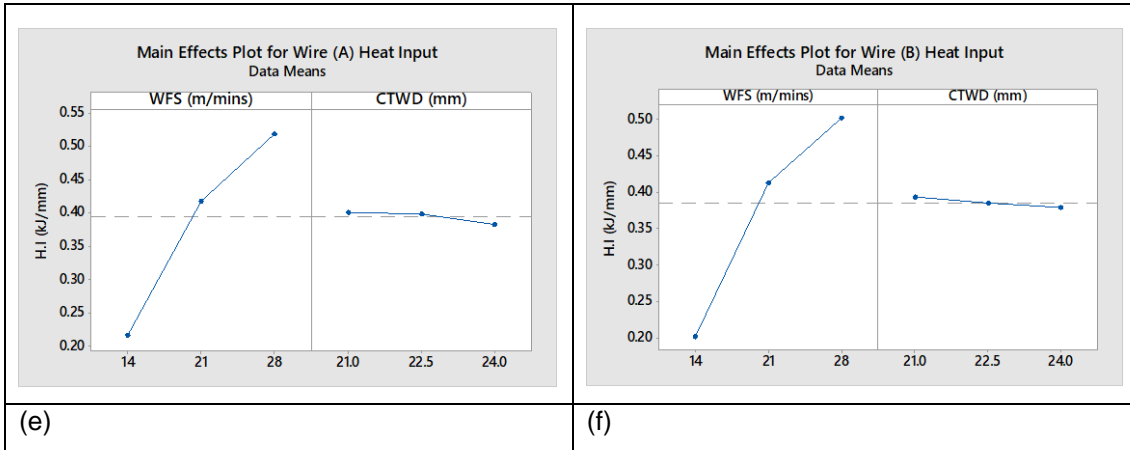


Figure 3-6 Effect of WFS and CTWD on average voltage (V), current (I) and instantaneous power (kJ mm⁻¹) outputs: (a) I_{wire (A)} (b) I_{wire (B)} (c) V_{wire (A)} (d) V_{wire (B)} (e) H.I_{wire (A)} (f) H.I_{wire (B)}

Increase in CTWD produced a rather marginal effect on electrical transient arc characteristics.

Figure 3-6(e) and 3-6(f) showed that H.I_{wire (A)} decreased by 4.5%, when CTWD was increased from 21mm to 24mm, while Figure 3-6(f) showed that H.I_{wire (B)} decreased by 3.6% at similar CTWD setting. This could be attributed to the minimal resistive heating effect on the wires, as they increased in length, producing a marginal decrease in heat input reaching the substrate.

The effect of CTWD could be associated to the empirical relationship between arc current, wire burn-off rate and wire stick-out (Allum, 1983; Smati, Z., 1986; Praveen et al., 2005).

The generally accepted mathematical description of the wire burn-off rate (BR) for continuous electropositive direct current (EPDC) GMAW was established by Lesnewich (1958) with respect to spray metal transfer mode, for a particular type of wire and diameter, as given in equation (3-8):

$$BR (m \min^{-1}) = \alpha I_{AVG} + \beta I_{AVG}^2 \quad (3-8)$$

where α , is a constant which accounts for the localised heating of the arc, at the tip of the wire, β is a factor which describes the distribution of resistance heating

along the length of the wire, I_{AVG} is the average current, and l is the electrical stick-out.

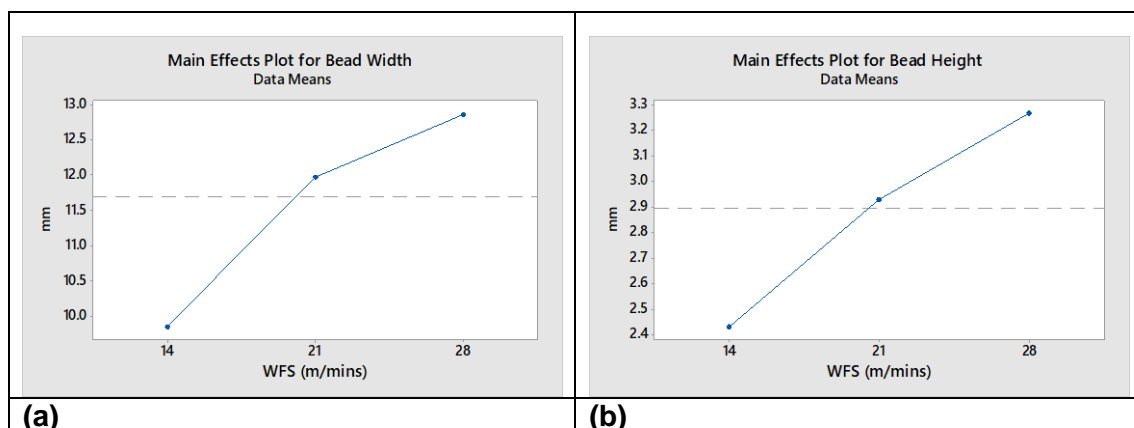
The first term of the equation defines the contribution of the arc energy owing to the voltage drop close to the wire tip, while the term on the right-hand side defines the contribution to the melting rate due to the wire extension heating (ohmic resistance heating effect). To achieve suitable metal transfer characteristics during pulsed direct current (DC) welding, the WFS must be balanced with the wire burn-off rate to maintain a constant arc-length (Almeida, P. M. S., 2012).

The marginal effect of CTWD on transient arc characteristics, observed in Figure 3-6, could therefore be due to a marginal effect of the resistance heating terms of equation (3-8).

The result showed that WFS can be significantly correlated with the arc current, voltage and heat input. The lead wire (A) generated a higher heat input compared to the trail wire (B), with $H.I_{Wire (A)}$, 3% to 8% greater compared to $H.I_{Wire (B)}$. This observation was also reported by Fang. fu *et al.*, 2012, who explained that the lead wire generates a higher heat input and enhances the penetration, while the trail wire produces a lower heat input and controls the bead shape and quality.

3.5.1.2 Results of effect of WFS on bead geometry

The effect of WFS on BW, BH, BP and BA are plotted in Figure 3-7



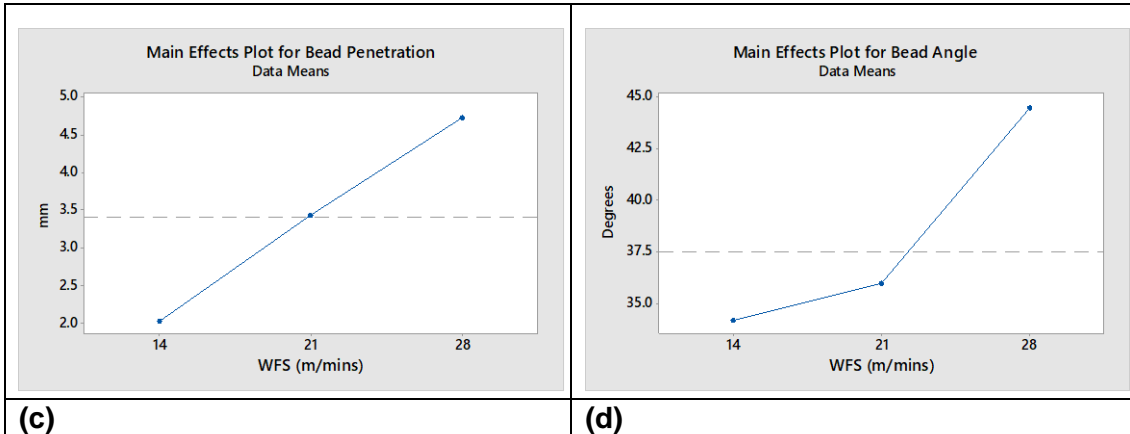


Figure 3-7 Effect of WFS on (a) BW (b) BH (c) BP and (d) BA

Figure 3-7(a) shows that BW initially increased strongly by 21.5%, to 11.97mm, as WFS increased from 14m/mins to 21m/mins. Thereafter, BW increased by 7.8%, to a maximum of 12.9mm, with further increase in WFS to 28mm.

In Figure 3-7(b), BH increased strongly by 20.6%, to 2.93 mm, with increase in WFS from 14m/mins to 21m/mins. Further increase in WFS to 28m/mins, produced 12.6% increase in BH, reaching a maximum of 3.30mm.

The BP is observed to increase steadily, with increase in WFS as shown in Fig 3-7(c). However, the increase was stronger between the low and medium WFS range of 14 and 21m/mins, increasing by 69% to the mid BP value of 3.43 mm. Further increase in WFS to 28m/mins, produced 37.6% increase in PD, to a maximum of 4.72 mm, between the medium and high WFS settings.

Figure 3-7(d) shows that BA was slightly affected by WFS between the low and medium WFS range of 14m/mins and 21m/mins, increasing marginally by 5.2% to 36°. But a further, increase in WFS from the medium to higher value of 28m/mins, produced a stronger effect of BA, increasing by 23.5% to 44.5°.

The characteristics effect of WFS is because as WFS increased, the mean current, heat input and WFS/TS ratio increased accordingly, resulting in weld beads that are larger in area per unit length, thus leading to a weld bead that is wider, taller, and deeper; making the contact angle to also increase.

The significant increase in BP observed, with increase in the mean current, could be attributed to effect of both higher heat input and momentum of impact of metal droplets on the weld pool Shoeb, M. (2013).

The measured BP was observed to be higher than the BH, for all combination of parameters and levels. The BH influences the strength of the weld and the number of stop/starts and hence, the number of layer or passes required to completely build a part. Its convexity could directly affect the strength of the deposited weldment. Shoeb, M. (2013). The relatively lower BH obtained, compared to BP, could be because the weld pool size was affected by cooling rate, which decreased with increasing welding current. Shoeb, M. (2013)

The trailing wire reheats the existing weld pool, which could enlarge the weld pool size, increase the temperature and the solidification time. This could give enough time for gravity to influence the weld bead shape, consequently producing a reduction in BH.

Excessive BP is generally undesirable for WAAM application, because of the tendency to increase remelting of previous deposits, which could be detrimental to surface quality of the beads. Hence, increasing the trailing wire WFS, relative to the leading wire WFS, may be advantageous in achieving optimum BP and quality, owing to the relatively lower heat input generated by the trailing wire, compared to the lead wire.

Another notable observation is that the effect of WFS on the transient electrical characteristics and measured bead geometry, was more significant at the low to mid WFS setting, compared to the mid to upper WFS setting. This could be attributed to interplay of electromagnetic attraction acting between the two arcs, which probably became more significant with increase in the applied mean current.

At a certain inter-wire distance, electromagnetic force is generated between the two arcs. Given a constant distance and angle between the wires, the electromagnetic force has a direct relationship with the two arc currents. (Fang, C. fu *et al.* (2012)

With respect to the induced pulsed current, the force generated on the arcs during tandem-GMAW welding could be calculated using Equation (3-9) (Fang, C. fu *et al.* (2012).

$$dF_{12} = \frac{\mu_o}{4} \times \frac{\cos\beta_1 - \cos\beta_2}{D} \times dl_2 \times t \times I_p \times I_b \times (1 - t) \times I_b \quad (3-9)$$

Where, F_{12} is the electromagnetic force between the two arcs, $\mu_o = 4\pi \times 10^{-7}$ is vacuum permeability, l_1 is the lead arc length, l_2 is the trail arc length, β_1 and β_2 are the angles between the differential units of trail arc and both ends of the lead arc, respectively, t is the time on pulsed peak, I_p is the peak pulsed current and I_b is the base pulsed current. D is distance between the two arcs.

From equation (3-10), at constant l_1 , l_2 , β_1 , β_2 and D , dF_{12} is determined by I_p , I_b and t (Fang, C. fu *et al.*, 2012).

Therefore, the magnitude of the electromagnetic force induced on the arc in tandem-GMAW process, depends on the magnitude of the peak current, base current, and duty ratio (Fang C, fu *et al.*, 2012).

3.5.1.3 Results of effect of travel speed on bead geometry

The effect of TS on BW, BH, BP and BA are plotted in Figure 3-8. The plot show evidence of a nearly linear correlation between TS and the measured bead parameters.

In Figure 3-8(a), BW initially decreased by 18.2%, between the lower and medium TS setting of 13mm/s and 20mm/s, to a value of 11.45mm. Thereafter, BW decreased by 12.5%, to 10.02 mm, with further increase in TS from the mid setting of 20mm/s to the highest setting of 27mm/s.

The BH followed a similar trend to BW, decreasing first by 12.6% between the lower and medium TS of 13mm/s and 20mm/s, to 2.86mm. Then further increase in TS from the mid to highest settings, produced 9.1% decrease in BH, to 2.1mm.

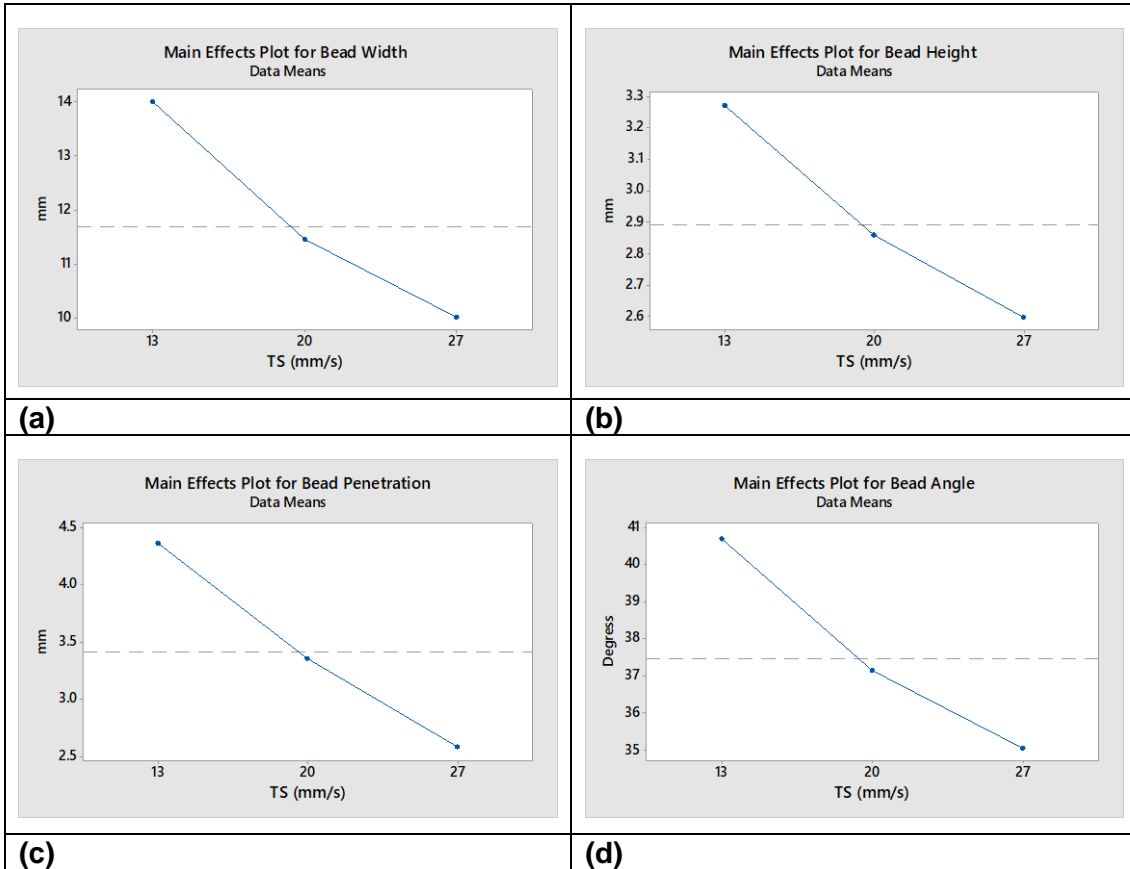


Figure 3-8 Effect of TS on (a) BW (b) BH (c) BP and (d) BA

In Figures 3-8(c) and 3-8(d), BP and BA decreased by 23.1% and 8.7 %, to 3.36mm and 37.2° respectively, with increase in TS from 13mm/s to 20mm/s.

Thereafter, BP and BA decreased by 23% and 5.7%, producing the lowest values of BP and BA of 2.59mm and 35.1° respectively, with further increase in TS from 20mm/s to 27mm/s.

The decrease in the measured bead parameters observed, is due to the fact that as TS was increased, the heat energy generated per unit length (heat input) and hence, amount of material deposited per unit length decreased, leading to a reduction in WFS/TS ratio. This consequently produced a narrower, shorter, and shallower weld bead, with a reduction in the bead angle.

The TS effect on BP is considered irrelevant since the high or low settings produced the same effect. However, since it is more desirable to achieve optimal wetting and fusion characteristics, using the middle settings of TS, within the limit

of parameters studied in this experiment, would be more beneficial with respect to the deposition process stability.

3.5.1.4 Effect of CTWD on bead geometry and quality

The effect of CTWD on BW, BH, BP and BA are plotted in Figure 3-9, and revealed that CTWD produced insignificant influence on BW and BH.

In Figure 3-9(a) BW showed insignificant increase of 0.58%, to a maximum of 11.82mm, with increase in CTWD from 20mm to 22.5mm. Further increase in CTWD from 22.5mm to 24mm, produced slight decrease in BW of 4.5%, to a minimum of 11.3mm.

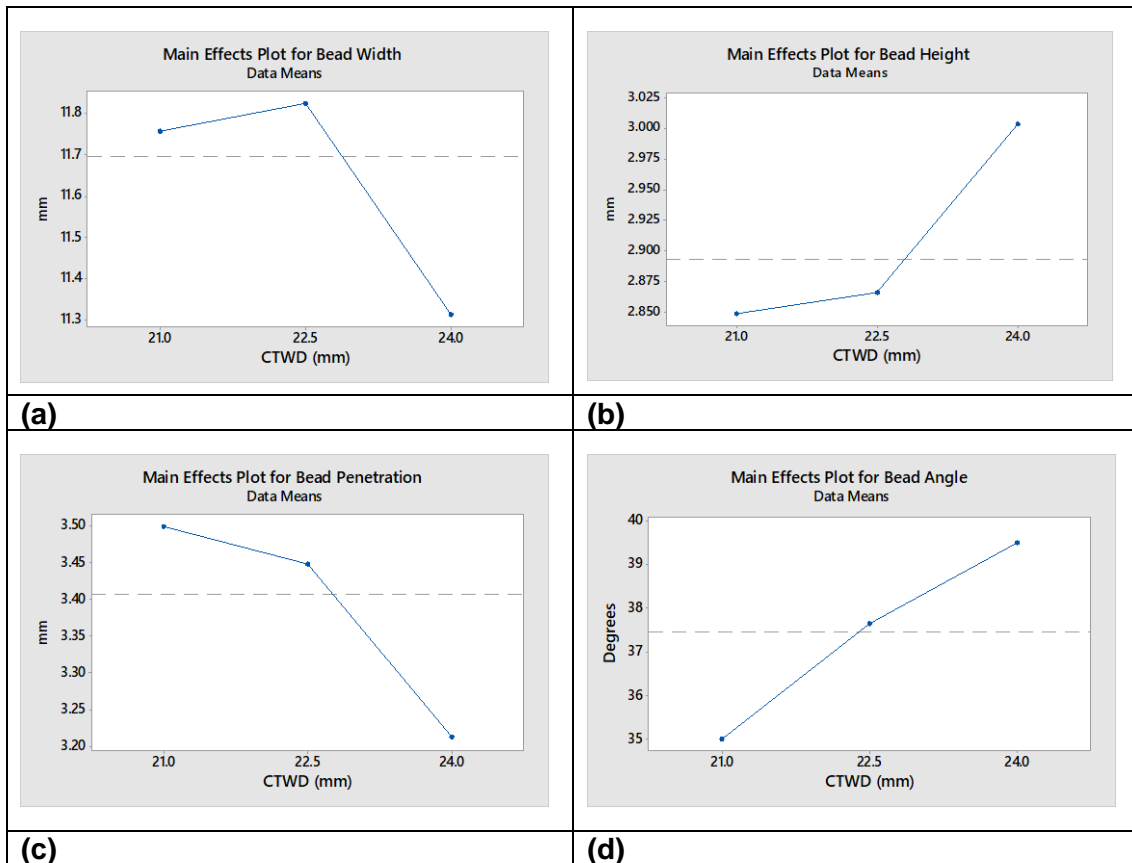


Figure 3-9 Effect of CTWD on (a) Bead width (b) bead height(c) Bead penetration (d) Bead angle

In Fig. 3-9(b), BH is observed to increase insignificantly by 0.7%, from 2.85mm to 2.87mm, with increase in CTWD of 21mm to 22.5mm. Further increase in CTWD to 24mm, produced a slight increase in BH of 4.8%, to a maximum of 3.00mm.

The initial slight increase in BW and BH was probably caused by a sudden change in metal transfer mode from short-circuit to spray transfer, owing to the increase in instantaneous arc power per unit length, with the initial increase in CTWD from the lowest setting. The subsequent increase in BH with the corresponding slight decrease in BW, when CTWD was further increased, could have resulted from increased resistive heating of the wire, leading to a relatively higher wire burn off rate.

Figure 3-9(c) reveals that BP initially reduced by 12% from a maximum of 3.5mm as CTWD was increased from 21mm to 22.5 mm, and thereafter reduced by 8.15% to a minimum, with increase in CTWD to 24mm.

Figure 3-9(d) showed that BA increased steadily by 12.8% to a maximum of 39.5° with increase in CTWD from 21mm to 24mm.

The decrease in PD is perhaps because increase in CTWD increased the resistive heating of the wire, which reduced the amount of current density, heat energy and arc pressure reaching the substrate.

Hence, increase in CTWD produced a slight increase in BH and BA, and decrease in BW and PD, which could be attributed to resistive heating effect of the wire, which produced a slight increase in burn off rate of the wires.

It is important to note that too high CTWD can result in lack of fusion defect, due to less heat reaching the substrate, to melt and fuse with the weld metal. It could also cause increased electromagnetic interference between the arc as the current increases, as shown in equation (5).

However, the effect of CTWD on voltage and current is minimal, probably due to the high WFS utilised and hence, overall high heat input generated.

Optimum CTWD setting is therefore required, as too short could cause frequent short-circuiting of wire into the weld pool, increasing the deposition instability and too long could cause increased electromagnetic arc interruption, loss of gas shielding, poor fusion, and unstable metal transfer.

3.5.1.5 Effect of Preheat temperature on bead geometry

The effect of preheat temperature on BW, BH, BP and BA are depicted with the plots in Figure 3-10.

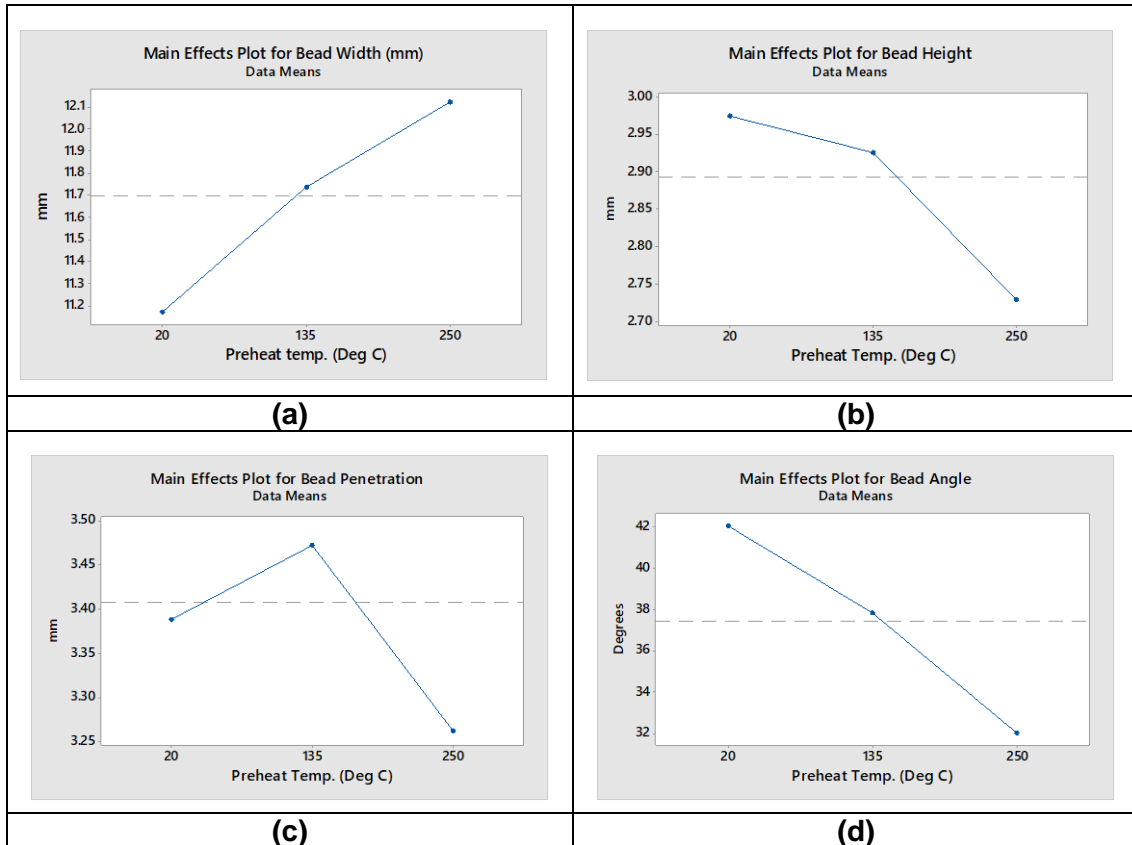


Figure 3-10 Effect of Preheat temperature on (a) Bead width (b) Bead Height (c) Bead penetration (d) Bead angle

Figure 3-10(a) shows that BW increased steadily by 8.5%, up to a maximum of 12.1mm, with increase in preheat temperature 20°C to 250°C.

In Figure 3-10 (b) BH showed a 12.8% decrease, to a minimum of 2.73 mm, with increase in preheat temperature from 20°C to 250°C.

It can be seen from Figure 3-10 (c) that the BA decreased steadily by 31.3% reaching a minimum of 32°, as preheat temperature was increased from 20°C to 250°C.

The increase in preheat temperatures resulted in higher temperatures of both the previously deposited metal and weld pool. Therefore, the interfacial tension and viscosity of the weld pool are expected to decrease owing to increase in its heat

content, leading to improvement in wetting properties of the molten metal. (Almeida, P. M. S., 2012). Therefore, the molten metal spreads to a greater extent, making the bead wider, higher, with decrease in the bead angle.

3.5.1.6 Statistical significance of measured bead responses

ANOVA plots and result tables of the applied tandem-wire process parameters versus the output bead parameters, produced using Minitab 17 statistical software, are shown in Appendix C (i – v). Variations in the measured outputs values were analysed using pooled standard deviation.

The ANOVA result table of WFS Vs BW, BH, BP and BA at 95% confidence level shows that the bead responses are statistically significant, Appendix C (i). Hence, the variations in the measured bead parameters are attributed to the applied tandem-wire process parameters.

ANOVA result table of TS versus bead parameters show that BW, BP and BH are statistical significance at 95% confident level. However, BA gave a high p-value, hence is statistically insignificant, Appendix C (ii). This could be due to measurement error resulting from the poor surface quality of the deposited beads, as seen in Figure 3-12.

The ANOVA result table of CTWD versus the bead parameters shows high p-values at 95% confidence level, Appendix C (iii). The large variation in the measured bead responses is attributed to the ‘heavy activity’ in the built-in arc length control, due to the intensive wave of the weld pool and frequent short-circuiting of the pulsed arc Goecke S. et al, (2001). This is the primary reason for the relatively large variations in the heat input, Appendix C (iv)b.

Similarly, the ANOVA plot of preheat temperature versus the bead responses show large p-values, Appendix C (v). Preheat temperature mainly influences the bead quality and fusion characteristics. The large error in the measured bead parameters is due to the poor surface quality of the deposited beads, which can be observed in Figure 3-12.

3.5.1.7 Effect of effect of tandem-GMAW high deposition parameter on deposited bead quality

The significant effect of travel speed on the geometrical quality of the single bead deposits. at low, medium, and high WFS settings is depicted in Figure 3-11. It is apparent that the bead quality visually appears better at lower WFS settings, for all values of TS applied, as seen in Figure 3-11(a).

However, relatively high WFS and high TS settings resulted in poor bead formation, with undercut defect and spatter as seen in Figures 3-11 (b) and 3-11 (c) respectively. Also, at higher WFS and lower TS settings, excessive penetration resulted.

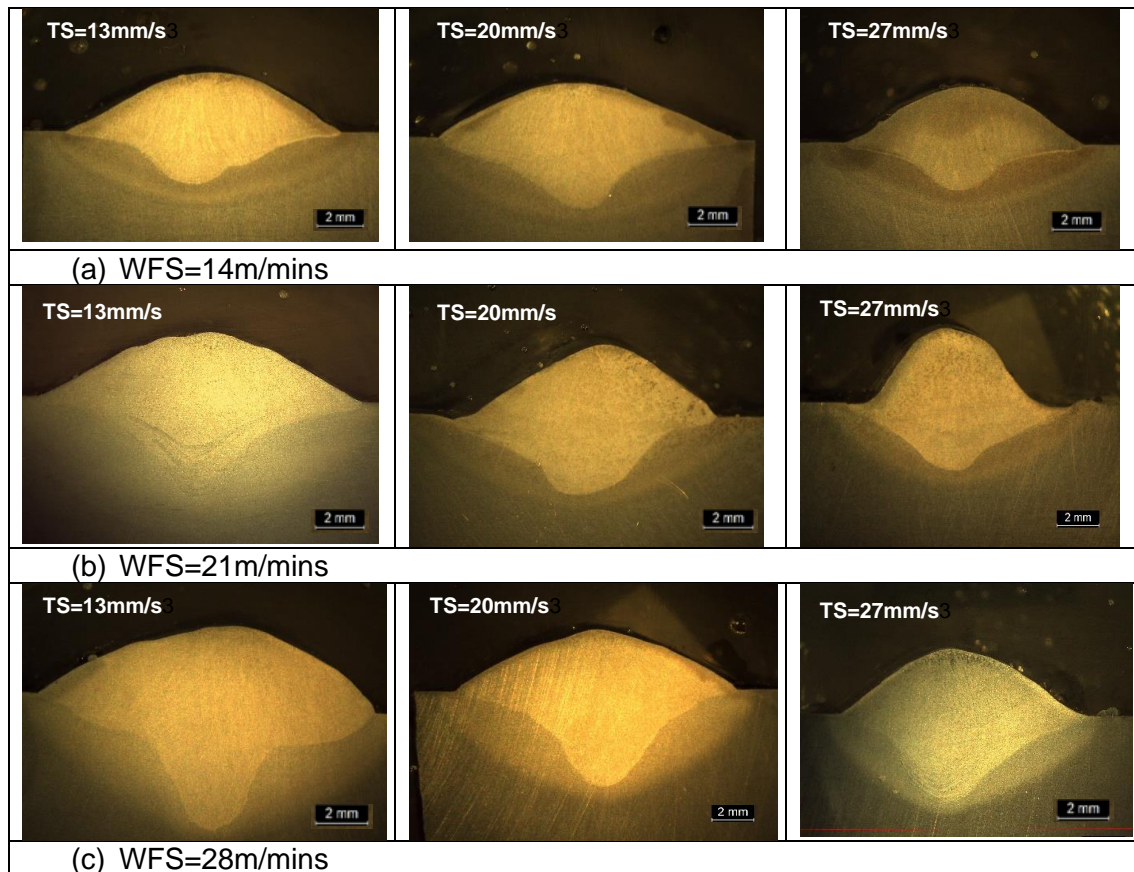


Figure 3-11 Cross sections of single bead deposited using Tandem wire, showing effect of TS on weldment surface quality, using 22.5mm CTWD, at (a) Low (b) Medium and (c) High WFS

High TS could result in peaky, undercut beads, while low TS produced broad bead geometry (Shoeb M., 2013). An appropriate BW prevents lack of inter-pass

fusion defect, which means high fluid state of the deposited metal, which is beneficial from the standpoint of optimum multi-pass overlapping bead profiles and surface quality (Mistry, J. P. 2016).

In this investigation, twenty-seven (27) single weld beads were deposited, with one replicate, making a total of 54 weld beads. Figure 3-12 show the surface appearance of the deposited beads.

The surface quality of the beads was visually inspected to determine their quality and acceptability. The quality criteria used to accept the deposited beads include—smooth and uniform bead appearance, with no surface defect or significant spatter.

The measured bead geometries showed expected correlations with the applied process parameters. Minimal or no spatter were generally observed during the deposition. However, the deposited weld bead profile was generally not uniform, most of the surfaces appeared poorly formed and defective. The defects observed included severe undercuts, excessive convexity, and overall poor surface finish.

Since the experiment was conducted with a replicate, in accordance with the experimental plan, there is a strong level of confidence that the observed poor bead quality is dependent on the deposition parameters and conditions. Hence, it is important to understand the reason for the poor bead profile and quality, to devise possible techniques for producing better weld bead quality, using the tandem-GMAW process.



Figure 3-12 Surface appearance of Tandem-GMAW deposited weld beads

Temperature gradient is the most significant factor that influences the degree of undercut. The size of temperature gradient is dependent on the size of the surface tension gradient, and the latter directly affects the driving force of the pool metal. Under other unchanged conditions, undercut of the weld will increase with increase in temperature gradient. With increase in welding speed, molten bath

temperature gradients near the fusion line area increases, and the dynamic aspect ratio of the bead also decrease, both conditions will increase the tendency for undercut formation (Zhenyang Lu and Pengfei Huang, 2011).

High TS could cause the surface tension temperature coefficient to change from negative to positive. Under this condition, the liquid weld metal will flow from the fusion line to the weld centre, if the region cannot be replenished by the metal in time, then undercut defect will be produced (Zhenyang Lu and Pengfei Huang, 2011).

A further literature review was conducted to provide insights on the next stage of experimental work required to produce defect free weld beads, of acceptable surface quality.

3.6 Characterisation of the effect of Tandem-GMAW secondary process parameters on bead geometry, surface quality and electrical transient characteristics

The preceding study showed that tandem-GMAW primary parameters of WFS and TS produce the most significant effect on the weld bead geometry. It also indicated that proper selection of process parameters is important to enhance control of the molten weld pool and produce acceptable weld bead quality. This is even more critical because, the lead arc in tandem-GMAW process produces a higher arc energy and controls the penetration, while the trail arc produces a relatively lower energy and controls the bead appearance (Fang, C. fu *et al.*, 2012).

Goecke S. et al, (2001) reported poor bead quality during Tandem-GMAW process, when spray arc mode was used on both wires, due to high arc pressure, increasing the risk of pushing materials out of the weld-pool. Heavy weld pool waves were also observed between the two arcs when the short arc mode was used. Synchronous pulsed current mode was indispensable for arc stability, but unstable deposition process was reported to occur due to intensive weld pool wave, which caused heavy activity in the built-in arc length control.

It was also found that using multiple and completely different parameter settings on both wires, and torch configurations could produce acceptable bead geometries. They noted that using higher WFSs seemed to promote arc stability, but higher spatter could occur. Hence, it was suggested that minimising the weld pool size, and ensuring accurate torch set-up, was critical to reducing problems of undercuts, while using an optimised pulse-parameters can reduce occurrence of spatters (Goecke, S. *et al.*, 2001).

It was also suggested that for optimum welding performance, the suitable WFS of the trailing wire should be about 1 – 2 m/mins greater than the WFS of the leading wire (Huang P. F. *et al.*, 2012).

Therefore, it was necessary to investigate whether the geometrical features and surface quality of the weld beads observed in the previous study, are influenced in the same way by tandem-GMAW secondary process conditions such as (1) Variations in WFS of lead wire (A) and trail wire (B), (2) Changes in torch travel directions and (3) Changes in tandem-wire configuration. It is only when the influence of these secondary conditions, on the final weld geometry is completely understood that the process can be efficiently applied in a fully automated tandem-GMAW setup (Ribeiro, R. A. *et al.*, 2015). The experiments were conducted using the equipment set-up and substrate dimensions presented in section 3.1.

3.6.1 Effect of variation in WFS of lead wire(A) and trail wire(B) on the bead geometry and surface quality

In this investigation, trials were conducted by steadily increasing the WFS of lead wire (A), while maintaining the WFS of trail wire (B), Table 3-3(a). Thereafter, the WFS of trail wire (B) was also gradually increased, while keeping the WFS of wire (A) constant, Table 3-3(b). All other parameters were kept constant.

Table 3-3 shows that pre-set deposition parameters applied in this investigation where, (a) WFS (A) > WFS (B) and (b) WFS (A) < WFS (B). Note that the total of WFS is the addition of the individual WFS.

Table 3-3 Pre-set parameters used to study effect of variation in WFS of lead wire (A) and trail wire (B), when (a) WFS wire(A) > WFS wire(B) and (b) WFS wire (A) < WFS wire(B)

(a) WFS wire (A) > WFS wire (B)

Trial No.	WFS (m/mins)		Total WFS (m/mins)	TS (mm/s)	CTWD (mm)
	Lead wire (A)	Trail wire (B)			
1	8	8	16	15	20
2	9	8	17	“	“
3	10	8	18	“	“
4	11	8	19	“	“
5	12	8	20	“	“
6	13	8	21	“	“

(a) WFS wire (A) < WFS wire (B)

Trial No.	WFS (m/mins)		Total WFS (m/mins)	TS (mm/s)	CTWD (mm)
	Lead wire (A)	Trail wire (B)			
1	8	8	16	15	20
2	8	9	17	“	“
3	8	10	18	“	“
4	8	11	19	“	“
5	8	12	20	“	“
6	8	13	21	“	“

3.6.1.1 Result of effect of variation in WFS of lead wire(A) and trail wire(B) on average arc heat input and deposited bead geometry

Figure 3-13 shows the effect of changing the WFS of wires (A) and (B), on the generated H.I and deposited BW, BH, BP and BA. It should be noted that the WFS value is the total for both wires and the torch was travelling in the leading direction.

From Figure 3-13(a), it can be clearly observed that when the WFS of lead wire (A) was equal to WFS of trail wire (B), the total heat input generated was higher in Wire A. But with variation in WFS, a higher heat input was produced, when the WFS of trail wire (B), was higher the WFS of lead wire (A).

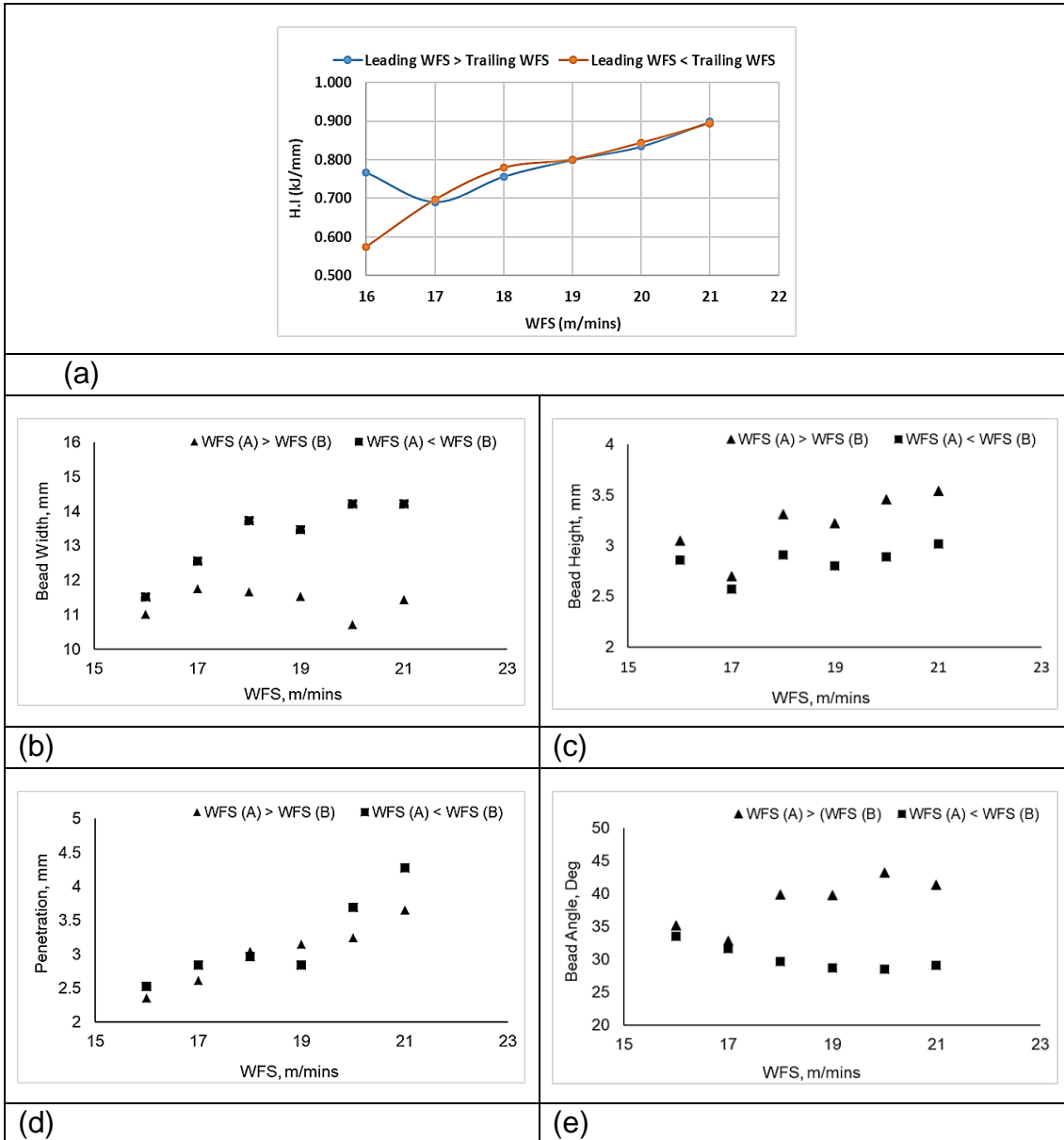


Figure 3-13 Effect of variation in WFS of lead wire (A) and trail (B), on deposited bead geometry (a) H.I (b) BW (c) BH (d) BP (e) BA

From Figure 3-13(b), it can be clearly observed that when a higher WFS was applied to the lead wire (A), relative to the trail wire (B), the deposited BW decreased. The magnitude of the decrease depended on the difference between the WFS of both wires.

In Figure 3-13(c), when the lead wire (A) was parameterised at a higher WFS over the trail wire (B), the deposited BH increased, compared to when lower WFSs was applied.

The effect of variation in WFS between wire (A) and wire (B) in Figure 3-13(d), does not seem to show a strong consistent trend with the BP. However, BP appeared to be higher when the WFS of the trail wire (B) was greater, compared to the WFS of lead wire (A).

From Figure 3-13(e) it is clearly evident that parameterising the lead wire (A) at a higher WFS over the trail wire (B), led to increase in the deposited BA.

The result shows that applying a higher WFS on the trail wire over the lead wire produces a higher H.I, larger BW and BP; smaller BH and BA. This could be due to the fact that the lead arc in tandem GMAW process does the heavy work of heating the wire and the substrate to form the molten pool, while the trailing wire fills the groove and at the same time smooths the weld surface (Goecke, S. *et al.*, 2001).

3.6.1.2 Effect of variation in WFS of lead wire(A) and trail wire(B) on the bead surface quality

The effects of parameterising the lead wire (A) and trail wire (B) at different WFSs, on the bead quality are shown using the deposited surface appearance in Figure 3-14. The transverse macro cross sections of the beads showing the effect of variation in WFS of lead wire (A) and trail wire (B) are displayed in Appendix D.

From Figure 3-14, it can be clearly seen that apart from the noticeable difference in size, the surface quality of the deposited beads are significantly affected by using different WFS settings in both lead and trail wires.

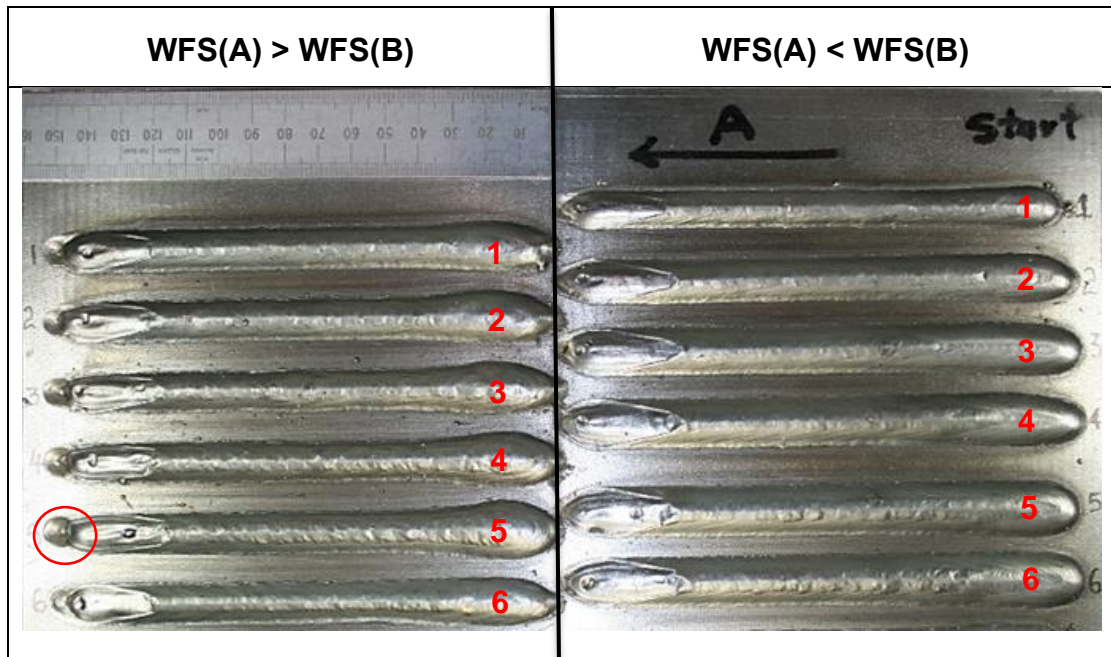


Figure 3-14 Surface quality of single pass beads and transverse cross sections obtained by varying the WFS between the lead wire wire (A) and trail wire (B)

It can be observed in Figure 3-14, that the surfaces of the beads deposited using a higher WFS on the trail wire (B), show flatter, uniform, smooth and symmetrical beads, devoid of defects or spatter, compared to those produced with a higher WFS of lead wire (A). This is because the trail wire controls the bead appearance, which effectively improved the quality of deposited weld metal (Fang, C. fu *et al.*, 2012).

Also, the “digging action” of the lead arc, underfill (stop/start) defects, (encircled in red), is clearly visible on the surfaces of the beads deposited, when a higher WFS was applied to the lead wire (A). This can however, be corrected by optimising the stop/start parameters. Hence, all the beads showed acceptable surface quality.

This demonstrates the possibility of producing acceptable weld bead quality, using different tandem-GMAW WFS settings on the lead and trail wires, but with the back wire parameterised at a higher WFS, compared to the front wire.

3.6.2 Effect of torch travel direction on bead geometry and deposited surface quality

Typically, bi-directional deposition strategy is utilised in WAAM process, which is beneficial for uniform wall geometry and maintaining accurate CTWD during deposition of the part.

This study therefore investigated the effect of travelling the tandem torch in both leading and trailing directions, on the geometry and surface quality of single bead deposits.

During the study, the rear wire was fed with a higher WFS, over the front wire, irrespective of the torch travel direction. Initially, the torch travelled in the leading direction, in which wire (A) is the lead wire, and wire (B) the trail wire. Thereafter, the torch was reversed to the trailing direction, whereby wire (A) was then the trail wire and wire (B) the lead wire.

The experiment was conducted using the equipment set-up and consumable described in section 3.1. Figure 3-15 shows a schematic illustration of the torch travel directions relative to the lead wire (A) and trail wire (B). The parameters utilised in the study are set out in Table 3-4.

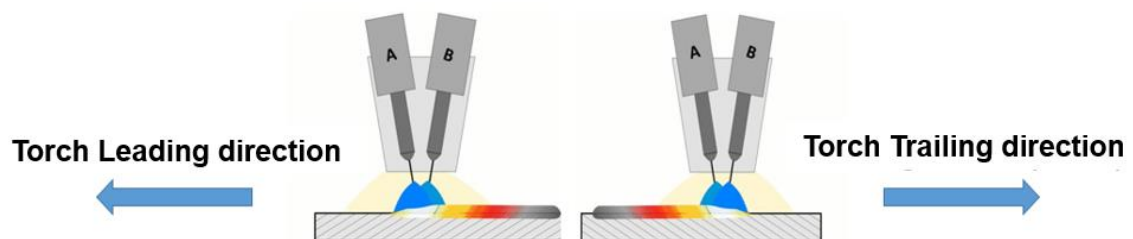


Figure 3-15 illustration of torch travel directions relative to the lead wire (A) and trail wire (B)

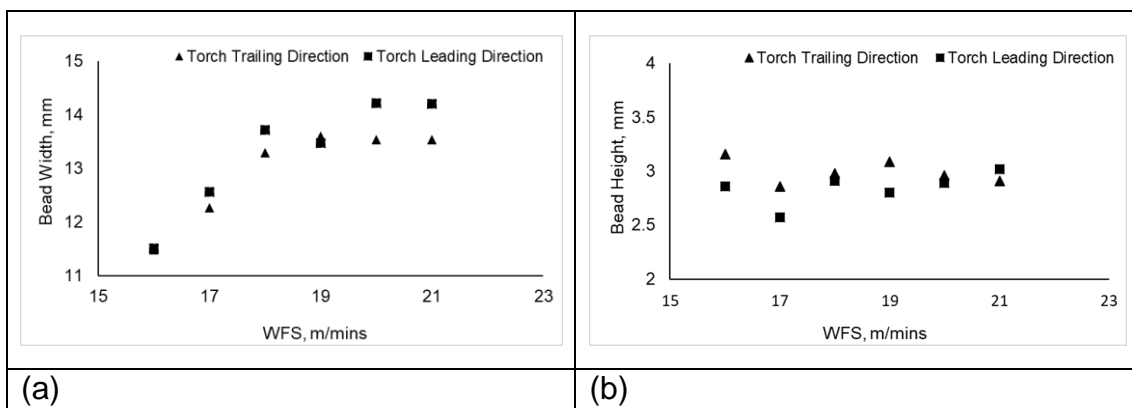
Table 3-4 Pre-set conditions applied in the study of effect of torch travel directions relative to lead wire (A) and trail wire (B)

Trial No.	WFS (m/mins)		Total WFS (m/mins)	TS (mm/s)	CTWD (mm)
	Lead wire (A)	Trail wire (B)			
Torch leading direction: Wire (A) is Front wire					
1	8	8	16	15	20
2	8	9	17	“	“
3	8	10	18	“	“
4	8	11	19	“	“
5	8	12	20	“	“
6	8	13	21	“	“
Torch trailing direction: Wire (A) is Rear wire					
1	8	8	16	“	“
2	9	8	17	“	“
3	10	8	18	“	“
4	11	8	19	“	“
5	12	8	20	“	“
6	13	8	21	“	“

3.6.2.1 Result of effect of torch travel direction on bead geometries

The result of effect of torch travel direction is depicted with the plots presented in Figure 3-16.

From Figure 3-16(a), it can be observed that the BW is wider when the torch travelled in the leading direction, compared to travelling in the trailing direction.



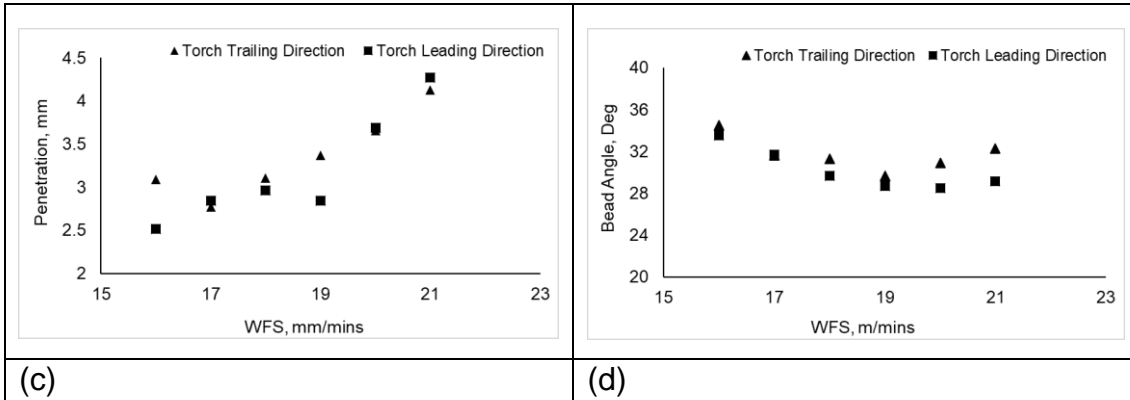


Figure 3-16 Effect of torch travel direction on deposited (a) BW (b) BH, (c) BP and (d) BA

Figure 3-16(b) showed that a higher BH was typically produced when the torch travelled in the trailing direction, compared to when it travelled in the leading direction.

In figure 3-16(c), BP does not show a clear trend with respect to the torch travel directions. However, it somewhat appears that at higher WFS settings, the BP increases when the torch was travelling in the leading direction.

In Figure 3-16(d), it can be clearly seen that relatively lower bead angles are produced when the torch was travelled in the leading direction, compared to when it travelled in the trailing direction.

3.6.3 Result of effect of torch travel direction on bead surface quality

The effect of torch travel directions on the bead quality is shown using the bead surface appearance and transverse macro cross sections of the deposited bead displayed in Figure 3-17 and Figure 3-18 respectively.

Figure 3-17 showed that excellent bead surface quality is produced irrespective of the torch travel direction. However, an important factor for achieving the improved bead surface quality was parameterising the rear wire at a higher WFS, over the front wire, irrespective of travel direction.

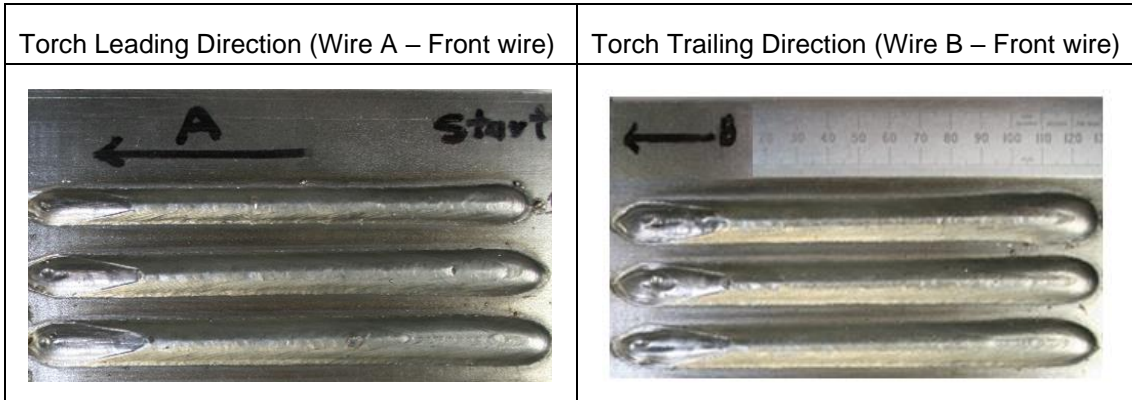


Figure 3-17 Effect of torch travel directions on surface quality of deposited bead

In Figure 3-18, the deposited beads all show good quality profile, devoid of defect or spatter.

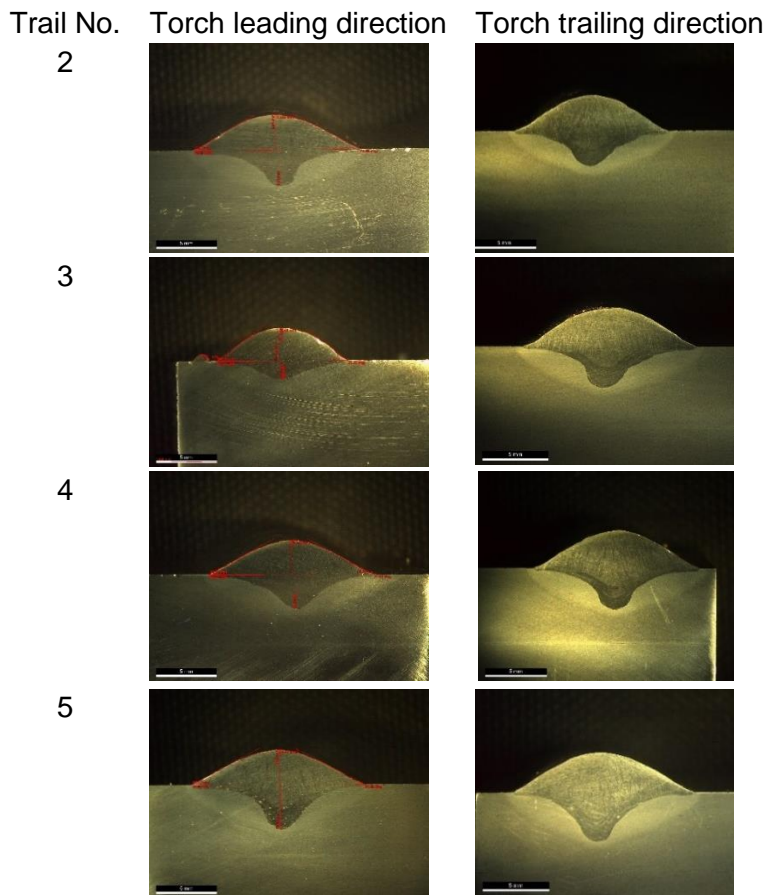


Figure 3-18 Effect of torch travel directions on transverse cross sections of the deposited bead

Though the same WFS setting was applied for both travel direction, (but always keeping the rear wire at a higher WFS), it is obvious that the torch travel direction

influenced the bead geometry to some extent. The main reason could be attributed to the difference between the actual electric transient characteristics of the trail and lead arc.

A larger BW and smaller BH was produced, when the lead wire (A), was the front wire. It could be concluded that in the torch leading direction, where the trail wire (B) is the rear wire, the impact of wetting of the molten metal was much stronger, causing a larger spread of the molten metal to increase the BW. It is also the case that the trail arc produces a lower energy and controls the bead appearance and improve the quality of deposited weld metal (Fang, C. fu *et al.*, 2012).

It can be also observed that the difference in width increased with the magnitude of the difference between the WFS of both lead and trail wires, Fig. 3-16(a). This could be particularly important, with respect to the stair-step effect produced during multi-pass deposition, when a bi-directional deposition strategy is utilised.

Hence, it would be advantageous to minimise the difference between the WFS of the lead and trail wire, to minimise the stair-stepping effect and improve the surface quality.

3.6.4 Effect of wire configuration (set-up) on heat input, bead geometry and deposited surface quality

The tandem-GMAW torch can be positioned such that the lead and trail wires are aligned either in series or parallel to each other. In the series configuration, the lead wire (A) and trail wire (B) are positioned such that one is in front of the other, depending on the torch travel direction. While in the parallel configuration, both the lead wire (A) and trail wire (B) are set side-by-side with each other irrespective of torch travel direction. This is illustrated in Figure 3-19.

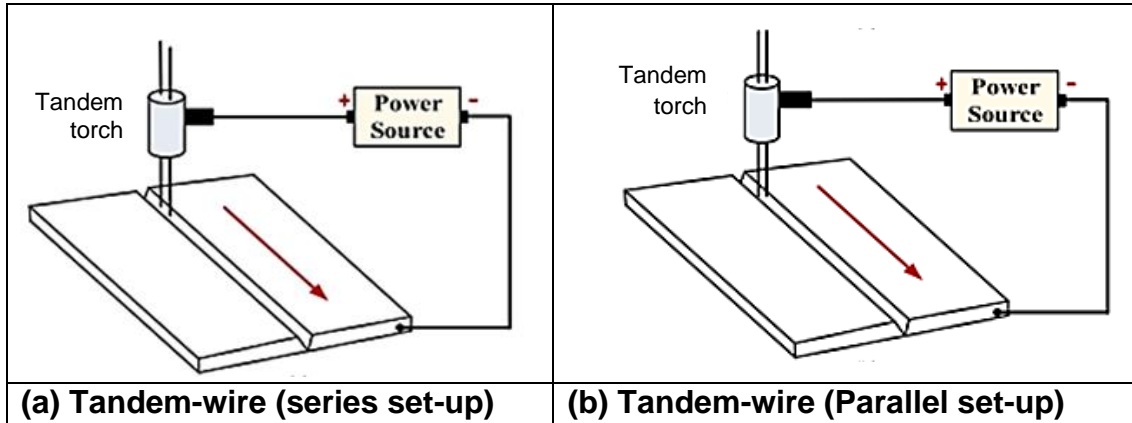


Figure 3-19 Illustration of tandem-GMAW wire configurations (a) Series (b) Parallel

The experiment was conducted using the equipment set-up and consumables detailed in section 3.1. The investigation of the effect of torch configuration was studied using the pre-set parameters given in Table 3-5.

Table 3-5 Pre-set conditions used to study the effect of wire configurations

Trial No.	WFS (m/mins)		Total WFS (m/mins)	TS (mm/s)	CTWD (mm)
	Lead wire (A)	Trail wire (B)			
1	4	4	8	7	20
2	4	6	10	7	"
3	6	6	12	7	"
4	6	8	14	10	"
5	8	8	16	10	"
6	8	10	18	10	"

3.6.4.1 Result of effect of wire orientations on generated heat input and deposited bead geometry

The experiments for tandem-GMAW series wire configuration were conducted by traveling the torch in the leading direction. The result of the experiment is plotted in Figure 3-20.

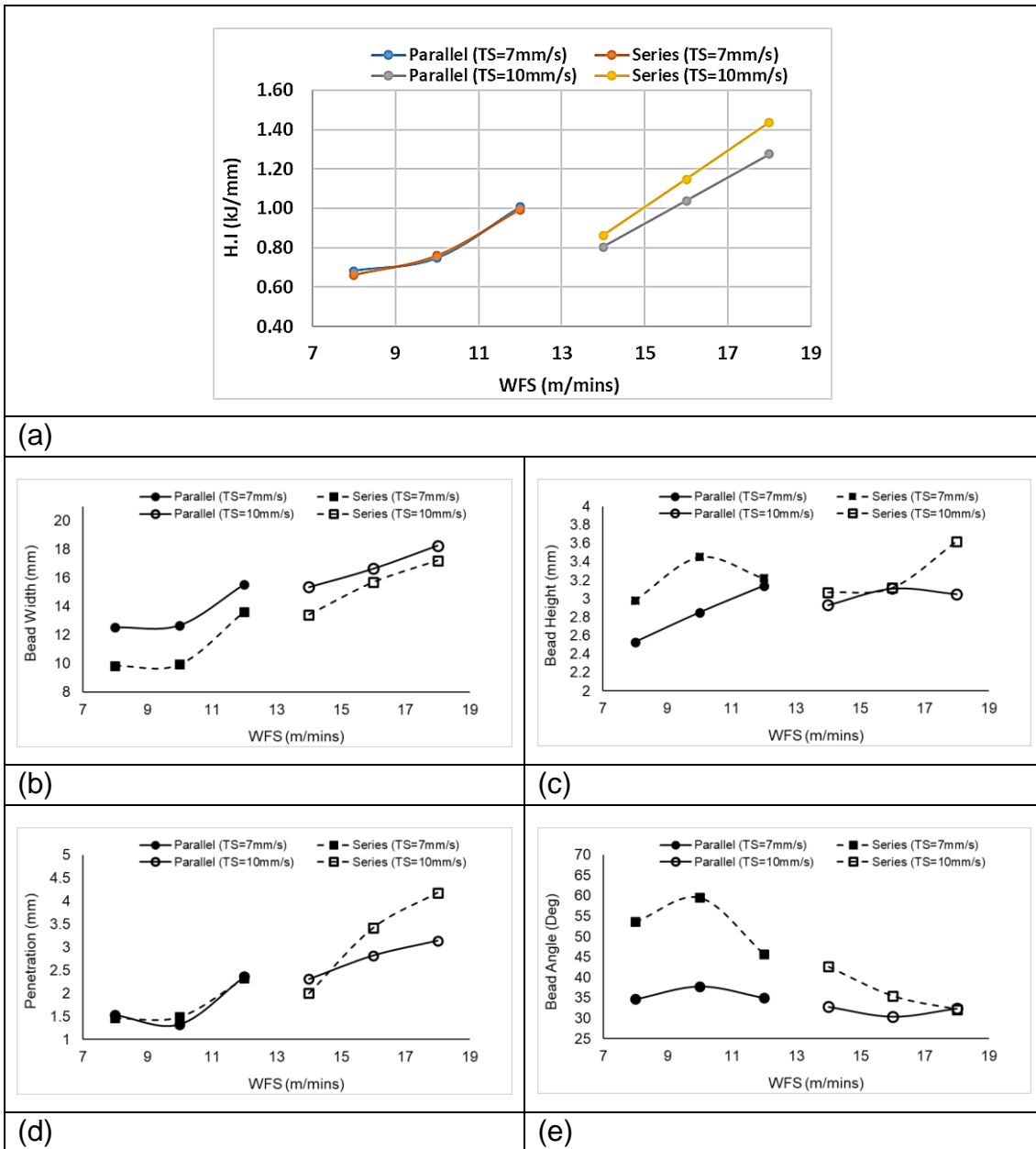


Figure 3-20 Effects of Tandem-GMAW parallel and series wire orientations, on deposited bead geometries (a) H.I (b) BW (c) BH (d) BP (e) BA

The plot in Figure 3-20 (a-e) shows the effect of wire orientations on the generated heat energy per unit length (heat input) and deposited bead geometries.

It can be observed that when the Tandem-GMAW lead and trail wires were positioned in parallel orientation to each other, a lower H.I was generated.

The parallel wire orientation produced a larger BW, but lower BH, BP and BA, compared to when the wires were set-up in series orientation. It can be concluded that under the series wire orientation, the arc is concentrated in the centre of the weld pool, hence, the impact and excavation of the droplet on base metal was much stronger, which produced a deeper BP.

3.6.4.2 Result of effect of Tandem-GMAW wire orientations on deposited bead surface quality

The effect of tandem-GMAW wire orientations on bead quality is shown using the deposited bead surface appearance and transverse cross-sections macro specimens, as shown in Figure 3-21. A clear difference in bead appearance and surface quality can be observed.

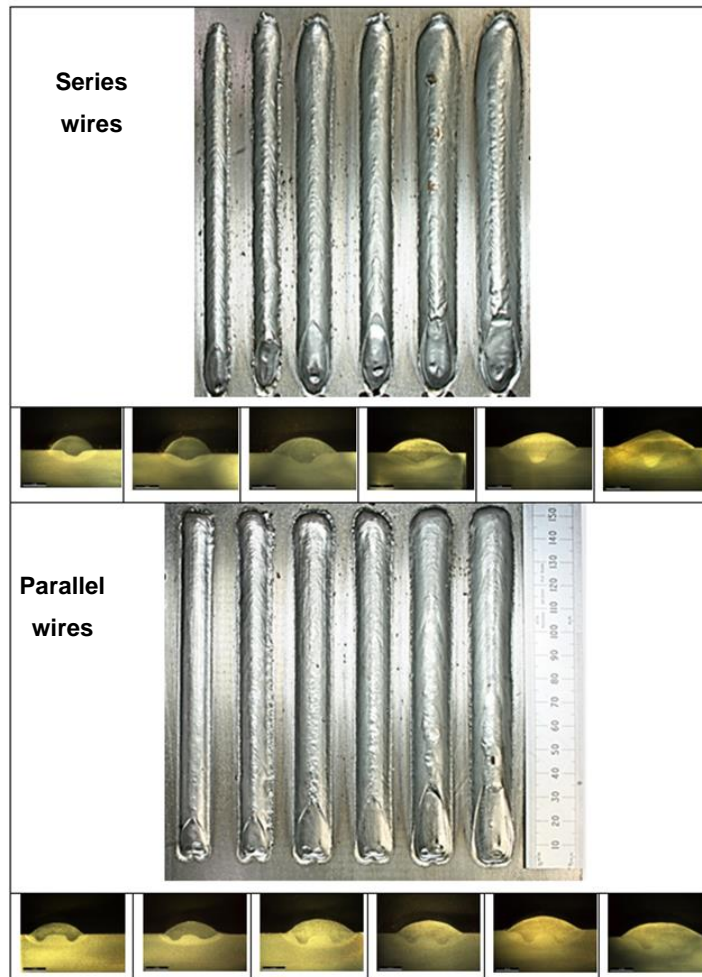


Figure 3-21 Weld bead surface and transverse cross sections obtained, showing effects of tandem-GMAW series and parallel wires configuration

The bead quality produced using both series and parallel wire orientation, equally showed good quality. However, the actual surface quality and bead profile of the deposits are significantly influenced by the wire orientation adopted in the study.

In Figure 3-21, the rippling effect observed on the top surface of the beads deposited using series wire orientation, is eliminated when the wires were configured in parallel. Also, slight spatter was observed during deposition, with the wires configured in series to each other. This was probably due to a higher build-up of molten metal underneath the wires in series configuration, which caused momentary unstable dip metal transfer.

The profile of the bead produced when the wires were configured in parallel to each other, appeared flatter and more uniform, compared to the series set-up.

A characteristics difference in the BP profile is also visible from the transverse cross section of the beads in Figure 3-21. The parallel wire orientation produced two distinct BP profiles, while the series wire induced a single BP profile. Hence, it is pertinent to say that the wire configuration could influence the dynamic droplet transfer during deposition, and hence, the surface quality of the deposit.

The profile of the arc and molten metal can be observed from the high-speed camera image of the weld pool captured during deposition, Figure 3-22. The torch travelled in the 'Y' direction.

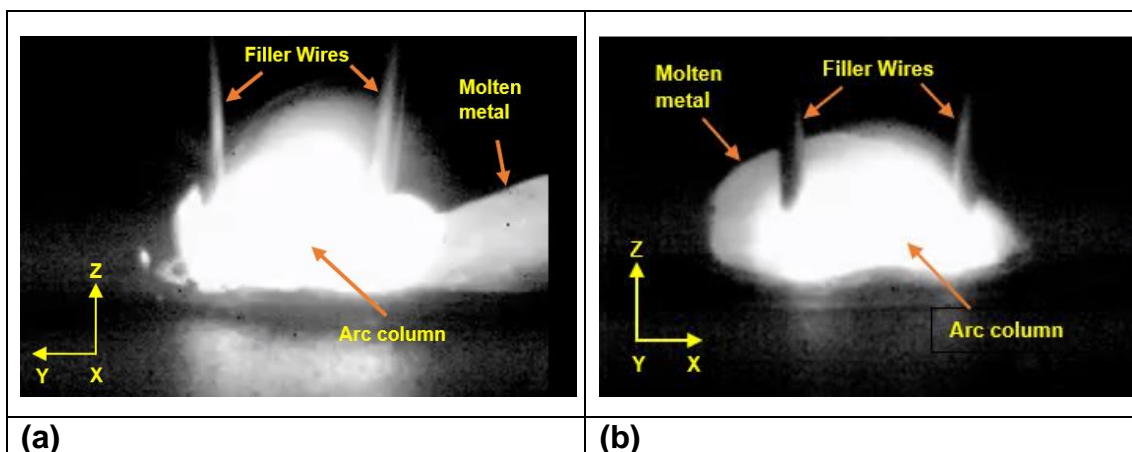


Figure 3-22 Tandem-GMAW weld pool visualisation, with wires configured in (a) Series and (b) Parallel, to each other

It can be seen in Figure 3-22(a) that the weld pool formed using the series wire configuration, is elongated along the direction of travel, and reheating of the weld metal by the trailing arc occurred. This effect causes the molten pool to remain longer at higher temperatures. (Fang, C. fu *et al.*, 2012)

But the arc produced using parallel wire configuration, is elongated in the perpendicular direction of torch travel, Figure 3-22(b). This effect could cause the widening and spreading of weld pool, enhancing the wetting and distribution of the molten metal. It could also induce a relatively higher cooling effect on the weld pool.

Additionally, heavy weld pool waves and short-circuit metal transfer could be minimised, using parallel wire configuration, due to lesser tendency for build-up of weld metal underneath the wires to occur, compared to the series configuration.

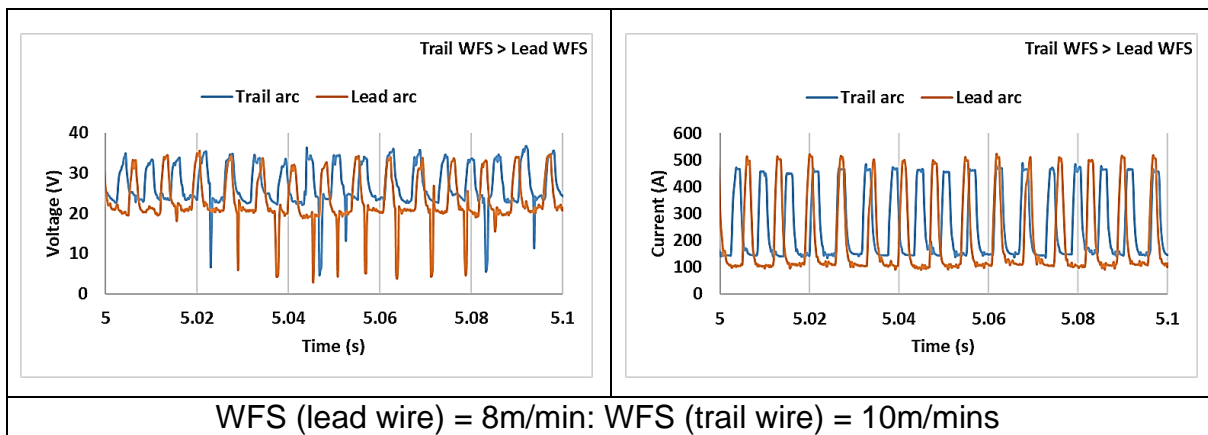
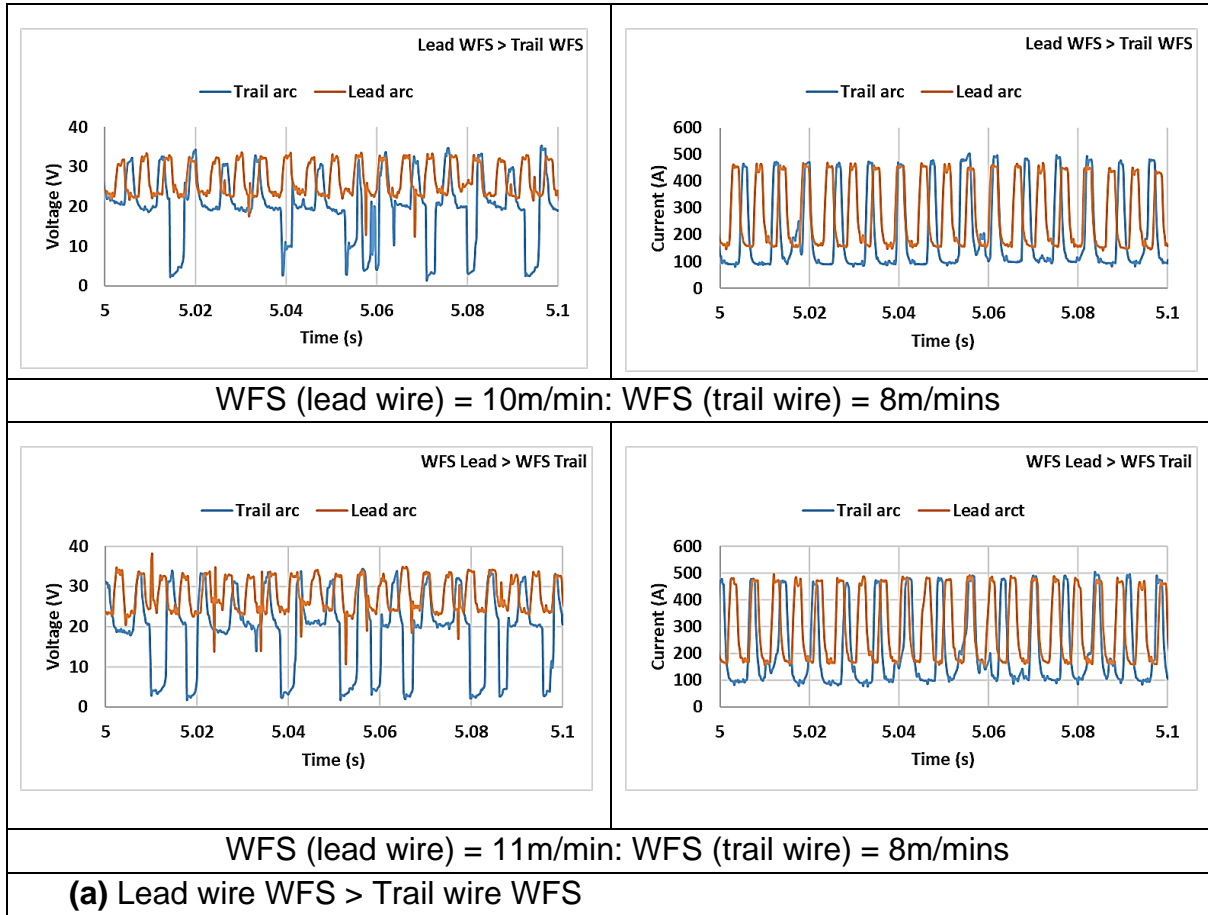
Therefore, it can be concluded that the relatively higher surface quality of tandem-GMAW parallel wire configuration, compared to the series wire set-up, appeared to result in essence, from the effect of a relatively wider wire distance in the transverse travel direction, causing the arc to spread away from the centreline of the molten pool. This thermal effect causes more heat to reach the adjacent areas in the base plate, which can probably explain the formation of a wider, lower, and shallower weld bead, with associated reduction in BA.

3.7 Effect of tandem-GMAW primary and secondary process parameters on electrical transient arc characteristics

This section presents an analysis of electric transient characteristics of tandem-GMAW lead and trail wires, captured during deposition. The analysis was conducted to examine any occurrence of arc instability during deposition, using the generated waveforms. The investigation was carried out using the experimental conditions set out in section 3.6.1 and Table 3-3.

The electrical transient arc data were recorded at every instant in time, for a duration of 11secs, at a sampling rate of 5kHz.

Figure 3-23(a) show the plot of voltage and current waveforms generated, when higher WFSs of 10m/mins and 11m/mins were applied to the lead wire, while the trail wire WFS was fixed at 8m/mins. Figure 3-23(b) also show the waveforms generated, using WFSs of 10m/mins and 11m/mins on the trial wire, while the lead wire WFS was held at 8m/mins.



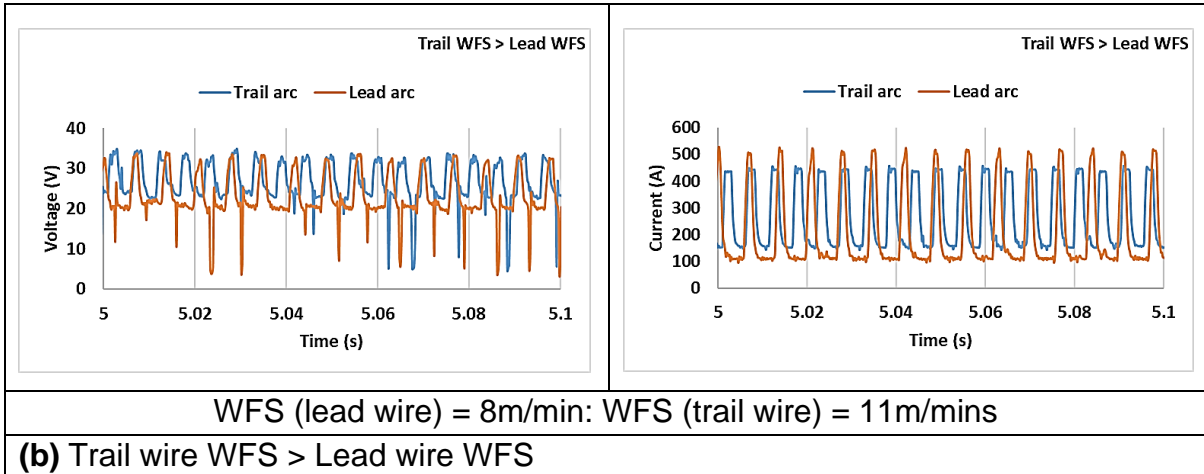


Figure 3-23 Effect of WFS on electrical transient, voltage (left plot) and current (right plot) when (a) Lead wire WFS > Trail wire WFS (b) Trail wire WFS > Lead wire WFS

The drops in voltage can be clearly seen from the waveforms in Figure 3-23, which could be caused by short circuiting of the wires in the molten weld pool.

Figure 3-23(a) showed that when the lead wire WFS (current) is greater than the trail wire WFS (current), the drops in the background voltage (short circuit) on the trail wire occurred more frequently, compared to the lead wire. Also, slight fluctuations in background current of the trail wire can be observed.

Conversely, in Figure 3-23(b), when the trail wire WFS > lead wire WFS, the drops in background voltage (short circuit) on the lead wire occurred more frequently, and also slight fluctuations in background current of the lead wire is evident.

This observation was also reported by Goecke, S. et al. (2001) who noticed that increased frequency of arc blow at higher WFS, occurred during the background period of one arc. He attributed it to possibly high arc pressure when the other arc is in pulse (peak) period.

The analysis also showed that the frequency of voltage drops increased with increase in the total WFS of both wires. It is also clearly evident from the waveforms, that the drops in the trail wire background voltage, Fig. 3-23(a), occurred over a longer time (short circuit duration), compared to the time in which

the drops in the lead wire background voltage occurred. This could be because the torch travelled in the leading direction during this study.

3.8 High speed camera visualisation of arc and weld pool

The behaviour of the weld pool was monitored visually using high-speed photography image. Some observations of the weld pool behaviour are presented as follows.

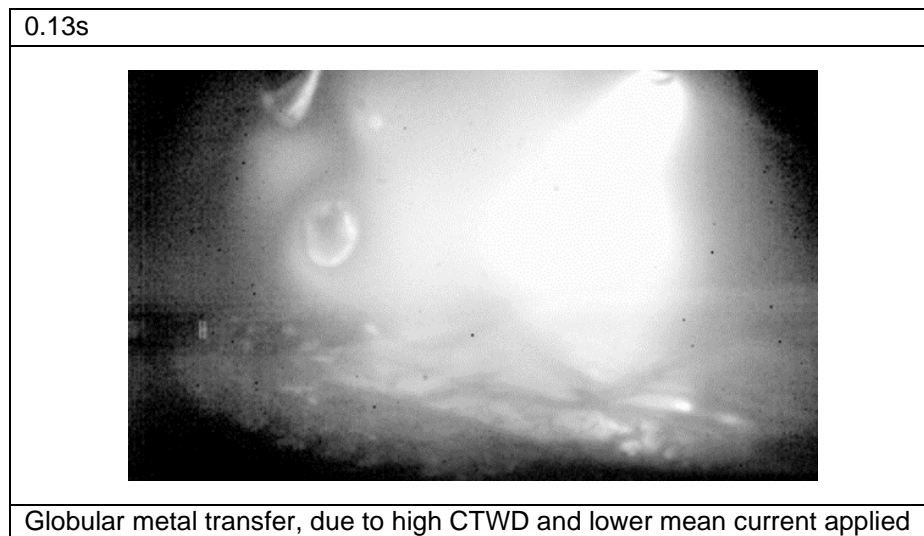


Figure 3-24 Weld pool behaviour using WFS of 5m/mins on each wire, TS of 20mm/s and 25mm CTWD

High CTWD increased the arc length, modifying the metal transfer from short-circuit to spray. A longer arc length, could also induce greater electromagnetic attraction on the arc, causing the metal to transfer axially. Hence, long arc lengths (CTWD) could produce erratic and preferential globular metal droplet detachment as revealed by the high-speed video images in Figure 3-24.

High weld pool wave can be observed in Figures 3-25 with the wires resting momentarily in the weld pool. Figure 3-26 show different stages of metal transfer cycle. Note the weld pool oscillation which could have been triggered by the pressure of the arc explosion, as current rises from the background cycle.

This suggest that metal transfer by short circuit could dominate (increase) as the weld pool volume increased through increase in total WFS of trail and lead wires.

Hence, the steady one-droplet-per-pulse (ODPP) metal transfer mechanism could have experienced some interruptions.

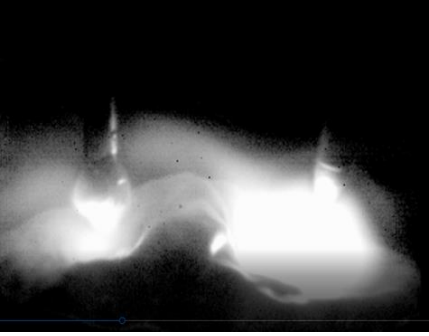

0.50s	1.15s
	
Lead wire in background current cycle and trail wire in peak current cycle, with high weld pool wave	Lead wire current rises, while trail wire short circuits momentarily in weld pool, with high weld pool oscillation

Figure 3-25 Weld pool behaviour, using WFS of 10m/mins on each wire, TS of 20mm/s and 20mm CTWD

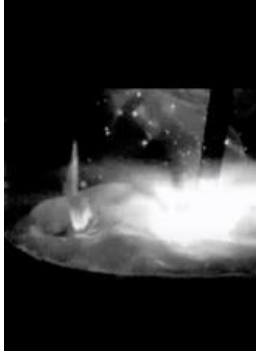



1.50s	1.52s	1.57s	1.58s
			
Lead wire in weld pool, approaching background current cycle, as trail wire current rises, with high weld pool wave	Lead wire resting momentarily in weld pool, as trail wire approaches background current cycle	Lead wire current rising to peak cycle, as trail wire current rescinding, showing high weld pool wave	Lead wire in peak current mode, as trail wire current rises, with high weld pool oscillation

Figure 3-26 Weld pool behaviour, using WFS of 10m/mins on each wire, TS of 20mm/s and 20mm CTWD

Local bulging of the molten metal can be observed, which is attributed to the horizontal components of the arc pressures of the two arcs, which drives the molten metal to flow towards the middle between the two wires (*Goecke, S. et al., 2001*). It was also suggested that for optimum welding performance, the

suitable WFS of the trailing wire should be about 1 – 2 m/min greater than the WFS of the leading wire (Huang P. F. et al., 2012).

3.9 Multi-layer deposition process study

The focus of the preceding single weld bead studies was to maximise deposition rate. Hence, the mid to high WFS settings were considered for the tandem process study. This present investigation, however, was focused on maximising the surface quality of WAAM part. Hence, the lower WFS settings were considered in this stage of the experiment.

Here, the influence of GMAW process parameters on multi-layer wall responses, including surface quality and metal deposition efficiency of WAAM structure, was studied using both Tandem-wire and Single-wire (SW) GMAW processes.

A series of preliminary experimental studies were conducted, to establish suitable deposition conditions, that can be used for the actual multi-layer wall deposition study.

Firstly, a single bead on plate study was conducted to provide suitable range of WFS and TS parameters, for producing acceptable bead geometries; bearing in mind that the tandem-wire process has a smaller parameter window compared to single-wire process (Goecke, S. et al., 2001).

Five WFS settings were selected to establish the tandem-wire parameter range, by progressively increasing TS, while the other parameters were kept constant. After deposition, the surfaces of the beads were visually inspected for defects and weld quality. The beads were termed acceptable (A), when they showed continuous and smooth surfaces, without defects such as humping, undercut, porosity, lack of fusion and excessive melting, or they were otherwise rejected and termed defective (D). Where the TS was too low for a give WFS and impracticable to deposit a bead, it was termed (n/a).

Furthermore, studies were conducted to evaluate the effect of CTWD on instantaneous arc characteristics, bead geometry and surface quality, using tandem-GMAW, with series and parallel configurations. Thereafter, the effect of

arc correction, CTWD and TS on arc characteristics, bead geometry and quality were studied using single-wire GMAW process. The experiments were performed using the set-up detailed in section 3.1

3.9.1 Determination of Tandem-GMAW lower deposition process parameter range for series and parallel configurations

This section presents a report of preliminary study conducted to investigate the operational range of lower WFS setting for Tandem-GMAW series and parallel wire configurations.

During the experiment, the torch TS was progressively increased for a given WFS setting until defective and/or poor bead formation occurred.

3.9.1.1 Determination of tandem-GMAW lower limit process parameter settings for series and parallel wire configurations

Tandem-GMAW series and parallel wire configurations were utilised in this study.

The range of WFS settings utilised for each wire were- (2.5, 3, 3.5, 4, 4.5 and 5) m/mins. CTWD of 20mm was maintained during the trials and the interpass temperature was limited to 75°C.

The deposited beads were visually examined and categorised as either- Acceptable (A) or Defective (D). The results of the trial are summarised in Table 3-6.

Table 3-6 Tandem-GMAW parameter range for (a) Parallel wire setup (b) Series wire setup

Tandem-GMAW (Parallel wire configuration)														
WFS wires (A/B) m/mins	Travel speed (mm/s)													
	2	3	4	5	6	7	8	9	10	11	12	13	14	15
2.5/2.5	n/a	D												
3/3	D	A	A	A	D	D	D							
3.5/3.5	D	A	A	A	A	A	D	D	D					
4/4	D	D	A	A	A	A	A	A	D	D	D			
4.5/4.5	D	D	A	A	A	A	A	A	A	D	D	D	D	D
5/5	n/a	n/a	D	A	A	A	A	A	A	A	D	D	D	D

(a) Parallel wire setup

Tandem-GMAW (Series wire configuration)																	
WFS Wires (A/B) m/mins	Travel speed (mm/s)																
	2	3	4	5	6	7	8	9	10	11	12	13	14	15	16	18	20
2.5/2.5	n/a	D	D	D	D												
3/3	D	D	A	A	A	D	D	D									
3.5/3.5	D	D	A	A	A	A	A	A	D								
4/4	D	D	D	A	A	A	A	A	A	D	D						
4.5/4.5	D	D	D	A	A	A	A	A	A	A	A	A	D	D			
5/5	n/a	n/a	D	A	A	A	A	A	A	A	A	A	A	A	A	A	A

(b) Series wire setup

The deposited beads were acceptable when the surfaces show continuous smooth and uniform weld profile, devoid of visual defects or significant spatter. The unacceptable beads showed discontinuous, uneven, and rough appearance; or exhibited physical defects like undercut, humping, underfill or overfill. The deposited beads were also classed as defective where erratic arc and unstable deposition occurred, leading to poorly formed bead geometry.

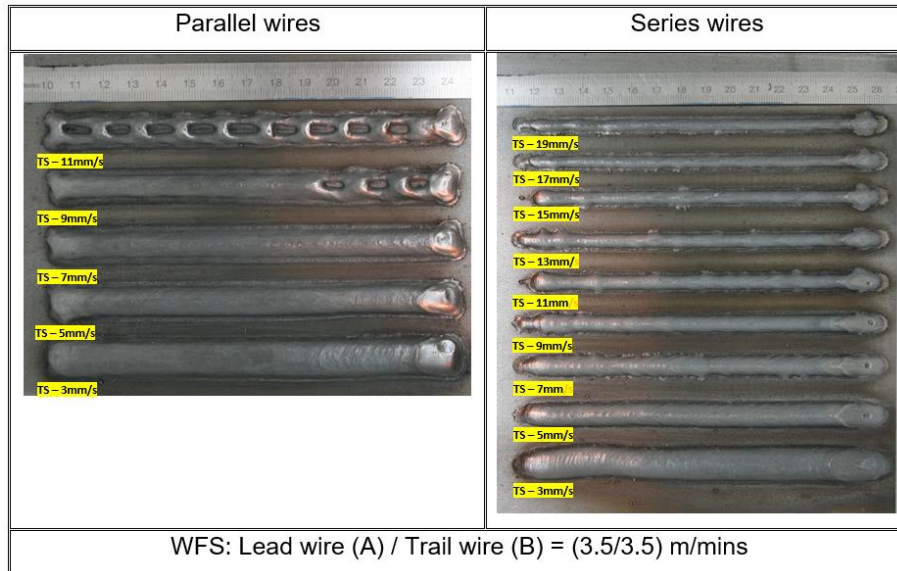
3.9.1.2 Susceptibility of Tandem-GMAW series and parallel wire configurations to defect formation, with increasing TS

The formation of acceptable bead profile and defects, with increase in TS, using tandem-GMAW process, with the wires configured in series and parallel are presented with the surface morphology of single weld bead deposits. Figure 3-27a and 3-27b, show the appearance of weld beads produced using two WFSs of (a) 3.5m/mins and (b) 5m/mins, respectively. The TS was gradually increased, while other parameters were kept constant.

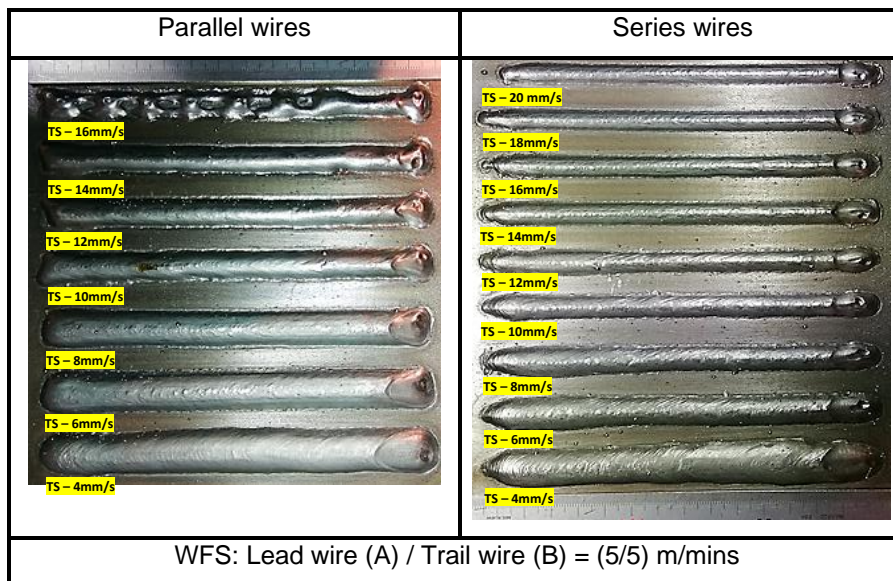
In Figure 3-27(a), using tandem-GMAW parallel wires setup, it can be seen that acceptable bead profile were produced up to 7mm/s TS. Formation of unstable and poor bead profile with appearance of humping defect occurred from TS of 9mm/s.

For the series wire setup in Figure 3-27(a), acceptable beads profiles were produced up to 9mm/s TS. Observation of the beads deposited with further

increase in TS beyond 11m/min, showed poor bead profiles, due to inadequate melting and fusion of the wires. This is attributable to insufficient thermal energy due to reduction in heat input at the higher TS utilised (Sun, L. *et al.* 2020).



(a)



(b)

Figure 3-27 Surface appearance of bead profiles deposited with lead and trail wires WFSs of (a) (3.5 and 3.5) m/mins and (b) (5 and 5) m/mins

In Figure 3-27(b), using tandem-GMAW parallel wires orientation, formation of poor bead profiles began from 12mm/s TS. Undercut defect occurred from TS of

14mm/s, and significant discontinuity (humping defect), developed from TS of 16mm/s.

Figure 3-27 show humping defect formed in high-speed Tandem-GMAW process, using parallel wire configurations. The humping morphology is characterized by open, unfilled spots in between the humped beads. The front of the molten pool exhibits a large depression known as the gouging region. It has been found that humping tends to occur when the travel speed exceeds a certain critical value (DebRoy, T. et al., 2018).

Using the tandem-GMAW series wire setup (Figure 3-27b), acceptable beads profiles were produced up to TS of 20mm/s. Visual observation of the process showed increased arc stability with minimal spatter from the mid TS levels. The lower TS values of 4 and 6 mm/s produced irregular bead profiles and generated enormous fumes, due to excessive deposition and accumulation of weld metal per unit area.

The cross sectional macrographs of representative etched specimens are shown in Figure 3-28. The samples were deposited with 4.5m/min WFS on both the lead and trail wires.

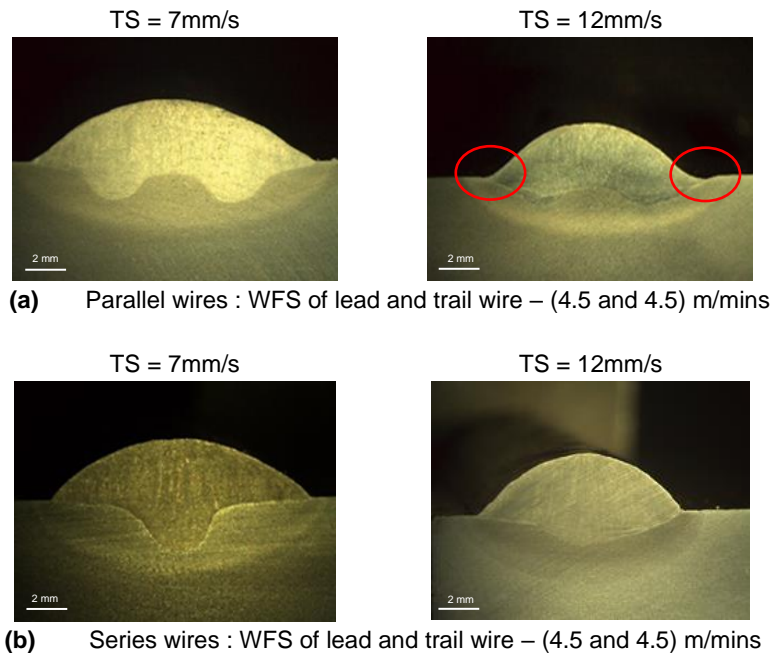


Figure 3-28 Macrographs of etched samples, deposited using WFS of 4.5m/mins, showing undercut defect formation, using Tandem-GMAW wire configurations of (a) Parallel (b) Series

In Figure 3-28(a), undercut defect can be observed on the bead profile deposited with TS of 12mm/s, using tandem-GMAW parallel wire set-up. But in Figure 3-28(b), the bead produced using tandem-series wire set up, at TS of 12mm/secs, showed acceptable bead profile.

Hence, it can be concluded that tandem-GMAW parallel wire orientation is more susceptibility to defective bead formation at higher TS, compared to series wire orientation.

This is perhaps due to higher interfacial tension and viscosity of liquid metal at the edges of the weld pool, owing to increased thermal cooling effect, caused by spreading away of the arc from the centreline of the molten pool (Kazanas, P. *et al.*, 2012)

Also, the weld pool of the parallel wire set-up, is relatively larger in width, but smaller in height (reinforcement), compared to the series wire set up. Hence, a situation in which the dynamic aspect ratio of the weld decreases, could occur,

and increase the tendency for undercut formation, where less weld metal could exist in the centre line of the bead, which can lead to underfil at higher levels of TS, if the region can not be replenished by the metal in time, which could worsen with increased surface tension as a result of higher thermal gradient (Zhenyang Lu and Pengfei Huang, 2011).

3.9.2 Effect of CTWD, on generated heat input, bead geometry and surface quality, using tandem-GMAW parallel and series wire configurations

The effect of change in CTWD on the current and voltage characteristics, bead geometry and surface quality, was investigated using tandem-GMAW series and parallel wire configurations. A WFS of 5m/mins was applied to the lead and trail wires and the TS was maintained at 10mm/s. The study was performed using the equipment set-up described in section 3.1 and deposition parameters detailed in Table 3-7.

Table 3-7 Pre-set deposition conditions utilised for investigating the effect of change in CTWD for Tandem-GMAW parallel and series wire configurations

Process wire condition	WFS (m/mins) (Lead/Trail)	TS mm/s	CTWD (mm)					Gas flow rate (l/mins)
			17	19	21	23	25	
Tandem-GMAW (Series wire)	5/5	10	17	19	21	23	25	30
Tandem-GMAW (Parallel wire)	“	“	“	“	“	“	“	“

The results of the experiment are presented as follows

3.9.2.1 Results of effect of change in CTWD of parallel and series wire configurations, on transient arc characteristics

Figure 3-29 show the plots of effect of CTWD on average heat input of single weld deposits, when the wires were arranged in series and parallel to each other.

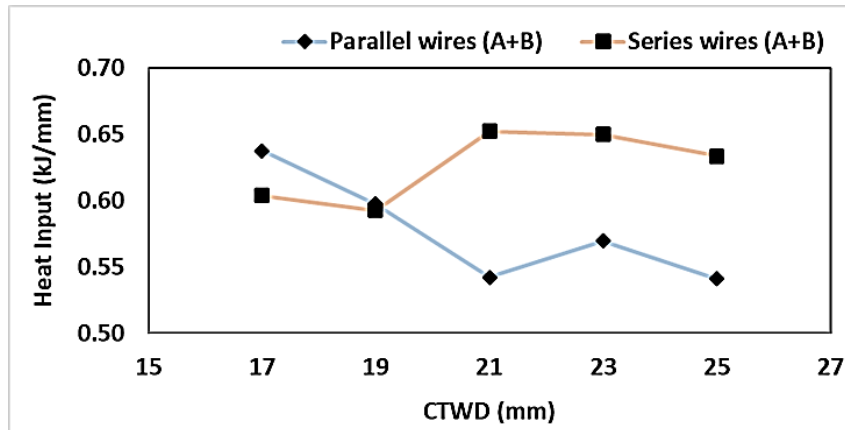


Figure 3-29 Effect of CTWD, on generated heat input using tandem-GMAW series and parallel wire configurations. [Standard error of plots (Parallel wires = 0.018; Series wires = 0.012)]

From Figure 3-29, using tandem-GMAW (series wire configuration) showed that, as CTWD was increased from 17mm to 21mm, a 7.7% increase in heat input to 0.65kJ/mm was produced. Further increase in CTWD from 21mm to 25mm, produced 3.1% decrease in heat input to 0.63kJ/mm. The reason for this observation is perhaps because the wires were in effect, short-circuiting in the weld pool, with the low CTWD, hence an initial rise in heat input, with increase in CTWD, indicating a change from dip to spray arc mode.

For Tandem wire (parallel configuration), increase in CTWD from 17mm to 21mm, produced 15% decrease in heat input to 0.54kJ/mm. Further increase in CTWD from 21mm to 25mm, produced no significant change in heat input

As earlier explained in section 3.5.1.1, the reason for the decrease in heat input, could be attributed to the effect of resistive heating of the wires, with increase in CTWD.

In general, the tandem-GMAW series wire set-up, produced a higher heat input, compared in parallel wire orientation. This could be due to the fact that the dynamic arc length could be effectively lower, due to effect of higher weld-metal build-up underneath the wires (higher BH).

3.9.2.2 Results of effect of change in CTWD of parallel and series wire orientation, on bead profiles and deposited bead quality

Figure 3-30 shows the plots of BW, BH, BP and BA, as a function of increasing CTWD, for parallel and series wire configurations

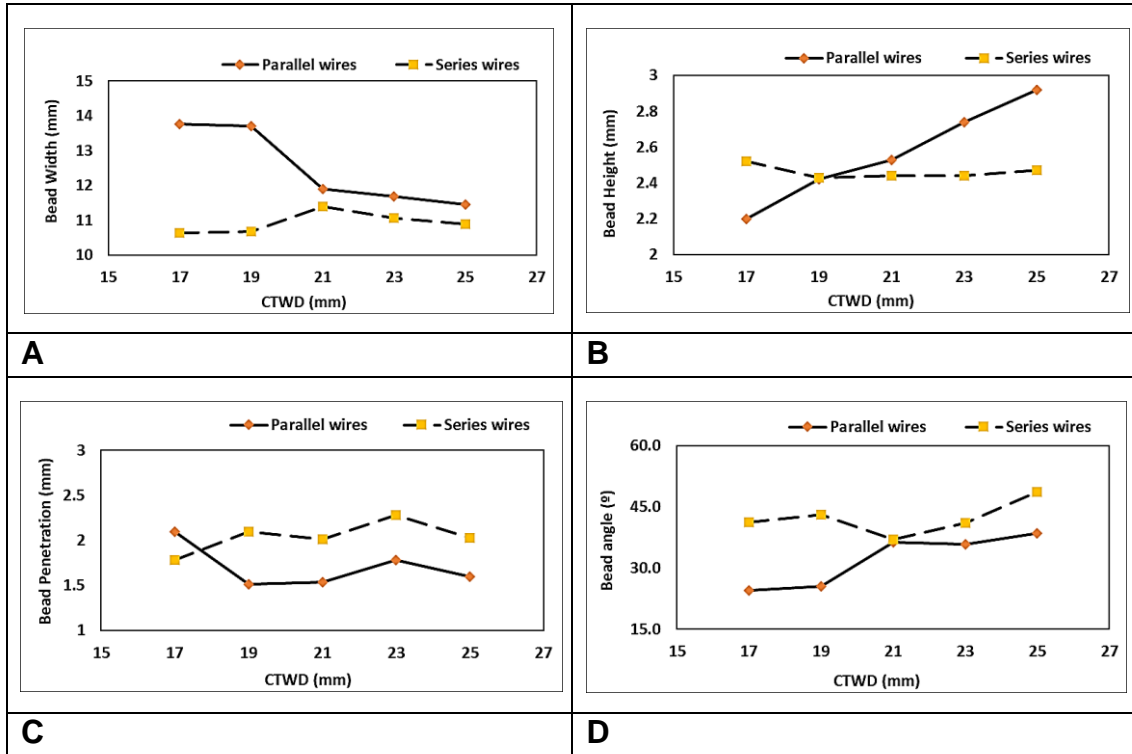


Figure 3-30. Effect of change in CTWD of series and parallel wires configuration on lead and trial arc characteristics (a) current (b) voltage (c) heat input

It is apparent from figure 3-30(a), that the BW produced using series wire configuration, increased initially by 7.5%, from a minimum of 10.6mm to 11.4mm, with increase in CTWD from 17mm to 21mm. Further increase in CTWD to 25mm, produced 4.4% decrease in BW. The initial increase in BW could be due to a change in metal transfer mode, from short-circuit to spray transfer, with increased torch stand-off.

The BW obtained with Tandem-GMAW parallel wire set up, initially decreased by 16.7%, with increase in CTWD, from a maximum BW of 13.8mm at 17mm CTWD to a minimum of 11.9mm at 21mm CTWD. A further increase in CTWD to 25mm, produced 3.9% decrease in BW.

In Figure 3-30(b), the BH of series wire set up appears relatively unchanged as the CTWD was increased, but the BH for the parallel wire set up increased significantly by 32.7%, from a minimum of 2.2mm at 17mm CTWD, to a maximum of 2.92mm at 25mm CTWD.

In Figure 3-30(c), BP of series wire set up, increased by 12.9%, from a minimum BW of 1.78mm at CTWD of 17mm, to 2.01mm at 19mm CTWD. Further increase of CTWD to 25mm, produced insignificant change in BP to 2.03mm.

BP for parallel wires set-up decreased by 26.7%, from a maximum of 2.1mm at 17mm CTWD, to 1.54mm at 21mm CTWD. Further increase in CTWD to 25mm, produced insignificant change in BP to 1.6mm. With long CTWD and arc length, PD decreased due to relatively low current density and arc pressure reaching the substrate.

Figure 3-30(d) shows that the series wire set up produced a minimum BA of 37° at a CTWD of 21mm, then increased to a maximum BA of 48.7° at CTWD of 25mm. The parallel wire set up shows a minimum bead angle of 24.5° at CTWD of 17mm, thereafter, the BA increased gradually to a maximum of 38.6° at 25mm CTWD.

The study gives an indication of how sensitive process parameters and processing conditions are to variations in CTWD which may naturally occur during manufacturing. In general, with increase in CTWD, tandem-GMAW series wire configuration, was observed to produce a lower BW and BH, but a higher BP and larger BA, compared to tandem-GMAW parallel wire set-up.

The resistive heating (high CTWD) produced a more significant effect when parallel wire set-up was utilised, compared to the series wire configuration. This can be seen with the steady increase in BH with use of parallel wire configuration (Figure 3-30b).

But the increase in CTWD, appeared to produce a lesser resistive heating effect, with the use of series wire configuration. This could probably be because the series wires were frequently in contact or near to the weld pool.

Effect of changes in CTWD, on weld bead quality and fusion characteristics, could also be seen from the surface appearance of the deposited beads displayed in Figure 3-31. The transverse macro sections showing the effect of change in CTWD of parallel and series wire orientation, on bead profiles and deposited bead quality are shown in Appendix E.

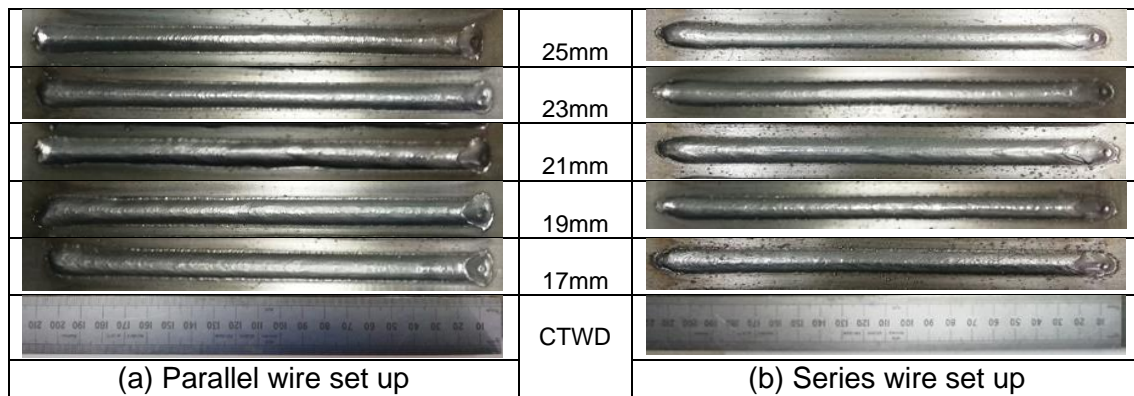


Figure 3-31 Weld bead surface appearances produced at different CTWD, and TS of 10mm/s, using Tandem-wire (a) Parallel configuration and (b) Series configuration.

Significant spatter generation occurred with the series wire configuration as seen in Figure 3-31(b), which could be attributed to the frequent short-circuiting and explosion of weld pool during molten metal transfer.

The dynamic response to variations in CTWD appeared different in both tandem-GMAW series and tandem-GMAW parallel wire configuration. The effect of CTWD on bead characteristics (such as BW and BH), was more significant with tandem-GMAW parallel wire configuration. Hence one can assume that the increase in BH was also influenced to some degree, by an increase of wire burn-off rate (BR), caused primarily by the resistance heating terms in equation (3-8).

Whereas, the effect was rather insignificant using tandem-GMAW series configuration, which could be attributable to possible frequent short-circuiting of the wires in the weld pool, hence the effect of resistive heating was kept nearly unchanged.

3.9.3 Effect of arc correction and CTWD on deposited bead quality, geometry and heat input generated, using single-wire GMAW process

Single-wire GMAW process was introduced in this stage of the investigation and a comparative evaluation of surface waviness produced using single wire and tandem-wire GMAW process was conducted in later sections.

The single-wire study was conducted using the Tandem-GMAW system, after disengaging the trail wire feeder, while connecting only the lead wire feeder. The tandem-wire GMAW system then functioned essentially as a single-wire GMAW system.

3.9.3.1 Effect of arc correction settings on surface quality of deposited bead, using single-wire GMAW process

Preliminary trials were conducted to determine the effect of applying arc length and pulse correction settings, on the quality of the deposited bead, produced using SW-GMAW process. Figure 3-32 shows the beads deposited using 4m/mins WFS and 5mm/s TS, without and with the application of arc length and pulse correction settings.

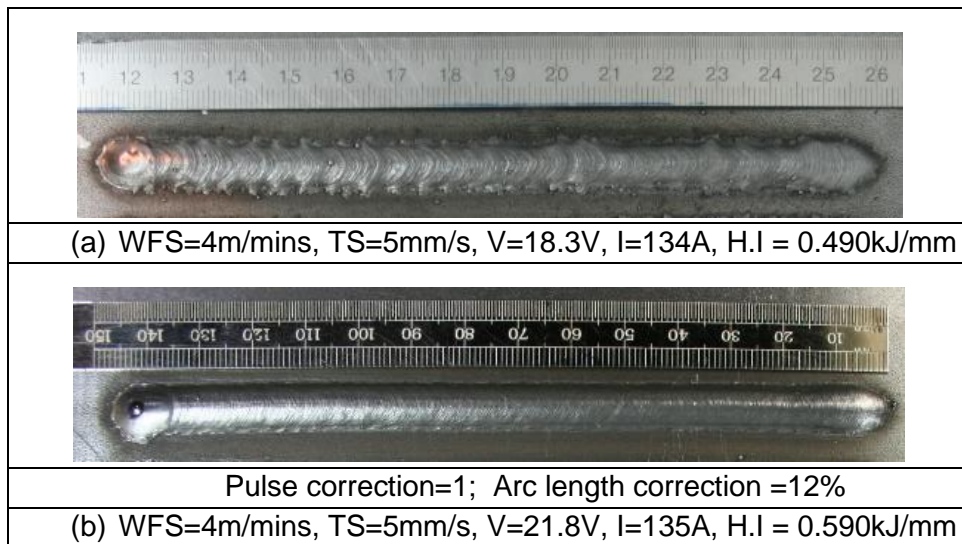


Figure 3-32 Examples of weld bead appearance produced using single-wire GMAW, with (a) without the use of arc and pulse correction (b) with use of arc and pulse correction

Comparison of Figure 3-32(a & b) clearly show a direct effect of arc length and pulse correction settings applied. The increase in arc length and pulse settings resulted in increased arc voltage and pulse duration respectively, which caused an increase in average instantaneous power per unit length, (heat input), and arc-spread. This effect is expected since the additional thermal energy enhanced the wire burn-off, increasing the fluidity and wetting of the weld metal, leading to improved fusion characteristics.

3.9.3.2 Effect of CTWD on geometry and surface quality of deposited bead, using single-wire GMAW process

The pre-set deposition parameters applied in this investigation are presented in Table 3-8 below

Table 3-8 Pre-set deposition conditions utilised in the study of CTWD and TS for Single-wire GMAW process

Process condition	WFS (m/mins)	CTWD mm	Travel speed, TS (mm/s)					Gas flow rate (l/mins)	Arc length correction	Pulse correction
			6	7	9	10	12			
Single wire	6	18	6	7	9	10	12	15	12%	1
	6	21	"	"	"	"	"	"		

The results of the experiment are presented graphically in Figure 3-33. It depicts the influence of TS, on the generated heat input and deposited bead parameters (BW & BH). with increase of CTWD from 18mm and 21mm, utilising SW-GMAW process.

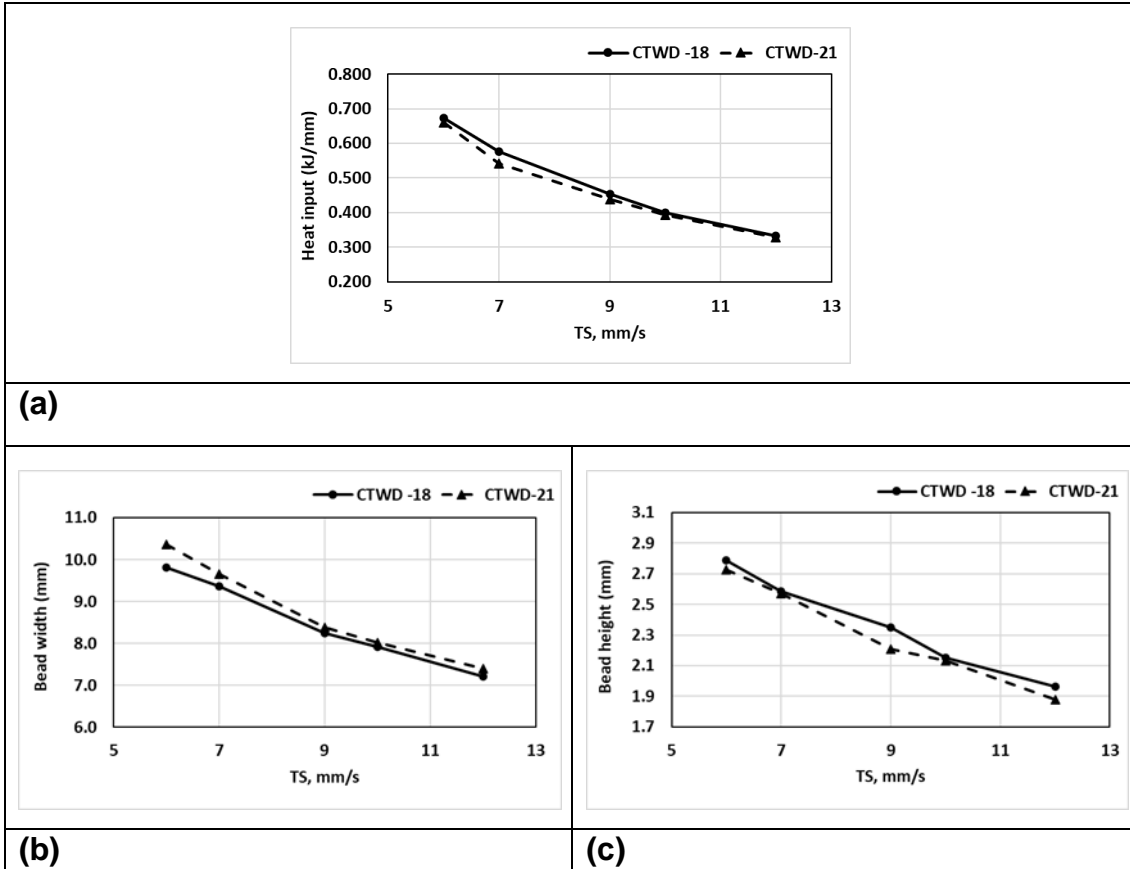


Figure 3-33 Effect of TS and CTWD on (a) Heat input (b) BW, and (c) BH, using SW-GMAW process

Figure 3-33(a) shows that heat input, decreased from a maximum of 0.674kJ/mm to a minimum of 0.333kJ/mm, with increase in TS from 6mm/s to12mm/s, using CTWD of 18mm. However, using 21mm CTWD, the heat input decreased from a maximum of 0.661kj/mm to a minimum of 0.329kj/mm, with increase in TS from 6mm/s to 12mm/s.

Hence, an increase in CTWD from 18mm to 21mm, resulted to a slight decrease in average heat input by 1.6%. This is attributed to the effect of resistive heating, contributing to the melting, due to heating of the extended wires (increased CTWD).

It can also be seen that a slightly larger BW and corresponding lower BH, was produced using 21mm CTWD, compared to CTWD of 18 mm. This in effect could be attributed to the relative spreading out of the arc, with increased of CTWD to 21mm.

Figure 3-33(b) clearly shows the significant effect of TS on BW and BH, with both values of CTWD. Increase in TS from 5mm/s to 12mm/s, produced a decrease in BH of 28.6% and 29.6% and corresponding decrease in BW of 26.3% and 28.8%, at CTWD of 18mm and 21mm respectively. This is attributed to the reduction in heat input and decrease in WFS/TS ratio, leading to decrease in the amount of metal deposited per unit length.

Figure 3-34 shows the surface appearance of the bead deposited using CTWD of 18mm and 21mm. Both beads produced using CTWD of 18 and 21 mm, show acceptable quality. But the bead produced using 21mm CTWD, showed a slight improvement in fusion characteristics, which could be attributed to enhanced burn off rate of the wire, owing to slight increase in resistive heating effect, on the extended wire. The rippling effect observed on the bead surface produced with the lower CTWD was eliminated with the use of the higher CTWD.

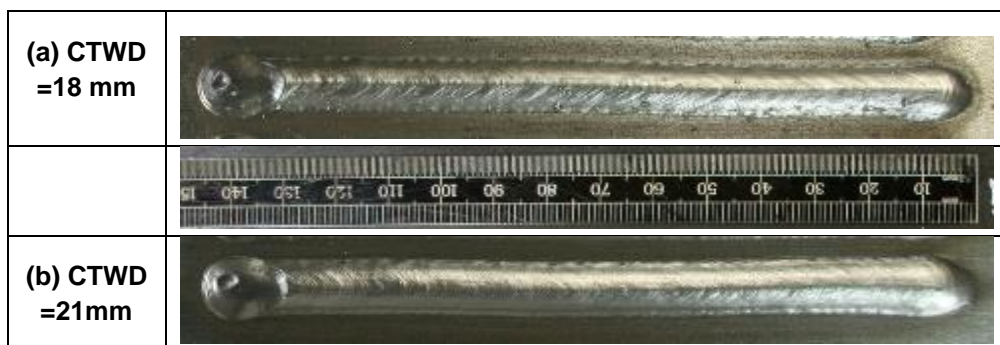


Figure 3-34 Morphology of weld bead surfaces produced using single-wire GMAW, with WFS= 6m/mins, TS = 7mm/s, and CTWD of (a) 18mm and (b) 21mm

The slight effect of CTWD on the weld bead quality of single layer deposits is expected since these results are directly associated with the metal transfer behaviour. To achieve optimum metal transfer conditions in GMAW-P process, it is important to ensure: (1) occurrence of stable metal transfer of droplets from the wire to the weld pool, (2) that the WFS is balanced with the burn-off rate to maintain a constant arc-length (Smati, Z., 1986).

Hence, controlled metal transfer characteristics, preferably one droplet per pulse (ODPP), should be always preserved in GMAW-P process, regardless of

changes in CTWD (Subramaniam, S. et al., 1999; Palani, P. K. and Murugan, N., 2006).

However, it should be noted that the weld bead and substrate fusion characteristics are highly influenced by CTWD. This is an important from a technical point of view because inaccurate predictions of the bead geometry during deposition can contribute to differential cumulative positioning errors in the horizontal distance between the welding torch and the part being manufactured.

Errors in CTWD are very likely to affect the processing conditions, and thus the final geometry and quality of the component produced.

3.10 Multi-layer wall deposition

Weld bead shapes and dimension are essential characteristics which determine the range of bead width that can be produced as well as surface quality of the built components. Thus, adequate selection and combination of deposition parameters is crucial to realising enhanced quality of both single-wire and tandem-wire WAAM parts.

Achievement of maximum build geometry for a given set of process parameters has a desirable effect on the build time and energy consumption because the required part thickness can be realised quicker (Griffiths, C. A. et al., 2016). Hence, the manufacture of large sized WAAM components would likely profits from use of bigger bead width and achievement of maximum effective wall width for a given set of deposition parameters, because it could significantly reduce WAAM costs.

In this section, the influence of primary parameters including WFS and TS, and the unique Tandem-GMAW secondary processing condition namely- wire configurations, on multi-layer wall responses including, effective wall width (EWW), average layer height (aLH), relative bead height increment (ΔH), standard deviation of average layer height (SdLH), SWav and MDE were evaluated. The evaluation was also conducted using single-wire GMAW process.

3.11 Experimental method for multi-layer wall deposition study

A total of 10 walls were built for this investigation, using a substrate of dimension 350x250x20 mm, as shown in Figure 3-35. Each of the wall consisted of ten (10) multi-layer deposits, 120mm in length and were deposited by travelling the torch in the leading direction. Interpass temperature was maintained at a maximum of 75°C during deposition and Ar/8%CO₂ was used as shielding gas during the trials.

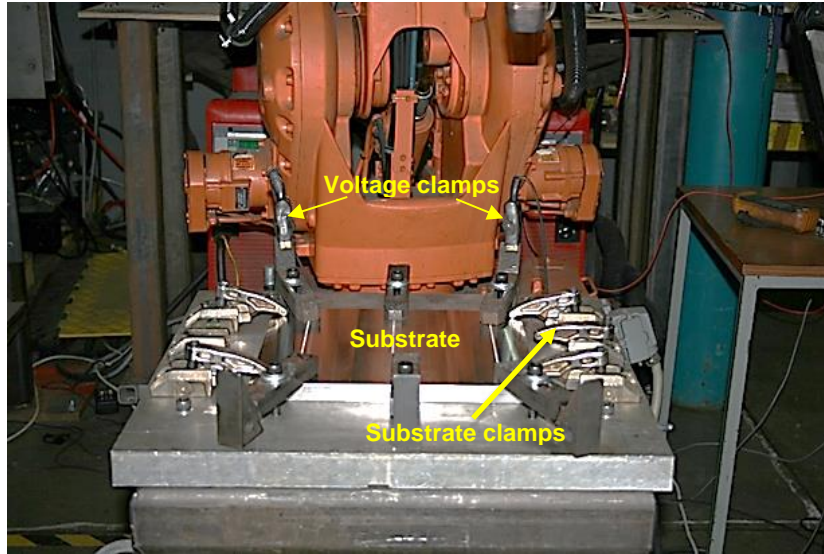


Figure 3-35 Experimental set-up

A schematic diagram of the deposition process is presented in Figure 3-36.

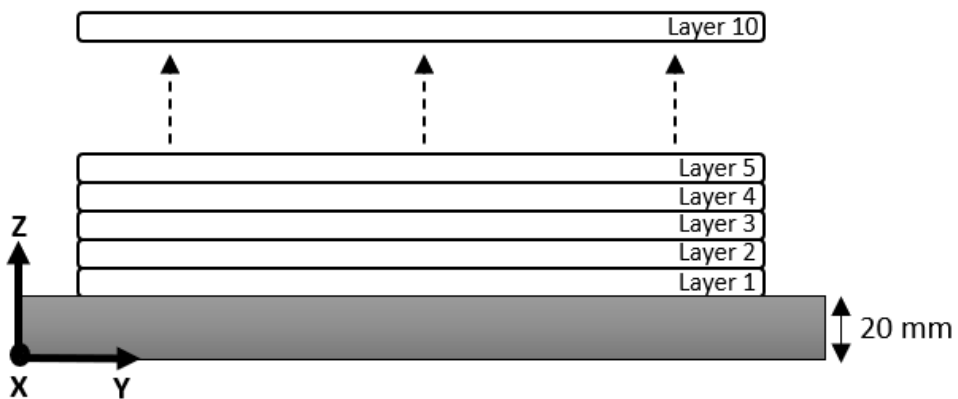


Figure 3-36 Schematic representation of the multi-layer wall deposition method

Parameter selection in this stage of the study was based on results obtained from the previous study in section 3.9.1. The nominal pre-set parameters and conditions used are presented in Table 3-9.

Table 3-9 Pre-set condition used to study multi-layer wall deposition

Deposition conditions	Wall No	Total WFS (m/mins)	TS (mm/s)	WFS/TS ratio
Tandem-wire (Series)	1	7	5	23.3
	2	7	7	16.7
	3	10	7.1	23.5
	4	10	10	16.7
Tandem-wire (Parallel)	5	7	5	23.3
	6	7	7	16.7
	7	10	7.1	23.5
	8	10	10	16.7
Single-Wire GMAW	9	7	5	23.3
	10	7	7	16.7

3.12 Results and discussion on multi-layer wall deposition study

The detailed pre-set process parameters used to study the multi-layer wall deposition and the measured wall responses are presented in Appendix F. Also examples of the 10-layer high walls deposited during this investigation are shown.

3.12.1 Results of effect of layer numbers and deposition process, on multi-layer wall characteristics

Investigate of the influence of layer numbers and deposition process namely single-wire (SW) GMAW, tandem-wire (series) and tandem-wire (parallel) set-up, on multi-layer wall characteristics, including relative bead height increment (ΔH), average Layer height (aLH) and standard deviation of layer height (SdLH), were conducted. The effect on other multi-layer wall responses, including WW, EWW, MDE and SWav were also evaluated, according to the pre-set parameters given in table 3-9.

3.12.1.1 Effect of layer numbers and deposition process, on relative wall height increment

The analysis was conducted using 7m/min WFS and WFS/TS of 23.3 and 16.7 as shown in Table 3-9.

Figures 3-37 show the plots of effect of layer numbers on ΔH , at different WFS/TS ratio, using a constant WFS of 7m/mins. The investigation was conducted for various walls built using single-wire GMAW and tandem-wire GMAW (series and parallel) configuration processes.

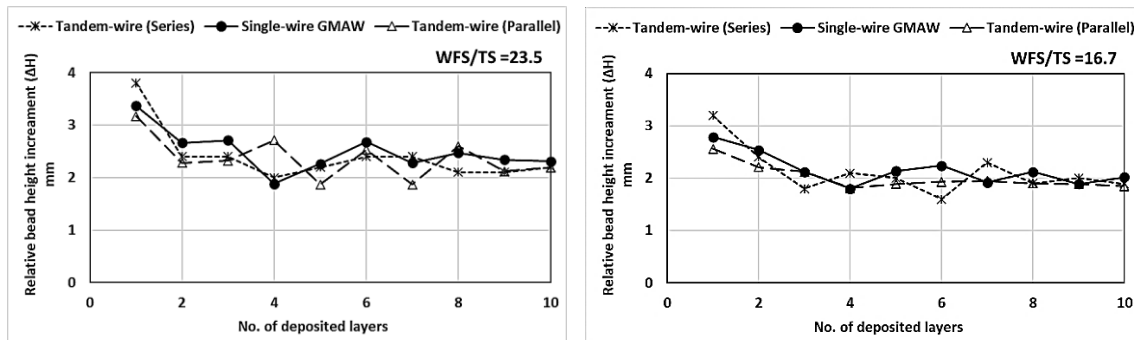


Figure 3-37 Influence of layer number and deposition processes on relative height increment, at 7m/min WFS, and WFS/TS of (a) 23.5 and (b) 16.7

It can be seen in Figure 3-37(a&b) that the maximum deviation in ΔH was achieved when the first layers were deposited. The reason for this observation is partly because the first layer was deposited on a large flat substrate, with a larger heat sink, which caused faster cooling of the first weld layer. This observation was also reported in the study by Almeida P.M.S. (2012).

Thereafter, ΔH decreased gradually as the layer number increased, tending to achieve a more stable condition as the deposition progressed. The largest ΔH was produced using Tandem-GMAW, series wire configuration, for both WFS/TS utilised in the study.

3.12.1.2 Effect of deposition process and WFS/TS on deposition stability/built consistency

The relative build consistency of the layer height during deposition has an effect on the arc stability and is also related to the deposition efficiency. This is because significant variations in the individual layer heights could produce large

differences in CTWD during deposition, leading to substantial variations in deposited metal per unit length between the layers.

This can consequently increase instability in metal deposition, leading to high spatter generation, loss of material, poor fusion characteristics and poor geometrical accuracy of the wall.

Standard deviation of the layer height (SdLH) measures how far apart the individual values of layer height are from the average layer height, and is related to the build accuracy and stability. SdLH was calculated and used as a measure of stability/consistency of the deposited bead height.

The test was conducted using 7m/min WFS and WFS/TS of 23.3 and 16.7 as shown in Table 3-9, and the results are presented in Table 3-10.

Table 3-10 Effect of deposition process and WFS/TS on average layer height (aLH) and standard deviation of Layer height (SdLH), using 10-layer high walls and WFS/TS of 23.3 and 16.7

Deposition Process	WFS (m/min)	WFS/TS	Avg. Layer height (aLH)	Stdev Layer height (SdLH)	Heat input (kJ/mm)
Single-wire GMAW	7	23.3	2.50	0.40	0.78
		16.7	2.16	0.30	0.56
Tandem-wire (Series)	7	23.3	2.43	0.51	0.79
		16.7	2.12	0.44	0.56
Tandem-wire (Parallel)	7	23.3	2.37	0.40	0.82
		16.7	2.01	0.23	0.59

From table 3-10, for the various deposition processes utilised, a decrease in WFS/TS produced a corresponding reduction in SdLH and aLH. The reduction in SdLH and aLH, with decrease in WFS/TS, could be attributed to the reduction in deposited metal per unit length, owing to increase of TS. The reduction in SdLH could perhaps be due to enhanced control of the relatively smaller weld pool volume, and optimum wetting and fusion characteristics. Hence, resulting in a more stable and consistent build up. with little or no weld metal overflow, compared to the higher WFS/TS (Xiong *et al.*, 2018).

It can be seen in Table 3-10, that tandem-GMAW parallel wire configuration, produced the overall smallest SdLH and aLH. But tandem-wire (series configuration), gave the highest SdLH, while single-wire GMAW produced the largest aLH, for the WFS/TS ratio utilised.

The highest SdLH obtained with the series wire configuration, could be because reheating of the weld pool by the trailing arc occurs, and probably over heating could occur. This causes the temperature of the weld metal to remain hot for a longer time, increasing the solidification period and providing sufficient time for gravity to influence the shape of the weld pool.

The parallel wire configuration enables faster solidification because of the two arcs placed side by side. No reheating of the weld pool occurs in this configuration enabling faster solidification and shorter weld pool which is less prone to instability and collapse. Hence, producing the lowest SdLH.

3.12.1.3 Effect of deposition process, on EWW, SWav and MDE of the multi-layer wall

The influence of single-wire GMAW, Tandem-wire (series configuraion) and Tandem-wire (parallel configuration) processes, on EWW and SWav and MDE in a 10-layer high wall are depicted in Figure 3-38.


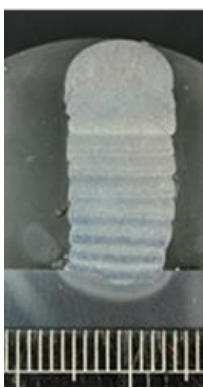
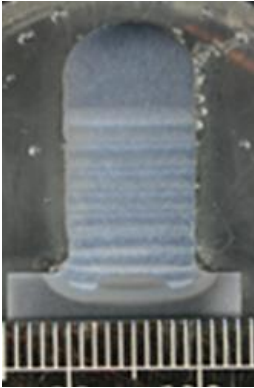
WFS- 7m/mins, (WFS/TS=16.7)		
Trial 10	Trial 2	Trial 6
		
EWW= 8.2mm	EWW=8.0mm	EWW=9.4mm
Single-wire GMAW	Tandem-wire (Series)	Tandem-wire (Parallel)

Figure 3-38 Influence of deposition process on EWW and Swav and MDE in a ten layer high wall of ten layers high, at 7m/min WFS

An obvious effect of the different deposition processes utilised in building the walls can be clearly observed from the transverse cross sections of the walls, built, using WFS/TS ratio of 16.7 and WFS of 7m/mins.

Tandem-wire (parallel configuration), produced the largest EWW, MDE and lowest SWav.

3.12.1.4 Effect of WFS/TS ratio and deposition process, on deposited WW and EWW

This section reports the effect of WFS/TS on deposited WW and EWW, using single-wire GMAW, tandem GMAW (series wires) and (parallel wires) processes. The pre-set deposition conditions used are detailed in Table 3-9.

Figure 3-39(a) and 3-39(b), show the results of the experiment conducted using WFSs of 7m/mins and 10m/mins respectively.

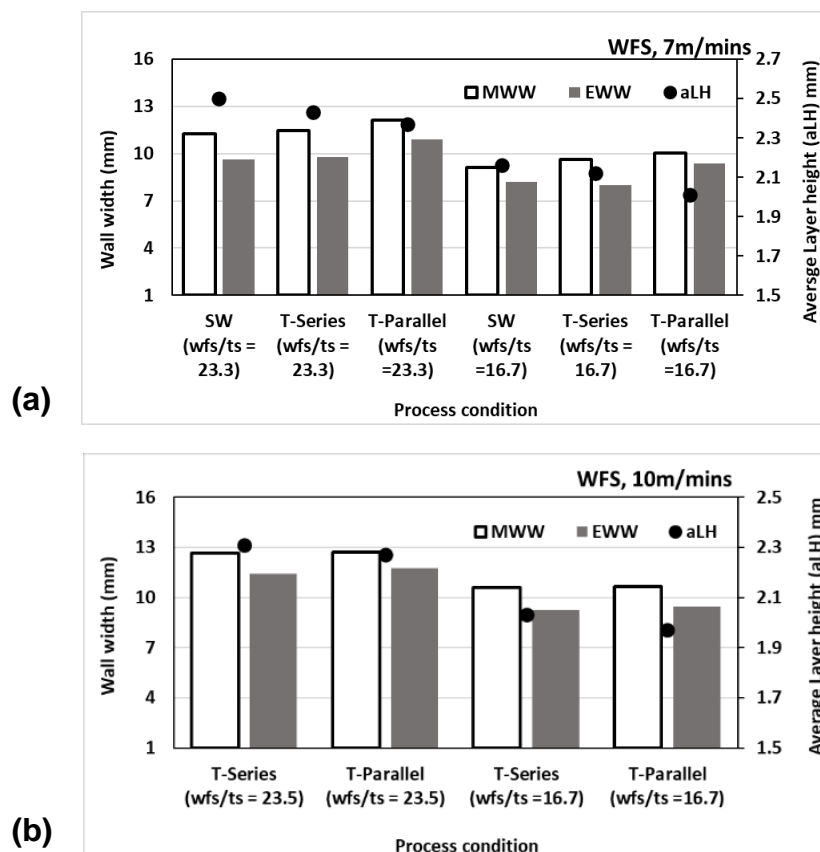


Figure 3-39 Effect of WFS/TS ratio on MWW and EWW of multi-layer walls, deposited using Single-wire GMAW, Tandem-wire (series) and Tandem-wire (parallel) processes, at WFS of (a) 7m/mins and (b) 10m/mins

Figures 3-39(a&b) showed that the WW and EWW produced using the different processes, are significantly influenced by the WFS/TS ratio utilised and decreased with decrease in WFS/TS ratio. This can be attributed to the reduction in heat input, at higher TS, leading to a decrease in deposition rate per unit layer length (Kazanas, P. *et al.*, 2012). Hence, WW and EWW showed an inverse relationship with aLH.

Figure 3-39(a) shows the result obtained at a constant WFS of 7m/mins, using the three deposition processes. SW-GMAW process produced the largest aLH of 2.5mm, but the smallest WW and EWW, whereas tandem-wire (parallel configuration), produced the smallest aLH of 2.01mm, but largest WW and EWW.

Although the same total WFS was applied to the different GMAW processes. however, the molten metal reheating and arc spreading effects, unique to the series wire and parallel wire processes respectively, does not occur in SW-GMAW process. Hence, the dynamic aspect ratio of the bead profile produced using the single wire process is expected to be higher, compared to the tandem wire processes.

Similarly, Figure 3-39(b) shows the result of the investigation conducted using tandem-wire (series) and tandem-wire (parallel) set ups, at constant WFS of 10m/mins. It is also clear that the largest WW, EWW and smallest aLH were achieved with tandem parallel wire configuration, compared to tandem series wire configuration.

3.12.2 Effect of TS, WFS and deposition process on surface SWav and EWW of the multi-layer walls

Surface waviness is a unique feature of the lateral wall of parts built using the WAAM process, the higher the SWav, the more material that will be removed to achieve the finished quality of the part (Dahat, S. *et al.*, 2020) and this has a determinant implication on the manufacturing cost of the final product.

The surface waviness was measured perpendicular to the torch travel direction, as described in section 3.3.3. This investigation was carried out to clarify the inter-dependence between the surface quality characteristics and the deposition

process parameters of WFS and TS, for single-wire (SW) and tandem-wire processes. Ten (10)-layer high walls were deposited for the study, using the pre-set process parameters given in Table 3-9.

3.12.2.1 Effect of travel speed and deposition process on SWav and EWW, at 7m/mins WFS

The effect of TS on SWav and EWW of multi-layer walls, deposited using a WFS of 7m/mins, for SW-GMAW, Tandem-wire (series) and tandem-wire (parallel) deposition processes is shown in Figure 3-40.

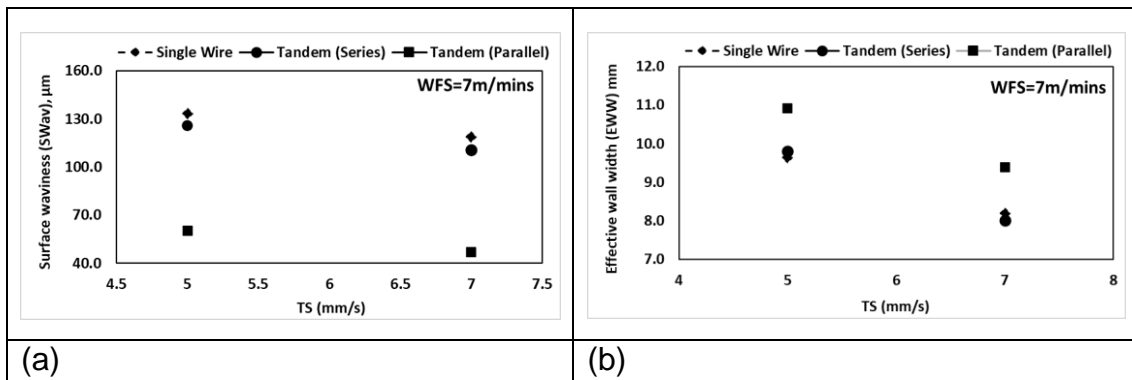


Figure 3-40 Effect of TS on (a) SWav and (b) EWW, at a constant WFS of 7m/mins

It can be observed in Figure 3-40(a) that using a WFS of 7m/mins, SWav decreased as TS was increased from 5mm/s to 7mm/s; while Figure 3-40(b) showed that EWW of the walls decreased with the increase of TS. This can be attributed to the reduction in the deposited weld metal per unit length, and hence a decrease in the layer height at the faster TS, leading to a less protruding “staircase” effect. In addition, the relatively lower heat energy could produce a more viscous and controllable weld pool volume, giving rise to a more accurate layer deposition, with little or no weld metal overflow, compared to the lower TS (Xiong *et al.*, 2018).

The Tandem-GMAW parallel wire configuration produced the lowest SWav and highest EWW. which is attributed to the improved spreading and wetting behaviour of the weld pool, by reason of the side-by-side configuration of the wires. Also, the configuration helps to minimise/avoid the disturbance from the trailing wire, on the weld metal deposited by the leading wire and vice versa,

through reduced weld pool turbulence. The single-wire GMAW process produced the largest SWav, which is expected since it also produced the largest aLH and consequently, a more protruding staircase effect.

The surface appearance of the built walls is displayed using the macrographs cross-sections in Figure 3-41.

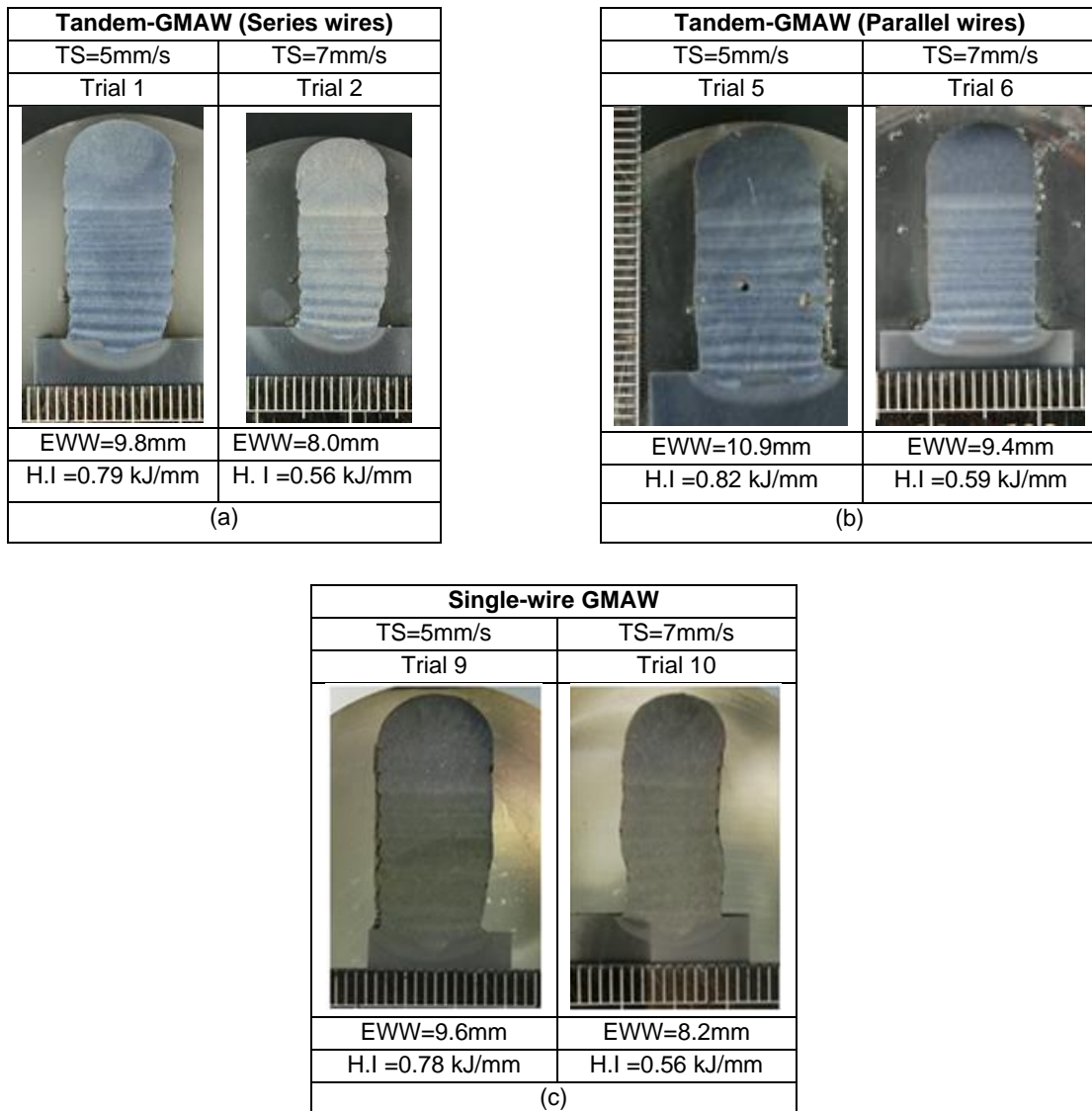


Figure 3-41 Cross-sectional macrographs of wall, showing effect of TS on EWW and SWav at 7m/mins WFS, for (a) Tandem-wire (Series) (b) Tandem-wire (Parallel) (c) Single-wire GMAW

The effect of increase in TS from 5mm/s to 7mm/s and deposition processes, on the surface quality of the walls is clearly noticeable. The optimum surface quality

at a constant WFS of 7m/mins, was produced with the higher TS and using tandem-wire parallel configuration.

3.12.2.2 Effect of travel speed and deposition process on SWav and EWW, at WFS of 10m/mins

The effect of TS on SWav and EWW of multi-layer walls, deposited using a higher WFS of 10m/mins, for Tandem-wire (series) and Tandem-wire (parallel) deposition processes is shown in Figure 3-42.

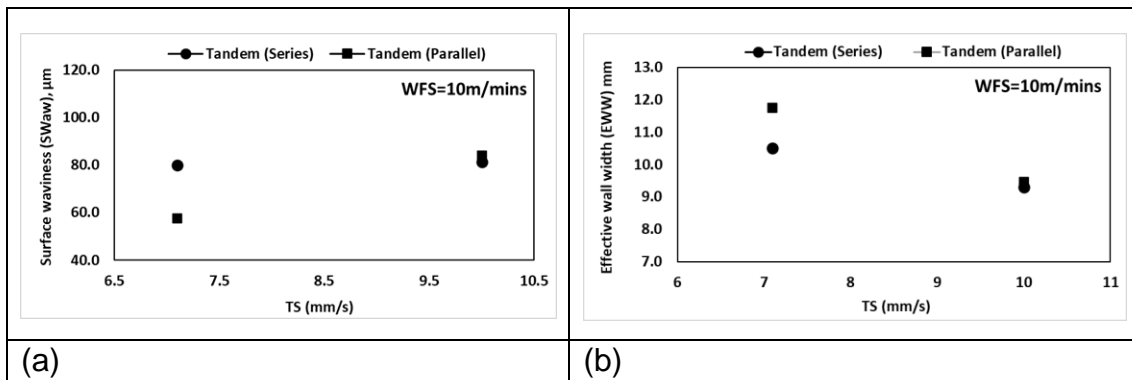


Figure 3-42 Effect of TS on SWav and EWW, at a constant WFS of 10m/mins

The result showed that using a higher WFS of 10m/mins and increasing the TS from 7.1mm/s to 10mm/s, produced an increase in SWav, Fig. 3-42(a); while the EWW decreased, Fig. 3-42(b)

The deterioration in the surface quality of the walls can be attributed to perhaps decreased fluidity of the molten metal, due to the reduced heat energy. At the higher TS, there is possibly insufficient time for adequate wetting and redistribution of the molten metal to guarantee satisfactory fusion between successive layers before the occurrence of solidification. Also, increased arc instability with increased TS, could have been a factor, owing to the spatter observed on the side walls (Xiong, J *et al.*, 2018).

The effect of increase in TS, at 10m/mins WFS, could also be observed through macrograph transverse cross-sections of the wall features, displayed in Figure 3-43, and built using Tandem series wire and parallel wire deposition configurations.





Tandem-wire (Series)		Tandem-wire (parallel)	
TS=7.1mm/s	TS=10mm/s	TS=7.1mm/s	TS=10mm/s
Trial 3	Trial 4	Trial 7	Trial 8
			
EWV=11.4	EWV=9.3	EWV=11.8mm	EWV=9.5mm
0.81kJ/mm	0.38kJ/mm	0.82kJ/mm	0.59kJ/mm
(a)		(b)	

Figure 3-43 Influence of TS on SWav and EWW of walls, deposited using (a) Tandem-wire, series set up (b) Tandem-wire, parallel set-up, at 10m/mins WFS

A noticeable deterioration in surface quality of the wall can be clearly observed when TS was increased from 7.1mm/s to 10mm/s, using the higher WFS of 10m/mins. The increase in deposition WFS, is also accompanied with high TS. The resulting low energy input per unit length of weld metal (heat input), perhaps limited the capability to melt both the filler and previously deposited weldment.

Kazanas, P. et al. (2012), found in their study that travel speed was the main determinant of surface quality, during the WAAM manufacture of inclined and horizontal wall features. They suggested that low WFS (current levels), and relatively low TS, which gives sufficient time for the redistribution, wetting and flattening of the melt pool, is generally beneficial and preferred for achieving better surface finish (Tian, Y. et al., 2017; Xiong, J et al., 2018).

3.12.3 Effect of WFS, on SWav and EWW, at constant WFS/TS ratio

The applied WFS has a direct linear relationship with the mean current and the arc energy. Holding the WFS/TS ratio constant keeps the heat input constant. Hence a constant amount of material is deposited per unit length, at constant WFS/TS ratio (Kazanas, P. et al., 2012).

Here, investigations were carried out to evaluate the effect of WFS and deposition processes on resulting SWav and EWW, in the manufacture of 10-layer high multi-pass walls, using Tandem-wire GMAW processes. It was conducted at a constant WFS/TS ratio, using WFSs of 7m/min and 10m/mins. The pre-set deposition conditions utilised is given in Table 3.9.

3.12.3.1 Effect of WFS on SWav and EWW, at WFS/TS of 23.5

This section evaluates the effect of WFS on SWav and EWW, at WFS/TS ratio of 23.5. The analysis was conducted using Tandem-wire (series and parallel) configurations, and deposited wall numbers 1,3,5 and 7, in table 3-9. The result is presented in Figure 3-44.

The result showed that at a constant WFS/TS of 23.5, SWav of the built walls decreased with increase in WFS from 7m/mins to 10m/mins for the tandem series case.

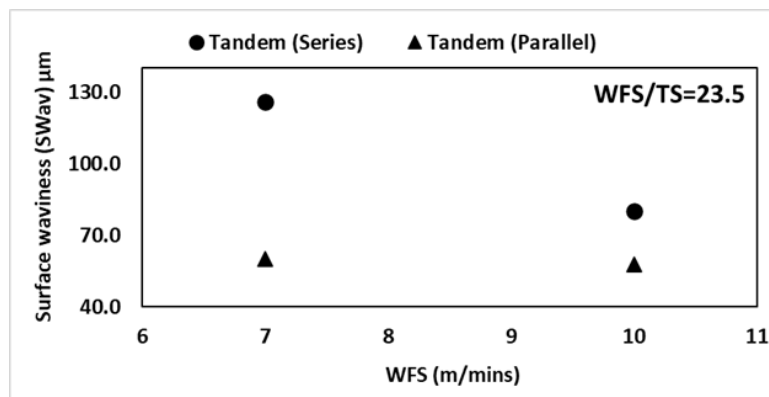


Figure 3-44 Effect of WFS and deposition process on SWav of walls deposited at a constant WFS/TS of 23.5

The surface quality of the walls can also be detected from appearance of the wall features, using cross-sectional macrograph of the walls in Figures 3-45. An improvement in surface quality of the wall is observed, with the use of both Tandem-wire (parallel) and Tandem-wire (series) set ups. The increase in WFS also produced a noticeable increase in EWW.





Tandem-wires (Series)		Tandem-wire (Parallel)	
WFS/TS = 23.5		WFS/TS = 23.5	
WFS=7m/mins	WFS=10m/mins	WFS=7m/mins	WFS=10m/mins
Trial 1	Trial 3	Trial 5	Trial 7
			
EWV= 9.8mm	EWV= 12.7mm	EWV= 10.9mm	EWV= 11.76mm
AIP=5.53kW	AIP=8.1kW	AIP=5.74kW	AIP=8.2kW
H.I =0.79 kJ/mm	H.I =0.81 kJ/mm	H.I =0.82 kJ/mm	H.I =0.82 kJ/mm

Figure 3-45 Effect of WFS and deposition process on EWW and surface quality of walls deposited at constant WFS/TS of 23.5, using tandem, (a) series wire configuration, and (b) parallel wire configuration

The improvement in surface quality with increase in WFS could be attributed to the increased instantaneous arc power (AIP), with enhanced melting energy, which produced a more stable arc, and promoted adequate fluidity and wetting of the weld pool. Simultaneously, the higher TS, worked in consonance to reduce the arc force and droplet impacts on the weld pool at the higher WFS, which could also be beneficial in preventing excessive weld metal accumulation, sagging and overflow (Xiong, J *et al.*, 2018).

3.12.3.2 Effect of WFS and deposition processes, on SWav and EWW, at WFS/TS of 16.7

Figure 3-46 shows the effect of WFS on SWav, using a lower WFS/TS of 16.9. The investigation was conducted using experiments with wall numbers 2,4,6 and 8, in table 3-9.

The result showed that increase in WFS from 7m/mins to 10m/mins, at WFS/TS of 16.9, produced a decrease in SWav on the walls deposited using Tandem-wire (series) set up. However, SWav increased on the walls deposited with Tandem-wire (parallel) configuration.

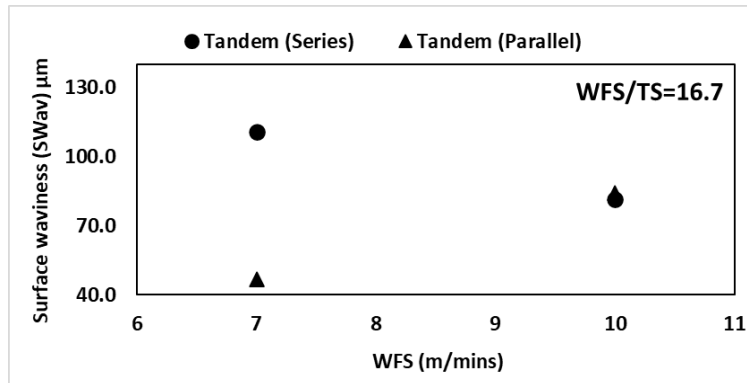


Figure 3-46 Influence of WFS on SWav, at a lower WFS/TS of 16.7, using Tandem-wire (series and parallel) setups

The surface quality of the walls produced with increase in WFS from 7m/mins to 10m/mins, and WFS/TS of 16.9, can also be observed from appearance of the wall features, through transverse cross-sectional macrographs of the walls, displayed in Figure 3-47. The increase in WFS produced a noticeable increase in EWW.

The walls deposited using tandem-GMAW series wire configuration, show improvement in surface quality, with increase in WFS. However, a significant deterioration in surface quality can clearly be observed on the wall deposited using the higher WFS and tandem-GMAW parallel wire configuration.

Tandem-wires (Series)		Tandem-wire (Parallel)	
WFS/TS = 16.7		WFS/TS = 16.7	
WFS=7m/mins	WFS=10m/mins	WFS=7m/mins	WFS=10m/mins
Trial 2	Trial 4	Trial 6	Trial 8
EWV= 8mm	EWV= 9.3mm	EWV= 9.4mm	EWV= 9.5mm
AIP=3.92kW	AIP=3.8kW	AIP=4.13kW	AIP=5.9kW
H.I =0.56 kJ/mm	H.I =0.38 kJ/mm	H.I =0.59 kJ/mm	H.I =0.59 kJ/mm
(a)		(b)	

Figure 3-47 Transverse cross-sections of walls, showing effect of WFS, at a constant WFS/TS ratio of 16.7, for (a) Tandem-wire, series set up and (b) Tandem-wire parallel set up.

A significant deterioration in surface quality with the lower WFS/TS ratio of 16.7, was observed on the wall produced using parallel wire configuration. But the counterpart wall produced using the series wire configuration, showed an improvement in surface quality.

This could be attributed to the earlier observation in section 3.9.1.2, which found that with increased TS, parallel wire configuration was more susceptible to undercut defect formation, compared to series wire configuration.

This could be related to the fact that the side-by-side arrangement of parallel wires, produced a higher interfacial tension and viscosity of liquid metal at the edges of the weld pool, owing to increased thermal cooling effect, associated with the spreading away of the arc from the molten weld pool centre. (Kazanas, P. *et al.*, 2012)

3.12.4 Metal deposition efficiency of Single-wire and Tandem wire GMAW processes

The amount of waste metal generated during WAAM of parts, can affect the commercial competitiveness of the process. Finding the right balance between increasing productivity and maximising wall geometry (material utilisation), while achieving acceptable mechanical performance is an essential requirement in adopting the WAAM process for component manufacture.

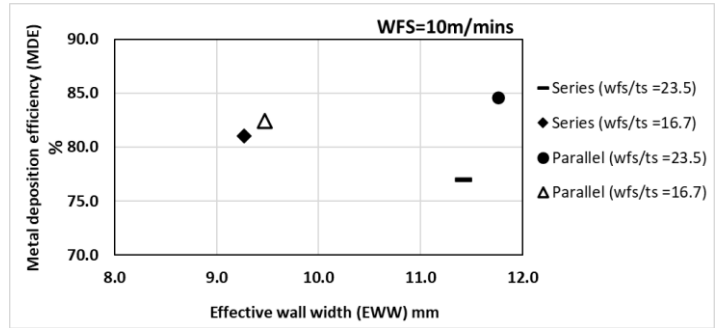
Metal deposition efficiency (MDE) relates to the percentage of the usable material deposited (material utilisation factor), which is the ratio of the effective wall area deposited, to the total wall area of material required to realise the effective wall area, as described in section 3.3.2.

This section evaluated the MDE of single-wire, tandem-wire (series) and tandem-wire (parallel) GMAW processes, in relation to the deposited effective wall widths (EWW). The analysis was conducted using the deposition conditions detailed in Table 3-9 and the result is presented in Figure 3-48.

Figure 3-48 show the relationship between MDE and EWW, for WFS of 7m/mins and 10m/mins.

Figure 3-48(a) showed that using single-wire and tandem-wire deposition processes, MDE of over 73% was achieved from a range of EWW of 8mm to 10.9mm, when a WFS of 7m/mins was utilised.

(a)



(b)

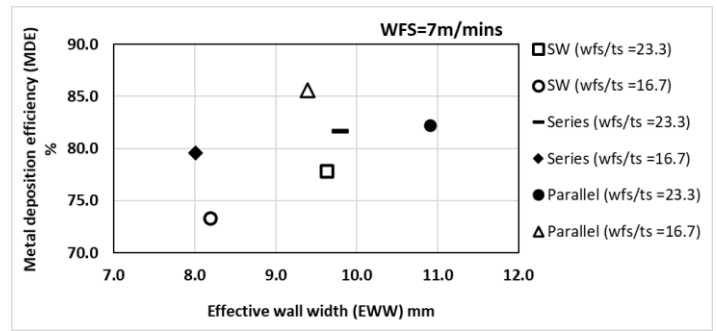


Figure 3-48 Relationship between MDE and EWW, for (a) SW-GMAW, Tandem-wire (series) and Tandem-wire (parallel) processes, using 7m/mins WFS (b) Tandem-wire (series) and Tandem-wire (parallel), using 10m/mins WFS

Whereas in Figure 3-48(b), the higher WFS of 10m/mins applied, produced MDE of over 77% and EWW of between 8.8mm and 11.8mm, using tandem-wire (series and parallel) deposition processes.

High EWW and MDE requires less post processing machining work to achieve the finish dimension of the product, therefore increasing the overall manufacturing efficiency of the process. This is highly desirable for WAAM application. In general, the optimum MDE, for all ranges of EWW and WFS/TS ratio, was achieved for walls built using tandem-wire parallel configuration.

Considering these are thin wall structures, the MDE could far exceed these values where a thicker walled structure is deposited, using an optimised deposition strategy.

3.13 Case study 1: Manufacture of a thin wall structure, using Tandem-GMAW parallel wire technique

This case study demonstrated the feasibility of utilising tandem-GMAW, parallel wires configuration, to build a thin rectilinear WAAM wall, and achieve excellent improvement in surface quality and dimensional tolerance of the part.

An S355 structural steel plate of dimension 350mm x 200mm x 20mm, was utilised as substrate to build the rectilinear wall, using ER120S-G wire. The chemical composition of the substrate and wire are presented in section 3.9. Ar8%CO₂ was used as shielding gas, at a flow rate of 30l/min. The set up of the experiment is shown in Figure 3-49.

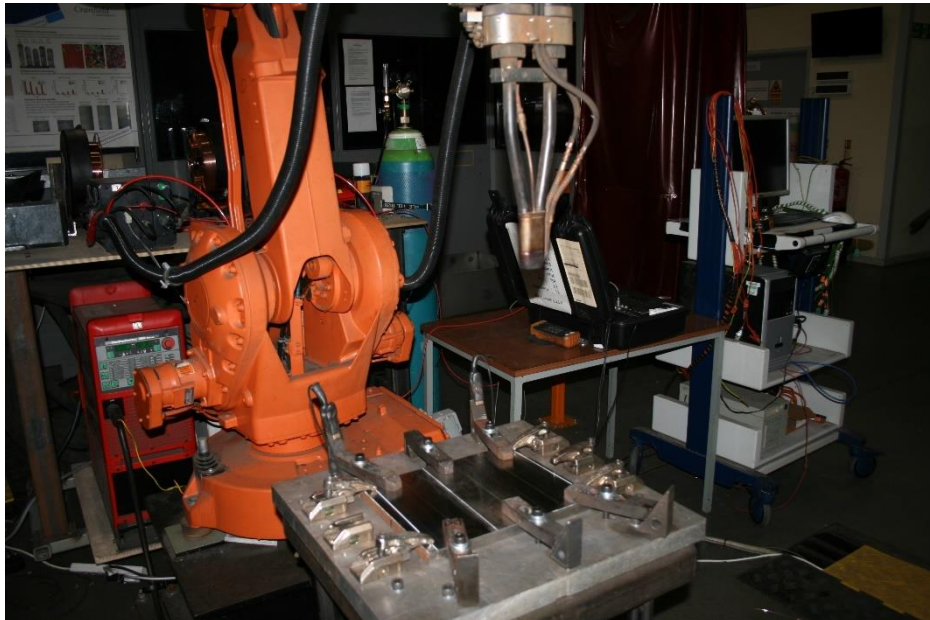


Figure 3-49 Experiment set-up

3.13.1 Manufacturing strategy

The pre-set deposition condition used to produce the demonstration wall was based on the process parameter of wall 5, studied in the previous section 3.11.

The experiment was previously conducted using a Uni-directional raster (or stringer) tool path trajectory. However, the manufacture of WAAM parts typically, require the multiple tool path directions. The manufacture of the rectilinear structure was conducted using bi-directional stringer (parallel) tool path strategy.

Table 3-11 gives the details of deposition parameters used in building the demonstration wall structure.

Table 3-11 Deposition condition utilised in building the demonstration wall

WFS (lead + trail) wire (m/min)	TS (mm/s)	TS (m/min)	WFS/TS	CTWD	Deposition technique
7	5	0.3	23.3	20	Tandem-GMAW (Parallel wire set-up)

During manufacture of the thin wall, the torch travelled from one end of the substrate to the other, in the Y-direction to deposit each weld layer. Afterwards, it accends in the Z direction, a distance equal to the layer height, and deposited the next layer in the Y-direction opposite to the previous layer. The cycle was repeated until the final build height was reached. Figure 3-50 show an illustration of the deposition procedure for the case study 1.

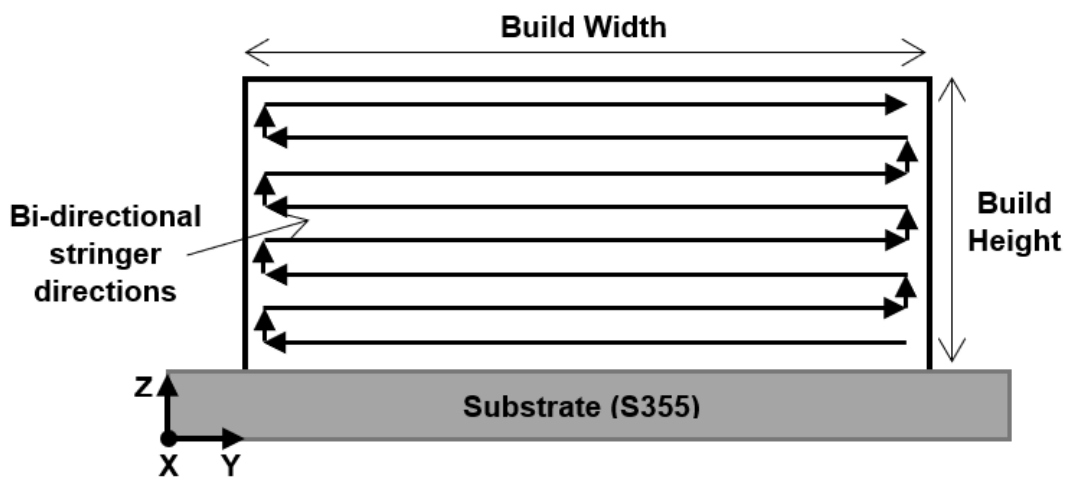
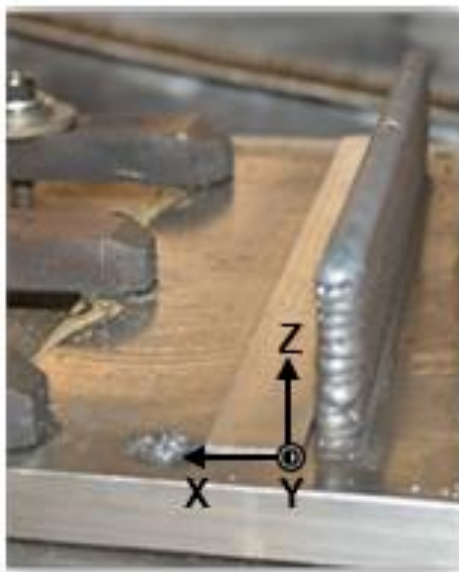


Figure 3-50 Illustration of bi-directional parallel tool path strategy utilised in building the demostration WAAM wall

3.13.2 Result and discussion of case study 1

Figure 3-51 show the surface appearance of the multi-layer wall, built using tandem parallel wire configuration. The front view is shown in Figure 3-51(a), while Figure 3-51(b) show the side view of the structural WAAM part.



(a)



(b)

Figure 3-51 Surface appearance of wall structure built using tandem-wire (parallel wire configuration, with dimensions 250 mm × 55 mm × 9.5mm (a) Front view (b) side view. Note the excellent surface finish and straightness of the WAAM part.

The result show outstanding geometrical accuracy, straightness, and surface finish of the WAAM part, produced using tandem-GMAW parallel wire deposition technique.

A comparison with similar wall structures built by the author in previous studies, using single-wire GMAW and tandem series wire set up, is presented in Figure 3-52.

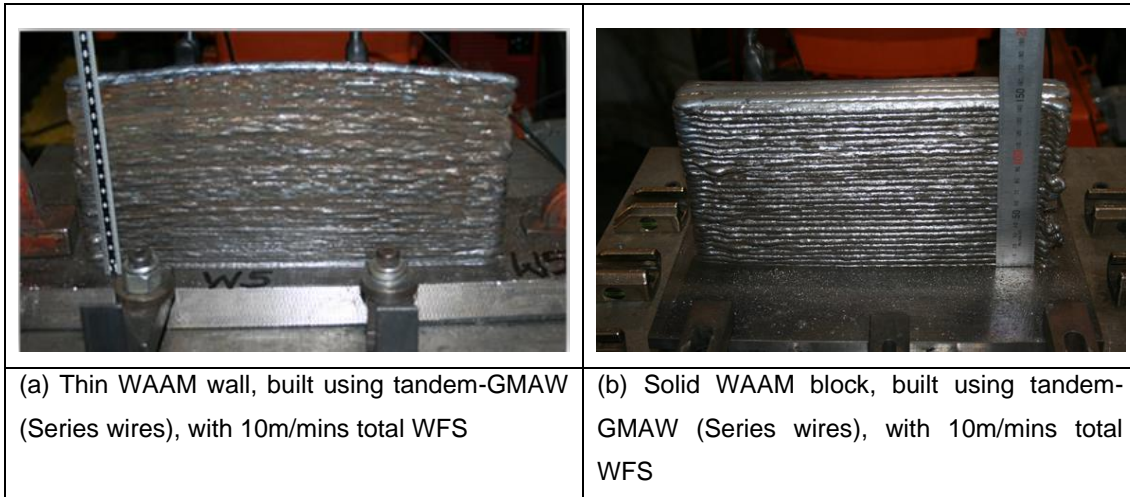


Figure 3-52 Surface appearance of WAAM structures built using tandem-GMAW series wire setup (a) Thin wall, deposited using ER120S-G and ER70S-G on each wire (b) Thick block, deposited using ER120S-G on both wires

The significant improvement in surface quality and dimensional tolerance of the part manufactured using Tandem-GMAW (parallel-wire), compared to the duo manufactured using Tandem-GMAW (series wire) technique is obvious.

The parallel wire configuration prevents reheating of the weld pool and produce a larger specific surface area of contact with the base plate. The increase in the surface contact area can enhance heat transfer through the base plate by conduction, thereby decreasing the temperature gradient in the melt pool and causing solidification to occur more uniformly, at a higher cooling rate.

This work demonstrated that large, high-quality structural steel components can be produced using Tandem-GMAW process, (at its characteristic high deposition rates), especially by configuring the tandem wires in parallel to each other.

The good geometrical accuracy of the manufactured parts, straightness and the excellent surface finish achieved, are three of the main attributes of this WAAM technique

3.14 High deposition and surface quality manufacture

The deposition tool path strategy utilised in fabricating a WAAM part, could significantly influence the surface quality of the final part. The influence of a particular strategy is even more important when the simultaneous improvement in both deposition rate and surface quality of the part is desired. Because the strategy utilised affects both the deposition rate, geometrical accuracy, and uniformity in material distribution within the part (Jaiswal et al., 2018).

In this study, a new approach utilising skin and core deposition strategy to manufacture a WAAM part was investigated. A combination of tandem-GMAW and single-wire GMAW processes were utilised, with the aim to maximise the deposition rate and surface quality of the built part.

It has been recognised that maximising deposition rate requires significant increase in WFS and hence higher heat input. This condition leads to increased material fluidity and potential for unstable and non-reproducible deposition process, which deteriorate the surface quality of the part. To minimise this problem, the part was divided into two sections, an outer (Skin) and inner an (Core) section (Poprawe, R. *et al.*, 2015), as illustrated in Figure 3-53.

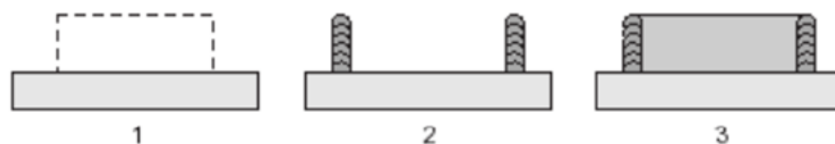


Figure 3-53 illustration of skin and core deposition technique

This technique allows different process parameters to be specified for each section. The core does not have strict requirement for surface or dimensional quality; hence its deposition rate can be maximised within the limit of the process parameter and deposition stability. On the other hand, the skin can be built at a lower deposition rate to maximise the surface quality, while ensuring adequate fusion performance (Poprawe, R. *et al.*, 2015).

This strategy was selected because of the ease to combine different deposition parameters and processing conditions proposed in this study. The strategy can be combined with different tool path approaches and deposition parameters to increase the process flexibility.

Parallel (stringer) deposition strategy was utilised in depositing the skin section, while oscillation (bi-directional stringer) strategy was used to build the core section; by employing a combination of tandem-GMAW (series wire configuration) and single-wire GMAW processes respectively.

To the best of the author's knowledge the use of this approach which combines the tandem-wire and single-wire GMAW process to build a skin and core structure, by WAAM technique have not been reported.

3.15 Skin and core parameter study

The section presents the process study conducted to develop suitable deposition process parameters, combined to build the skin and core sections of a WAAM structure, using single-wire GMAW and Tandem GMAW (series wire configuration), processes respectively. Minitab 17 statistical software was used to plan the experiment and plot the results.

The materials and equipment set up used to conduct this experiment are described in section 3.9. After deposition, the samples were prepared according to the method detailed in section 3.10, followed by measurement of the bead parameters, based on the procedure detailed in section 3.11.

The process parameter study for the skin section was presented first, followed by the process parameters study for the core section.

3.15.1 Generation of process parameters for deposition of skin section

This study was conducted to establish suitable range of bead parameters to build the skin section of a WAAM part. Single-wire GMAW process was used, achieved by temporarily disengaging the trail wire feeder, from the tandem-wire GMAW system, technically converting it to a single-wire GMAW system.

Thirty-two (32) beads on plate welds were deposited for the investigation, according to the pre-set process parameters given in Table 3-12.

Table 3-12 Single-wire GMAW process parameters used to study bead parameters optimisation for depositing the skin section

Parameters	Level							
WFS (m/mins)	4	5	6	7				
Travel speed (TS), mm/secs	5	6	7	8	9	10	11	12
Pulse correction	1							
Arc length correction, %	12							
CTWD, mm	20							
Shield gas (flow rate)	Ar/8%CO ₂ (15l/mins)							

3.15.2 Results of parameter study for deposition of the skin section

Linear and contour plots were generated using Minitab 17, to show the main and interaction effects of single-wire GMAW process parameters on the deposited bead responses and heat input generated for the skin section. The detailed experimental design matrix utilised for depositing the skin section and measured responses obtained from the investigation is presented in Appendix G.

3.15.2.1 Effect of process parameters on bead geometry and generated heat input for skin section

The linear and contour plots in Figure 3-54, show the relationships between the input process parameters and measured responses including (BH, BW and H.I).

It can be observed from the linear plot of Figure 3-54(a), that for a given WFS, the BH, BW and generated H.I show a significantly linear relationship with TS, decreasing steadily as the TS was increased from 5 mm/s to 12 mm/s.

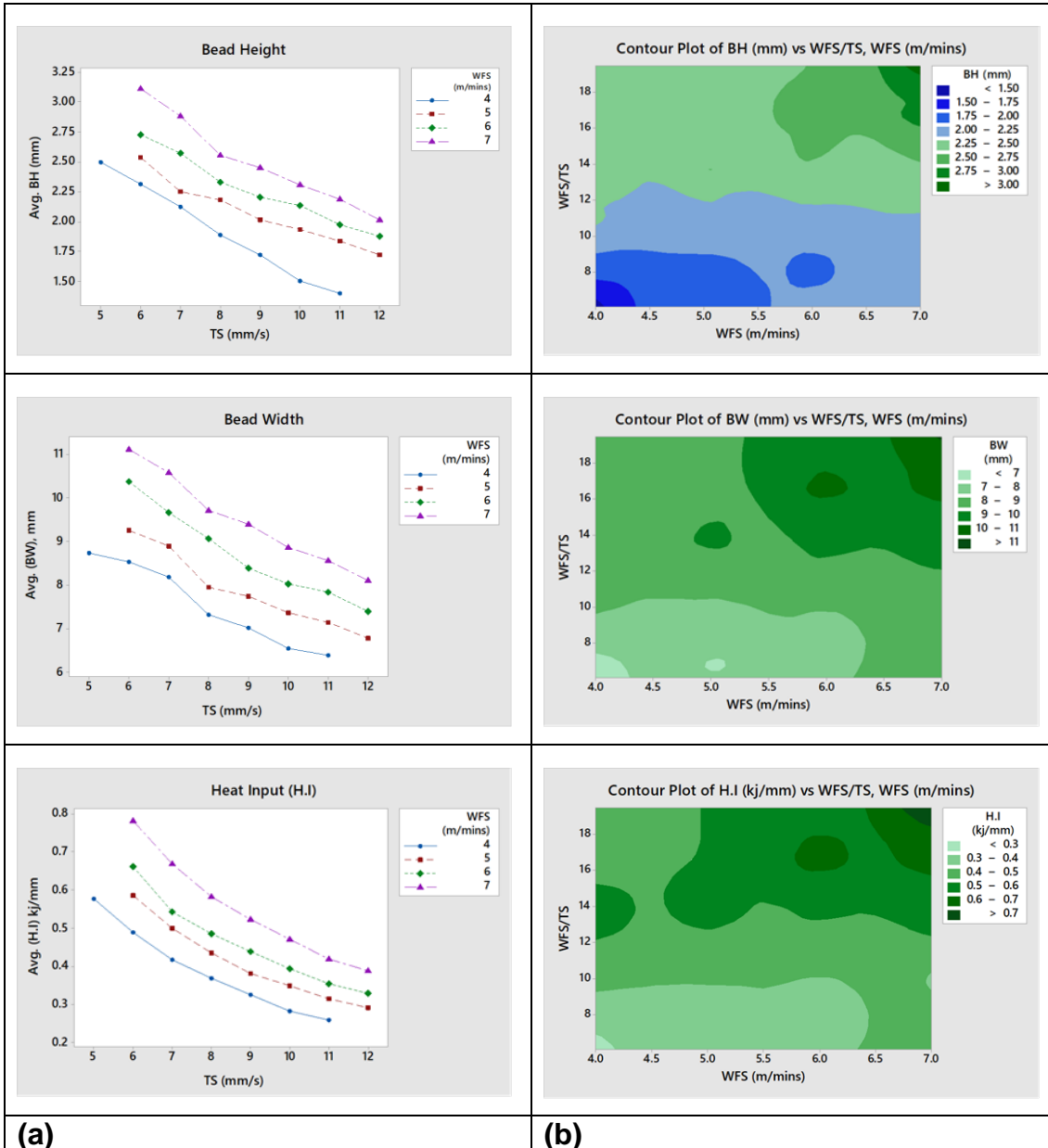


Figure 3-54 Interaction effects of single-wire GMAW process parameters on measured bead responses, presented using (a) Linear and (b) contour plots

The contour plot in Figure 3-54(b), show the combined effect of WFS/TS ratio and WFS, on the BH and BW. It indicates that WFS/TS ratio of between (8 – 18), will produce a range of BH, BW and H.I. of (1.5 – 3.0) mm, (7 – 11) mm and (0.3 – 0.7) kJ/mm, respectively, required for depositing the skin section.

However, the lower limit of WFS and higher limit of TS, should be avoided, due to the potential to produce defective beads, due to the low heat input generated.

3.15.3 Generation of process parameters for deposition of core section

This section presents the study conducted to generate suitable deposition process parameters to build the core section of a WAAM part, using Tandem-GMAW (series wire) process.

The focus was to develop a range of bead parameters (particularly BW and BH), for building the core section of a WAAM block. In developing the parameters, the WFS of the rear wire was maintained at 2m/mins, higher compared to that of the front wire.

Twenty-five (25) beads on plate welds were deposited for this investigation. The pre-set parameters and levels used is given in Table 3.13.

The detailed experimental design matrix utilised for depositing the core section and measured responses obtained from the investigation is presented in Appendix H.

Table 3-13 Tandem-GMAW, series wire parameters used to study bead parameters optimisation for depositing the core section

Parameters	Range				
WFS, m/mins (Front/Back) wire	9/11	10/12	11/13	12/14	13/15
Total WFS (m/mins)	20	22	24	26	28
Travel speed (TS), m/mins	1.08	1.2	1.32	1.44	1.56
TS (mm/s)	18	20	22	24	26
CTWD, mm	20				
Shielding gas	Ar/8%CO ₂				

3.15.4 Results and discussion of process parameter study for core section

Representative macrograph cross section of the bead profiles, developed for the core section, are presented in Figure 3-55. The macrographs show uniform bead profiles of excellent geometrical and surface quality, devoid of any defect.

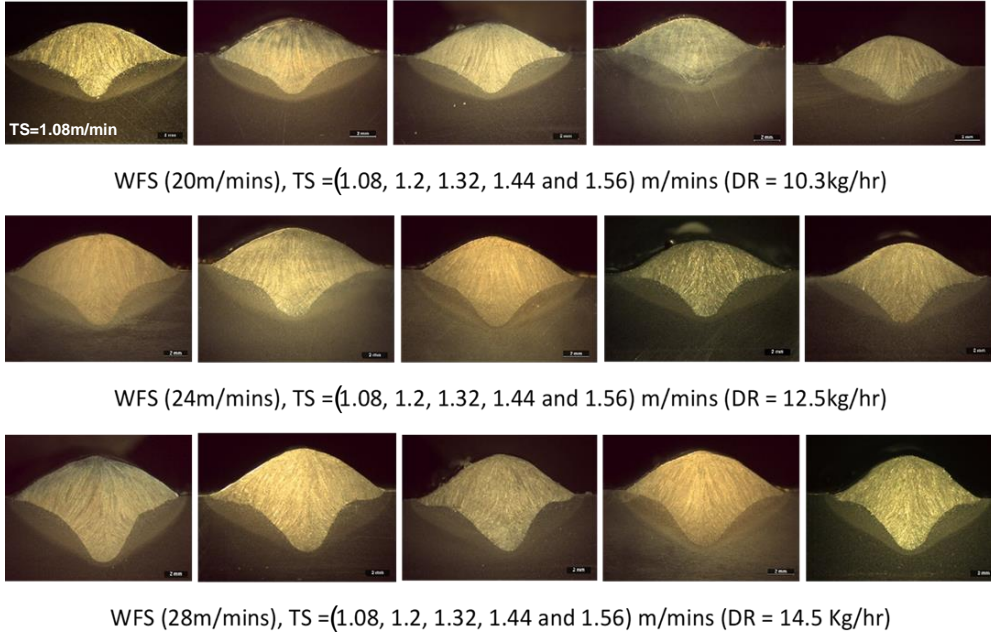


Figure 3-55 Cross sectional macrographs of deposited bead, produced using Tandem-GMAW (series wire) configuration

3.15.4.1 Effect of process parameters on bead width for core section

The effect of WFS and TS on the measured bead width, for depositing the core section is depicted by the plot in Figure 3-56.

Increase in WFS from 20m/mins to 24m/mins, increased the BW by 8.6% to a maximum of 12.95mm. Further increase in WFS from 24m/mins to 28m/mins, produced a negligible change in BW.

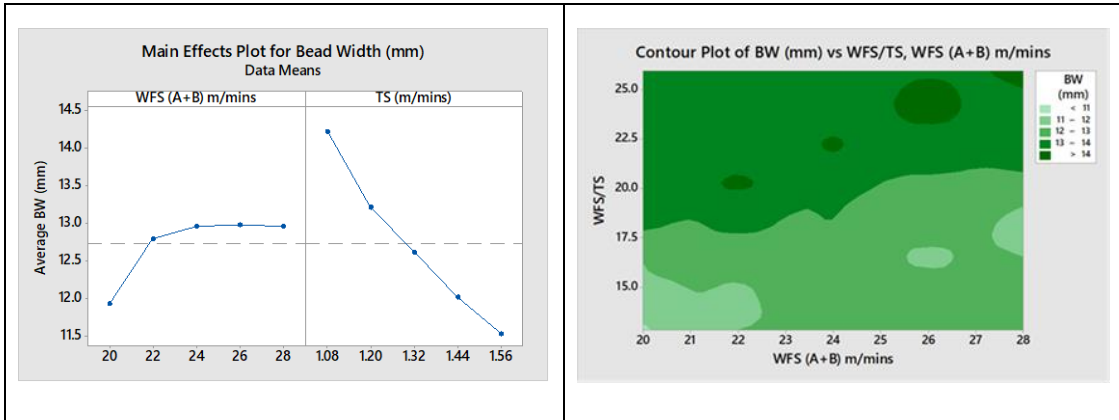


Figure 3-56 Effect of process parameters on bead width for core section

Increase in TS from 1.08m/mins to 1.32/mins, produced 11.4% decrease in BW to 12.6mm. A further increase in TS to 1.56m/mins, produced 8.7% decrease in BW to 11.5mm.

The contour plot showed that for the different combination of Tandem-GMAW (series wire) process parameters, (namely WFS and TS) utilised, WFS/TS ratio range of (15 – 25), will produce a range of BW of (11 – 14) mm, suitable to build the core section of a WAAM part.

3.15.4.2 Effect of process parameters on bead height for core section

The effect of WFS and TS on the measured bead height, for the core section is depicted by the plot in Figure 3-57.

The increase in WFS from 20m/mins to 24m/mins, produced 12.2% increase in BH to 2.86mm. A further increase in WFS to 28m/mins, produce 19.2% increase in BH to 3.41mm.

The increase in TS from 1.08m/mins to 1.32m/mins, produced 8.4% increase in BH to 2.94mm. A further increase in WFS to 28m/mins, produce 8.5% increase in BH to 2.69mm.

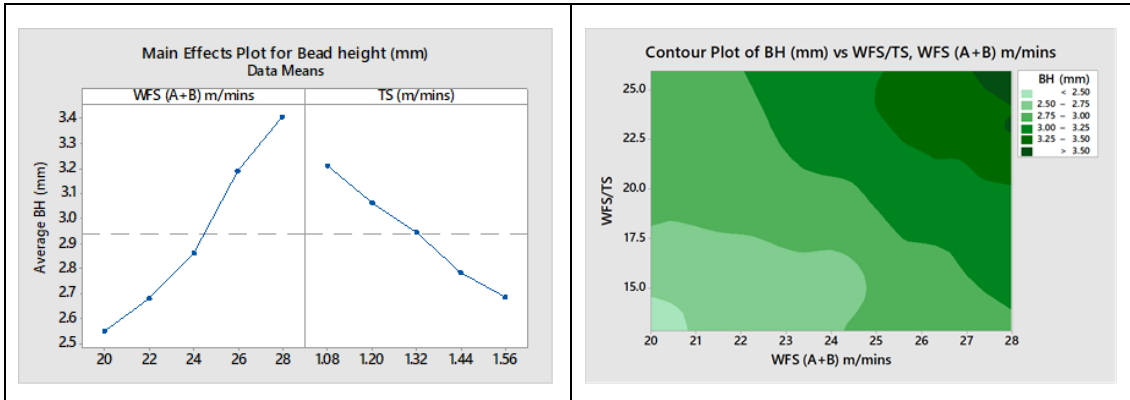


Figure 3-57 Effect of process parameters on bead height for core section

The contour plot in Figure 3-57, showed that for the different combination of Tandem-GMAW (series wire) process parameters, (namely WFS and TS) utilised, WFS/TS ratio range of (15 – 25), will produce a range of BH of (2.5 – 3.5) mm, applicable for building the core section of a WAAM part.

3.15.4.3 Effect of process parameters on heat input and deposition rate produced for the core section

The contour plots in Figure 3-58 depicts the generated heat input and deposition rate (DR) that can be achieved using Tandem-GMAW series wire process, within the limit of the applied process parameters.

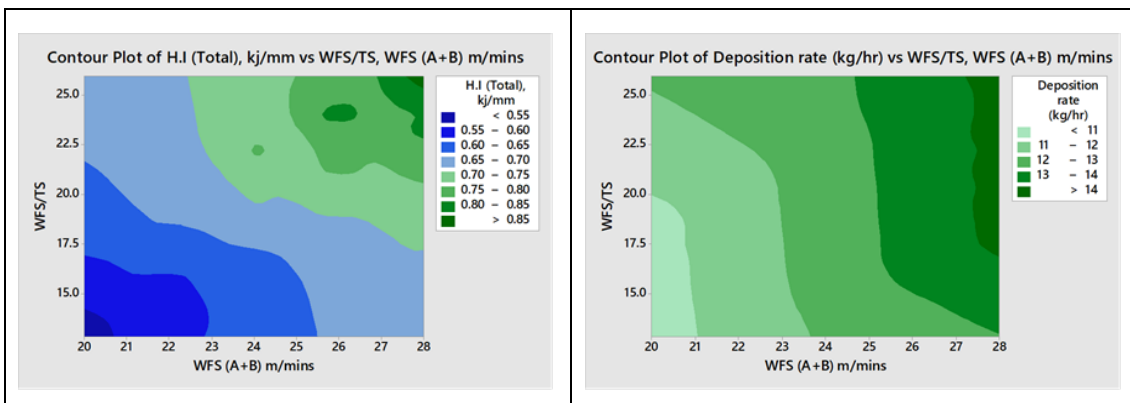


Figure 3-58 Interaction effect of Tandem-GMAW (series wires) configuration process parameters, on deposition rate, shown using (a) Linear and (b) Contour plots

The plot shows that for the range of WFS utilised in the study, WFS/TS ratio of (13 – 25), will produce a range of heat input and high deposition rate of between (0.55 – 0.85) kJ/mm and (10.3 and 14.5) Kg/hr, respectively for the core section.

The result of the experiment showed that BH respond more significantly to changes in WFS, than BW and increase in WFS above 24m/mins produced no further change in BW (Figure 3-58). This may be because by increasing the WFS, mean current increased and caused the arc column to be more concentrated (constricted) in the centre of the weld pool, producing more effect on the BH, rather the BW.

In conclusion, the build rate is maximised with the following combination of parameters: WFS_{high} , TS_{low} , and WFS/TS_{high} . However, increase in BW is relatively negligible when WFS/TS is greater than approximately 21.

3.16 Case study 2: WAAM of large structural part, using skin and core deposition technique

This section presents a case study demonstrating the feasibility of producing a WAAM part, using skin and core deposition technique. Findings from the previous experiment in section 3.15, provided the basis for selecting the deposition parameter utilised in this section.

Table 3-14, gives a summary of the range of achievable bead parameters, i.e., BW, BH, DR and H.I, using tandem-GMAW (Series wire) and Single-wire GMAW processes

Table 3-14 Bead output range of tandem-GMAW (Series wire) and single-wire GMAW processes, for single layer deposits. The intervals represent minimum and maximum achievable dimensions for WFS/TS ratios of (15 – 25) and (8 – 18) respectively.

Deposited bead parameter	Tandem-GMAW (series wire configuration)	Single-wire GMAW
BW (mm)	11 – 14	8 – 11
BH (mm)	2.5 – 3.5	1.75 – 3.0
DR (kg/hr)	11 – 14	2.1 – 3.7
H.I. (kJ/mm)	0.55 – 0.85	0.4 – 0.7

3.16.1 Materials and consumables

An S355 structural steel plate of dimension 350mm x 200mm x 20mm, was used as substrate to build the block and the deposition wire was ER120S-G. The

chemical composition of the substrate and deposition wire are presented in section 3.10.1. Ar8%CO₂ was used as shielding gas, at a flow rate of 30l/min.

3.16.2 Equipment set-up

The equipment set up utilised is shown in Figure 3-59. The substrate was affixed to the support base, using bolts, to minimise movement from distortion.

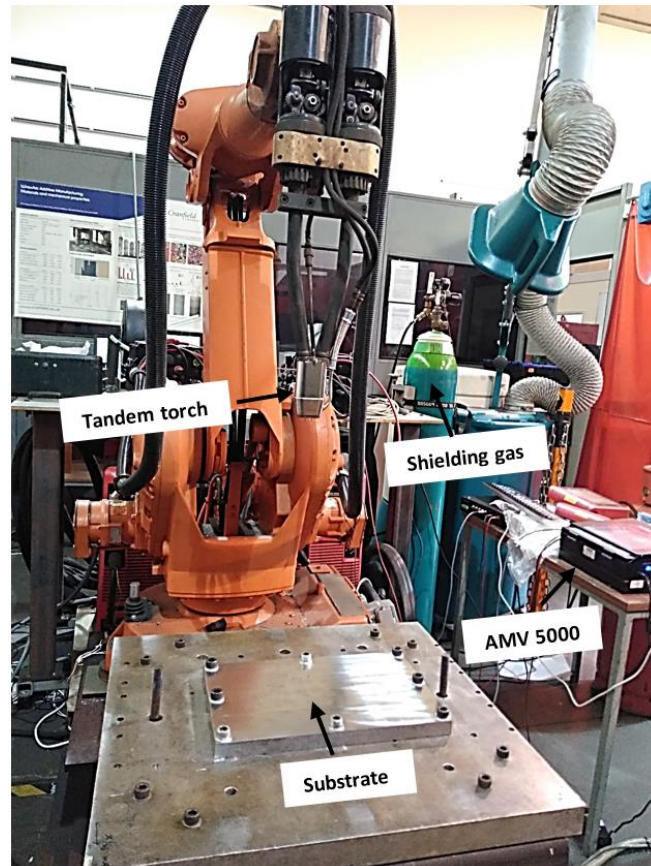


Figure 3-59 Equipment set-up, used for building the skin and core part (Substrate bolted to support table)

3.16.3 Manufacturing procedure

The preceding WAAM parametric studies were conducted using single-bead and multilayer configuration, without torch weaving or lateral oscillation. From table 3-15, it can be observed that tandem-GMAW series configuration, produced single bead thickness between 11mm to 14mm, while the single-wire GMAW process achieved a width range of between 8 mm to 11mm, in this study.

However, the manufacture of WAAM parts with thicker wall thickness will require overlapping of multiple connecting and interconnecting weld beads. Therefore, the overlapping distance or centre distance between the individual adjacent skin and core beads will need to be considered, because it can significantly affect the surface quality and flatness of the build part Rodriguez, N. *et al.* (2018).

The overlap distance between each adjacent bead was taken as 66.66% (Suryakumar, S. *et al.*, 2011). A layer height of 3mm was selected for the core parameter, and 2.5 mm for the skin, for building the WAAM part.

Table 3-15 gives the input process parameters used to instruct the GMAW power source and motion systems, to actualise production of the demonstration part.

The robotic program utilised in implementing the manufacture of the skin and core part is provided in Appendix I.

Table 3-15 Parameter utilised in building the demonstration wall

Parameter	Core section	Skin section
WFS, m/mins	24	6.5
TS, mm/s (m/mins)	21 (1.26)	8 (0.48)
Bead height (mm)	3	2.5
WFS/TS	19.05	13.4
Bead width (mm)	13.05	9.5
H.I (kJ/mm)	0.69	0.55
Deposition rate (Kg/hr)	12.8	3.5

The manufacture of the skin and core structure was implemented using a combination of two deposition tool path strategies. A stringer (parallel) bead technique was used to deposit the skin section, while an oscillatory (wide-weave) strategy was used to build the core section of the part. Figure 3-60 show a schematic illustration of the tool paths utilised.

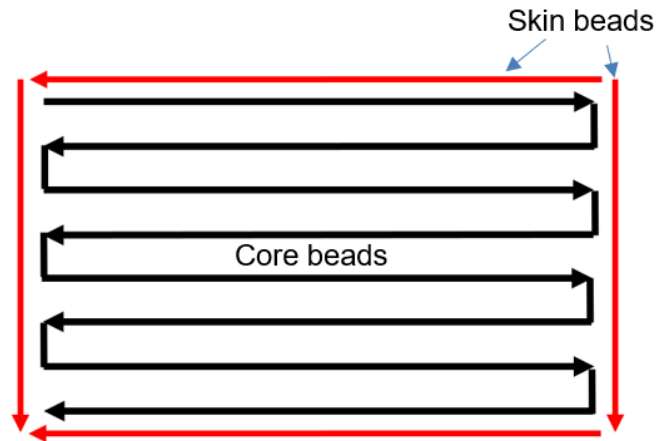


Figure 3-60 Deposition tool path strategy, showing combination of Parallel beads and wide oscillation beads, for depositing the skin and core sections respectively

The first layer of skin and core deposit is shown in Figure 3-61, with the superimposed arrows, showing the directions of deposition tool path.

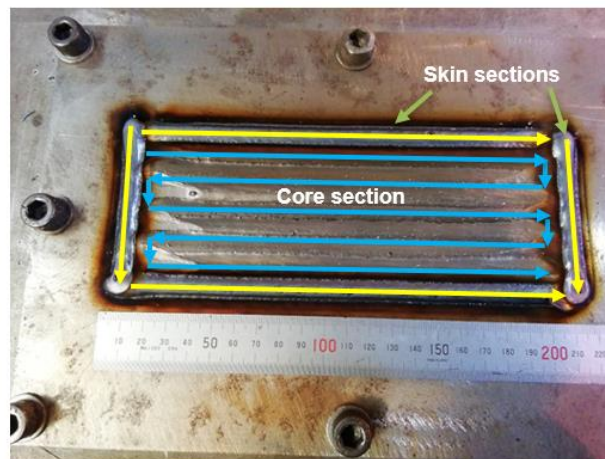
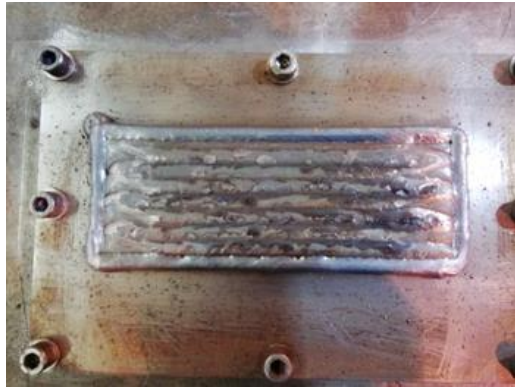
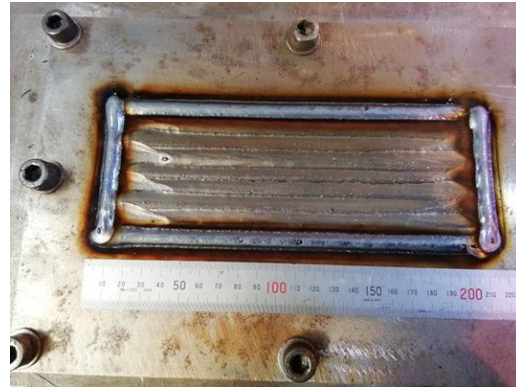


Figure 3-61 First layer of skin and core deposits, showing the tool path directions

Figure 3-62 show the surface appearances of the deposited skin and core part for the first layer. Figure 3-62(a) was deposited without an external trailing shield, while Figure 3-62(b) was built using an external argon gas trailing shield, supplied at a flow rate of 70l/mins,



(a)



(b)

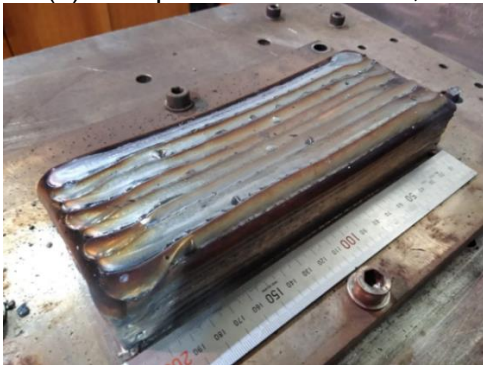
Figure 3-62 Skin and core structures, built (a) without external trailing shield (b) with external argon gas trailing shield

The improvement in surface quality with the use of the external argon trailing shield is very clear. This improvement is due to the fact that the additional supply of argon gas, provided enhanced protection of the molten metal from atmospheric oxidation. It also offered additional cooling effect, thus reducing the thermal accumulation of the weldmetal. This decreases the temperature gradient in the melt pool, causing enhanced solidification to occur at a higher cooling rate, thus improving the surface quality.

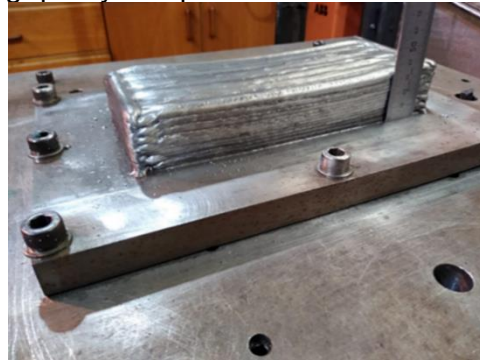
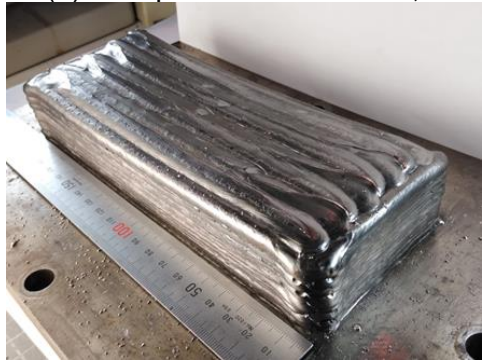
Figure 3-63 shows the completed WAAM block, manufactured using the skin and core deposition technique.



(a) Completed WAAM block, showing quality of side surface



(b) Completed WAAM block, showing quality of top surface



(c) Completed WAAM block, showing dimensional and surface quality after wire brush cleaning

Figure 3-63 Surface morphology of large WAAM block deposited using skin and core deposition strategy, measuring 220mm x 90mm x 55mm in dimension

It is obvious that excellent dimensional and surface quality of the WAAM part was realised using this method, while also achieving substantial deposition rate.

Maximization of build rate is highly desirable in AM processes, to reduce manufacturing costs and time. This work has demonstrated the ability to achieve a deposition rate greater than 10kg/hr, without significant deterioration to the surface quality of the WAAM part. The overall BTF ratio achievable with this

technique is expected to be well close to 1.5, which Williams et al. (2016) suggested is required to maximise manufacturing costs.

It has also been suggested that build rate increases with the square of the layer height (Rodriguez, N. *et al.*, 2018). But this work has shown that build rate can be further increased, up to 4 times the layer height, using tandem-wire process, as shown in Table 3-15. Utilising skin and core technique could ensure this build rate, without significantly compromising the surface quality.

3.17 Conclusions

The manufacture of large sized components through AM is the biggest potential application for WAAM for manufacture of heavy walled components. Such components generally require wide wall width and one major challenge encountered during their fabrication is the optimization of process parameters, which affect the weld quality and deposition process stability. The optimum solution for achieving the desired component quality and productivity is always a compromise due to the complex interactions of the several processing parameters.

Hence, one of the pertinent questions in this study was whether it was possible to overcome the high deposition challenges associated with the use of high deposition energy processes, such as tandem GMAW process, by implementing a wide-range of process parametric studies. In the work, the surface and geometrical characteristics were the outputs of the WAAM deposition process, because they can determine the quality, integrity, and manufacturing cost efficiency of the built part.

This work has demonstrated the feasibility of utilising tandem-wire and single-wire GMAW processes, for WAAM purposes, in which simultaneous increase in deposition rate and surface quality of a part was achieved, through the use of skin and core deposition technique.

Some key findings from the study are summarised as follows:

- The result of the single bead experiment found that the lower to medium range of tandem parameters, produced a more significant effect on the output bead characteristics, compared to the higher settings
 - The lead arc in a tandem-GMAW system, produces a higher heat input, compared to the trail arc.
 - WFS and TS parameters produce a more significant effect on the PD. This could be attributed to the high current density and strong impact of the molten metal droplets, detachment from the wire tip, on liquid weld pool.
- Shoeb, M. (2013). The aspect ratio, i.e., ratio of (BW/BP), is expected to

decrease, which is associated with reduction in the bead quality, and increase in the time required to build a part

- CTWD was found to produce an insignificant effect on H.I and bead characteristics. However, accurate and optimum CTWD setting is critical, to ensure the required metal transfer mode is maintained, to produce stable deposition and reproducible bead characteristics.
- Consistent high quality bead deposits, devoid of defects, can be produced with tandem series wire configuration, when the WFS of the rear wire is set about 2m/mins higher compared to the front wire.
- An interesting aspect in this study was that the incremental height of multi-layer walls produced using parallel wire configurations, were found to be more consistent and reproducible along the z-direction, resulting in a multi-layer deposition pattern with very little deviation from the average layer height, shown from the calculated standard deviations. This is important for maintaining accurate and consistent CTWD, hence the stable ODPP metal transfer process
- This study showed that TS and WFS are important factors that can be used to control the SWav in the build, due to effect on the wetting behaviour of the deposited beads. The results indicated that TS has a strong influence on SWav and relatively lower SWav profiles are produced using smaller WFS, in combination with suitable lower TS.
- Single-wire GMAW process produced the largest aLH, but the smallest WW, EWW and MDE. It also produced the highest SWav, of the three deposition wire configurations
- The parallel wire configuration gives the lowest surface waviness, at relatively higher WFS/TS ratio, but could produce higher surface waviness at lower WFS/TS ratio, due to poor wetting characteristics resulting from higher TS regimes. But interestingly, the result showed that the SWav for the series wire configuration, was independent of the amount of deposited metal per unit length (WFS/TS), and thus heat input
- It comes as no surprise that the MDE and achievable EWW range increased with higher WFS. The higher arc power, HI, and arc spread most

probably play an important role in improving the wetting behaviour of the liquid weld pool onto the previous solid layer.

- The optimum MDE, EWW and surface quality of a WAAM part can be achieved with tandem-GMAW parallel wire configuration. However, this may be limited by the practical requirement to travel around corners and along round tool path directions, during manufacture of typical WAAM parts.

3.17.1 Recommendations

- ✓ Conduct more research into alternate path generation that considers the complexities of the tandem-wire deposition system, as well as its relationships with the properties of the final component.
- ✓ Study alternate deposition strategies to further maximise the build rate
- ✓ Select skin and core parameter combinations which are not on the edge of the working range
- ✓ In case of more than one suitable combination, consider productivity factors, such as maximising WFS and LH
- ✓ Conduct detailed study of external trailing shielding, to characterise the effect of weldment properties
- ✓ Maximise productivity by depositing more than one part in the same cell

4 Experimental study of thermal cycle generation and heat treatment in WAAM fabricated 2.25Cr 1Mo alloy

4.1 Experiment and procedures

4.1.1 Deposition Materials

An S355 rectangular steel plate supplied by West Yorkshire Steel Ltd; of dimension 450x450x30 mm was used as substrate. Lincoln electric ER90S-G (LMN 20) low alloy steel welding wire was used as the deposition material, since this was considered a near composition equivalent to F22, and the shielding gas used was Argo-shield light, comprising nominally 93% Ar, 5%CO₂ and 2%O₂. The nominal composition of the substrate and deposition wire are given in Table 4-1.

Table 4-1 Composition of substrate and deposition wire

Substrate composition											
C	Si	Mn	P	S	Cr	Ni	Mo	Nb	Cu	V	
0.20	0.55	1.60	0.025	0.025	-	-	-	-	0.55	-	
Wire composition											
C	Si	Mn	P	S	Cr	Ni	Mo	Nb	Cu	V	CE
0.08	0.61	0.90	0.007	0.005	2.48	0.04	1.00	0.01	0.0	0.01	0.48

4.1.2 Equipment set-up and parameters

The WAAM deposition system used comprised of a six-axis ABB robot, Fronius CMT 8000 MIG/MAG power source, Fronius wire feeder and clamping jig as shown in Figure 4-1(a). The deposition process was instrumented to evaluate the transient arc current and voltage characteristic during the build-up. The arc current and voltage readings were monitored and recording using AMV5000 weld data monitoring system, at a sampling rate of 5 kHz, as shown in Figure 4-1(b).

Prior to the actual block deposition, preliminary trial runs were conducted to determine combinations of GMAW process parameters suitable for depositing a sound weld block. The process parameters utilised is given in Table 4-2.

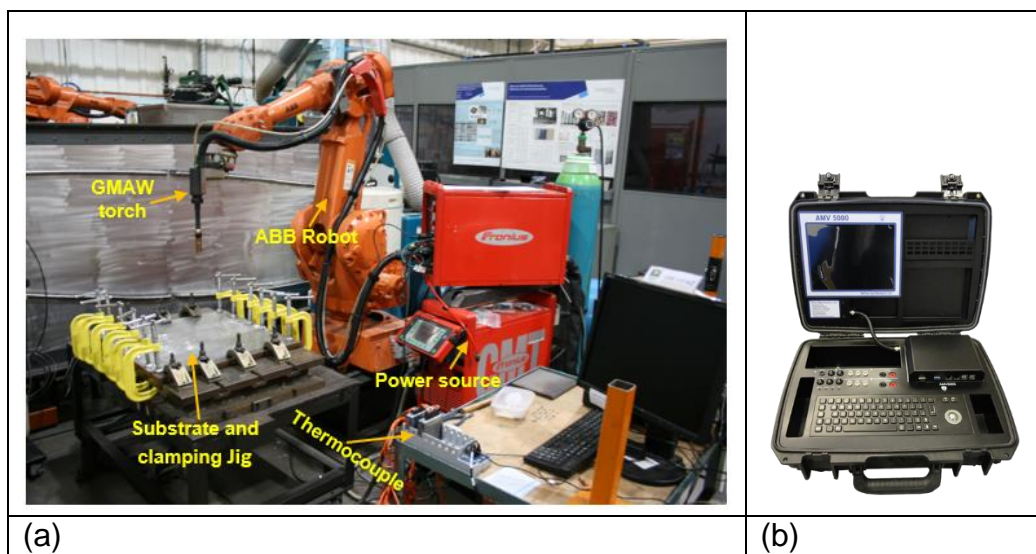


Figure 4-1 (a) Equipment set-up (b) AMV 5000 weld data loggers

Table 4-2 Deposition parameters for building the WAAM test block

Parameters	Settings
Wire feed speed, m/mins	8.5
Travel speed, mm/sec (mm/mins)	8.5 (510)
Contact tip to work distance CTWD (mm)	18
Gas flow rate (l/mins)	20
Arc length correction factor (%)	-15%
Pulse correction factor	1.5
Interpass temperature range (°C)	200 – 250

4.1.3 Manufacture of test block and thermal cycle measurement

A bi-directional long axis (stringer) deposition strategy was adopted in building the block. In this approach the torch deposited a weld pass from one end of the weld and ascended to the programmed home position. It automatically returned to the start position after stepping before depositing the next pass. This process continues until the layer width is completed. After completing a particular layer, the torch moved to the opposite end of the previous layer's start position and repeated the cycle. This process was continued until the 21st layer height was completed.

The test block was deposited in a stair-step manner, by stepping the torch by 5mm inwards at specific start position to allow for attachments of thermocouples.

The torch was stepped inward when negligible change in temperature was observed on the tracking thermocouple point below the deposited layers. This technique was adopted to minimise the direct heating and burning of the thermocouples by the arc during subsequent passes. Figure 4-2 illustrates the geometry of the test block.

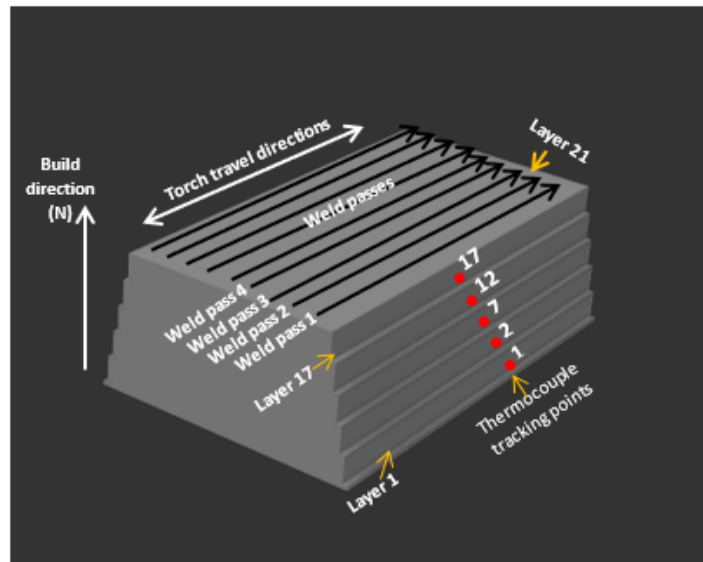


Figure 4-2 Illustration of WAAM test block, showing deposition strategy and thermal cycle measurement procedure

The temperature measurements were captured in-situ using R-type thermocouples. The thermocouples were attached into the weld pool, just behind the arc using the methods described in Bramfitt, B. L. and Speer, J. G (1990).

The thermocouple was linked to a digital LabVIEW equipment which captured and stored the temperature measurements at a sampling rate of 10 kHz. To investigate the cooling rate along the deposited block, the temperature measurement was tracked at four (5) different points along the height of the block. The thermocouple attachments are illustrated as shown in Figure 4-2.

4.1.4 Non-destructive test on block

After deposition, the block was machined. Dye penetrant test was conducted to assess the quality of the block and check for any surface defect. Thereafter, 100% volumetric examination by ultrasonic method was conducted to ascertain

the internal quality of the WAAM block. The ultrasonic test was conducted according to ASTM A578 Level C standard.

4.1.5 Heat treatment study

Several initial heat treatment trials were conducted to select suitable range of Post Deposition Heat Treatment (PDHT) parameters. The study was conducted in accordance with the guidance given in ASME boiler and pressure vessel code section VIII and EN13445 unfired pressure vessel construction codes, as applicable to heat treatment of 2.25Cr 1Mo alloy. A total of nine (9), WAAM samples (A – I) were used in the study. The range of heat treatment parameters applied is given in Table 4-3.

Table 4-3 Post deposition heat treatment (PDHT) matrix

Post deposition heat treatment (PDHT) parameter matrix		Peak temperatures (°C)		
		670	690	710
Heating/cooling rates (°C/hr)	25	A	B	C
	50	G	H	I
	75	F	E	D

During the heat treatment, the specimen was heated to the peak temperature, by gradually ramping up the temperature at the specified heating rate. After reaching the peak temperature, the specimen was soaked for 1hrs (based on 25mm thickness) at the peak temperature, followed by furnace cooling to room temperature, at a similar rate to the heating rate.

Figure 4-3(a) illustrates the heat treatment cycle, while Figure 4-3(b), shows the heat treatment furnace used in conducting the experiment.

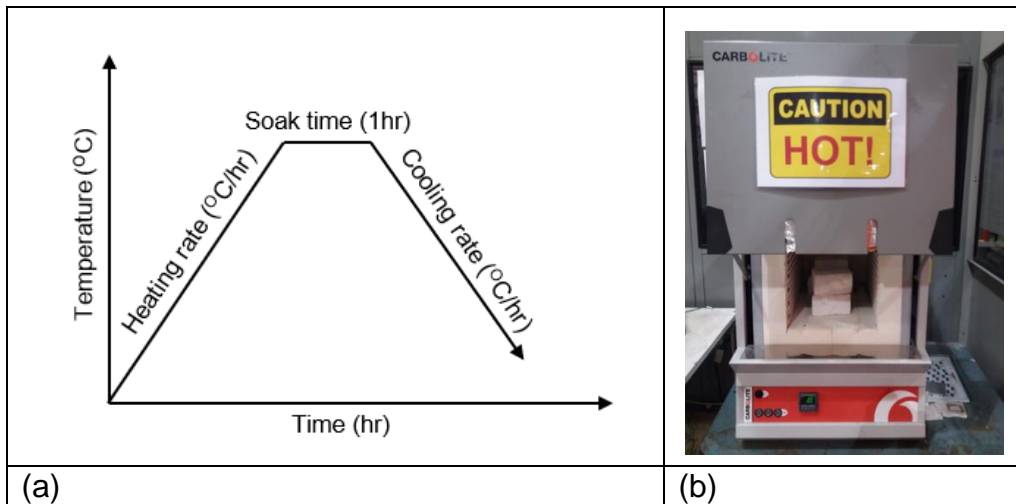


Figure 4-3 Heat treatment furnace used in this study

4.1.6 Microstructural and mechanical analysis

Ten (10) sub-block segments of dimensions (210 x 75 x 25) mm were extracted from the deposited large WAAM block as shown in Figure 4-4.

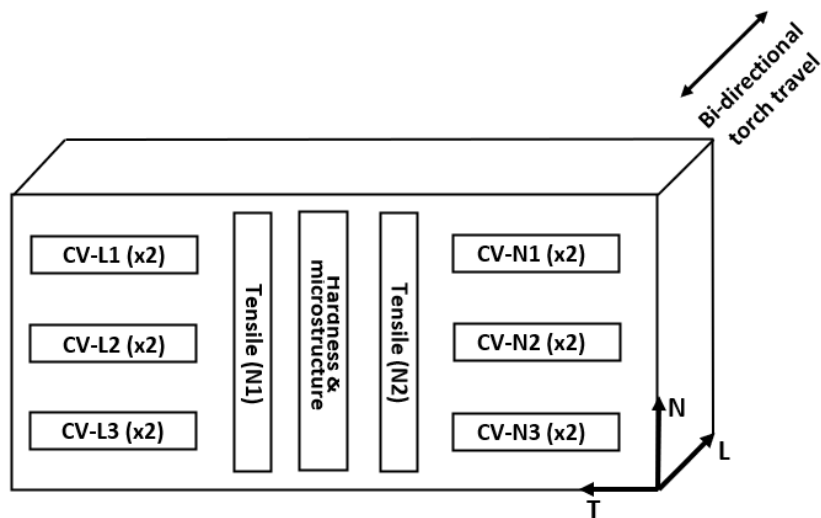


Figure 4-4 Mechanical test matrix

Nine of the sub-block segments were heat treated, while one was used in as-deposited condition. Cross-sectional test specimens for mechanical and microstructural analysis were obtained from each of the block segments according to the test matrix shown in Figure 4-4.

Transverse sections of the samples were prepared for metallographic examination by conventional grinding and polishing methods. Standard

metallographic practice (ASTM E3-11) was utilised in the sample's preparation. After grinding, the samples were etched with 2% Nital and LePera's solutions to reveal specific microstructures. The procedure for conducting LePera's etching is described in LePera, F. S (1979).

Microstructural formations, including inclusion characteristics and Charpy fracture morphology were examined using optical microscope (Nikon Eclipse ME600) and scanning electron microscope (Tescan S8000G), equipped with an Oxford Instruments energy dispersive spectrometer (EDS). The grain size was analysed from XRD pattern, obtained using X-ray diffraction equipment (Siemens D5005) with Cu-K α ($\lambda=1.5406 \text{ \AA}$) with a scanning angle from 20° to 90° and a scanning speed of $2^\circ/\text{min}$.

The SEM inclusion analysis was performed on an unetched specimen, at 8000x magnification. The inclusion size, area fraction and number density were analysed using imageJ analysis software.

Microhardness tests were conducted along the height of the samples at room temperature, in both as-deposited and heat-treated conditions. Vickers microhardness tester (Zwick/Roell Indentec) with a load of 500g and load dwell time of 15secs was used. The micro indentations were made along the plane transverse to the torch deposition direction.

Tensile and Charpy impact tests were conducted on five representative samples, one in the as-deposited and four heat treated conditions. Two cylindrical cross-sections were utilised in evaluating the tensile property of each representative sample. The tensile test pieces were machined to a nominal gauge length of 30mm and gauge diameter of 6 mm. The test was conducted according to ISO 6892-1:2009 Method B.

Charpy v-notch (CV) tests at -59°C were performed on specimen gauge size of 55x10x10mm, using a RKP450 (Zwick-Roell Company, Ulm, Germany) impact testing machine, equipped with a 600J hammer. The test was conducted according to BS EN ISO 148-1:2010 standard.

Two CV samples were each extracted from the top, middle, and bottom portions of the block sub-segments along the deposited height. The notches were placed on the longitudinal (L) and normal (N) planes of the block as follows- (CV-L1 and CV-N1) top section, (CV-L1 and CV-N2) middle section and (CV-L3 and CV-N3) bottom sections, from the top surface of the block as shown in Figure 3.6. The charpy impact fractographs were examined by SEM analysis.

4.2 Results presentation

The results of the various test and analysis conducted on the WAAM block deposited using 2.25Cr 1Mo wire is presented as follows.

4.2.1 Manufactured WAAM block

The manufactured large WAAM block showing the first two layers is presented in Fig 4-5(a), while the completed block (consisting of 21 layers) is shown in Figure 4-5(b). Angular distortion of the substrate occurred during deposition which subsequently stabilised as the build progressed.

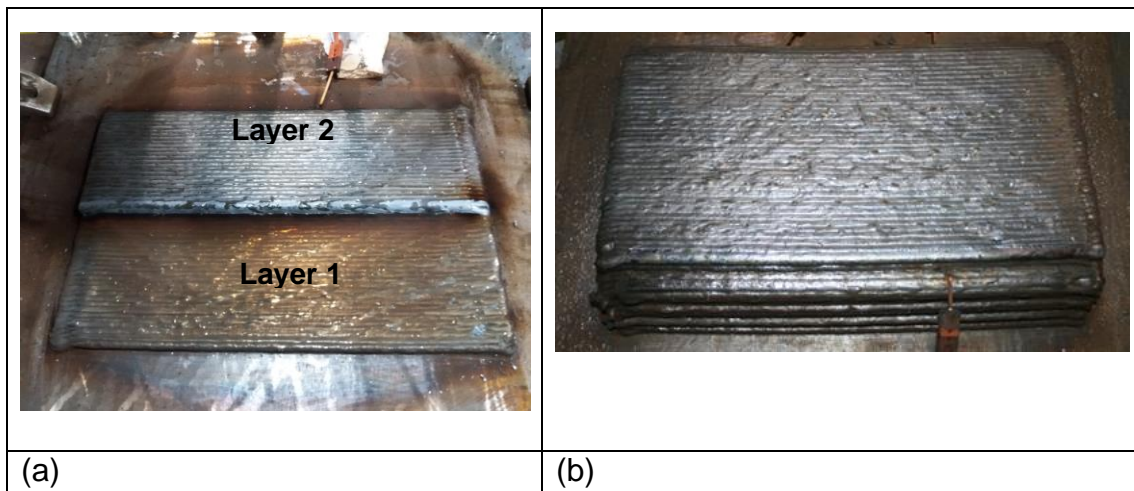


Figure 4-5 WAAM deposited block (a) First two layers (b) Completed block (21-layer)

After completion of deposition, the WAAM block was machined to a finished dimension as shown in Figure 4-6.



Figure 4-6 Machined WAAM block, measuring (320 x 210 x 75) mm

4.2.2 Non-destructive test of WAAM block

Dye penetrant test was conducted to determine the presence of surface breaking defects on the built block, as shown in Figure 4-7. Visual inspection of the surface of the WAAM block did not find any surface defect.



Figure 4-7 Dye penetrant test on WAAM block

Thereafter, ultrasonic examination was conducted (at element test house), to ascertain the internal soundness of the WAAM block. The result revealed some sporadic internal discontinuities, mainly inclusions and porosity. These were however negligible and the WAAM block was deemed acceptable according to ASTM A578 Level C standard.

4.2.3 Thermal cycle evolution during WAAM block deposition

Thermal cycle generation during WAAM deposition process significantly influence the microstructures and grain morphology developed as the material

solidifies. Analysis of the generated thermal cycle can thus provide a basis for determining the microstructural changes occurring in the material (Rodrigues, T. A. *et al.*, 2019).

Temperature readings were tracked using R-type thermocouples (with temperature range of (-50 to 1760^oC). It was attached in the molten weld metal of the first pass of layers 1, 2, 7, 12 and 17, just behind the arc during deposition of the WAAM block, as illustrated in Figure 4-2.

The plots of the measured temperature readings versus time are presented in Figure 4-8. The plots show the thermal histories of the block, comprising of the first four passes at the tracking points positioned on layers 1, 2, 12 and 17.

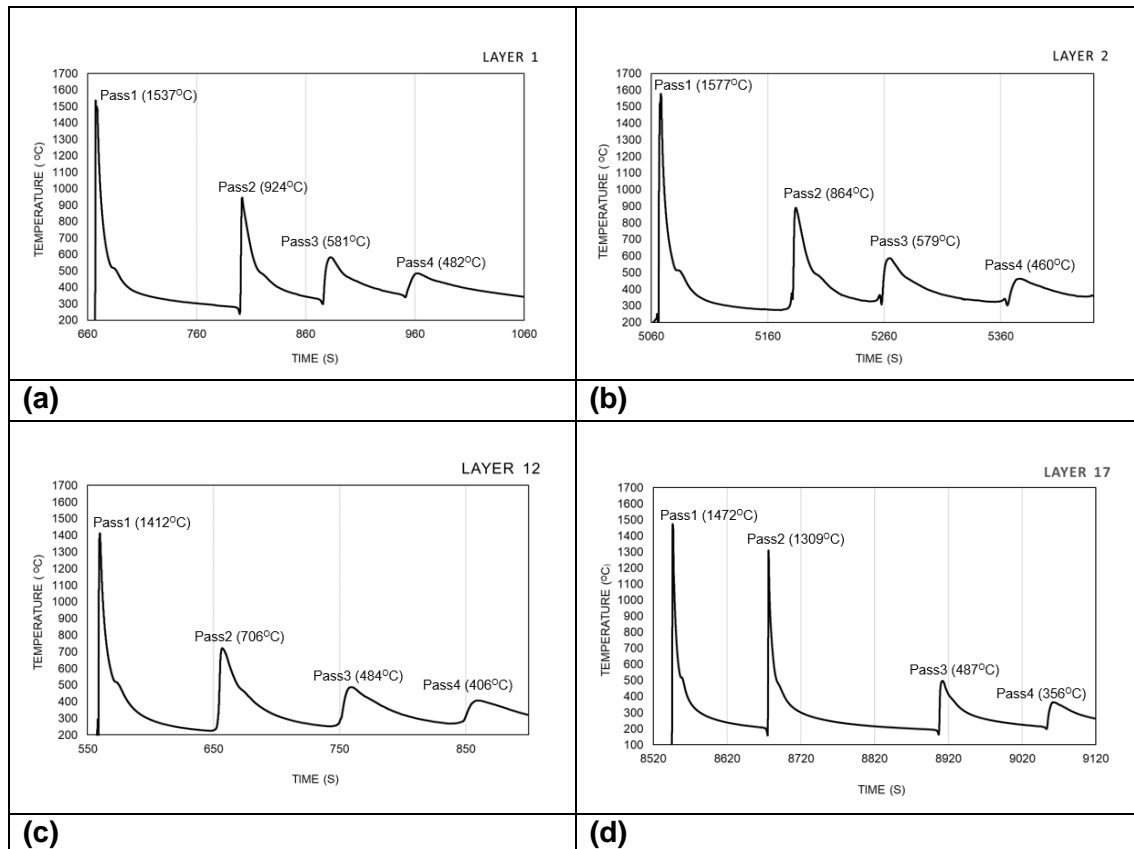


Figure 4-8 Thermal cycle measured during deposition of WAAM block (Using R-type thermocouples, with temperature range of -50 to 1760^oC)

Considering the tracking point in layer 1, Figure 4-8(a), the temperature of the first thermal cycle (i.e., pass 1) was measured as 1537^oC. As subsequent passes were deposited (i.e., Pass2, Pass3. Pass4, etc.), the temperature measured at

the tracking point on layer1, continued to decrease from the initial peak temperature, as the torch moved farther away (i.e., 1537- 924 - 581 - 482) °C.

After pass 4, the temperature measured at the tracking point, became relatively steady, with negligible thermal effect. This diminishing temperature pattern is also observed on the thermal cycle tracking points on layers 2, 12 and 17.

As the number of layers increased, the peak temperatures continued to decrease. Re-austenitisation of materials, for example in layer2, is expected to have occurred at least twice, depending on the peak temperature, as seen from the table. Thereafter, the effect of temperature continued to decrease with successive deposited layers.

At relatively constant heat input, cooling rate depends on the interpass temperature and effect of heat sink from the deposit material and substrate (Grong, O. & Matlock, D. K., 1986).

The cooling rates were computed by measuring the average temperature gradient between (800 – 500) °C (Krauss, G., 1980). It is generally recognised that within this limits of temperature, microstructural evolution could be affected by the cooling rates (Rodrigues, T. A. *et al.*, 2019). Hence cooling rate was not calculated for passes where the peak temperature was below 800°C.

The cooling rates obtained are presented graphically in Figure 4-9. The cooling rates experienced in the WAAM block, during deposition, increased with increasing number of deposited layers, varying between 23.6 and 40°C/s. High cooling rates could lead to formation of predominantly martensite microstructure (Grong, O. & Matlock, D. K., 1986), depending on weld metal composition.

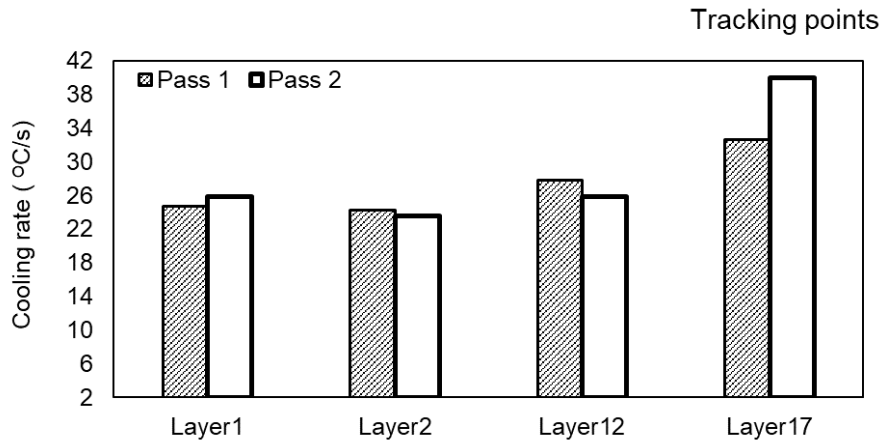


Figure 4-9 Cooling rates (from 800 to 500°C) obtained during deposition of WAAM block

4.2.4 CCT curve of deposited WAAM alloy

The continuous cooling transformation (CCT) diagram of alloy 2.25Cr 1Mo steel, with a comparable chemical composition to ER90S-G wire used in this study is given in Figure 2-45 above.

The cooling rate calculated from the thermal cycle curves ranged between 23.6 and 40°C/s. These values were superimposed on the CCT curve, as shown in Figure 4-10, giving a hypothetical indication of the potential metallurgical phases formed during deposition of the WAAM block. The CCT curve gives Ac3 and Ac1 temperatures as 925 and 815°C respectively.

The superimposed cooling curve suggests that the as-deposited WAAM microstructure could consist primarily of a mixture of martensite and bainitic structures. The relatively high proportions of Cr and Mo in the wire composition, have the potential to produce high hardenability and promote the preferential evolution of lower temperature phases such as bainite and martensite, in the WAAM alloy (Castro, R.J. and De Cadenet, J. J, 1968).

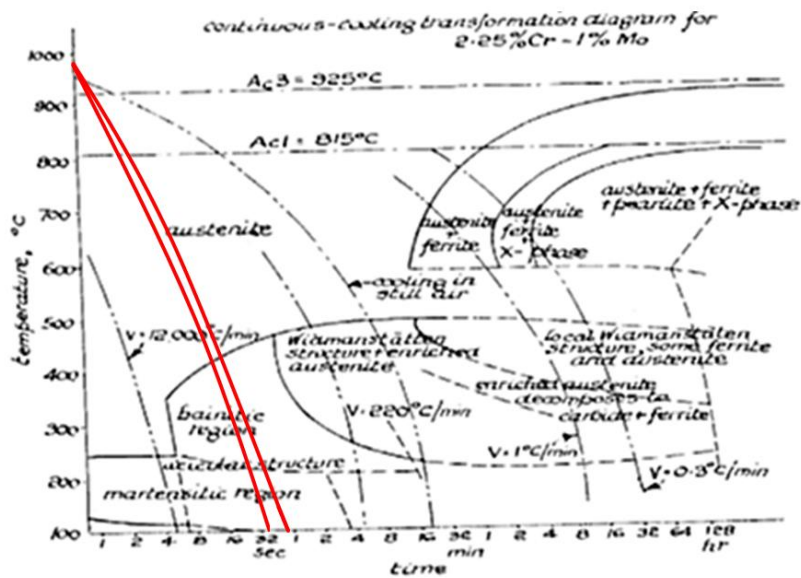


Figure 4-10 Superimposition of experimental cooling rates on CCT curve of a similar 2.25Cr 1Mo alloy.

4.2.5 Post deposition heat treatment (PDHT) of WAAM block

The high cooling rate and uneven heating and solidification which occurred during deposition of the block have the potential to produce hard martensite microstructure and generate high residual stresses and distortion. This could lead to cracking and premature failure of the WAAM alloy, hence heat treatment was conducted to produce desirable properties (Kalyankar, V. D. and Chudasama, G., 2018).

Prior to heat treatment, the machined WAAM block was split into sub-block segments of equal size, with dimensions measuring 210x75x25 mm, as shown in Figure 4-11.

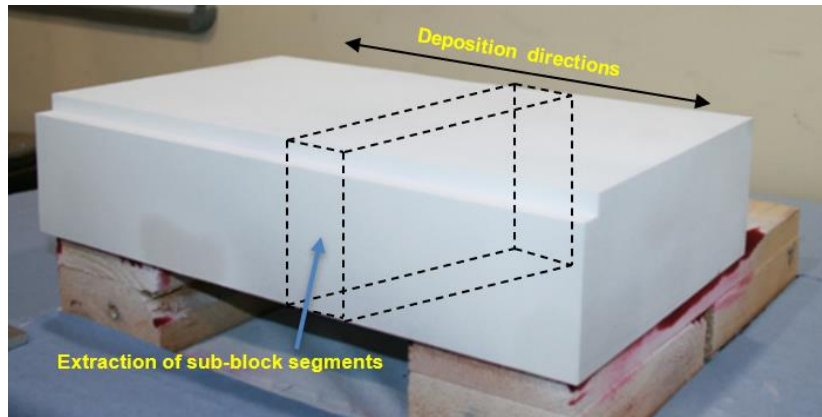


Figure 4-11 Extraction of individual sub-block sub-segments, from the deposited WAAM block (measuring 210x75x25)

The post deposition heat treatment was conducted as described in section 4.1.5, and according to the heat treatment matrix given in Table 4-3.

4.2.5.1 Influence of thermal cycle and PDHT on hardness of WAAM block

Vickers microhardness hardness analysis was performed to evaluate the effects of thermal cycle and PDHT on the hardness properties of the WAAM weldment, as described in section 4.1.6. The hardness was measured in the as-deposited and heat-treated conditions, along the full height of the large WAAM block.

A total of 96 indentations (comprising 3 rows of 32 columns), were made at intervals of 2mm and 3mm along the build and transverse (travel) directions respectively, as illustrated in Figure 4-12.

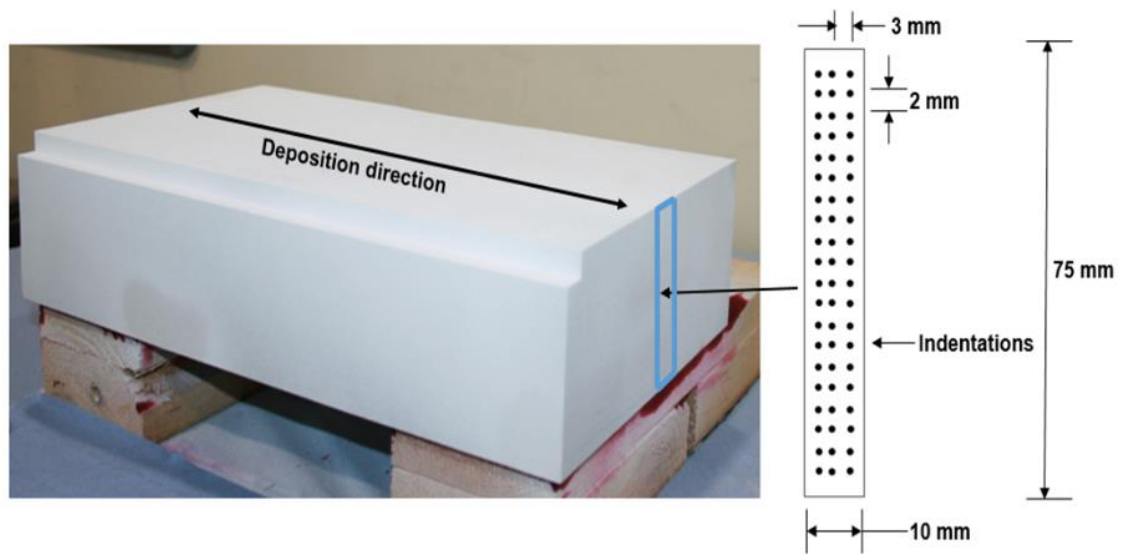


Figure 4-12 Micro-hardness measurement method

The plot of average hardness values with respect to the build height, in the as deposited is presented in Figure 4-13(a).

The scatter plot showed a significant variation hardness values measured on the block, in as-deposited condition, and ranged between 236 and 361HV. This indicated heterogeneity in hardness and could also be associated with microstructural variations in the deposited WAAM block (Wang, X. L *et al.*, 2017).

The variations in microhardness values could be due to two factors. One is the relatively small load applied. The smaller the load, the smaller the area fraction of phase covered by the indentations. Secondly, the microhardness changes with respect to the position of deposited bead within the entire structure. This is because of changes in cooling rates, grain sizes and tempering effects occurring within the built.

The plot also showed increasing hardness gradient along the built height, indicating that hardness value increased with increase in the number of deposited layers.

Figure 4-13(b) shows the scatter plot of hardness values measured along the built height of the block, after PDHT, obtained using four representative heat-treated samples. The samples include the following:

- Sample F: Heat treated to 670°C, at a heat/cooling rate of 75°C
- Sample G: Heat treated to 670°C, at a heat/cooling rate of 50°C
- Sample H: Heat treated to 690°C, at a heat/cooling rate of 50°C
- Sample I: Heat treated to 710°C, at a heat/cooling rate of 50°C

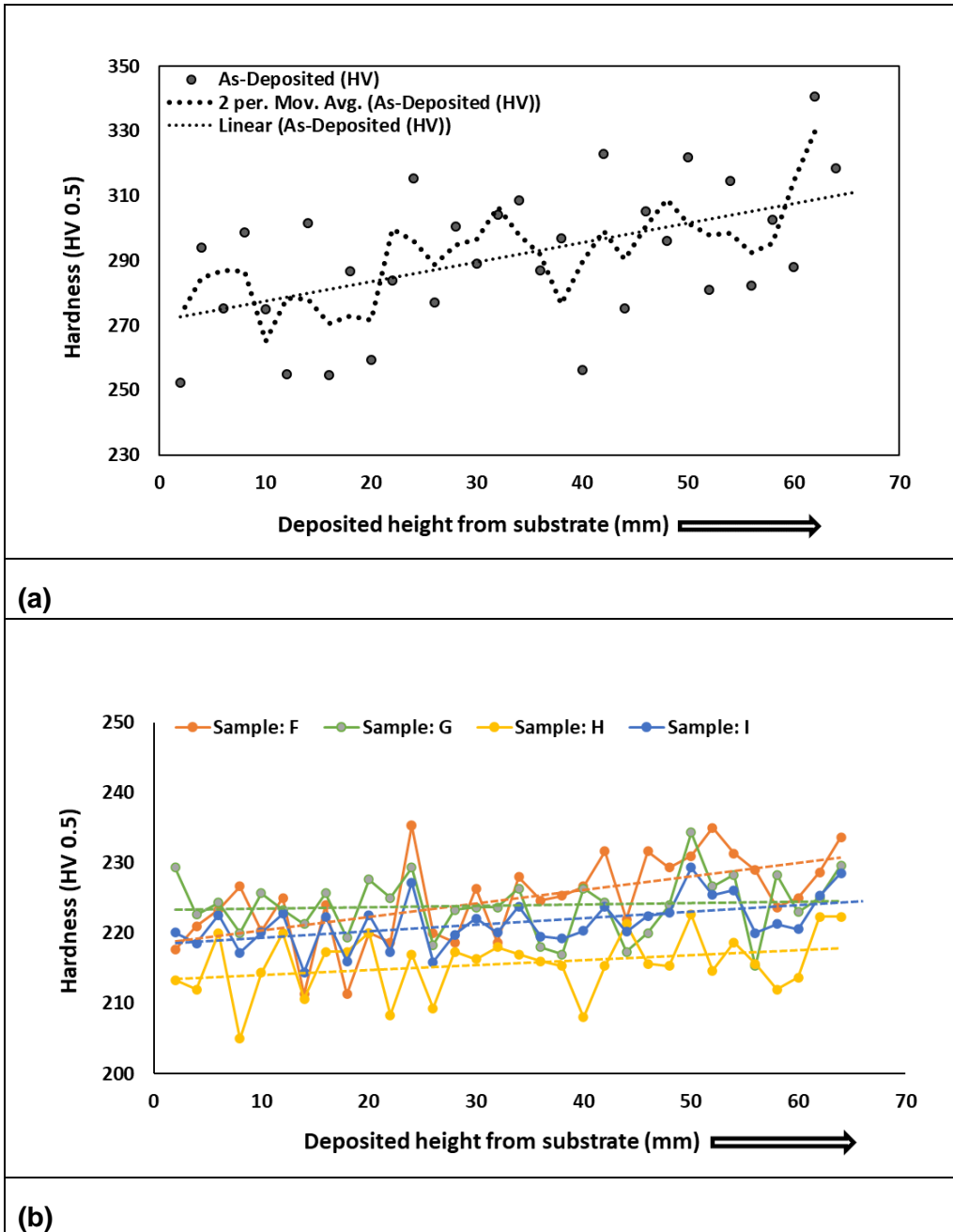


Figure 4-13 Hardness survey taken along the built height of the WAAM block, in (a) as-deposited, and (b) PDHT conditions

A plot clearly shows a reduction in the hardness gradient obtained after PDHT. Also, the variation in the measured hardness values also reduced, ranging between 193 and 246HV.

The standard deviation in hardness measurements, computed for the block samples in as-deposited condition was 22. While the heat-treated samples were between 4 and 6. The lower standard deviation value of the heat treated WAAM samples show that the applied heat treatment perhaps produced a more homogenous microstructure and softening of the hard martensitic phases, developed during manufacture of the WAAM block (Zhang, L. *et al.*, 2015).

The graph in Figure 4-14, shows the measured hardness values, plotted to compare the effect of the different heat treatment parameters applied in the study. Thirty (30) indentations were used in this analysis, covering about 1/3 of the build height.

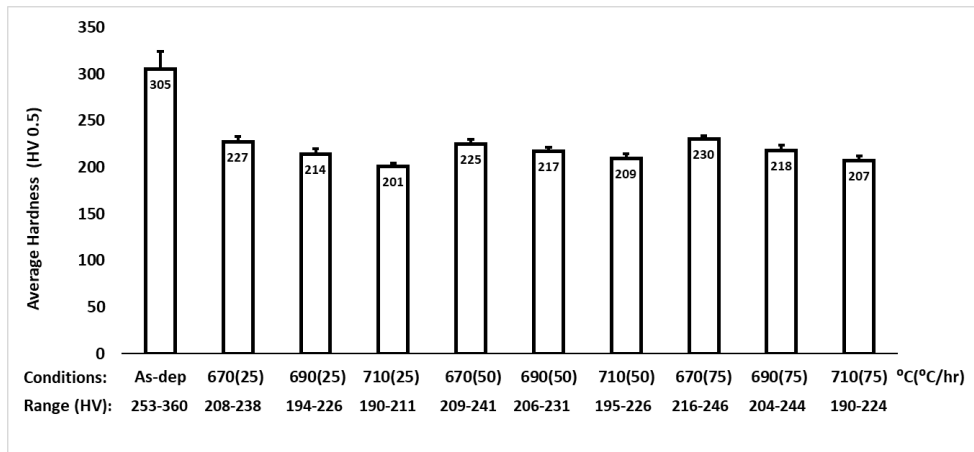


Figure 4-14 Comparing the effect of PDHT parameters, with respect to as-deposited sample. Error bars indicate variations in hardness value.

It shows that the maximum hardness measured on the WAAM alloy in as-deposited condition was 360HV; while the maximum hardness measured in the heat-treated condition was 246HV.

The maximum hardness of 360HV measured in as-deposited samples, indicates the presence of hard martensitic phases in the WAAM alloy. The reduction in the

peak hardness to 246HV, after PDHT, indicates the formation of tempered martensitic phases.

At a constant heating/cooling rate, the hardness of the WAAM alloy is observed to decrease as the heat treatment temperature was increased. But considering a given heat treatment temperature, a change in heating/cooling rate appears to produce a minimal change in the measured hardness. The effect of heating/cooling rate on hardness property is therefore less significant, compared to effect of temperature change (Hollomon, J.H. and Jaffe, L.D, 1945).

4.2.6 Microstructure of as-deposited WAAM alloy

The samples for microstructural analysis were obtained as illustrated in Figure 4-15, and the microstructures were analysed along the build height corresponding approximately to locations within the top, middle, and bottom sections of the block, as shown.

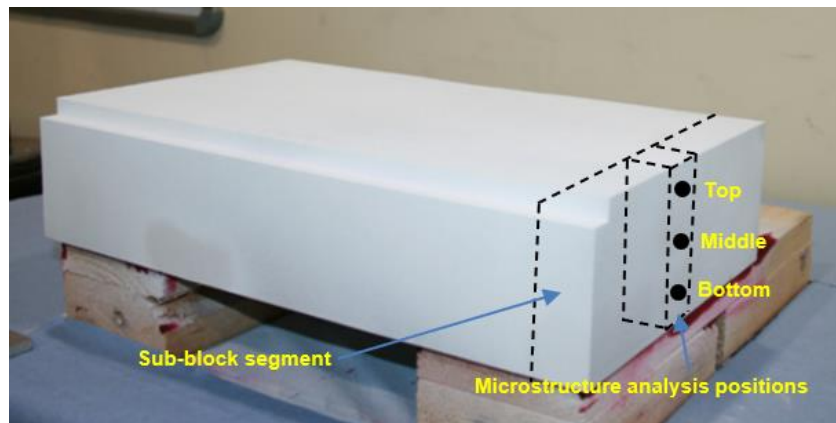


Figure 4-15 illustration of microstructure analysis on WAAM block samples

Figure 4-16 displays the representative microstructures obtained at 200x and 400x magnifications, after etching with 2% Nital solution, in as-deposited condition. The microstructure consists of a mixture of reheated fine and coarse grain structures, corresponding to different peak temperatures.

The microstructure appears to consist of mainly martensite (M) and bainite (B) structures. Other microstructural constituents such as different ferritic structures

and retained austenite could also have existed, but their low dimensions, coupled with the low resolution of the micrographs limited their accurate identification.

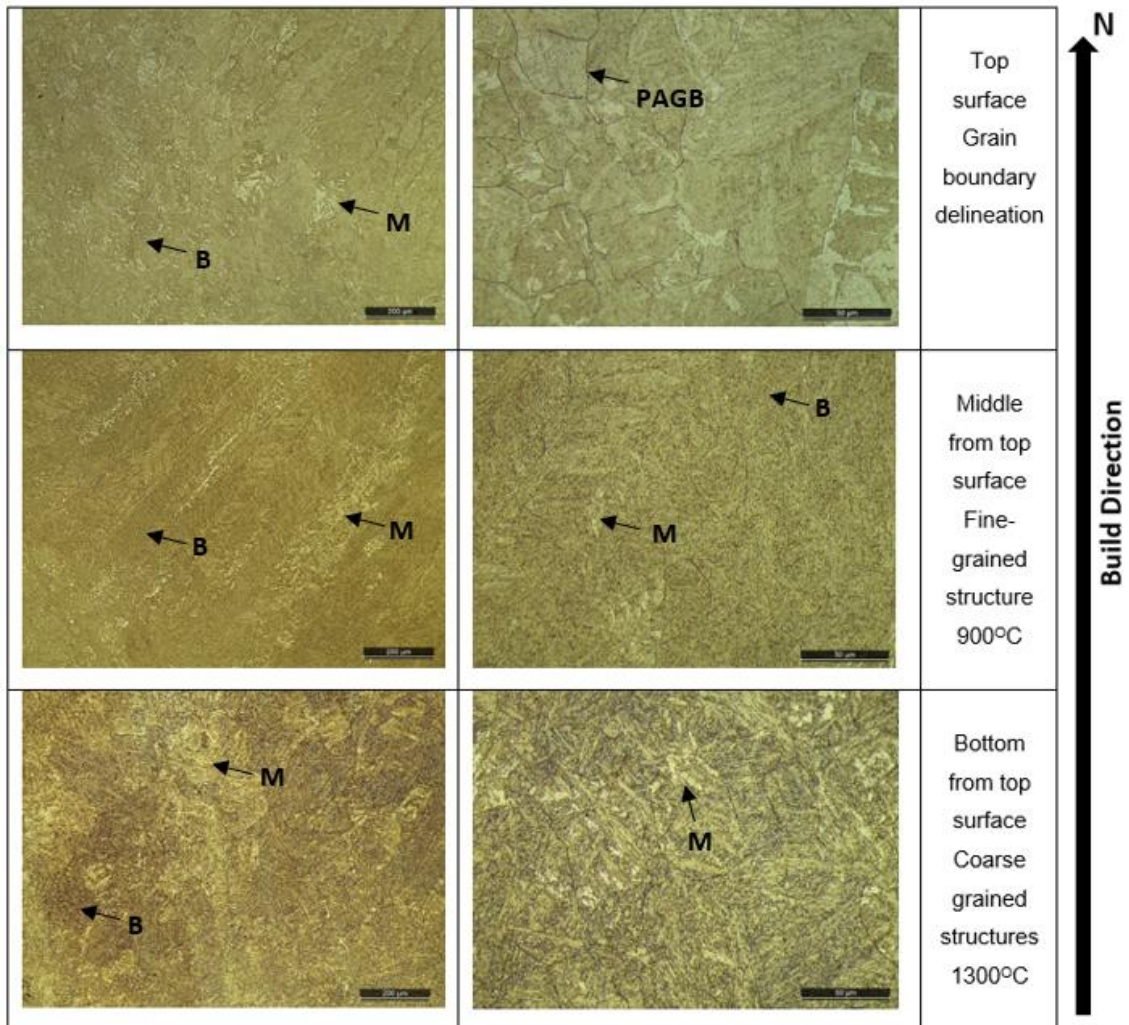


Figure 4-16 Microstructure of WAAM block sampled along the deposited height (lower and higher magnifications)

SEM microstructure analysis of the block sample was conducted at higher magnification (10000x), in as-deposited condition, after etching with Le’Pera solution. The microstructure was identified according to the method described by LePera, F. S., in which martensite appeared white, bainite appeared black and ferrite appeared gray (LePera, F.S., 1979).

Figure 4-17 present the SEM image of the WAAM microstructure. The microstructure shows a heterogenous dispersion of martensitic (M), bainitic (B)

and ferritic (F) structures. Dispersion of black spherical particles were also visible within the microstructure. EDS chemical analysis of the particles showed that they contain high proportions of Mn and Si. This perhaps indicates they are non-metallic oxide inclusions of Mn and Si, as reported in (Na, H. et al., 2018).

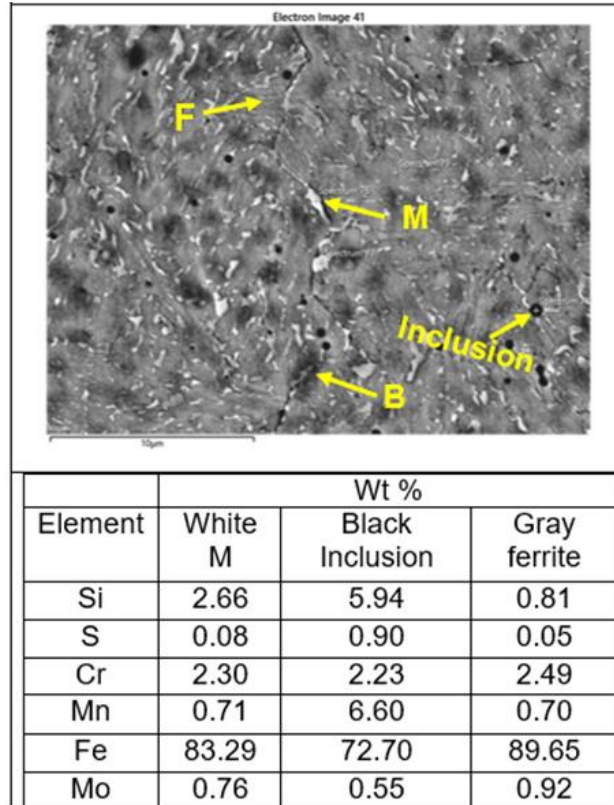


Figure 4-17 High magnification, SEM-EDS image of WAAM block sample, showing heterogenous dispersion of microstructural phases

The multi-pass deposition process could result in the formation of martensite-austenite (M-A) constituents, due to subsequent passes reheating the previously deposited material at lower temperatures. The presence of necklace-type M-A constituents in the intercritical coarse-grain heat affected zone (ICCHAZ) region of the WAAM alloy is not desirable. This is because they could cause deterioration in charpy impact toughness, due to the effect of stress concentration at the M-A constituents (Rodrigues, T. A. et al., 2019; Wu, K. et al., 2020).

4.2.7 Microstructure of WAAM alloys after PDHT

Figure 4-18 show SEM micrographs of Le'Pera etched microstructures for the selected as-deposited and heat-treated WAAM ER90S-G samples.

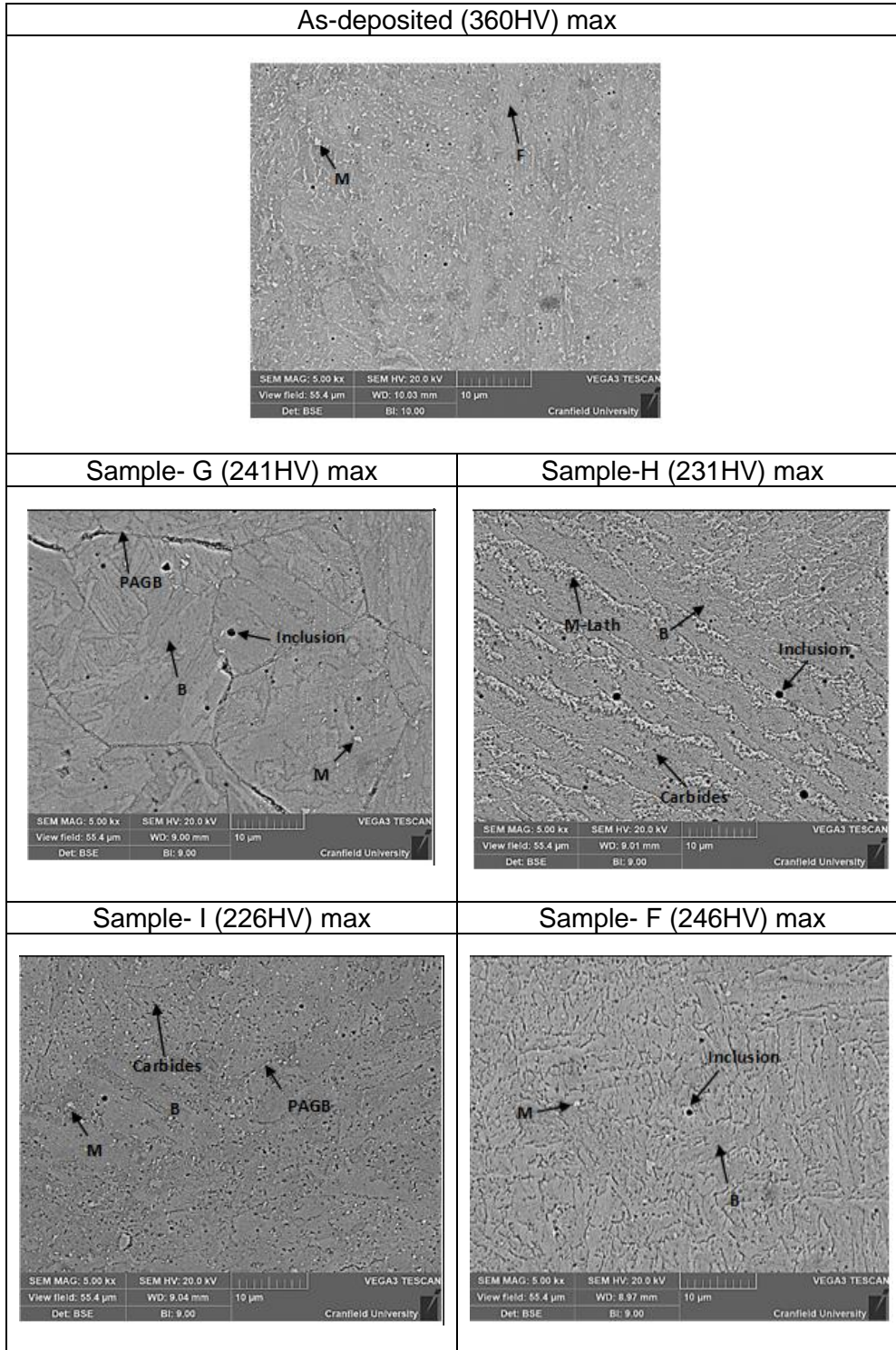


Figure 4-18 Le'Pera etched microstructures of WAAM 2.25Cr 1Mo alloy (in as-deposited and heat-treated conditions)

After heat treatment, the microstructure showed a transformation from predominantly fine martensitic and bainitic structures to a combination of tempered martensite, granular bainite and ferrite structures. Precipitates of carbides and inclusions are also visible within the microstructures (Peddle B. E. & Pickles C. A., 2001; Andrén, H. O. et al., 1995; Wu, K. et al., 2020). The grain sizes appear enlarged with higher delineation of prior austenite the grain boundaries (PAGB) which is visible in sample G.

4.2.8 Analysis of inclusion in the WAAM block

The distribution of inclusions in the WAAM block was sampled within the top 25mm, middle 50mm and bottom 75mm sections of the block. Thirty (30) macrographs of randomly sampled inclusions were used for the analysis. The samples were obtained from polished and unetched metallographic sections of the WAAM block in the as-deposited condition. Figure 4-19 shows representative SEM macrographs of inclusion distributions obtained at 8000x magnification.

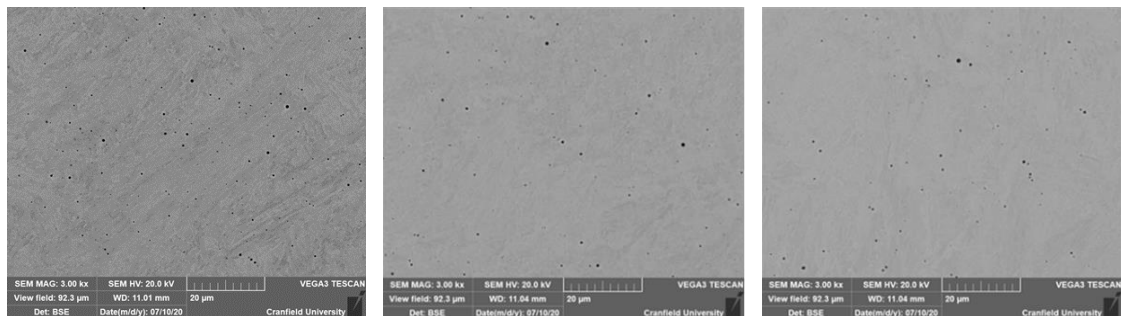


Figure 4-19 Distribution of inclusions in the deposited block

The distribution showed several micro-size inclusions which were predominantly spherical in shape and have been trapped owing to the high freezing rate of the weld metal (Andrén, H. O. et al., 1995). The inclusions were generally non-uniformly distributed. Table 4-4 shows the measured inclusion characteristics determined by quantitative analysis.

It was observed that the inclusion mean size (average diameter of $0.371\mu\text{m}$), was smallest in the bottom section of the deposited block, followed by the middle and then top sections showing the largest average inclusion size of $0.424\mu\text{m}$. This can be attributed to the possible thermal dissolution of larger inclusion sizes

during subsequent deposition passes. (Babu, S. S. *et al.*, 2004; Hong, T. *et al.*, 2000).

Table 4-4 Characteristics of oxide inclusions in the deposited weld block

<i>Block section</i>	Inclusion counts	Area fraction (% Area)	Mean size (µm)
<i>Top</i>	4591	0.492	0.424
<i>Middle</i>	5559	0.486	0.398
<i>Bottom</i>	5594	0.487	0.371

The inclusion number density (5594) was observed to be highest in the bottom section and lowest (4591) in the top section of the block. A higher volume of inclusion may be detrimental to the toughness property of the WAAM metal, owing to initiation of brittle failure (Tweed and Knott, 1983).

The cooling rate obtained during manufacture of the block was earlier found to be higher in the top section, compared to the bottom section. Hence, the inclusion number density observed is contrary to the report by other authors who found that higher cooling rates produced smaller inclusion particle sizes, with higher number density (You, D. *et al.*, 2017) and more inclusion will be obtained with the increase in oxygen content (Chen, C. *et al.*, 2014). Hence, the expectation would be for the higher inclusion density and smaller size to occur in the top section of the WAAM block.

Quantitative chemical analysis of the inclusions were performed by SEM (EDS) technique as shown in Figure 4-20.

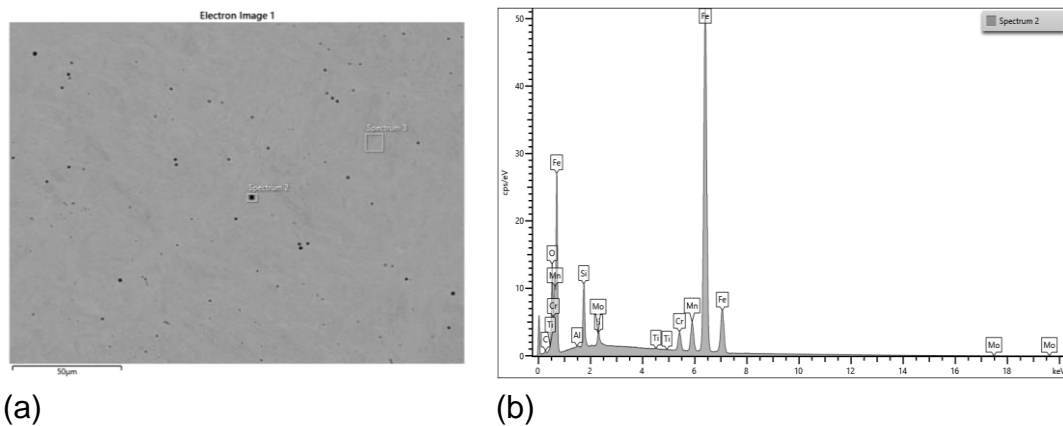


Figure 4-20 WAAM sample showing (a) Distribution of inclusion (b) EDS chemical analysis spectra

Analysis of the inclusions showed silicon (Si) and manganese (Mn) peaks, indicating the particles are primarily $\text{MnO} \cdot \text{SiO}_2$ inclusions (Koseki, T., 2005).

4.2.9 X-Ray diffraction analysis of WAAM alloy

X-ray diffraction analysis was conducted on selected WAAM samples in as-deposited and heat-treated conditions. Samples G, H and I, heat treated to temperatures of (670, 690 and 710) °C respectively, at 50 °C/hr heating rate, were used for the analysis. The XRD spectra of the samples, are shown in Figure 4-21.

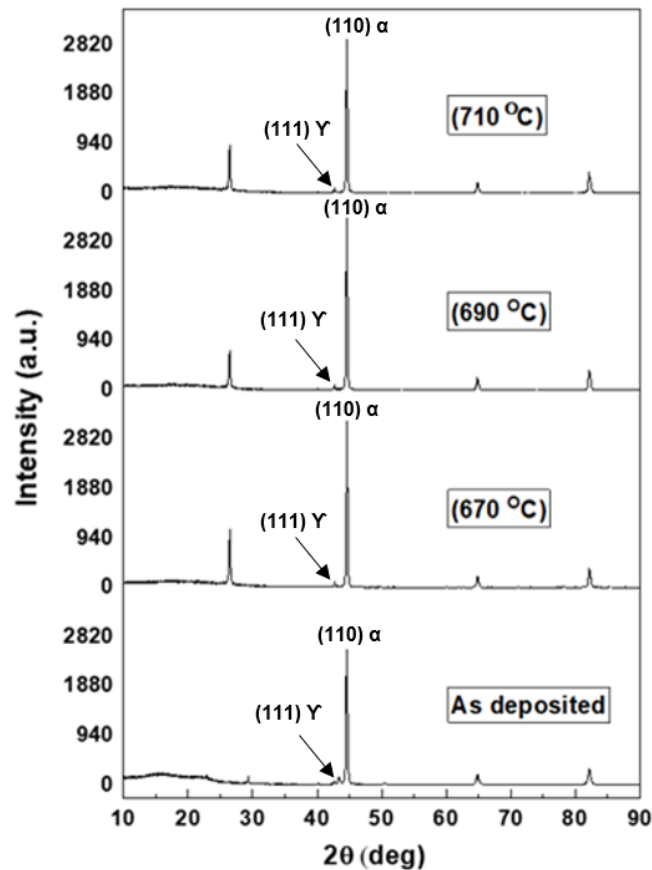


Figure 4-21 XRD spectral of ER90S-G WAAM weldment in as-deposited and heat-treated conditions, showing the retained austenite {111} planes, and ferritic {110} planes.

The XRD plot shows a relative increase in the peak intensity of the ferrite phase, with increase in heat treatment temperature from 670°C to 710°C. It also shows a small peak of retained austenite, which appeared to decompose with increase in temperature, but the transformation was not entirely completed.

The increase in tempering temperature is expected to produce an increase in the microstructure grain size, which could be accompanied with a decrease in dislocation density.

4.2.10 Tensile and charpy impact toughness tests

Tensile and charpy impact tests were conducted on the WAAM sample in as-deposited condition. The representative heat-treated samples utilised for further

mechanical tests were selected after assessing the hardness values obtained from the PDHT study.

4.2.10.1 Influence of thermal cycle and PDHT on strength of WAAM alloy

Tensile properties of the WAAM specimens were measured using a 30-ton (294kN) capacity, Instron 5582 testing machine. The yield strength was evaluated by 0.2% strain offset stress. Two tensile test-pieces per sample were extracted from the normal plane (N), along the build direction as shown in Figure 4.4.

The result of tensile tests conducted on the samples in as-deposited and PDHT conditions is presented in Table 4-5.

The results showed that the room temperature yield strength (YS) and ultimate tensile strength (UTS) of the samples decreased after heat treatment. Average percentage elongation before failure of the samples increased from 19% in the as-deposited condition, to approximately 21% after heat treatment.

Table 4-5 Tensile test results of block samples in as-deposited and PDHT conditions

Samples	UTS (MPa)		Avg. UTS: MPa(ksi)	0.2%YS (MPa)		Avg. 0.2%YS: MPa(ksi)	Elongation %(EL)		Avg. %EL
As-dep.	863	848	856(124)	570	713	641(93)	17.8	20.2	19.0
G	661	660	661(96)	550	545	548(80)	22.6	18.47	20.6
H	632	629	630(91)	520	515	518(75)	20.6	20.6	20.6
I	599	600	599(87)	473	477	475(69)	19.5	22.72	21.1
F	667	663	665(97)	625	438	531(77)	18.6	22.79	20.7
Substate (S355)	470	630		335	345		22	22	22

The maximum UTS and YS of the as-deposited WAAM samples were (863 and 713) MPa respectively. Considering the samples heat treated at the rate of 50°C/hr, the maximum UTS and YS of the samples were (661 and 550) MPa respectively.

The reduction in tensile strength after PDHT is consistent with the reduction in hardness earlier observed. The tensile values are generally within the range specified in this study.

Increase in heat treatment temperature from 670 to 710°C, produced a decrease in the tensile strength. The highest PDHT temperature of 710°C applied to sample 'I', at a heating/cooling rate of 50°C/hr, produced the lowest tensile values (of 531MPa YS and 665MPa UTS), compared to 670 and 690 °C. The values were lower than the minimum specified in this study.

The sample 'F', heat treated at the rate of 75°C/hr to 670°C peak temperature, showed a wider range in YS, compared to sample (G) heat treated at the rate of 50°C/hr to the same peak temperature. This could be attributed to the formation of local brittle zones, due to the faster heating rate. This is because high heating rate could produce insufficient tempering of the 2.25cr 1Mo weldment, which could lead to formation of partial or non-uniformly tempered hard martensitic or bainitic microstructures in the WAAM material (Kalyankar and Chudasama, 2018).

4.2.10.2 Effect of thermal cycle and PDHT on charpy impact toughness of WAAM alloy

The charpy impact tests were performed at sub-zero temperature of -60°C. The detailed charpy impact test results of the ER90S-G WAAM samples, obtained in as-deposited and PDHT conditions are given in Appendix K.

Figure 4-22 gives the average charpy impact energy absorbed by the samples during the tests. It is obvious from the result that the average impact energies achieved from the heat-treated samples were significantly higher, compared to the impact energy obtained from the as-deposited WAAM samples.

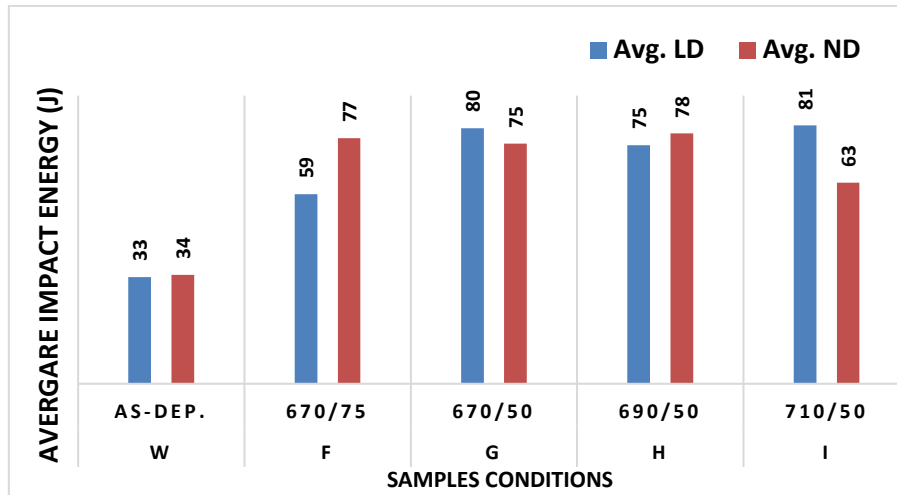


Figure 4-22 Average charpy impact tests obtained at -60°C

The highest average impact energy obtained with the PDHT samples was approximately 80J, compared to 34J obtained in as-deposited condition, representing an increase in charpy impact toughness of up to 135%.

The applied heat treatment temperatures did not show any clear trend with the impact toughness values obtained in the samples. However, lowest heat treatment temperature of 670°C appeared to produce the highest charpy impact toughness, suggesting that impact toughness probably increased with decrease in tempering temperature, within the limit of the parameter utilised.

4.2.10.3 Analysis of charpy impact fracture morphology

In evaluating the fracture morphology of the WAAM samples in both as-deposited and heat-treated conditions, one half of the broken impact test sample was used for SEM fractographic analysis. The second half was prepared by metallographic method for hardness and microstructure analysis. The charpy fracture morphology of representative samples in as deposited and heat-treated conditions are presented in Figures 4-23.

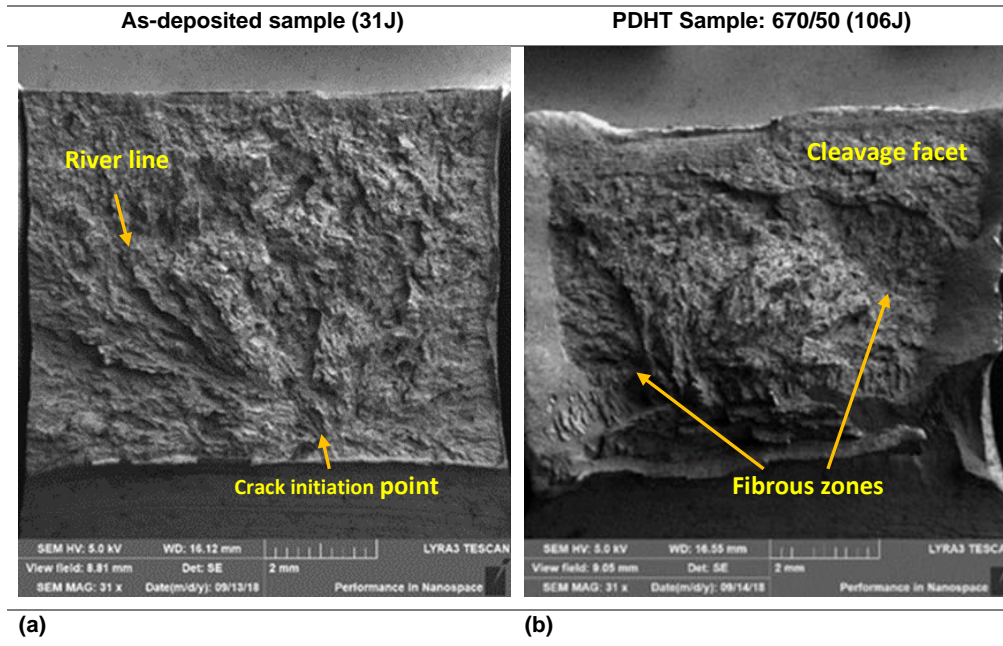


Figure 4-23 Charpy impact fractured samples (a) As-deposited (b) PDHT

The fracture surface of the sample in the as-deposited condition were characterised by the presence of predominantly bright, crystalline cleavage facets (transgranular fracture) as shown in Figure 4-23(a). River marks pattern can also be observed. The river marks begin from areas with pre-existing discontinuity, which preferentially promotes the initiation of the brittle fracture and are generally perpendicular to the advancing front of the crack (Barbosa, C. *et al.*, 2011). This is more indicative of a brittle fracture mode.

The top view of the PDHT fracture sample shows a small area of cleavage facet near the final fibrous zone. But the sample mostly showed various degrees of dull and large fibrous zones, Fig. 4-23(b). This fracture morphology is more indicative of a ductile fracture mode.

Figure 4-24 shows detailed SEM images of the charpy impact fracture zones of the samples. The as-deposited sample show shallow and non-equiaxed dimples. Conversely, the PDHT samples show predominately cup and cone dimples, with widespread micro-void coalescences. The dimples in the PDHT samples also appear more equiaxed and deeper compared to the as-deposited counterpart.

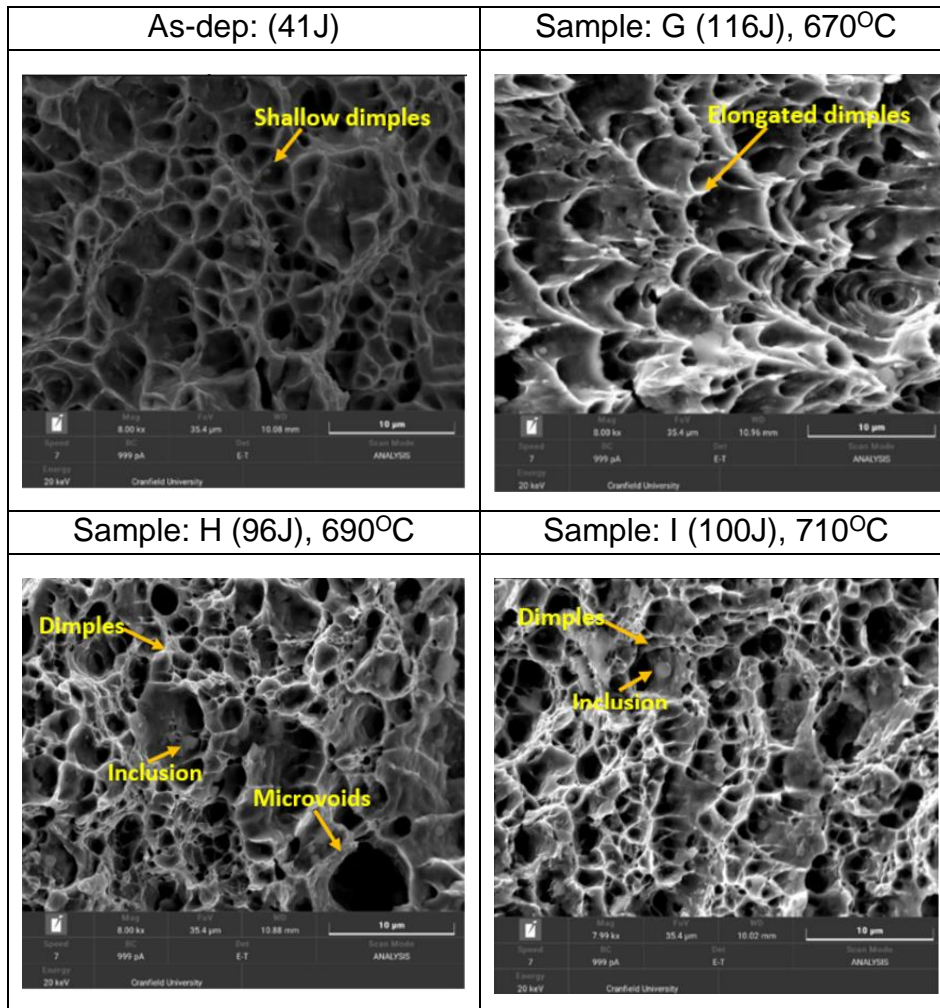


Figure 4-24 SEM images of charpy v-notch impact samples in as-deposited condition and heat-treated at 50°C/hr heating/cooling rate

The dimples in the sample heat treated at 670°C temperature and heating rate of 50°C/hr appeared more elongated. This is indicative of a larger plastic deformation zone and hence higher absorption of impact energy before final failure (Sun, C. *et al.*, 2018).

Microstructure is the most important factor which determines the toughness and strength of steel alloys. The grain size, non-metallic inclusions or solute alloy elements also have additional important influences (Zhang, T. *et al.*, 2015).

The microstructures of the charpy v-notch specimens are shown in Figure 4-25. In the as-deposited condition, the microstructure show needle-like and brittle

martensitic structures, which are indicative of higher strength, but could potentially be detrimental to impact toughness.

The microstructures of PDHT samples show tempered martensitic and granular bainite (bainite and M-A constituent). The grain sizes appear enlarged with delineation of the grain boundaries. High dispersion of carbides is also visible as seen in sample 'I'. These features are all associated with reduction in strength due to tempering of the hard microstructure and are consistent with the earlier microstructural observations.

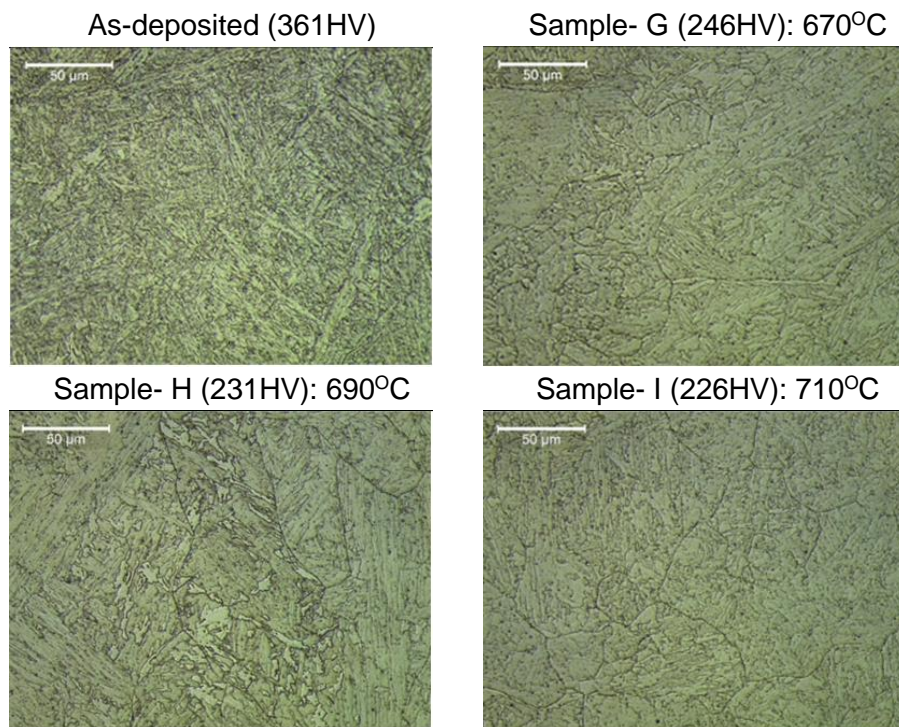


Figure 4-25 Microstructure of charpy v-notch samples, in as-deposited condition and PDHT at a heating/cooling rate of 50°C/hr

4.2.11 Deterioration in charpy impact toughness

Poor charpy impact toughness was observed in some of the samples tested in the heat-treated condition. The low values were predominantly concentrated in the samples extracted from the bottom sections of the WAAM block. An example is seen in sample G, Figure 4-26.

The SEM fractographs of sample G, extracted from the bottom section of the block, shows a characteristic brittle cleavage fracture, and the presence of

needle-like, irregular particle. The presence of several ruptured particles is also visible on the fractograph, Figure 4-26(a).

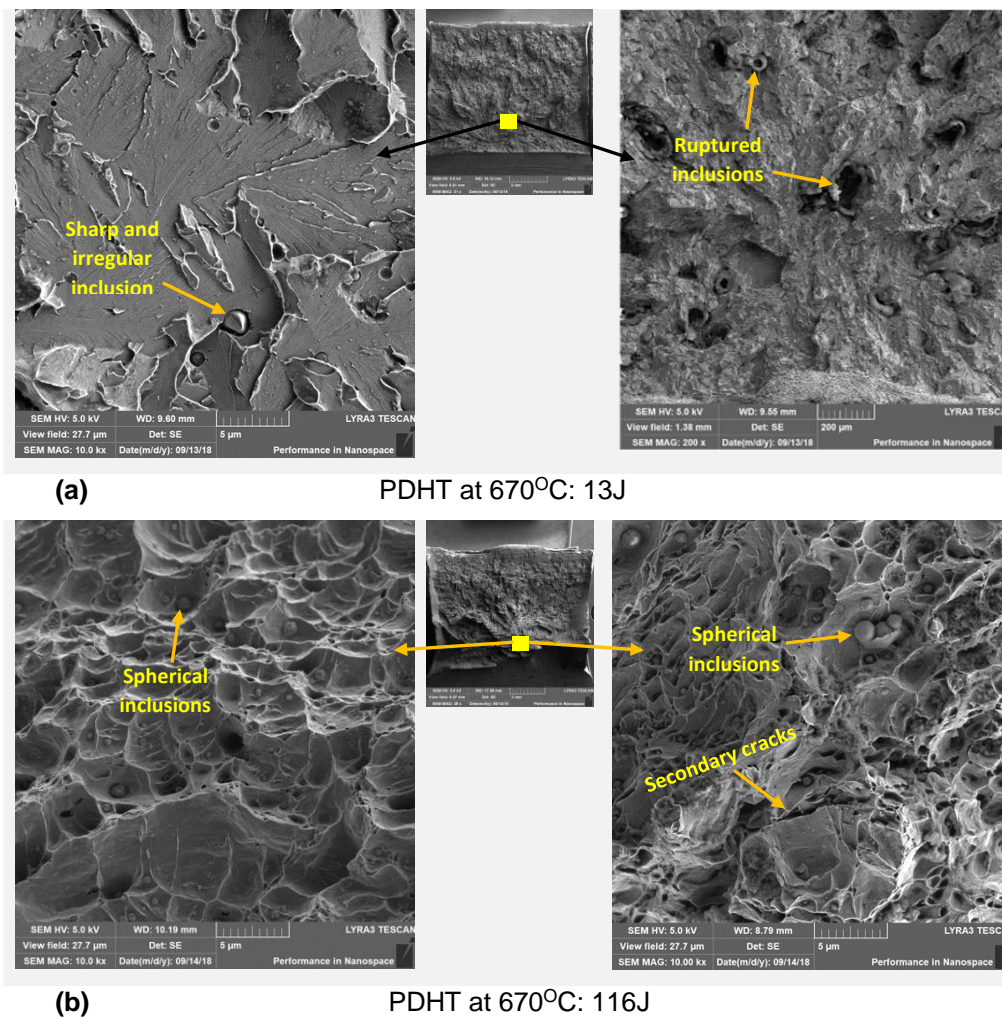


Figure 4-26 Charpy impact fracture WAAM sample G, obtained from: (a) bottom section of block, showing ruptured and irregularly shaped particles (b) top section of block, showing unruptured and spherical particles

However, the charpy fractograph surface of sample G, extracted from the top section of the WAAM block, revealed the presence of several spherical unruptured particles, Figure 4-26(b). The presence of extensive fibrous zones is also visible, indicating a ductile failure mode, which perhaps contributed to the excellent charpy impact toughness of the sample.

The ruptured particles, in the bottom section of the WAAM block, could perhaps be oxide inclusions, which are heterogeneous constituents of the microstructures,

formed during solidification of the deposited 2.25Cr 1Mo weldment (Andrén, H. O. et al., 1995).

Oxide inclusions are generally known to be able to transform the Charpy impact toughness morphology from ductile to cleavage fracture, which could lead to reduction in impact toughness of weld metal, such as found in this study (Elrefaey, A. *et al.*, 2018).

The ruptured particles could also be carbide precipitates formed during PDHT process of WAAM 2.25Cr 1Mo weldment. It has been reported that the dominant carbide which precipitates in 2.25Cr 1Mo weldment after heat treatment is $M_{23}C_6$. At 530°C cementite (M_3C) are precipitated, at 600°C precipitation of M_2C occurs, while above 660°C $M_{23}C_6$ precipitates are produced. The M_2C precipitates consist of a mixture of Mo-Cr carbides (Andrén, H. O. et al., 1995). Detailed analysis of the ruptured particles will be required to accurately identify them.

4.2.12 Quality of deposited WAAM block

Non-destructive examination of the machined WAAM block revealed a fully dense and sound deposit devoid of any surface breaking defect such as lack of fusion or porosity. Volumetric examination of the internal structure of the WAAM block using the ultrasonic technique showed few sporadic indications, attributed to the presence of inclusions and porosity. The porosity is thought to result from atmospheric contamination from the ingress of draught or momentarily low gas shielding.

However, the result of the ultrasonic test was acceptable in accordance with ASTM A578 Level C standard. To minimise experimental error, portions of the WAAM block where defects were identified were excluded during extraction of mechanical test samples.

4.2.13 Evolution of thermal cycle and effect on microstructure of deposited WAAM alloy

During the WAAM deposition process, different sections of the previously deposited layers experienced a complicated thermal history (including rapid

heating, melting, cooling, solidification, and even partial remelting). Relatively high temperature gradients and repeated thermal cycling at any specific location were also generated in the block, as observed in Figure 4-8 (Ge, J. *et al.*, 2018). Hence, the microstructure developed in any section of the WAAM part is directly influenced by the specific thermal history of the materials in that position (Ge, J. *et al.*, 2018).

As the deposition of new passes/layers progressed, the magnitude of temperature induced by the heat from the electric arc, measured at a particular tracking point continued to diminish.

The increase in cooling rate with successive deposition of material is partly because of high heat sink, which increased as the WAAM block increased in size, leading to increase in heat dissipation through previously deposited materials (Ge, J. *et al.*, 2018). The temperature at the tracking point subsequently attained relative stability with further deposition of new passes and layers.

Dissipation of heat through the WAAM metal has a pre-heating effect on previously deposited layers. This is likely beneficial in reducing residual stresses, because of reduction in thermal gradient between successive deposited layers (Bhadeshia H.K.D.H. and Honeycombe R.W.K, 2006; Ge, J. *et al.*, 2018). The preheating effect on previously deposited material could cause the microstructure to temper for longer leading to increased prior austenite grain size, lower hardness, and strength, compare to subsequent weld deposits (Shi, Y. and Han, Z., 2008).

Excessive heat accumulation was not a major concern in this study because the large thickness of the block promoted effective dissipation of thermal energy by conduction through the WAAM part (Grong, O. & Matlock, D. K., 1986).

By superimposing the calculated cooling rates of the block on the CCT curve, Figure 4-10, it could be inferred that martensite formation probably began just before the bainite nose was reached. Hence, it could be possible that the early transformation started off as bainite, but that martensitic transformation prevailed as temperatures lowered and gradually became the dominant phase.

The zones in the WAAM alloy consists of high-temperature and low-temperature reheated zones, with corresponding peak temperatures of approximately 1,400°C and 800°C, respectively (see Figure 4-8). Consequently, the microstructure in these zones could be characterised by coarse and fine-grained structures respectively (Yang, L. *et al.*, 2015).

Subtleness in microstructure and nomenclature could make conclusive designation of martensitic and bainitic structures, in absolute terms misleading. The Le'Pera etched microstructure in as-deposited condition, showed high dispersion of white martensitic structures within the bainite-ferrite matrix as shown in Figure 4-17 and 4-18. After heat treatment, the WAAM deposit displayed a combination of tempered martensite, bainite and ferrite microstructures. Dispersion of large dark spherical particles identified as oxide inclusions are also visible. Apart from the larger inclusion particles, the heat-treated samples also display a fine-scale dispersion of dark particles within several areas, which perhaps are carbides precipitation, observed mostly in samples H and I, in Figure 4-18.

4.2.14 Inclusion characteristics

Non-metallic oxide inclusions of SiO₂ and MnO, formed from deoxidising elements including silicon and manganese are integral constituents of weld metal irrespective of the metal deposition process utilised. The inclusion characteristics depend on the wire composition, number of passes, heat input and solidification behaviour of the deposited metal (Pamnani, R. *et al.*, 2016).

Chemical analysis of the inclusions in the manufactured block, showed they are composed of Si and Mn oxides, Figure 4-20. This is expected as these elements are the main deoxidising agents present in the wire composition used. These non-metallic inclusions in weld metal can act as sites for nucleation of acicular ferrite microstructure or initiation point for the propagation of cleavage crack (Bose-Filho, W. W. *et al.*, 2007; Avazkonandeh-Gharavol, M. H. *et al.*, 2009).

Quantitative analysis showed that the smallest inclusion size occurred in the bottom section of the WAAM block, compared to the top portions. Also, the

inclusion number density at the bottom section was about 22% higher, compared to the numbers in the top section of the WAAM block.

But this study found that the cooling rate at the top section of the block was a least 36% higher than the bottom section, and the general knowledge, is that higher cooling rate leads to formation of higher number density and finer inclusion sizes. Hence this observation cannot be conclusively taken as representative of the complete WAAM block, especially because of the small size of the sample used for the analyse.

However, the tendency for the oxide inclusions to act as initiation sites for brittle failure, and lead to poor charpy toughness of the WAAM alloy could be higher within the bottom section of the WAAM block, owing to the relatively higher number density of inclusion present (Pamnani, R. et al., 2016).

4.2.15 Effect of thermal cycle and heat treatment on deposited mechanical properties

The microstructure of the 2.25Cr 1Mo WAAM alloy in as-deposited condition consisted of a combination of hard and brittle martensite, bainite, ferrite and M-A constituents. It also likely consisted of carbide precipitates which are rich in elements including Fe, Cr, Mo, Mn, and C. The thermally stable oxides such as Mo₂C is a major factor which impacts high strength and hardness to 2.25Cr 1Mo alloy (Wang, W. et al., 2013). The presence of martensite and blocky M-A constituents also impact higher strength and hardness to the alloy (Wu, K. et al., 2020).

4.2.15.1 Effect on hardness

Typically, the heat generated during metal deposition is dissipated through the part and substrate by conduction mode, by forced convection mode through the shielding gas or by radiation to the environment (Rodrigues, T. A. et al., 2019). The conduction mode of cooling is mostly influenced by the size of the built part and the large substrate which acts as heat sink, increasing heat dissipation through previously deposited layers of the part (Rodrigues, T. A. et al., 2019)

The increase in hardness with increasing layer height is consistent with the increase in cooling rate shown in Figure 4-9. The top section of the block was observed to be approximately 10% higher in hardness, compared to the bottom section. This is attributed to the reduction in tempering due to effect of fewer thermal cycles and the higher cooling rate (larger heat sink), experienced by materials deposited within the top section of the block (Elrefaey, A. *et al.*, 2018).

The longer the bottom sections of the WAAM block are exposed to prolonged heating, the more the potential for increased precipitation and agglomeration of carbides from the solution matrix. This could further cause the coarsening of carbides and grain growth, leading to further reduction in hardness (Yadav, H. K. *et al.*, 2017).

Thermal cycle variation and cooling rates play a significant role in the microstructure of weld metal developed during the deposition process (Elrefaey, A. *et al.*, 2018), and lead to the development of heterogenous microstructure in the weld metal (Pandey, C. *et al.*, 2019).

The microstructural inhomogeneities of the weldment, lead to variations in mechanical properties of the deposited 2.25Cr 1Mo WAAM alloy. Hence, the materials are typically heat treated after deposition, to relieve locked in stresses, temper the hard microstructure to reduce the hardness and restore its toughness (Elrefaey, A. *et al.*, 2018).

The tempering temperature applied, produced a decrease in hardness and tensile strength with a corresponding increase in percentage elongation to fracture. The decrease in hardness during tempering could be attributed to the weakening of precipitation strengthening, owing to the precipitation, and coarsening of carbides (Tao, P. *et al.*, 2010) and decrease in dislocation density (Elrefaey, A. *et al.*, 2018).

The 25°C/hr heating/cooling rate utilised, produced the lowest hardness value, which was lower than the limit set for this study. The heat treatment duration associated with this heating/cooling rate is the longest. Hence, the tendency to produce further reduction in strength and hardness exist, owing to prolonged

coarsening of carbides, which could also increase with the peak temperature utilised (Ahmed, S. R. et al., 2015).

Therefore, the 25°C /hr heating and cooling rate should be applied with caution or avoided altogether, due to the tendency to cause degradation in property of the WAAM alloy, through spheroidization of carbides (Chovet, C. and Schmitt, J. P., 2011).

After PDHT, the maximum hardness of the WAAM alloy in as-deposition condition reduced by about 31.9%. The reduction in hardness of the WAAM alloy is vital in providing an optimum property that can meet the overall material design specification for oil and gas application.

4.2.15.2 Effect on tensile strength

The strength of the WAAM alloy in as-deposited condition is higher than that of the heat-treated counterpart. The higher strength can be attributed to solid solution strengthening, which is one of the main mechanisms by which 2.25Cr 1Mo alloy achieves its strength (Wang, W. et al., 2013).

The PDHT applied to the WAAM material led to a reduction in the strength and a corresponding increase in ductility. The major factor responsible for this observation can be attributed to softening of the WAAM alloy as a result of tempering of the hard and brittle microstructures (Elrefaey, A. et al., 2018).

Two main reasons can be hypothesized for the softening of the PDHT WAAM alloys. One is a result of decrease in the amount of solid solution strengthening elements in the matrix microstructure. The heat treatment is accompanied with increased carbides precipitation, which reduces the concentration of solute element, leading to decrease in the strength of the alloy (Wang, W. et al., 2013).

The second reason can be attributed to decrease of dislocation strengthening. Increase in temperature from 670°C to 710°C, caused the grain size to increase. With increase in grain size, the volume fraction of grain boundaries reduces and produces a decrease in dislocation density. Further increase in temperature could also have caused the dislocations to move, combine and finally cancel or

annihilate each other (Sun, C. *et al.*, 2018). The reduction in dislocation density likely led to a corresponding reduction in dislocation strengthening effect (Elrefaey, A. *et al.*, 2018).

4.2.15.3 Charpy impact toughness

Toughness is an essential mechanical property of a steel weld metal and generally decreases as the chromium content increases (Andrén, H. O., Cai, G. and Svensson, L. E., 1995).

The as-deposited WAAM sample produced lower impact toughness values compared to the PDHT samples. This could be attributed to the presence of heterogenous microstructure, consisting of hard and brittle martensitic and blocky martensite-austenite (M-A) constituents (Pandey, C. *et al.*, 2019). Untempered martensite and blocky M-A constituents are detrimental to impact toughness because they are brittle phases and can act as stress raisers leading to the generation and propagation of cracks through the ferrite grain (Wu, K. *et al.*, 2020).

Premature failure may not be completely prevented because it is not possible to entirely eradicate the heterogeneity developed in the WAAM alloy, due to its high hardenability and the use of multiple layer deposition technique unique to the WAAM process. However, the potential for the premature failure can be reduced by utilising an efficient heat treatment process (Pandey, C. *et al.*, 2019).

Charpy impact toughness increased significantly following PDHT, by up to 150%. The reason for the increase follows the earlier explanation, which is attributed to softening of the WAAM alloy, owing to the tempering of the hard and brittle microstructures (Elrefaey, A. *et al.*, 2018). The softer the material, the greater the plastic deformation region. In addition, large plastic deformation region will lead to a slower crack propagation and larger absorbed energy (Sun *et al.*, 2018).

The tempering heat treatment could also have caused the decomposition of the brittle M-A constituents into carbide (Wu, K. *et al.*, 2020). Hence, it can also be inferred that the applied PDHT parameters promoted solute redistribution and

homogenisation leading to the improvement in mechanical properties, especially impact toughness over the as-deposited samples (Wang, W. et al., 2013).

4.2.16 Deterioration in charpy impact toughness

Charpy impact test results of the PDHT WAAM alloy showed some sporadic and low charpy impact values, within the bottom section of the WAAM block. Analysis of the impact fractured surfaces of the samples (Figure 4.26), revealed the presence of several ruptured and dissolved particles.

One probable cause for the observed degradation in impact toughness could be attributable to further coarsening of carbide precipitates, as well as alteration of their crystal structure and shape (Wang, W. et al., 2013). This is in fact potentially true for the WAAM weldments which lay within the bottom section of the deposited block, because of being subjected to perhaps a prolonged tempering effect. The prolonged tempering arises from a combination of repeated thermal cycle of successive deposited passes, in addition to the subsequent PDHT applied.

Prolonged tempering of the lower section of the block could lead to drastic reduction in strength and degradation of charpy impact property of the heat treated WAAM alloy (Chovet, C. and Schmitt, J. P., 2011). This could occur through the mechanism of Ostwald ripening of carbide particles (Speich, G. R., 1969; Bhadeshia H.K.D.H. and Honeycombe R.W.K., 2006), also termed second phase coarsening, generally thought to be a slow, diffusion-controlled process, and could occur after phase change (Baldan, A. 2002). The increase in tempering time, could have caused the smaller particles to shrink and large ones to particles grow, which is characteristic of Ostwald ripening (Ning, A. et al., 2019).

It is generally known that inclusions of suitable characteristics, including size, shape and composition could provide sites for heterogenous nucleation of acicular ferrite (Zhang, T. et al., 2015). Several spherical oxides inclusions were observed both in the unloaded microstructural samples and charpy impact fracture samples of the WAAM alloy.

EDS analysis of the (unruptured particles) inclusions revealed that they were mainly composed of oxides of Mn and Si. (Fig 4.17 and 4.20). However, no evidence of nucleation of acicular ferrite at these inclusions were found by optical or SEM observations. This could be expected because molybdenum and chromium promote the formation of bainite in preference to acicular ferrite (Bose-Filho, W. W. et al., 2007).

The size and distribution of inclusion could also be related to Ostwald ripening mechanism. Inclusion may experience thermal excursions, undergo complex spatial motion caused by fluid flow conditions in the weld pool (Hong, T. *et al.*, 2000). These thermal excursions could lead to repeated growth, dissolution, and rapid collision and coalescence of inclusions, which may be more pronounced in certain regions of the weld pool. Coarsening of inclusions could be accelerated by collision and coalescence induced by velocity gradients (Babu, S. S. *et al.*, 2004).

Hence, the temperature history of inclusions is important in their growth and dissolution rates (Hong, T. *et al.*, 2000); and the presence of relatively high-volume fraction of inclusions in the notched zone of Charpy samples, could also initiate premature ductile fracture. (Hong, T. *et al.*, 2000) and lead to lower impact toughness (Na, H. et al., 2018).

Therefore, it is imperative that the PDHT applied to WAAM alloys, provide sufficient tempering to produce increased ductility and improved mechanical performance; while avoiding very high tempering temperature or longer exposure time which could produce unacceptable deterioration in the performance of the weldment (DuPont, J. N. et al., 2017).

As a general requirement, 2.25Cr 1Mo alloy weldments require heat treatment after deposition, to restore its desirable properties. This work has demonstrated that PDHT temperature of 670°C at 50°C/hr heating/cooling rate, applied to a 25mm thick WAAM weldment; is suitable for achieving the overall optimum material requirement, within the limit of the experimental conditions.

The PDHT parameter of 670°C at 50°C/hr heating rate, gave the following static mechanical properties:

- Hardness: 209HV min, 241HV max
- Elongation: 18.5% min
- Yield strength: 545 MPa (80 Ksi) min
- Tensile strength: 660 MPa (96 Ksi) min
- Charpy impact toughness: 75J min avg. at -60°C.

Finally, in answering the research question, this study has demonstrated the ability of heat treated WAAM ER90S-G alloy, to meet typical requirements of a Schlumberger material specification, for ASTM A182 F22 forgings utilised for the manufacture of marine oil and gas components. It is however acknowledged that more extensive testing per industry best testing practice codes, likely to include fracture toughness and fatigue, in macro and full-scale testing environments would be required to confirm fitness for purpose, before deploying the part in service.

4.3 Conclusions

To manufacture heavy-walled marine components by the WAAM technique, using alloy 2.25Cr 1Mo wire composition, the effects of repeated thermal cycle and heat treatment on the microstructure, hardness, strength and charpy impact toughness properties were investigated and the results are summarised as follows:

- This study has successfully demonstrated the suitability of utilising WAAM technology in the manufacture of large heavy-walled 2.25Cr 1Mo steel components, of acceptable quality and mechanical property, that can meet typical specifications required for marine oil and gas applications, subject to further testing in line with industry testing codes for WAAM products.
- The thermal cycle generated along the built height of the part, resulted in microstructural heterogeneity, which led to variations in mechanical properties.

- Cooling rate during the deposition process, depended on the built layer height and increases as the size of the WAAM block increased
- The hardness of the WAAM block was about 10% higher in the top section compared to the bottom section of the block, due to tempering effect of successive passes
- The as-deposited WAAM alloy produced relatively high hardness, strength and relatively low average charpy impact toughness of 34J, which was higher than the average required value of 27 J. But with a high maximum hardness of 360HV
- The presence of heterogenous microstructure, consisting of brittle martensitic and bainitic structures, is attributed to the poor charpy impact toughness of the WAAM alloy in as-deposited condition
- The applied PDHT was effective in reducing the microstructural heterogeneity and hardness variations along the deposited height of the WAAM block, leading to improved mechanical properties. Charpy impact toughness after PDHT increased by up to 176%, with a maximum hardness of 246HV
- The numerous numbers of disintegrated MnO.SiO₂ inclusions, coupled with possible presence of spheroidized carbide precipitates, observed in the fracture surfaces of the heat treated WAAM alloy, are attributed as the major cause of deterioration in charpy toughness of the WAAM alloy, in the bottom sections of the block.
- PDHT temperature of 670°C and a heating/cooling rate of 50°C/hr, is considered the optimum parameter, for meeting the overall minimum specified requirement, within the limit of the experiment.

5 Experimental modification of alloy 2.25Cr 1Mo composition, using the Tandem-GMAW

5.1 Hypothesis and technical approach

The review of literature has shown the potential and benefit of creating optimised wire compositions suitable for manufacture of WAAM components, as well as the capability to actualise it using the tandem-GMAW process. Furthermore, the importance of Nickel, in improving low temperature charpy impact toughness of weld metal has been highlighted.

Till date, studies attempting to modify the composition of 2.25Cr-1Mo alloy wire by use of tandem-WAAM process have not been reported. The overall aim of this work is to produce an optimised low alloy steel composition, for WAAM deposition, which can provide improved strength and low temperature impact toughness performance, superior to 2.25Cr 1Mo alloy; and to achieve this at a lower cost, without the need for expensive alloying additions or equipment.

The investigation will specifically target the modification of alloy 2.25Cr 1Mo base composition, by mixing it with Mn4Ni2CrMo alloy, using the tandem-GMAW process, and to study the effect of increasing the nickel content on the resulting microstructure, tensile and charpy impact toughness properties of the resulting WAAM alloys, in as-deposited condition. The result of this study will potentially lead to-

- (a) The design of a commercial heat of new consumable wire composition, exhibiting improved as-deposited strength and toughness properties and/or
- (b) The development of a novel tandem-GMAW deposition process, in which different low alloy steel wire compositions are simultaneously used to fabricate a part by the WAAM technique, thereby achieving enhanced in-situ static and low temperature impact performance of the components.

5.2 Experimental procedure

5.2.1 Materials

An S355 steel plate of dimension (350x250x20) mm was used as substrate. It was mechanically cleaned using an iron brush and degreased with acetone just before deposition. Commercially available 2.25Cr 1Mo and Mn4Ni2CrMo GMAW wire compositions, designated ER90S-G and ER120S-G respectively, were used for the study. Table 5-1 gives the chemical composition of the wires and substrate used. The shielding gas used was Argo-shield light, at a flow rate of 30 l/min.

Table 5-1 Chemical compositions of tandem deposition wires and substrate

Materials	AWS A5.28	C	Cr	Mo	Mn	Ni	Si	S	V	P	Cu	Nb/Zr	Ti	Al	CE
Bohlen 900-IG	ER120S-G	0.09	0.32	0.51	1.87	1.82	0.72	0.01	0.01	0.011	0.07	0.01	<0.01	0.01	0.36
Lincoln LMN20	ER90S-G	0.08	2.48	1.00	0.90	0.04	0.61	0.005	0.01	0.007	0.0	0.01			0.48
Substrate	S355	0.20	-	-	1.60	-	0.55	0.025	-	0.025	0.55	-	-	-	

5.2.2 Equipment setup

The tandem-GMAW WAAM system employed in this study is displayed in figure 5-6. It consists of two electrically synchronised Fronius TransSynergic 4000, Time twin Digital MIG/MAG GMAW power source. One power source is termed the master (A) and the other slave (B). The master power source provides the lead arc, while the slave power source is the trail arc. The wires are feed into a common weld pool by the synchronous push-pull movement of two separate wire feeder systems. The torch manipulation was performed using a 6-axis ABB robot. Figure 5-1 shows the equipment set up.

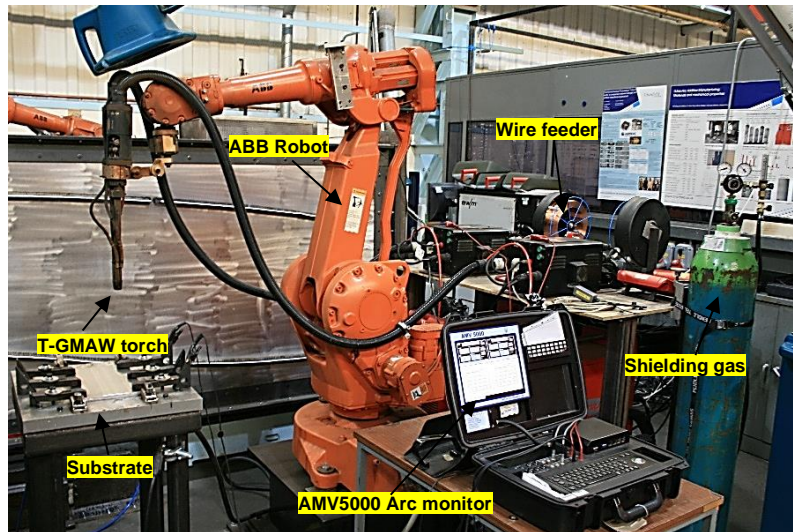


Figure 5-1 Tandem GMAW set-up

Figure 5-2 illustrates the torch setup with lead wire (A) and trail wire (B), positioned in series configuration. When the torch travels in the leading direction, wire A is the front wire, and when it travels in the trailing direction, wire A becomes the back wire. Synergic pulsed current arc characteristics was utilised to melt and transfer the metal droplets.

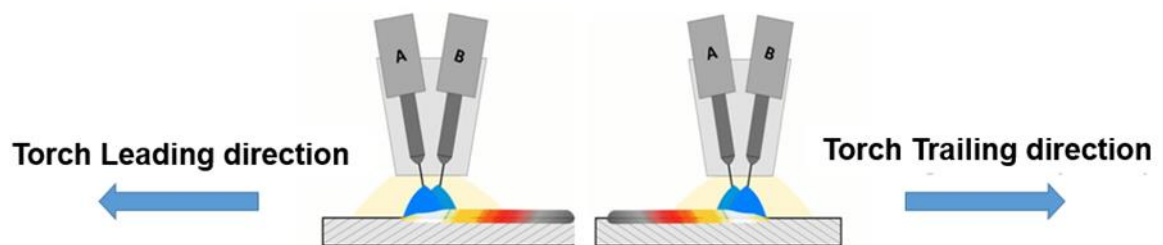


Figure 5-2 Tandem WAAM: Wire setup and travel directions

The instantaneous current and voltage characteristics were recorded using AMV5000 arc data logger, at a sampling frequency of 5 KHz.

The heat input generated during deposition was calculated using the formula in equation (5-1) and (5-2) (Gu, J. et al., 2018).

$$H.I = \left(\sum_{i=1}^n \frac{I_i \times U_i}{n} \right) / TS \quad (5-1)$$

Where I_i (A) and U_i (V) are instantaneous current and voltage; TS is the travel speed (mm/s)

Total heat input of the tandem-GMAW process, Q is given as:

$$Q = q_1 + q_2 \quad (5-2)$$

Where q_1 is the heat input of wire A, and q_2 is heat input of wire B

5.2.3 Experimental plan

The wires were mixed by simultaneously feeding them into the same weld pool. Modified compositions of the wires were obtained by varying the wire feed speed of both wire feeders, with respect to the proportions of each wire required in the mix. The plan adopted in mixing the wires is shown in Table 5-2. Seven different modified weldments of ER90S-G and ER120S-G compositions were deposited for the investigation.

Table 5-2 Composition modification plan adopted in this study

Trial No.	Wire Feed Speed [Wire (A/B)], m/mins	Mixing proportion [Wire (A/B)] (%)	Deposition Travel Speed (mm/secs)
1	10/0	100/0	10
2	7.5/2.5	75/25	
3	6.3/3.8	62.5/37.5	
4	5/5	50/50	
5	3.8/6.3	37.5/62.5	
6	2.5/7.5	25/75	
7	0/10	0/100	

5.2.4 Manufacture of test samples

Prior to producing the actual test block samples, preliminary process investigations were conducted to develop suitable tandem-GMAW process parameters for depositing weld beads of acceptable quality. The studies were conducted in another report by the author. The process parameters utilised to deposit the test block in this study are presented in table 5-2. Rectangular test blocks of approximately 280mm x150mm x35mm in dimension, were built using bi-directional multi-layer wall deposition strategy.

The procedure involved depositing single weld beads along the +Y direction. The torch was then stepped (in the direction +X), a length equal to the bead step size, before depositing subsequent weld beads. This process was repeated until a total of four beads were deposited per layer. Thereafter, the torch ascended (in the vertical direction H), to a distance equal to the layer height, and moves to the opposite end of the previous layer before depositing the next set of weld bead in the direction -Y. This cycle was continued until a total wall height of 150 mm was reached. Figure 5-3 illustrate the deposition procedure.

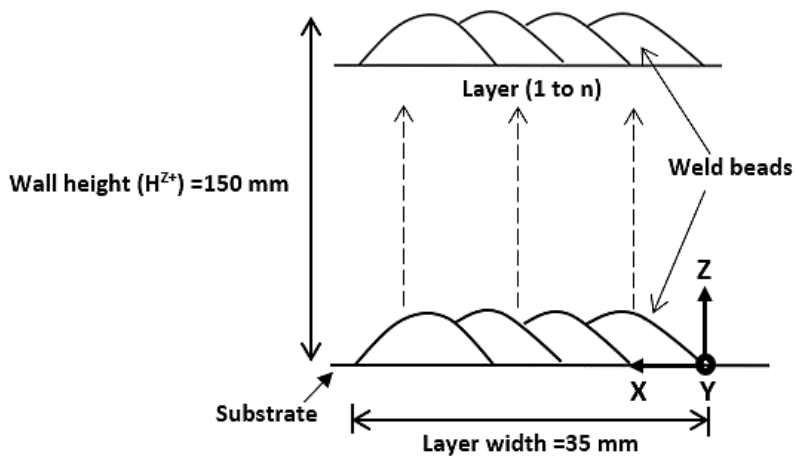


Figure 5-3 Procedure for depositing the test blocks

5.2.5 Non-destructive examination (NDT)

Volumetric non-destructive examination of the deposited blocks was conducted after machining using X-ray radiography method. The test was carried out to determine the internal soundness of the deposited weld metal.

5.2.6 Elemental analysis

The actual elemental compositions of the deposited WAAM alloys were determined by inductive coupled plasma optical emission spectrometer (ICP-OES). Localised elemental composition of the deposits was analysed by SEM, utilising energy dispersive spectrometry (EDS).

Theoretical elemental composition of the various WAAM alloys, obtained by mixing different proportions of ER120S-G and ER90S-G in the same weld pool, was estimated using the expression given in equation (5-3).

$$\text{Theoretical Elemental Composition } (C_o) = \frac{(C_A \times WFS_A) + (C_B \times WFS_B)}{(WFS_A + WFS_B)} \quad (5-3)$$

Where C_A and C_B are the specific elemental contents of wire A and B respectively, in wt%; WFS_A and WFS_B are the set wire feed speeds of Wire A and B respectively, in m/min. The density of the modified alloy compositions was assumed to be like that of the base wires, ER90S-G and ER120S-G.

5.2.7 Microstructure and mechanical analysis

Microstructure and mechanical test specimens were extracted from the various WAAM weldments, according to the test matrix shown in Figure 5-4.

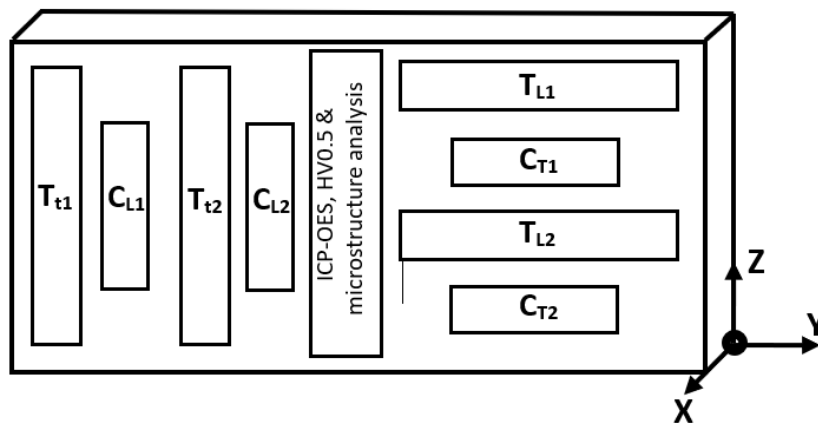


Figure 5-4 Chemical and microstructure and mechanical test plan of deposited block

Metallographic coupons were extracted and prepared by grinding with 120#, 240#, 1200# and 2500# grit SiC papers. This was followed by a mirror finish polish, using 3 μ m diamond paste and colloidal silica suspension. 2% Nital and Le'Pera solutions were used to etch the samples, to reveal specific microstructural details. Examination of the microstructure and fracture morphology were performed using optical microscope (Nikon Eclipse ME600) and scanning electron microscope (Tescan S8000G), equipped with an Oxford Instruments energy dispersive spectrometer (EDS).

The distribution and characteristics of oxide inclusions particles formed in the deposited WAAM alloys, including inclusion sizes, area fraction and number density, were determined on polished unetched surfaces. The analysis was conducted by SEM at 20 keV and 10000x magnification in backscattered mode. The electron beam interaction spot size, (with specified beam conditions into an Iron based sample) of roughly 2.4 microns across, was used to characterise the inclusions. Eight random fields were sampled on each WAAM alloy for the analysis. Quantitative analysis of each sample containing a minimum of 30 inclusions was performed using image J software.

Microhardness test were conducted on the deposited WAAM alloys in the build direction (H), at room temperature, according to ASTM E384-17/E92. A Zwick/Roell Indentec Vickers microhardness tester, with a load of 500g and dwell time of 15secs was used for the test. A total of 80 hardness indentations were made per test sample, along the build (Z) direction. Micro-indentations were made in steps of 0.5mm between individual measurements and in two rows spaced 2mm apart, as illustrated in Figure 5-5.

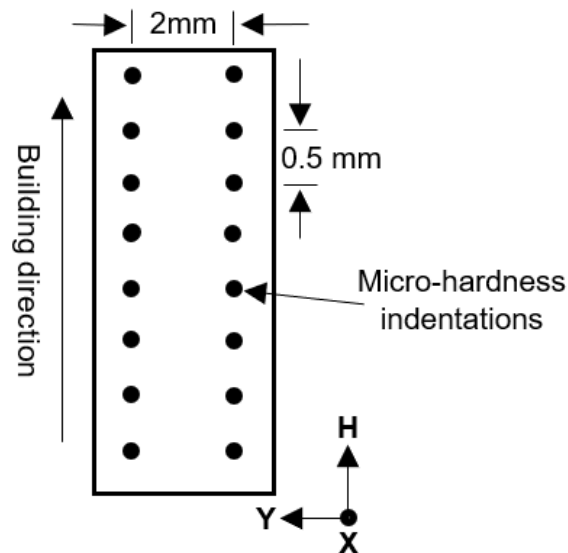


Figure 5-5 Micro-hardness test method

Tensile tests were performed on the WAAM alloys at ambient temperature, using an Intron 5500R electromechanical universal tensile testing machine, with a 30kN load cell, equipped with a laser extensometer. The test was conducted according

to ASTM E8/E8M-08. The yield strength (YS), and Ultimate tensile strength (UTS) were obtained from the stress-strain curves. YS was estimated using the 0.2% offset technique. The percentage elongation to fracture (ϵ) was directly obtained from the elongation at fracture data recorded by the laser extensometer.

Four tensile test coupons were used per WAAM alloy for the study. Two of the test coupons were extracted from the longitudinal (parallel, 'Y') and perpendicular (Normal 'Z') planes of the block, as shown in Figure 5-4. The test coupons were machined into dog-bone shapes of 30mm gauge length. Figure 5-6 shows the tensile testing process.

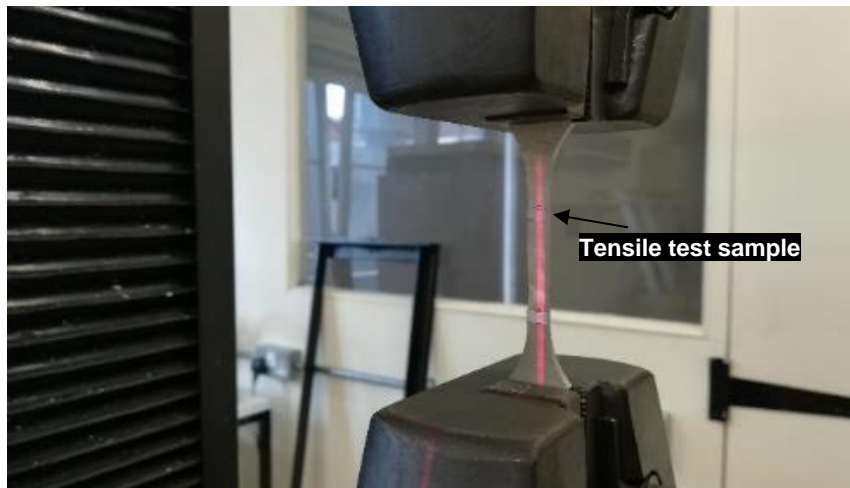


Figure 5-6 Instron 5500R tensile testing set-up, showing the test sample gripped in-between the fixed and movable machine jaws and laser extensometer illumination line

Charpy v-notch tests were performed on standard test specimens of dimension 55x10x10 mm, using a 600J Charpy impact v-notch testing machine, at -30°C . The tests were conducted on notches cut in the samples in both the longitudinal (parallel) and perpendicular (Normal) planes of the WAAM alloys. Four Charpy tests were conducted per WAAM alloy, using two specimens extracted from the longitudinal and perpendicular planes of the deposited WAAM alloys.

5.3 Result presentations

This section presents the results of the work carried out to modify the base chemistry of alloy 2.25Cr 1 Mo solid wire composition, using a solid wire with relatively higher nickel content, designated Mn4Ni2CrMo. The results from the succeeding sections provided the data for evaluating the effect of mixing commercially available welding wires namely, ER90S-G and ER120S-G wire, using the tandem-GMAW process, on the nickel content and property of the WAAM weldments.

5.3.1 Manufactured test samples

Figure 5-7 shows examples of the completed blocks in this study, manufactured using WAAM.

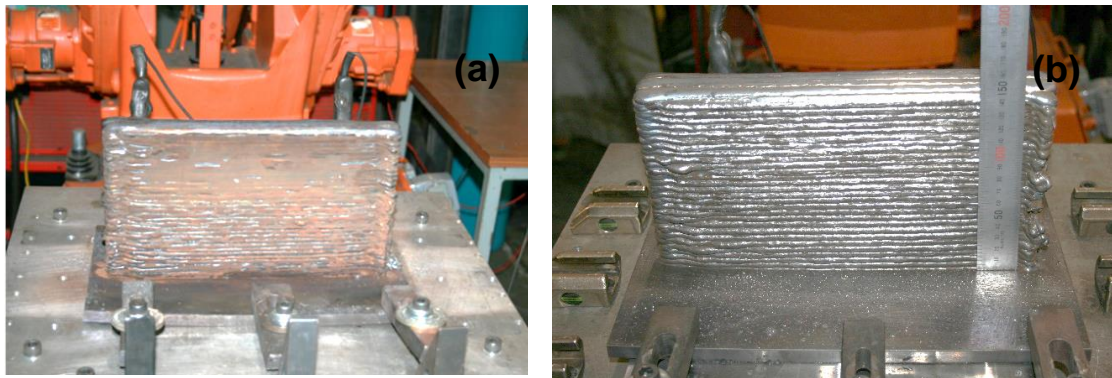


Figure 5-7 Appearance of tandem-GMAW deposited test block. (a) Before and (b) After wire brush cleaning

Stable metal deposition conditions were generally achieved during the process, when both wires (A) and (B) were parameterised with equal or nearly equal WFS values. But the weld metal deposition process became less stable when the difference in WFS of both wires was relatively large, such as when the wire mixing proportions of 75% and 25% was utilised.

The reduced stability in deposition process occurred due to the difference in the metal transfer mode between both wires. The lower wire mixing proportion of 25% was achieved with a WFS of 2.5 m/mins, and the resulting low arc current produced a globular metal transfer condition. Conversely, the higher wire mixing

proportion of 75% achieved using a relatively higher WFS of 7.5 m/mins, produced a spray metal transfer condition, due to the higher arc current generated.

This condition triggered a slight interruption in the metal transfer, as the molten metal produced at a WFS of 2.5m/mins, was observed to be frequently 'expelled out' of the molten weld pool, as it transferred from the wire, instead of continuously dropping into the weld pool. The situation was more significant when the torch travelled along the edge of the test block during deposition. But when the torch travelled within the middle part of the WAAM block, the transferring molten metal was contained within the relatively large surface area of the block.

As a result of this observation, the various test specimen were extracted within the middle sections of the test blocks, to minimise experimental error. Table 5-3 gives the average current, voltage and heat input values, measured during deposition of the test blocks.

Table 5-3 Preset tandem-GMAW parameters utilised for this study and measured arc characteristics obtained during deposition, using 10mm/s TS. Note (1) and (2) represent the two tandem-GMAW power sources

Mixing Proportion	WFS (mm/mins)		Avg. Current (A)		Avg. Voltage (V)		Avg. Heat Input (Kj/mm)		Total (H.I) (Kj/mm)
	WFS ₁	WFS ₂	I ₁	I ₂	V ₁	V ₂	Q ₁	Q ₂	Q
ER90S-G (100%)	5	5	128.4	124.7	21.9	21.3	0.273	0.266	0.54
ER120S-G (25%)	2.5	7.5	69.6	175.1	18.3	24.1	0.127	0.422	0.55
ER120S-G (37.5%)	3.8	6.3	109.2	147.3	20.5	22.6	0.224	0.333	0.56
ER120S-G (50%)	5	5	129.4	126.8	21.5	21.9	0.278	0.278	0.56
ER120S-G (62.5%)	6.3	3.8	148.3	109	22.5	20.3	0.334	0.271	0.61
ER120S-G (75%)	7.5	2.5	179.5	72.5	23.7	17.5	0.425	0.127	0.55
ER120S-G (100%)	5	5	129.1	126.2	21.2	21.7	0.274	0.274	0.55

From table 5-3, it can be observed that the H.I obtained during this study was found to be highest with the modified WAAM composition, containing 62.5% ER120S-G composition, and was about 9% higher.

5.3.2 NDT result of test blocks

After deposition, the blocks were machined to a rectangular shape. The surface of the blocks were visually inspected for any surface breaking defects. The results showed sound weldments, with no external surface defect.

X-ray examinations were performed to ascertain the internal quality of the WAAM weldments. The results showed sound and acceptable internal quality of the blocks. Figure 5-8 shows an X-ray radiograph image of the internal section of the WAAM block.



Figure 5-8 X-ray radiograph image of WAAM test block, showing sound internal structure of the weld metal

5.3.3 ICP-OES chemical analysis of WAAM alloys

This section presents the results of investigation conducted to evaluate the effect of mixing ER90S-G and ER120S-G wire compositions, on the chemical composition of the modified WAAM alloys. The results of ICP-OES chemical tests conducted on the various WAAM blocks, with different proportions of ER90S-G and ER120S-G wire compositions are presented in Table 5-4.

Table 5-4 Results of ICP-OES tests conducted on deposited WAAM alloys, showing percentage indicating proportion of ER120S-G, and balance is ER90S-G

C	Si	Mn	P	S	Cr	Mo	Ni	Al	Cu	Ti	V, Zr	ER120S-G (%)
0.07	0.5	0.76	0.007	0.012	2.45	1.03	0.03	<0.01	0.07	0.02	<0.01	0
0.07	0.54	0.98	0.008	0.011	1.89	0.93	0.48	<0.01	0.06	<0.01	<0.01	25
0.07	0.55	1.07	0.009	0.012	1.57	0.85	0.73	<0.01	0.06	<0.01	<0.01	37.5
0.08	0.56	1.15	0.01	0.011	1.4	0.81	0.9	<0.01	0.06	<0.01	<0.01	50
0.08	0.58	1.3	0.011	0.011	0.99	0.71	1.23	<0.01	0.05	<0.01	<0.01	62.5
0.08	0.59	1.37	0.011	0.01	0.76	0.62	1.38	<0.01	0.05	0.02	<0.01	75
0.08	0.61	1.55	0.012	0.01	0.29	0.51	1.83	<0.01	0.04	<0.01	<0.01	100

The result shows a gradual change in the chemical content of the WAAM alloys, as the proportion of ER120S-G was increased in the mixture. The elemental content of Ni in the modified alloys varied between (0.48 – 0.9 – 1.38) wt%, when the proportion of ER120S-G wire composition in the mixture was (25 – 50 – 75) %, respectively.

5.3.4 Analysis of actual and theoretical composition of WAAM alloys, as a function of wire mixing proportions

This section presents an evaluation of the elemental content of the modified WAAM alloys, in relation to the actual and calculated compositions. The theoretical elemental compositions of the WAAM alloys were calculated according to equation (5-3).

Figures 5-9 shows the graphs of actual and theoretical elemental composition of deposited WAAM alloys, as a function of the wire mixing proportions. The analysis was conducted for the important elements including Cr, Mo, Ni, Mn, and Si.

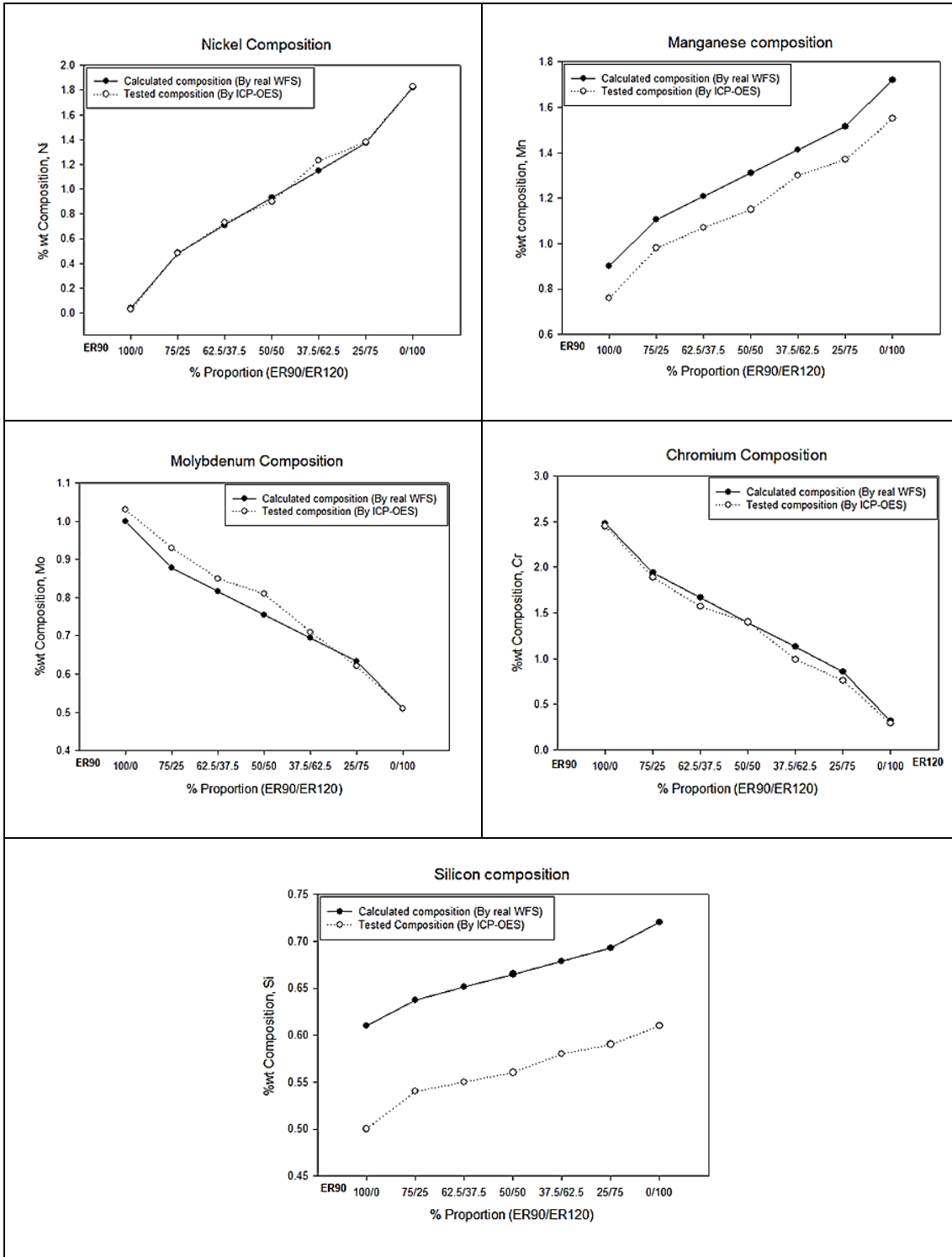


Figure 5-9 Plots of actual tested and calculated elemental content of WAAM alloys, as a function of ER120S-G and ER90S-G base wire compositions

It can be seen from the plots that the contents of Ni, Mn and Si increased while those of Cr and Mo decreased, due to the controlled increase in the proportion of

ER120S-G wire composition, relative to that of ER90S-G in the modified mixtures, as they were gradually feed at different WFSs into the same weld pool.

Another important observation from the plots showed that, whereas no significant difference in absolute terms, occurred between the actual and theoretical contents of nickel, chromium and molybdenum, a large difference can be seen between the actual and theoretical contents of silicon and manganese, with respect to the composition of the modified WAAM alloys. This is attributed to oxidation of the elements, leading to formation of oxides which either form slag or remain as constituent part of the weld metal inclusion particles (Sindo Kou, 2003).

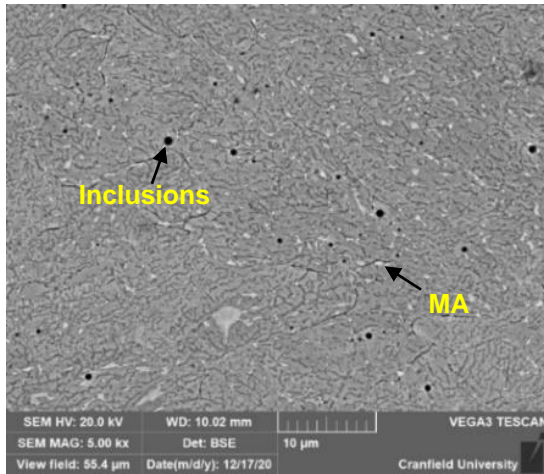
5.3.5 Microstructural evolution of WAAM alloys

Microstructure analysis of the deposited alloys are presented in this section. The samples used for analysing the microstructural formations were prepared according to the procedure detailed in section 5.2.7.

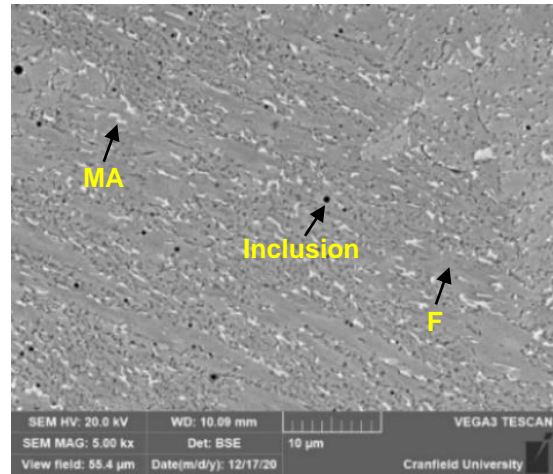
The representative microstructures of the WAAM weldments, etched using 2% Nital are presented in Appendix L.

Figure 5-10 displays the representative microstructures of WAAM weldments etched Le'Pera solutions.

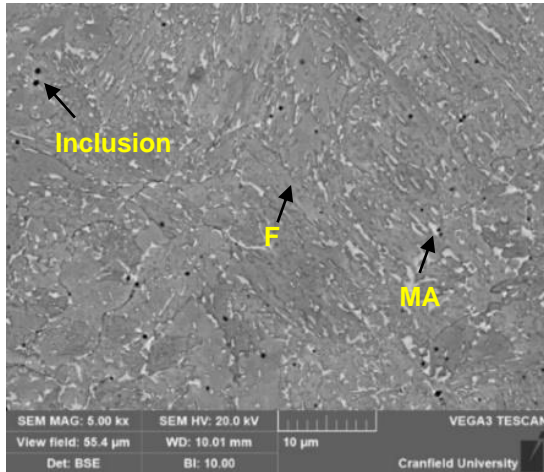
ER90S-G (100%) (HV-344 Max): 0.03 wt.% Ni



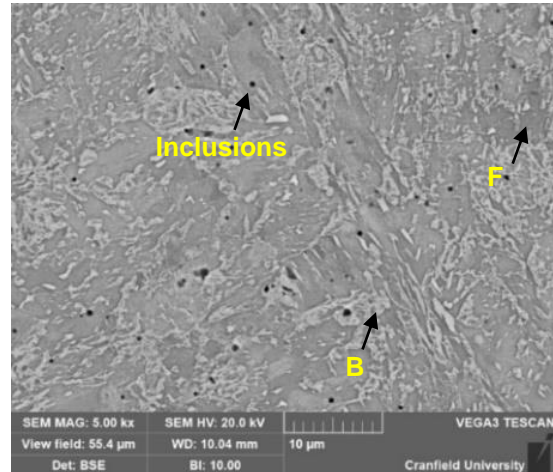
ER120S-G (25%) (HV-319 Max): 0.48 wt.% Ni



ER120S-G (50%) (HV-319 Max): 0.90 wt.% Ni



ER120S-G (75%) (HV-290 Max): 1.38 wt.% Ni



ER120S-G (100%) (HV-302 Max): 1.83 wt.% Ni

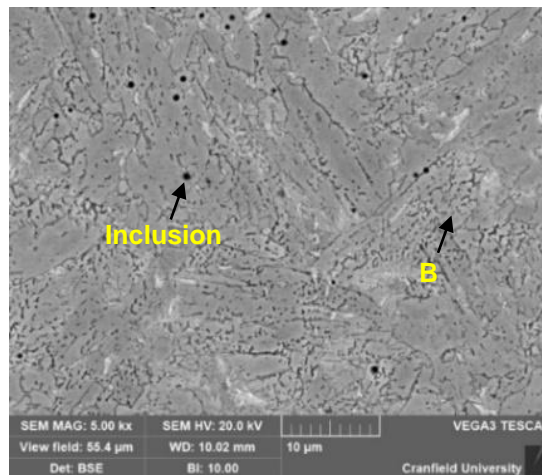


Figure 5-10 Micrographs sections of Le'Pera etched WAAM alloys showing combination of different microstructure including, Martensite (MA), Bainite, (B) Grain boundary ferrite (GBF), Ferrite with side plate (FSP), Acicular ferrite (AF).

Observations of the microstructures of Le’Pera etched ER90S-G WAAM weld metal, containing pure ER90S-G, at 0.03wt% Ni, show heterogenous grain structure, which is predominantly martensite, while the pure ER120S-G, containing 1.83%wt Ni, show a coarse grain microstructure, with lower fractions of martensite, but higher fractions of bainitic and ferritic microstructures.

The microstructure of the modified compositions showed mixtures of different proportions of martensite, bainite, grain boundary ferrite, acicular ferrite fractions and inclusion particles.

5.3.6 Analysis of inclusions in deposited test blocks

This section presents the results of the investigation conducted to characterise the distribution and sizes of oxide inclusion particles formed in the WAAM alloys. The analysis was performed according to the procedure detailed in section 5.2.7. and the results are presented in table 5-5

Table 5-5 Analysis of inclusion in deposited WAAM alloys

ER120S-G proportion (%)	Avg. area fraction (μm^2)	Number of Inclusion	Max. Inclusion diameter (μm)	Avg. Inclusion diameter (μm)
0	6.35	272	1.433	0.4115
25	5.13	290	1.438	0.3743
37.5	4.66	464	1.095	0.2434
50	4.36	253	1.254	0.3370
62.5	4.77	847	1.003	0.1796
75	4.60	247	1.421	0.3410
100	4.13	249	1.189	0.3190

It can be observed that the base wire composition ER90S-G, show the largest inclusion diameter of (average, 0.4115 μm and maximum, 1.433 μm), compared to ER120S-G wire composition. The modified compositions do not appear to show a consistent trend in the size and density of inclusions, with respect to increasing proportion of ER120S-G.

However, the modified composition which contained 62.5% proportion of ER120S-G wire, produced the smallest inclusion diameter (average of 0.1796 μm and maximum size of 1.003 μm), but have the largest oxide inclusion number density of 847.

The composition containing 37.5% ER120S-G, shows the second largest inclusion size of (average, 0.2434 μm and maximum, 1.095 μm), with the inclusion density numbering 464.

5.3.7 EDS chemical analysis of inclusions and weld metal oxygen test

The inclusion composition was analysed by SEM – EDS technique as explained in section 5.2.7. Figure 5-11(a) shows the distribution of inclusions in the block sample, while Figure 5-11(b) shows the morphology and EDS spectrum analysis of the inclusion particles.

The inclusions are predominantly spherical in shape. The EDS spectrum show peaks of Mn and Si, indicating the presence of manganese and silicon oxides.

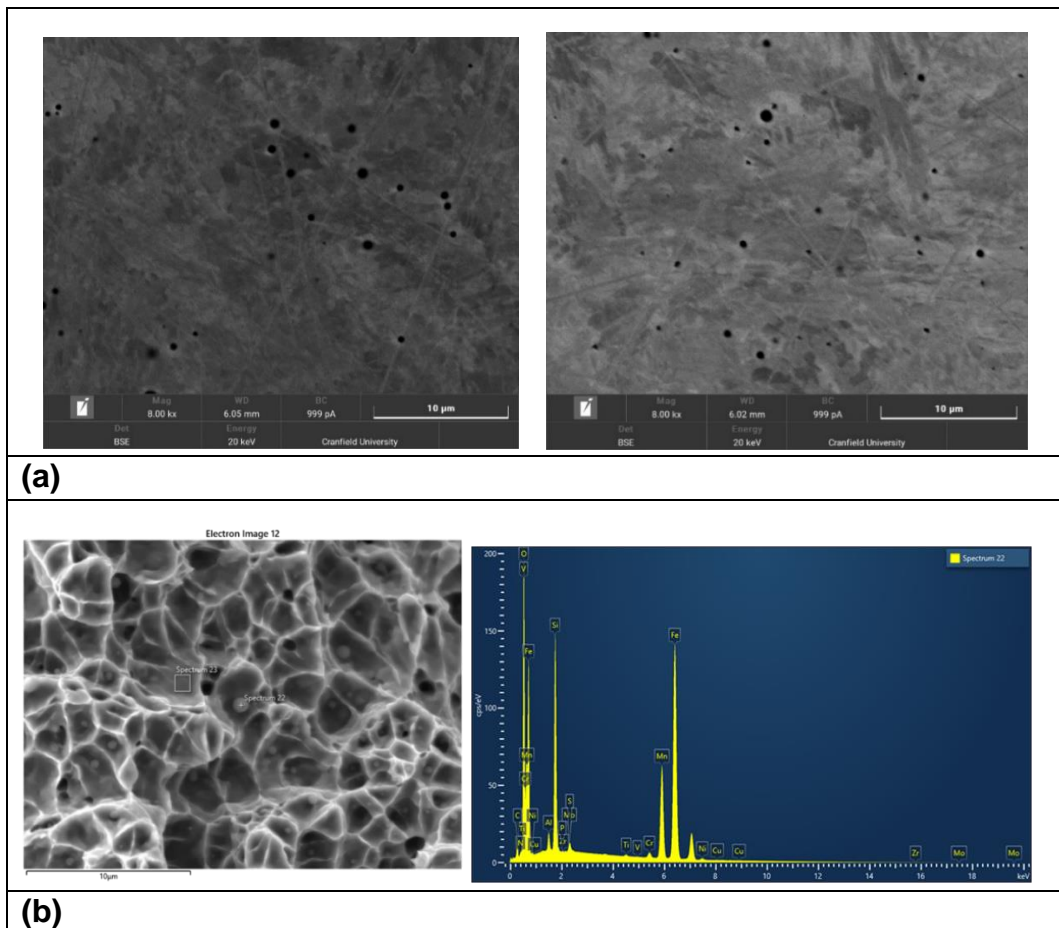


Figure 5-11 Inclusion characteristics (a) Distribution in unetched WAAM samples (b) Morphology of inclusion in a Charpy fracture sample and EDS analysis of inclusion chemical composition

Weld metal oxygen content analysis was conducted by the combustion method. The test was conducted on the pure ER90S-G and modified WAAM composition containing 50% ER120S-G. An additional oxygen chemical test was conducted on a counterpart wrought 2.25Cr 1Mo steel material, designated (ASTM A182 F22), for comparison.

The oxygen chemical analysis was conducted by element test house, in Manchester, and the result is displayed in Figure 5-12. It can be seen from the results that the oxygen content in the modified composition containing 50%ER120S-G was 0.034%, while the wrought F22 alloy contained 0.004% O₂, which is 750% lower compared to the tested WAAM alloy.

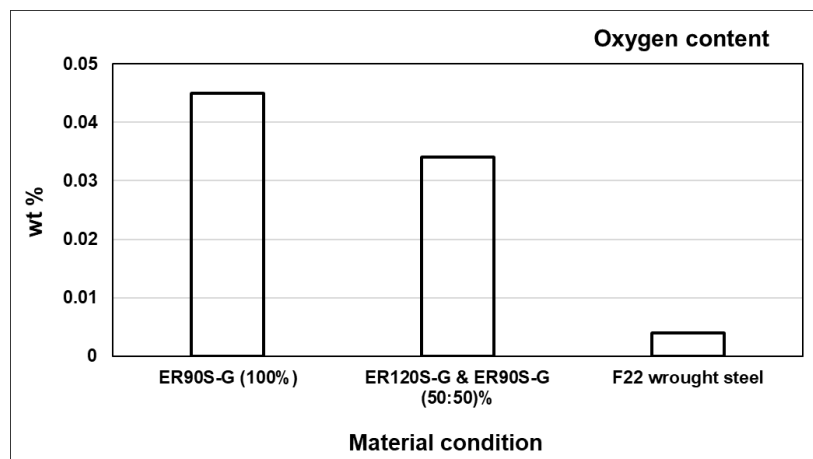


Figure 5-12 Weld metal oxygen content analysed by combustion method

5.3.8 Results of mechanical test

This section presents results of an investigation conducted to evaluate the mechanical performance of the WAAM alloys, with respect to the proportion of the base wire compositions in the alloy. The mechanical tests conducted on the WAAM alloys include micro-hardness, tensile and charpy impact toughness tests as described in section 5.2.7

5.3.8.1 Micro hardness results

Vickers micro-hardness indentations were made on the WAAM alloys at room temperature, according to the illustration given in Figure 5-5 and procedure described in section 5.2.7.

The average hardness values of the WAAM alloys measured in this study are presented in Table 5-6. and graphically represented as shown in Figure 5-13.

Table 5-6 Hardness of modified compositions, as a proportion of ER120S-G in the WAAM alloys and wrought 2.25Cr 1Mo steel metal

<i>Proportion of ER120S-G</i> (%)	<i>Hardness (HV0.5)</i>		
	Min	Max	Average
100	247	302	272
75	254	290	271
62.5	253	300	279
50	247	319	279
37.5	251	319	286
25	260	319	278
0	256	344	283

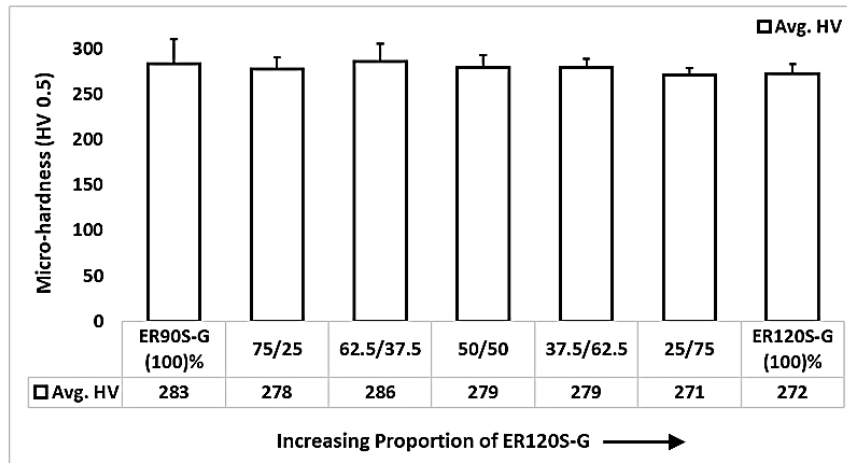


Figure 5-13 Average Hardness of deposited WAAM alloys and wrought 2.25Cr 1Mo steel metal

From the above results, the base ER90S-G weldment, produced the highest hardness of 344HV (due to its higher hardenability CE). The maximum hardness values of the modified WAAM alloys show a slight decreasing trend as the proportion of ER120S-G was increased in the mixture. However, the average hardness values appear relatively unchanged, ranging between 271 and 286 HV. The decrease in hardness with increase in ER120S-G could be attributed to reduction in hardenability and increased formation of perhaps acicular ferrite microstructures.

5.3.8.2 Tensile test result of WAAM alloys

The result of the investigation carried out to evaluate the effect of modifying 2.25Cr 1Mo WAAM alloys on the tensile performance is presented in this section.

Four tests were conducted per WAAM sample at room temperature, as described in section 5.2.7. All failures were observed to occur outside the gauge length of the specimens.

The average values of yield strength (YS), ultimate tensile strength (UTS) and percentage elongation to fracture (%EI), for the WAAM alloys were determined from stress strain diagrams. Representative stress strain curves are displayed in Appendix N. The tensile test result is summarised as shown in Figure 5-14. The tensile properties of the substrate used is also shown.

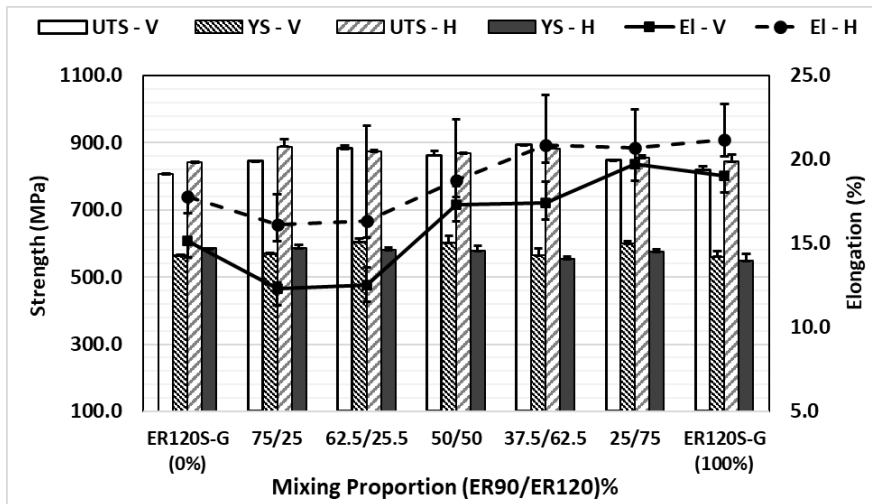


Figure 5-14 (a) Plot of tensile test results of the deposited WAAM alloys. [Substrate material property (S355): UTS (470-630) MPa; YS (335-345) MPa; EI (22) %]

The average UTS values for ER120S-G weld metal measured in the parallel and perpendicular deposition directions were slightly higher by 1.93% and 0.87% respectively, compared to those of the pure ER90S-G alloys.

From the plot, average UTS and EI of the modified WAAM alloys increased after the mixing and are higher than the pure ER90S-G composition. The static YS and UTS of the different modified WAAM alloys showed relative similarity, in both measurement directions.

The modified composition, containing equal proportion of ER120S-G and ER90S-G exhibited average YS of 603MPa and 579MPa respectively, in the vertical and horizontal deposition direction, which was 6.5% and 6.7% respectively higher than the pure ER90S-G composition. It also gave an average UTS of 862MPa and 869MPa, in the vertical and horizontal deposition direction respectively, which was 6.6% and 3.1% respectively, higher compared to the pure ER90S-G composition.

The percentage elongation (EI%) of the modified WAAM alloys increased with increasing proportion of ER120S-G. The values ranged between (16.6 and 20.8) % when measured in the parallel deposition direction, and between (12.3 and 19.7) % measured in the perpendicular direction.

The %EL of the modified WAAM composition containing equal proportion of ER120S-G and ER90S-G, measured in the vertical and horizontal deposition directions; were 17.3% and 18.8%, respectively, while the pure ER90S-G gave elongation values of 15.2% and 17.8%, in similar directions

5.3.8.3 Charpy impact toughness test results

Charpy impact tests were conducted on the deposited WAAM alloys in as-deposited condition, at -30°C, according to ASTM E23. The result of charpy impact test measured with respect to the proportion of ER90S-G and ER120S-G in the modified WAAM alloys is presented in Figure 5-15.

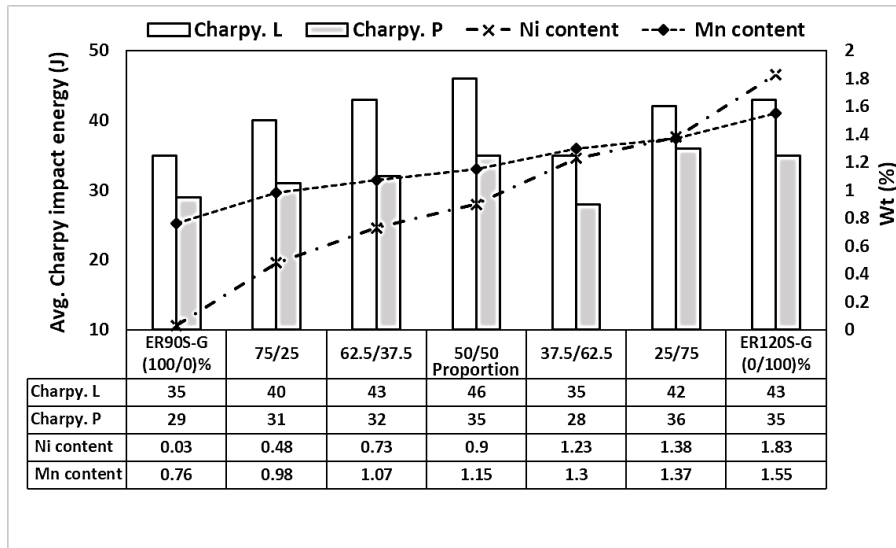


Figure 5-15 Influence of composition modification on sub-zero temperature Charpy impact toughness performance of WAAM alloys

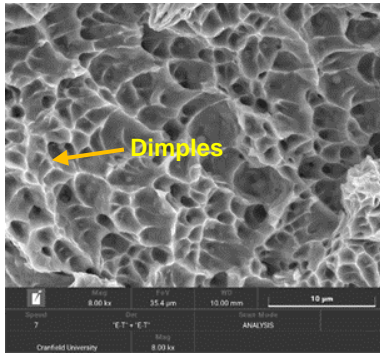
The average Charpy impact energy of the pure ER120S-G WAAM samples, obtained in the longitudinal (L) and perpendicular (P) deposition directions were 43J and 35J respectively. These values were 23% and 15% respectively, higher compared to the pure ER90S-G WAAM alloy, measured in the same directions.

The Charpy test results also showed that the modified WAAM composition, containing equal proportion of ER120S-G and ER90S-G, with a nickel content of 0.91wt%, gave the highest Charpy impact toughness of 46J and 35J, in the longitudinal and perpendicular deposition directions respectively. These values are higher by 31.4% and 20.7% respectively, compared to the pure ER90S-G WAAM alloy, measured in similar deposition directions.

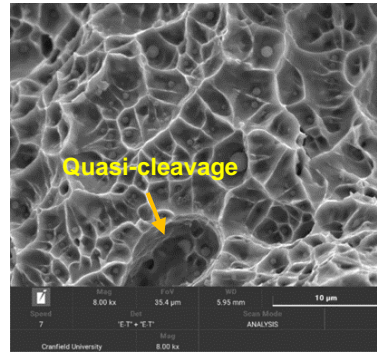
5.3.9 Fracture surface morphology of WAAM alloys

The Charpy impact fracture surfaces of the various WAAM alloys were evaluated by SEM technique. Figure 5-16 shows the Charpy impact fracture surface morphologies of the representative WAAM alloys, in as-deposited condition.

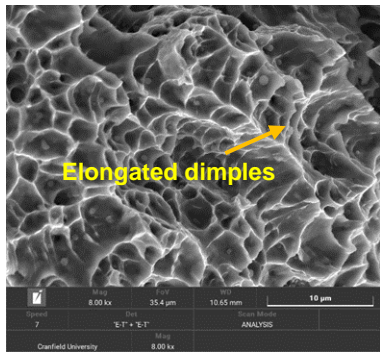
ER90S-G (100%) – 37J



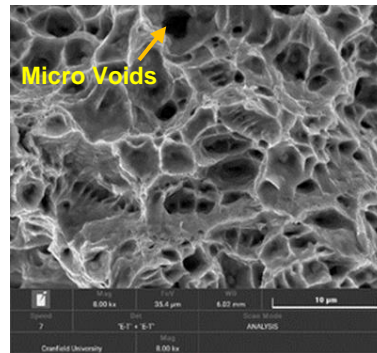
ER120S-G (25%) – 36J



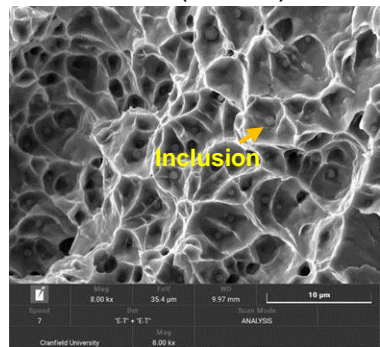
ER120S-G (37.5%) – 30J



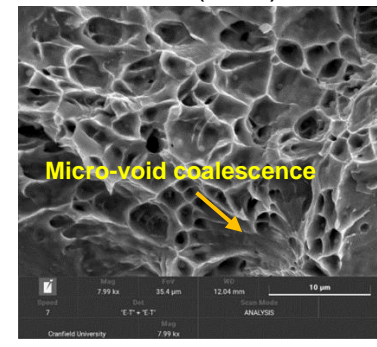
ER120S-G (50%) – 43J



ER120S-G (62.5%) – 29J



ER120S-G (75%) – 46J



ER120S-G (100%) – 37J

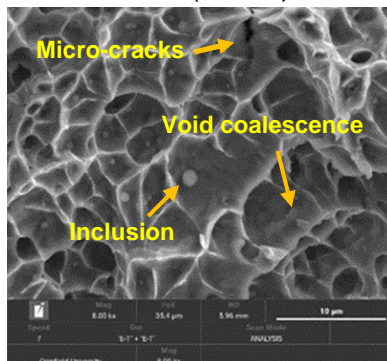


Figure 5-16 Charpy impact fracture morphology of different WAAM samples, in as deposited condition, as a proportion of ER120S-G composition

The fracture surfaces of all the WAAM samples exhibited a mixture of quasi-cleavage and dimples features. Large and small micro voids are also visible. Coalescence of micro voids and elongated dimples are observed on the surfaces of the modified WAAM samples.

It can be observed that the diameters of dimples present in the fracture surface of the modified WAAM alloys with higher Ni content, are larger compared to the dimples present on the impact fractured samples, containing lower Ni content. This could indicate improvement in the toughness of the modified WAAM alloy, owing to possible formation of higher volume fraction of acicular ferrite microstructure, through increased Ni content.

Inclusion particles are clearly visible on all the fractured surfaces, which possibly played a part in the fracture behaviour of the alloys. In general, the WAAM alloys failed by quasi-cleavage fracture.

The macrograph images of the fractured samples obtained for the different WAAM composition are presented in Appendix O.

5.4 Discussions

WAAM technology has been hailed as a suitable substitute for traditional subtractive manufacturing method, utilised in the manufacture of oil and gas components made from alloy 2.25Cr 1Mo steel material.

The excellent properties of alloy 2.25Cr 1 Mo steel composition is a major driver for its wide use in the marine oil and gas industry. However, unavailability of suitably optimised alloy 2.25Cr 1Mo wire composition, adapted for WAAM technology, is a challenge in deploying the technology for the manufacture of oil and gas components. The commercial GMAW solid wire of similar composition to alloy 2.25Cr 1Mo wrought steel, available for WAAM deposition is designated ER90S-G. However, it has a lean chemistry compared to the counterpart wrought material.

The high hardenability of 2.25Cr 1Mo alloy, coupled with the multiple thermal cycles generated during WAAM deposition process result in the formation of

heterogeneous microstructures, consisting of high-volume fraction of hard martensitic structures, oxide inclusions, etc. in the deposited WAAM alloy. This microstructural formation has a detrimental effect on the as-deposited mechanical property of 2.25Cr 1Mo WAAM alloy, particularly, the low temperature impact toughness (Abson, D. J., 2018).

It is an established knowledge that alloying elements play special role in influencing the microstructure and properties of weld metals; hence, the characteristics weld metal properties, such as impact toughness can be improved by designing new wire compositions or modifying the existing ones.

In this study, the base composition of 2.25Cr-1Mo (using ER90S-G solid wire), was modified in a controlled manner, with Mn4Ni2CrMo composition (using ER120S-G solid wire). The overall objective was to optimise the nickel content in the resulting WAAM alloy to improve its mechanical properties in as-deposited condition, particularly, the sub-zero temperature Charpy impact toughness.

Nickel was the main element targeted in achieving the improvement, because of its ability to enhance low temperature impact toughness of weld metal, through formation of desirable microstructures, primarily acicular ferrite (Bose-Filho, W. W., 2007).

5.4.1 Effect of increased nickel content on microstructure

The subtleties in microstructural identification and nomenclature, makes it difficult to conclusively categorise the various martensitic, bainitic and ferritic structures in the WAAM alloys in absolute terms (Kang, B. Y. et al., 2000).

Though nickel was the target element for achieving the improvement in mechanical properties of the deposited alloys, the presence of other elements in the base compositions including Cr, Mo, and Mn, is expected to also play some roles in influencing the microstructures developed in the modified WAAM alloys.

The microstructure of the modified samples containing a higher proportion of ER90S-G, such as the composition containing 25% ER120S-G, is expected to contain higher fractions of lower temperature phases like martensite and lower

bainitic structures, because of the higher contents of Cr and Mo (Bose-Filho, W. W., 2007).

As the proportion of ER120S-G composition was increased in the mix, preferential evolution of higher temperature microstructures like, acicular ferrite is anticipated to increase, due to increase in nickel content (Setiyanto, N. A., et al., 2019). Formation of retained austenite is also expected to increase with increasing proportion of ER120S-G, due to the increase in the content of Mn and Ni in the alloys. This is because, Ni and Mn as austenite stabilisers, lower the eutectoid transformation temperature, thereby retaining more austenite at room temperature, as illustrated in Figure 2-44, of section 2.8.2. (Sidney H. Avner, 1974).

5.4.2 Effect of increased Ni content on inclusion evolution

The result of oxygen combustion test presented in section 5.3.7, revealed that the oxygen in the deposited WAAM metal about 750% higher compared to the counterpart F22 wrought alloy. The EDS analysis showed high manganese and silicon peaks, inferring that some of the dissolved oxygen in the WAAM weld metal was precipitated as MnO.SiO₂ oxide inclusions.

The characteristics of weld metal oxide inclusions such as- composition, number density and size distribution, can influence the properties of the weld metal (Hong, T. et al., 2000), and their presence could be detrimental to the properties of weld metal including the charpy impact toughness (You, D. et al., 2017), especially when they occur in relatively large amounts (Pamnani, R. *et al.*, 2016; Barrick, E. J. and Dupont, J. N., 2020). This is because that could potentially act as sites for nucleation of intragranular crack, when they are not potent to preferentially nucleate acicular ferrite (Setiyanto, N. A., et al., 2019; Barrick, E. J. and Dupont, J. N., 2020).

The modified WAAM alloy, containing 62.5% ER120S-G produced the highest inclusion number density, approximately 235% higher, when compared to the WAAM composition containing 50% ER120S-G. See table 5-5 in section 5.3.6.

5.4.3 Effect on hardness

The effect of controlled mixing of ER90S-G and ER120S-G wire compositions on the microstructures formed in the modified alloys can also be observed through their effect on hardness property.

If all the austenite in a C-Mn weld metal were to transform to martensite, it is expected that the maximum hardness value for low carbon martensite would be 340HV, bainite would be approximately 325HV, acicular ferrite will be approximately 265HV, while allotriomorphic ferrite will have a maximum hardness of 250HV (Bose-Filho, W. W., 2007). Hence, it is expected that the maximum hardness value measured in this study, will be related to the alloy with the highest volume fraction of martensitic microstructure.

A maximum hardness of 344HV was obtained in the pure ER90S-G WAAM metal, while the pure ER120S-G gave a hardness of 302HV. The hardness of the modified compositions varied between these values, within a relatively narrow range of 290 and 319 HV.

The high hardness of pure ER90S-G is attributed to its high hardenability, due to the relatively higher content of Cr and Mo (Sidney H. Avner, 1974; Jorge, J. C. F. et al., 2001). These elements are able to impact a deeper through thickness hardenability compared to Ni (Sidney H. Avner, 1974).

The hardness obtained in the modified compositions slightly decreased with increasing proportion of ER120S-G, up to the composition containing 50% ER120S-G, owing to decrease in hardenability.

Thereafter, the reduction in hardness became more significant from the composition containing 62.5% ER120S-G, due to greater increase in Ni and Mn content, in place of Cr and Mo. This is expected because the property of the modified WAAM alloys is determined by the interaction of the different elements present in the base compositions (Sidney H. Avner, 1974; Kang, B. Y. et al., 2000).

5.4.4 Effect on strength

The strength of pure ER120S-G composition is comparable to that of ER90S-G. Ni and Mn impact strength through solid solution strengthening. Also, the high Ni content in ER120S-G is expected to enhance formation of high-volume fraction of acicular ferrite microstructures, helping to refine the grain (Bose-Filho, W. W., 2007). Smaller grain sizes have a greater total grain boundary area, hence can offer higher resistance to dislocation movement, thereby increasing the yield strength of the alloy (William D. Callister and David G. Rethwisch, 2011).

The various modified compositions show marginal differences in UTS and YS values, which is due to the combined effect of Cr, Mo, Mn, and Ni contents in the alloys. Any decrease in strength, through reduction in the content of Mo and Cr, was largely compensated for by the corresponding increase in the content of Ni and Mn, hence the comparable UTS and YS values observed in the modified alloys.

5.4.5 Effect on impact toughness

The sub-zero temperature charpy impact toughness of the modified alloys was observed to increase, as the nickel content was increased, through increase in the proportion of ER120S-G composition.

The increase in charpy impact toughness is expected to result from the formation of higher volume fraction of acicular ferrite microstructure (Huang, G. et al., 2018), which has a characteristic nature consisting of fine interlocking (basket-weave) ferrite grains, within the austenite grains (Babu, S. S., 2004; Huang, G. et al., 2018; Kang, B. Y. et al., 2000).

This chaotic arrangement of the microstructure is attributed to the increase in the toughness of the modified alloys, owing to the resistance it offers to cracks, as they propagate through the materials, during the charpy test, (Babu, S. S., 2004; Huang, G. et al., 2018).

Interestingly, the charpy impact toughness value measured in this study was observed to peak in the modified WAAM composition containing 50% ER120S-

G, with Ni content of 0.9wt%. Afterwards, the value dropped sharply to a minimum, in the composition containing 75% ER120S-G.

A further increase in nickel content, through increase in the proportion of ER120S-G wire composition, produced lower charpy impact values. See Figure 5-15.

A similar observation was reported by some authors including Setiyanto, N. A. et al., 2019; Sun, Y. et al., 2012, and Kang, B. Y. et al., 2000. The authors achieved a maximum charpy impact toughness in their studies, with nickel contents of 0.7wt%, 1wt% and 0.91wt% respectively. They found that a further increase in Ni content deteriorated the impact toughness property of the material. Nova et al., attributed the deterioration in impact toughness to the evolution of hard MA phases and coarse grain structure in the weld metal (Setiyanto, N. A. et al., 2019).

Kang et al, explained that the deterioration in impact toughness observed with further increase in Ni content, was due to the presence of high content of Mn in the weldment. This led to formation of predominantly martensitic microstructures, which were susceptible to propagation of intergranular brittle cracks. A maximum Mn content of 1wt% was recommended to minimise the formation of martensitic microstructures (Kang, B. Y. et al., 2000).

One explanation for the sudden drop in charpy impact toughness of the WAAM alloy containing 1.23wt% Ni and 1.3wt% Mn content, that was observed in this study, could perhaps be due to the formation of high fractions of martensite-austenite (M-A) constituents (consisting of high carbon martensite and some retained austenite) in the reheated microstructures (Huang, G. et al., 2018).

M-A constituents can decrease the toughness of the weld metal when they exist in the notched surface, owing to nucleation of microcracks in the boundary between the M-A constituent and ferrite matrix, which further grow into the matrix when the stress concentration increases more than the critical stress of the M-A constituents (Huang, G. et al., 2018).

But further detailed microstructural identification and accurate volume fraction analysis, would be required to ascertain this factor.

It is a general knowledge that the characteristics and volume fraction of oxide inclusions could influence Charpy impact toughness of weld metals. The presence of high number density of oxide inclusion particles could deteriorate the weld metal impact toughness, by acting as stress raisers, leading to nucleation of cleavage cracks (Pamnani, R. *et al.*, 2016).

The analysis of inclusion particles conducted in this study found a significantly high number density of inclusion particles in the modified WAAM composition containing 62.5% ER120S-G, and 1.23wt% Ni. This perhaps could have played a role in the sudden drop in Charpy impact toughness observed in this composition, which incidentally was the lowest Charpy value obtained in this study.

5.5 Conclusions

A study to modify alloy 2.25Cr 1Mo wire composition, using Mn4Ni2CrMo solid wire composition, to produce an optimised composition with improved as-deposited static strength and low temperature toughness properties led to the following conclusions.

- The tandem-GMAW process is suitable for producing modified weldment compositions, with improved microstructure and mechanical properties, by tailored feeding of selected solid wire compositions, in the same weld pool
- The modified WAAM alloys exhibited superior mechanical property compared to the baseline ER90S-G composition
- The modified WAAM alloy, containing equal proportion of ER120S-G and ER90S-G wire compositions, with Ni and Mn contents of 0.9wt% and 1.15wt% respectively, produced the optimum mechanical performance, in as-deposited condition, found in this study.

Recommendation

- Detailed microstructural analysis is required to provide adequate data to correctly ascertain the possible role of the various microstructural constituents in the sudden drop in charpy impact toughness, observed in this study
- Investigate the use of external argon trailing shield to minimise atmospheric oxidation of the alloying elements and possibly produce further improvement in charpy impact toughness.

6 Experimental study of corrosion performance of WAAM alloys exposed to a simulated sour service environment

6.1 Experimental procedure

6.1.1 Equipment set up

General Corrosion experiments were conducted using a cylindrical laboratory glass cell, to evaluate the corrosion performance of a number of WAAM deposited low alloy steel samples.

A sour gas (CO₂/H₂S) composition, comprising 1%H₂S and 98%CO₂, was passed through the test samples immersed in a simulated sea water environment, consisting of 1%wt. NaCl solution. The gas was passed into the glass cell using a mass flow controller, at a flow rate of 30ml/sec and atmospheric pressure. The exit gas was passed through a sodium hydroxide solution (NaOH) scrubbed and further passed through a hydrogen gas flare to burn off any remaining H₂S gas.

The experimental equipment and set up are presented in Figure 6-1. Table 6-1. displays the experimental test matrix and parameters applied in the investigation.

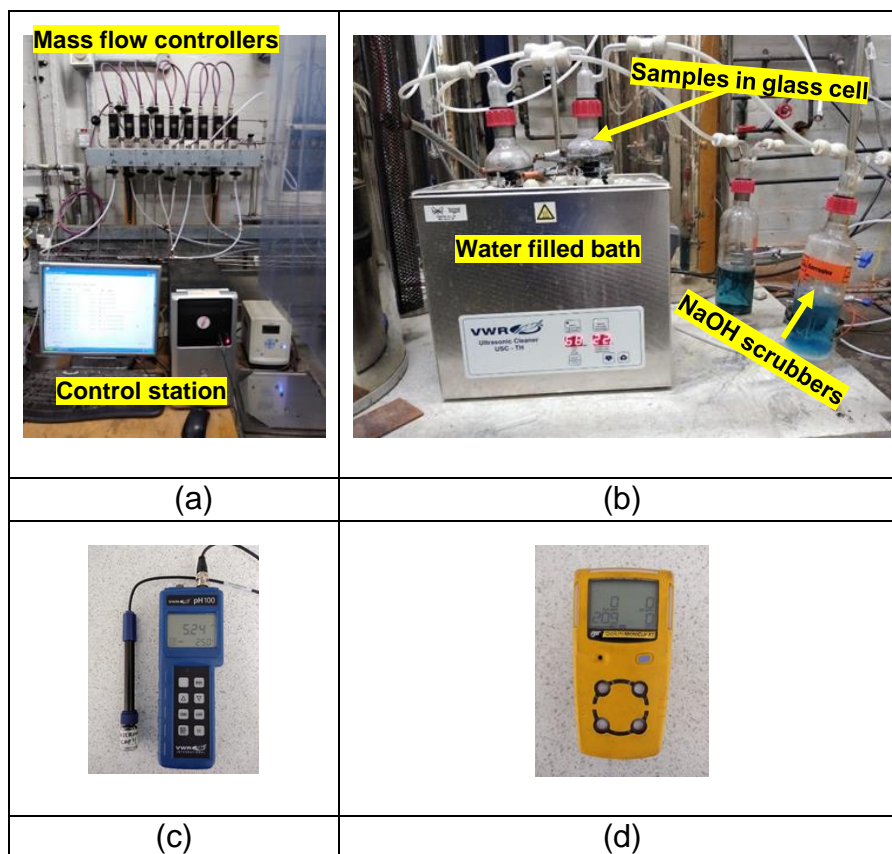


Figure 6-1 Equipment and set up showing (a) Mass flow controller (b) Glass cell bottles immersed in a temperature-controlled water bath (c) ph meter, and (d) H₂S gas monitor

Table 6-1 Experimental matrix and test parameters for corrosion study

Test Samples	Experimental matrix- Glass cell					
	Number of trials	Duration (hr)	Temperature (°C)	Test solution (ph.)	Test Gas (flowrate)	Total pressure
WAAM metal and F22 (LAS)	3	24	20	1 wt%. NaCl (3.5)	1% H ₂ S in CO ₂ (30ml/min)	Atm.
	4	72	20			
	2	24	60			

6.1.2 Test materials and compositions

A total of five (5) different rectangular WAAM specimens of approximate dimension 20x50x4.8 mm were machined from the bulk material. The bulk materials were obtained from another study conducted by the author and presented in chapters 4 and 5 of this work.

ASTM A182 F22 wrought steel, of similar composition was used to compare the corrosion performance of the WAAM alloys. The test samples are described in Table 6-2.

Table 6-2 Samples utilised for corrosion tests

Samples	Designation	Manufacturing process	Conditions	Hardness (HV), max
1	ER90S-G	Single-wire GMAW	As-deposited	341
2	ER90S-G	Single-wire GMAW	Heat-treated	234
3	ER90S-G	Tandem-wire GMAW	As-deposited	344
4	ER120S-G	Tandem-wire GMAW	As-deposited	302
5	ER90S-G & ER120S-G (1:1)	Tandem-wire GMAW	As-deposited	319
6	ASTM A182 F22	Forged	Wrought	251

The chemical compositions of the samples are given in Table 6-3

Table 6-3 Chemical composition of test samples

Materials	C	Si	Mn	P	S	Cr	Mo	Ni	Al	Cu	Ti	V, Zr
ER90S-G	0.07	0.5	0.76	0.007	0.012	2.45	1.03	0.03	<0.01	0.07	0.02	<0.01
ER90S-G: ER120S-G (1:1)	0.08	0.56	1.15	0.01	0.011	1.4	0.81	0.9	<0.01	0.06	<0.01	<0.01
ER120S-G	0.08	0.61	1.55	0.012	0.01	0.29	0.51	1.83	<0.01	0.04	<0.01	<0.01
F22- Wrought	0.12	0.23	0.51	<0.005	<0.003	2.48	0.99	0.20	0.02	0.17	<0.01	<0.01

6.1.3 Choice of test method

The ASTM procedure Standard Practice for Laboratory Immersion Corrosion Testing of Metals (G31–12) provides a standardized method for directly measuring mass loss in laboratory immersion tests to determine the general corrosion rates of metals. Although immersion test procedures provide empirical measures of the overall magnitude of reaction which can be used to determine average corrosion rates, but, unlike electrochemical measurement method, it does not provide the instantaneous corrosion rates that are required for performance model development.

Hence, measuring the mass change in test specimens is not enough to understand the corrosion mechanism or quantify the effects of environmental variables. Nonetheless, other analysis, including microscopic examinations of

reacted specimens to detect pitting and identify corrosion products, can be conducted to gain understanding of the corrosion behaviour.

Most of the mass loss usually occurs within a few days prior to passive stabilization. The instantaneous corrosion rate decreases significantly as the surface stabilizes and becomes much lower than the average cumulative rate that would be measured in an immersion test after any cumulative test duration, Ebert, W. L., & Gattu, V. K. (2020).

The mass loss corrosion test method was utilised in this study, because of time constraint, due to delay from school closure and stringent safety requirement associated with the use of H₂S gas. Also, mass loss method is sufficient for conducting a comparative corrosion test, which is the scope of this study.

6.1.4 Sample preparation and testing

The samples were prepared and tested according to the method described in NACE ASTM G31, (31). In the process, 1 wt% NaCl solution was prepared by pouring 3 litres of deionised (DI) water in a large cylindrical glass bottle and adding 30.2 g of sodium chloride salt. Hydrogen chloride (HCl) solution was added to the mixture to adjust the pH to the required value. The test glass cell was filled with the NaCl solution, up to about $\frac{3}{4}$ of its volume. It was then placed in a heated water bath, with the temperature set to the desired test value. Nitrogen gas (N₂) was passed through the solution for 2hrs to deoxidise it.

Before immersion, the surfaces of the individual specimen were polished sequentially using 240, 600 and 1200 grit SiC paper. They were rinsed with using acetone and allowed to dry in air. The weight of each sample was measured thrice and recorded, before immersing in the test solution. Five samples representing the individual test condition were immersed together. The solution was purged again for a further 1hr. The N₂ gas was then turned off while the CO₂/H₂S gas was immediately introduced into the system at the set pressure and flow rate. The flow of the gas was maintained throughout the duration of the test.

After the test, the CO₂/H₂S gas was turned off and the solution was purged for approximately 2hrs to remove any residual CO₂/H₂S gas. The pH of the solution

was measured before the corroded samples were retrieved. The samples for weight loss analysis were cleaned using a plastic scrubber and rinsed in acetone to remove the corrosion product. They were then dried in air before their weight was measured and recorded. Two of the samples were retained for surface and corrosion products analysis. The different experimental conditions were repeated 2-4 times, to find out reproducibility of the experiments.

The corrosion products and surface morphology were observed using scanning electron microscopy (SEM). The elemental composition of the corrosion product was analysed using energy dispersive spectroscopy (EDS), with an acceleration voltage of 20 kV. Identification of the phase composition of corrosion products was performed using X-ray diffraction (XRD) Cu K α X-ray source operated at 40 kV and 150 mA.

According to NACE TM0169/G31-12a: Assessment method for corrosion degradation, the weight loss/gain and corrosion rate of the samples can be determined from the expressions given in equations (6-1).

$$\text{Weight loss/gain, } W \text{ (g)} = W1 - W2 \quad (6-1)$$

Where: $W1$ is the initial average weight of the sample, before corrosion test, and $W2$ is final average weight of the sample, after corrosion test.

Furthermore, using the initial and final weight of the specimen, the corrosion rate, CR [mm/yr.] can be calculated from equation (6-2).

$$\text{CR} = \frac{8.76 \times 10^4 \times W}{A \times T \times \rho} \quad (6-2)$$

Where the constant 8.76×10^4 is a specific unit described in standard ASTM G1-90 (1999) for the formula to give the result in mm/yr. W [g] is the weight loss of the specimen, A [cm 2] is the surface area of the specimen exposed to the environment, ρ [g/cm 3] is the density of the material tested and T [hours] is the time the specimen was exposed (time of the test).

6.2 Results presentation

A total of nine tests were performed to investigate the influence of exposure time and temperature on the corrosion performance of the WAAM samples, using the weight loss/gain method and the experimental test matrix presented in Table 6-1.

Figure 6-2 shows the appearance of the glass test bottles before and after test.

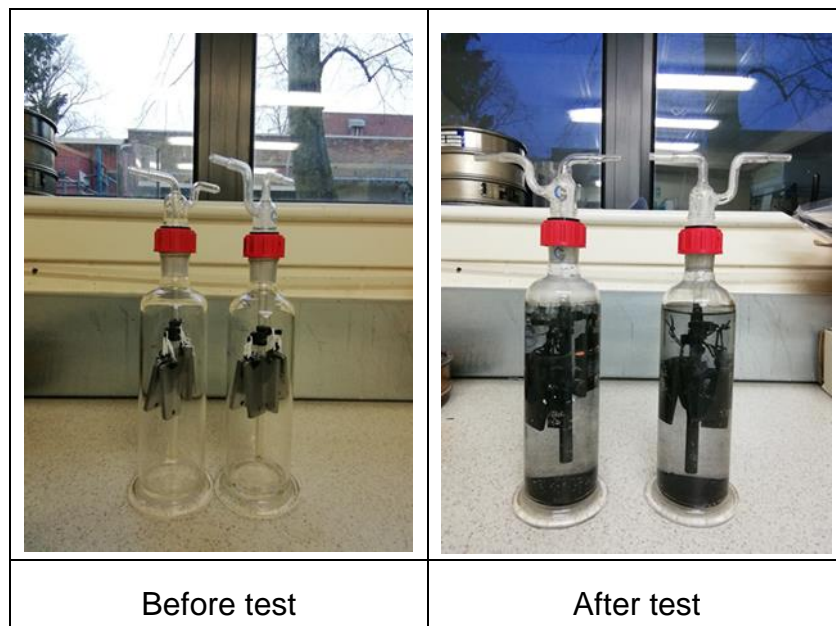


Figure 6-2 Appearance of test bottle content before and after test

Observation of the glass cell bottles, with the samples after the tests show dark corrosion products residues that gathered at the bottom of the bottles.

6.2.1 Macroscopic surface appearance of samples after test

The appearance of the samples before and after removal of the corrosion product layer is shown in Figure 6-3. No significant morphological variations were observed on the corrosion surface layer of the samples, under a given exposure condition. The corrosion products on the surface of the samples exposed for 24hrs were relatively flat, thin and with some areas showing no significant corrosion Fig. 6-3(a). The samples exposed for the 72 hours duration Fig.6-3(b), showed a relatively darker, uniform, and thicker corrosion product film, covering the whole of the surface.

Figure 6-3(c) shows the surface appearance of the samples exposed at 72hrs after removing the corrosion products. The corrosion products are observed to form patches of adhesives films on the steel surface.



Figure 6-3 Surface appearance of samples after exposure to corrosion

6.2.2 Weight loss of WAAM samples

In evaluating the comparative corrosion performance of the various WAAM samples, the experiment was repeated three times and their weight loss was computed using equation (1). Figure 6-4 gives the plot of average weight loss of the individual WAAM samples.

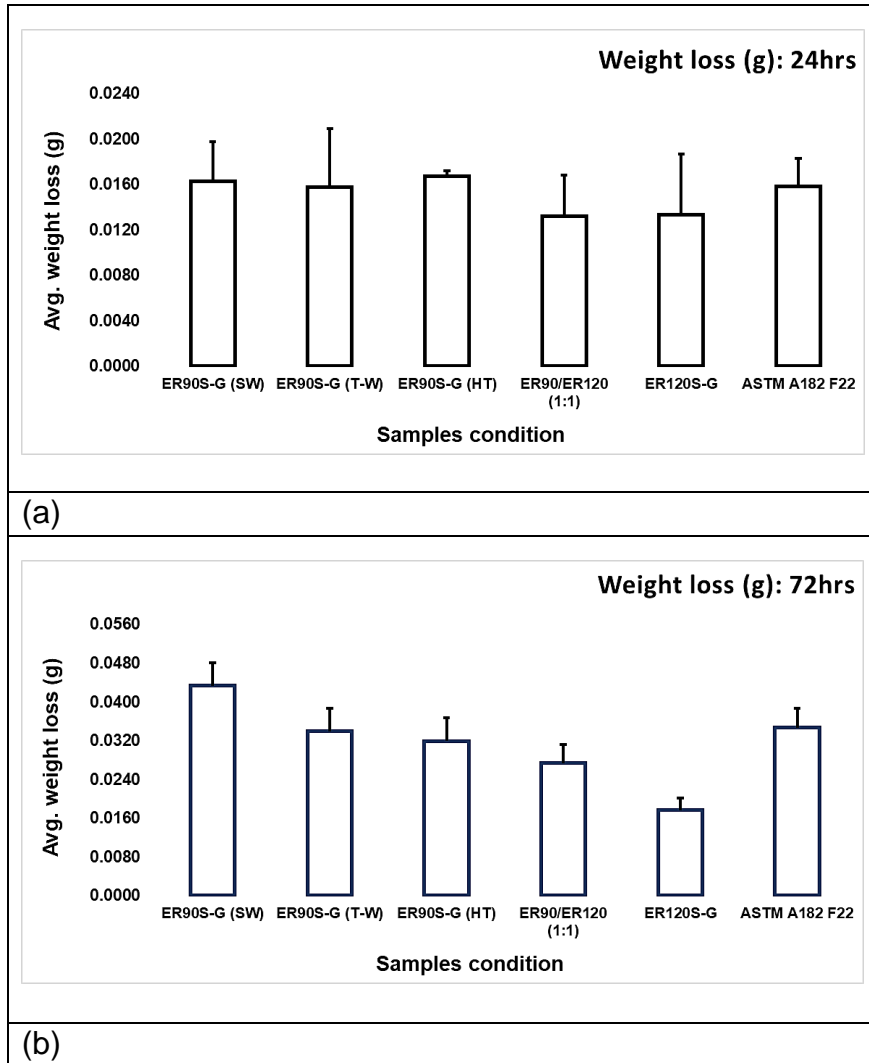


Figure 6-4 Comparative evaluation of WAAM weight loss after (a) 24hrs and (b) 72hrs test duration

It can be observed from Figure 6-4(a), that the average weight loss of WAAM ER120S-G is the lowest, which is (0.0132g). The average weight loss of the wrought F22 sample is slightly higher (at 0.0158g), compared to WAAM ER120S-

G; but it is either comparable or slightly lower than those of the counterpart WAAM ER90S-G samples.

In Figure 6-4(b), the average weight loss of ER120S-G is also observed to be lowest, followed by the modified WAAM composition containing equal proportions of ER120S-G and ER90S-G compositions. The average weight loss of wrought F22 was observed to be lower only than ER90S-G samples, deposited using the single-wire GMAW process.

6.2.3 Effect of exposure duration

The effect of exposure time on the corrosion weight loss was evaluated with multiple repeats of the experiment. Exposure durations of 24hrs and 72hrs was utilised, and the temperature of the environment was maintained at 20°C. The result of the test is summarised in Figure 6-5.

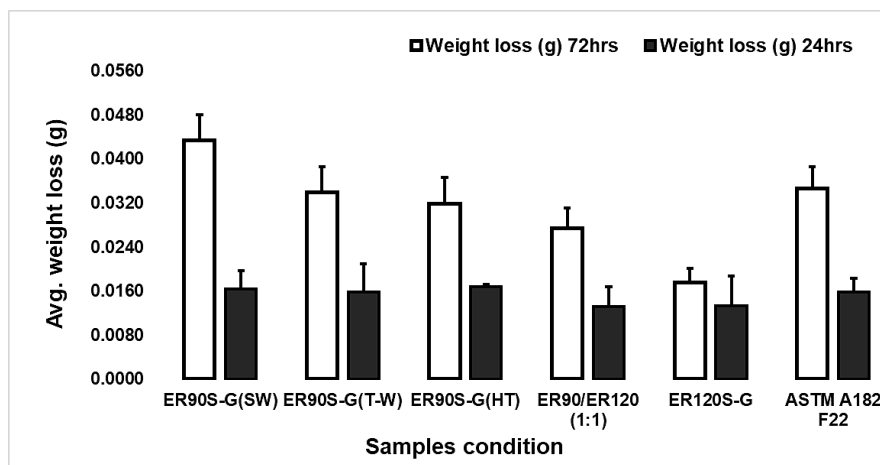


Figure 6-5 Effect of exposure duration on corrosion weight loss

From Figure 6-5, the samples exposed for a duration of 72hrs showed higher weight loss compared to the samples exposed for 24hrs. The average weight loss of WAAM ER120S-G exposed for 72 hrs was the lowest at (0.0176g), followed by that of ER120S-G/ER90S-G WAAM modified composition, at (0.0273g) The wrought F22 sample exposed for 72hrs, somewhat showed a similar or slightly lower weight loss of (0.0347g), compared to the counterpart ER90S-G WAAM samples.

6.2.4 Effect of temperature

To evaluate the effect of temperature on the corrosion weight loss of the samples, tests were conducted at temperatures of 20 and 60°C. The tests were conducted over 24hrs duration, with multiple repeats of the test to reduce the experimental error. The result of the test is presented in Figure 6-6.

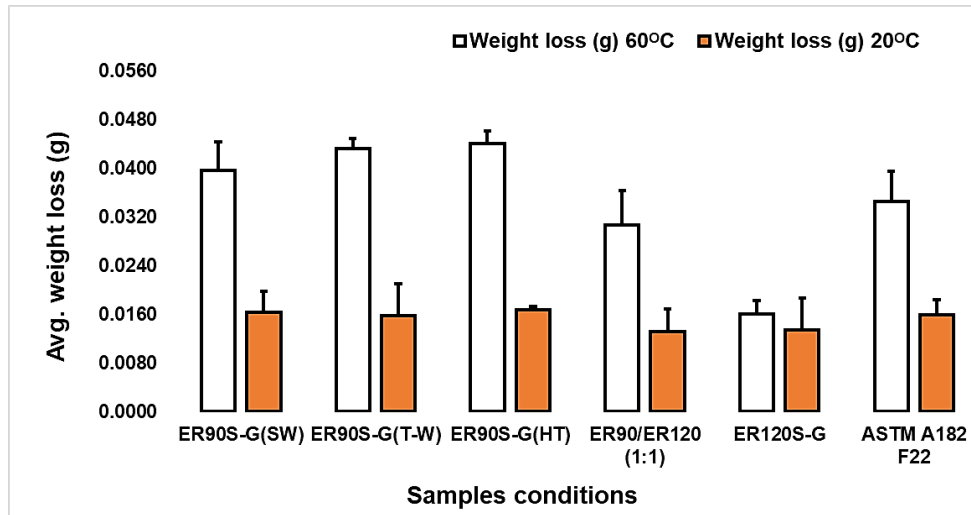


Figure 6-6 Effect of exposure temperatures on corrosion average weight loss

The result of the experiment shows that increase in temperature led to increase in the corrosion weight loss of the samples. The average corrosion weight loss of ER120S-G at 60°C exposure temperature, was the lowest (at 0.0160g) amongst all the samples. This was followed by the average weight loss of the mixed composition at 0.0307g. The average weight loss of the wrought F22 sample, at 0.0345g, was lower than the counterpart ER90S-G WAAM samples.

6.2.5 SEM surface morphology of corrosion samples

SEM surface micromorphology of representative corrosion samples exposed for 24 and 72hrs are shown in Figure 6-7. The macrograph sections were obtained at magnifications of 100x and 1000x.

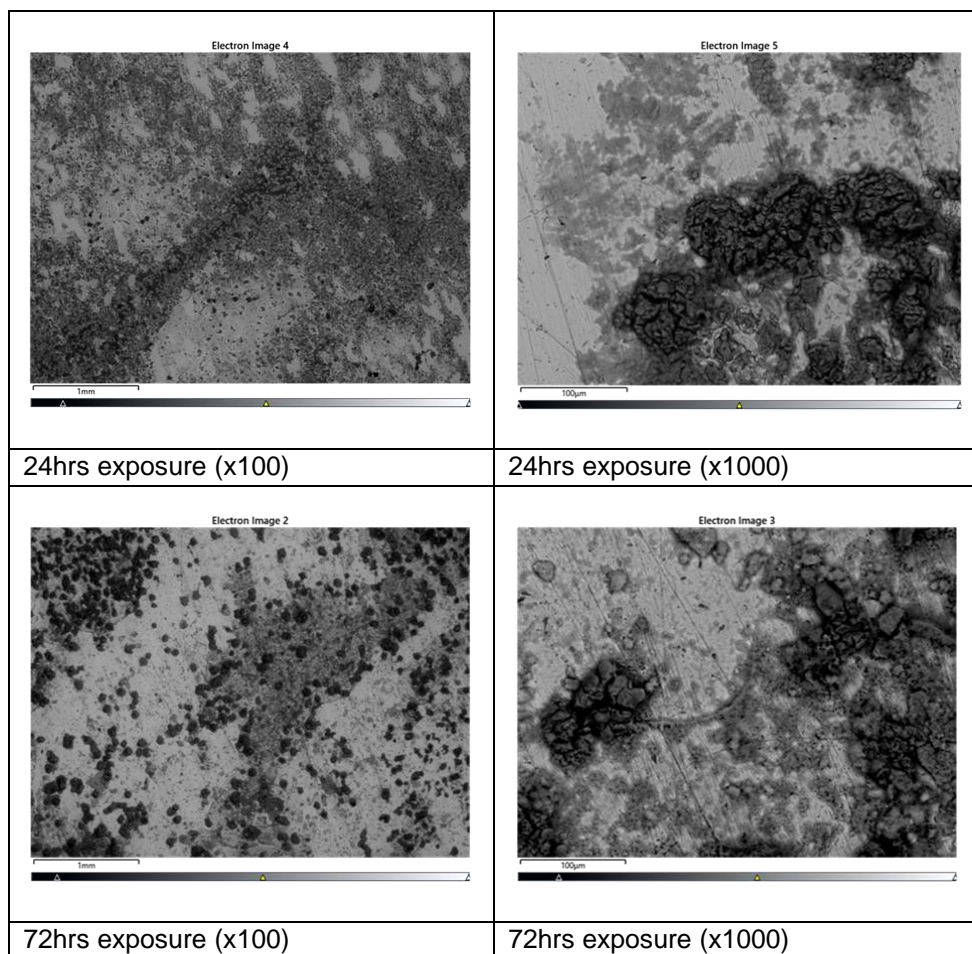


Figure 6-7 SEM macrographs of corrosion samples

From the macrographs, it was evident that the samples exposed for 24hrs, showed lighter or lesser corrosion attack, occurring within a relatively smaller surface area. Its appearance was more representative of general corrosion attack. However, the sample exposed for 72hrs showed more conspicuous and severe corrosion. The corrosion appeared to be representative of a localised pitting attack and occurred within a relatively larger surface area.

6.2.6 Analysis of corrosion product

The phase composition of the corrosion product film was determined by the X-Ray diffraction technique. The analysis was conducted on representative samples exposed for 24 and 72hrs. This was done to determine whether the test duration had an effect on the type and properties of corrosion product films formed. The results of the XRD analysis are presented in Figure 6-8.

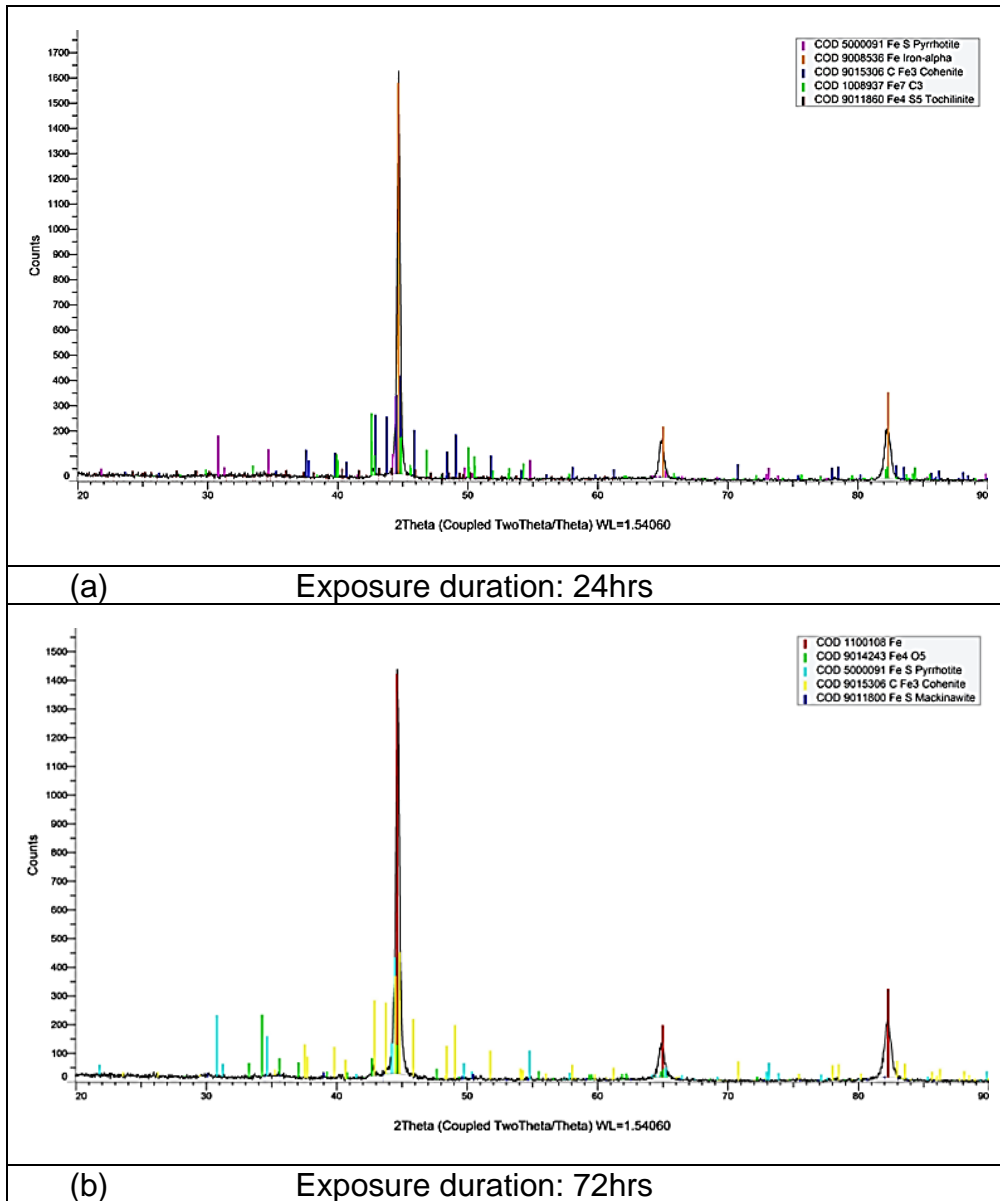


Figure 6-8 X-Ray diffraction analysis of corrosion product film (a) Obtained after 24hrs (b) after 72hrs

The XRD analysis of corrosion product layer for the sample exposed for 24 hrs showed the presence of Pyrrhotite (FeS), Cohenite (Fe_3C), Tochilinite (Fe_4S_5), Fe_7C_3 and Fe_4O_5 . While the corrosion product films on the sample exposed for 72hrs were identified to include Pyrrhotite (FeS), Cohonite (Fe_3C), Mackinawite (FeS) and Fe_4O_5 .

Further evaluation of the phase composition of the corrosion scale by EDS analysis, was conducted to determine the chemistry of the amorphous compounds, table 6-4.

Table 6-4 EDS analysis of corrosion samples, in wt %

Test duration	C	O	Na	Si	S	Cl	Cr	Mn	Fe	Total
72hrs	3.68	17.55	1.46	0.38	3.71	0.49	2.53	0.62	69.57	100
24hrs	3.23	17.59	2.02	0.43	2.54	0.58	2.67	0.6	70.33	100

The elemental analysis of the corrosion product film showed the presence of some elements of interest including Fe, O, S and C. The corrosion product also became rich in Na and Cl. No significant difference was observed in the elemental content of the samples exposed for 24 and 72hrs.

6.3 Discussion

The use of WAAM components in marine environments will likely not be spared from sour service corrosion attack. The choice of material for this environment is typically predicated on the need to achieve adequate resistance against corrosion degradation. This is crucial even at low H₂S levels, because of the desire to prevent potential catastrophic safety risk and undesirable repair or replacement costs (Kermani, B. et al., 2006).

In recognising the increasing demand for utilisation of WAAM manufactured components for marine oil and gas applications, this study set out to throw more insight on the corrosion performance of WAAM manufactured low alloy steel materials, exposed to sour gas compounds in a simulated marine environment. The performance was compared with that of a wrought counterpart.

As mentioned above the metallurgy of WAAM manufactured alloy material differs from that of the wrought alloy in some respect. This is primarily due to the specific alloying content and the effect of multiple high thermal cycle experienced during deposition of the WAAM alloy. Thermal variation leads to heterogeneity in the microstructure and properties of the WAAM alloy.

The average corrosion weight loss of the samples tested at 20°C and exposed for 24hrs and 72hrs is shown in Figure 6-4. The results indicated that the corrosion performance of wrought F22 sample was either commensurate or slightly higher than the counterpart WAAM ER90S-G samples, taking into consideration the experimental error. Their unique microstructural differences are attributed to this observation.

The effect of heat treatment on the corrosion performance of WAAM ER90S-G is not very apparent for the 24hrs exposure test. However, the test results obtained after exposure for 72hrs, seemed to indicate that heat treatment is more effective in reducing the corrosion degradation at longer exposure time, compared to as-deposited ER90S-G samples.

Comparison of the average weight loss of all the samples showed that ER120S-G exhibited the highest corrosion performance, followed by the sample which contained equal proportions of ER120S-G and ER90S-G.

This could be attributed to its higher nickel content. A study by Wen et al. (2016), showed that nickel shifts the corrosion potential of steel towards the positive direction, lowering the corrosion current density. This encourages the formation of homogenous and dense corrosion products film, leading to enhanced corrosion (Wen, C. et al., 2016).

The importance of microstructure on corrosion performance has also been highlighted. It was reported that refining the grain size reduced an alloy's SSC susceptibility (Jarvis A. R., 1992; Iannuzzi, M. et al., 2017). Hence, the well-known ability of Ni to produce grain size refinement, through formation of acicular ferrite microstructure, could perhaps have contributed to the high corrosion performance.

The corrosion product films on the surface exposed for 72hrs appeared thicker, and more uniformly distributed over a larger surface area of the sample, compared to the samples exposed for 24hrs. Patches of adhesive films were also observed on the surface of the samples exposed for 72hrs, which perhaps prevented the layered exfoliation of steel surface (Wen, C. et al., 2016). However,

the extension of corrosion time from 24hrs to 72hrs, led to increase in corrosion rate of the samples.

The as-deposited ER90S-G showed the highest weight loss, compared to ER120S-G. This could be attributed to the ease at which nickel replaces some atoms in the corrosion product film, giving rise to the formation of cation exchange field. Thus, nickel influences the ion distribution of the corrosion film, causing the steel to display a cation ion-selective property leading to improved corrosion performance (Wen, C. et al., 2016).

On the other hand, low chromium steel particularly with Cr levels in the range of 3-5 wt%, (such as ER90S-G) have been reported to exhibit excellent corrosion resistance in a sweet service (CO_2) environment, (depending on the prevailing environmental and metallurgical conditions); which was attributed to the formation of FeCO_3 and $\text{Cr}(\text{OH})_3$ corrosion products. However, under a sour service condition, H_2S could significantly influence the type and properties of corrosion product film precipitated. This interaction could lead to the formation of FeS , which steadily weakens the chromium enriched corrosion film and reduces its protective performance (Jianbo, S., 2016).

Both the corrosion degradation of the material and the rate at which the corrosion products are formed can be accelerated by temperature (Gao, S. *et al.*, 2017). From Figure 6-6, it is clear that the increase in temperature from 20 to 60°C accelerated the corrosion damage.

The corrosion products identified on the samples exposed for 24hrs primarily consisted of Pyrrhotite and Tochilinite, which are the more stable forms of iron sulphide films. However, Pyrrhotite scale in addition to Mackinawite (an unstable form of FeS) scale was observed in the corrosion product of samples exposed for 72hrs.

The corrosion surface morphology of the samples exposed for 24hrs was more representative of a general or uniform corrosion attack. While localised corrosion was observed on the surface of the sample exposed for 72hrs. This could have resulted from the presence of less stable mackinawite corrosion products as

earlier reported, and which probably formed a partially protective corrosion product layer on the surface of the sample, leading to localised corrosion attack (Esmaeely, S. N. and Nešić, S., 2019).

6.4 Conclusions

The glass cell methodology was successfully utilised in evaluation of the sour corrosion performance of a number of WAAM deposited low alloy steels, in a simulated sea water environment and enabled comparison to the performance of a wrought alloy, under the same corrosion conditions. The primary findings, under the test conditions utilised in this study include:

- The corrosion performance of WAAM ER120S-G was highest, followed by the modified ER90S-G/ER120S-G composition, which was attributed to effect of the higher nickel content.
- The corrosion performance of the wrought F22 steel was similar or marginally higher compared to the counterpart ER90S-G.
- The heat treated ER90S-G WAAM sample seemed to show higher corrosion performance at longer exposure time, compared to the as-deposited counterpart
- Corrosion weight loss of all the samples generally increased with increase in reaction temperature, under the test conditions.
- Increase in pH from 3.5 to between 5.8 and 7.1 was observed in all the tests, which could further confirm the absence of FeCO_3 corrosion products
- Increase in reaction time from 24hrs to 72hrs, caused a corresponding increase in corrosion, over the former
- Analysis of the corrosion products formed after exposure to the $\text{CO}_2/\text{H}_2\text{S}$ mixed gas environment, showed that Pyrrhotite and Cohonite were the main iron sulphide scales formed on the samples exposed for 24hrs. General corrosion was more evident on the samples exposed for 24 hrs,

- Pyrrhotite and Mackinawite precipitate were observed on the surface of the samples exposed for 72hr. The Mackinawite corrosion product film could have been undermined by the progressing corrosion, hence did not form uniformly, leading to localised corrosion attack on the samples.

6.4.1 Recommendations

- Additional and detailed analysis to measure the thickness and identify the types of corrosion products on all the various samples, will provide more insight on the cause(s) of the difference in corrosion weight loss observed, with respect to the specific test condition.
- The use of a bigger corrosion test vessel with a wider opening is recommended. This will help to minimise experimental errors which could occur from possible preferential galvanic corrosion of the samples when in contact with each other. This will also help to minimise disturbance or damage to the corrosion product layers while retrieving the samples from the corrosion glass cell
- Ensure the individual test samples are placed at similar distance from the gas entry point. This will help minimised the possibility of the flowing gas preferentially impinging and interacting with the corrosion process and corrosion product of the relatively closer samples over the farther ones.

7 OVERALL CONCLUSIONS

From the research questions, the following conclusions can be drawn from this study:

- The deposition rate achieved during manufacture of WAAM parts, can be substantially increased above 3kg/hr for steel, while simultaneously producing the part with excellent surface quality, through the use of tandem series wire configuration and single wire GMAW processes, combined with skin and core deposition strategy.
- Components manufactured via WAAM can meet and exceed the overall minimum static tensile, hardness and charpy impact toughness properties, required for manufacture of marine oil and gas components, after PDHT. However, fracture toughness testing will be required to ascertain the ability of WAAM parts (with shown higher oxygen and inclusion content compared to forgings, which has potential to reduce toughness), to meet the required dynamic crack resistance performance.
- While wrought 2.25Cr 1Mo steel can marginally perform better than the WAAM counterpart of similar composition, when exposed to sour gas environment, a modified alloy 2.25Cr 1Mo, with a nominal composition containing, 1.4Cr, 0.81Mo and 0.9Ni can out-perform the original composition, when utilised in a similar environment.

Other conclusions that can be drawn from this study include the following:

- A better control on the bead geometry and higher surface quality deposits can be achieved through the use of tandem GMAW series wire configuration, when the lead WFS is set slightly lower than the trail wire WFS
- Tandem parallel wire configuration is best for building WAAM parts, from the point of view of achieving the optimum width range, surface quality and MDE, compared to tandem series wire configuration or single wire GMAW process

- Argon trailing shield can be used to enhance the surface quality and potentially reduce the manufacturing lead time, of WAAM parts. However, the effect on the resulting properties of the part, needs to be clarified.

7.1 Further suggestions for future work

With the aim of increasing the technology readiness level of WAAM parts manufactured using 2.25Cr 1Mo steel, for marine oil and gas application, and high productivity tandem wire GMAW for WAAM component manufacture, it is recommended that further research be undertaken in the following areas:

- An assessment of methods to reduce the relatively high bead penetration depth, produced by the unique electrical arc characteristics of tandem GMAW process, should be explored for WAAM.
- A full evaluation of the fracture toughness behaviour of the as-deposited alloy 2.25Cr 1Mo weldment produced via WAAM is recommended.
- Heat treatment studies is recommended for the tandem modified WAAM alloy, containing equal proportions of ER120S-G and ER90S-G, to fully assess the potential to maximise the properties
- Volumetric NDT examination and defect analysis should be conducted on the component manufactured using the skin and core strategy, to ascertain the internal soundness, especially within the intersection areas of the skin and core layers in the part, with the purpose of enhancing the robustness of the applied process control algorithms.
- Design and testing of a tandem torch setting up jig or device, is suggested to ensure the tandem torch is accurately set with minimum error, at all times.
- Investigation of the effect of argon trailing shield on the deposited WAAM alloy property and estimation of the potential manufacturing time saving achievable from use of such a device.

REFERENCES

1. Abson, D. J. (2018). Acicular ferrite and bainite in C–Mn and low-alloy steel arc weld metals. *Science and Technology of Welding and Joining*, 23(8), 635–648. <https://doi.org/10.1080/13621718.2018.1461992>
2. Aglan, H. A. *et al.* (2013) 'Effect of Preheating Temperature on the Mechanical and Fracture Properties of Welded Pearlitic Rail Steels', *Engineering*, 05(11), pp. 837–843. doi: 10.4236/eng.2013.511101.
3. Ahmed, S. R., Agarwal, L. A. and Daniel, B. S. S. (2015) 'Effect of Different Post Weld Heat Treatments on the Mechanical properties of Cr-Mo Boiler Steel Welded with SMAW Process', *Materials Today: Proceedings*. Elsevier Ltd., 2(4–5), pp. 1059–1066. doi: 10.1016/j.matpr.2015.07.002
4. Aleksander, R. S. (2012) SAG-FW Welding of C90 Riser Steel Connectors. Master's thesis, NTNU
5. Alimardani, M., Toyserkani, E. and Huissoon, J. P. (2007), A 3D dynamic numerical approach for temperature and thermal stress distributions in multilayer laser solid freeform fabrication process, *Optics and Lasers in Engineering*, 45(12), p. 1115-1130.
6. Allum, C. J. (1983), MIG welding- Time for a reassessment, *Metal Construction*, 15(6), p. 347- 353.
7. Almeida, P.M.S. and Williams, S. (2010), "Innovative Process Model Of Ti-6Al-4v Additive Layer Manufacturing Using Cold Metal Transfer (CMT), Welding Engineering Research Centre (WERC), Cranfield University, pp. 25-36.
8. Almeida, P. M. S (2012) Process control and development in wire and arc additive manufacturing. PhD, Cranfield University

9. Al-Quzweny, M. B., Hadi, S. M. and Owaid, A. I. (2016) 'Determining Metal Surface Waviness Parameters and Height Liquid Surface Wave by Tracking Reflected Laser Speckle', *International Journal of Advanced Research in Engineering and Technology (IJARET)*, 7(2), pp. 69–77. Available at: <http://www.iaeme.com/IJARET/index.asp%5Cnhttp://www.iaeme.com/IJARET/issues.asp%5Cnwww.jifactor.com%5Cnhttp://www.iaeme.com/IJARET/issues.asp?JType=IJARET&VType=7&IType=2>

10. Andrén, H. O., Cai, G. and Svensson, L. E. (1995) 'Microstructure of heat resistant chromium steel weld metals', *Applied Surface Science*, 87–88(C), pp. 200–206. doi: 10.1016/0169-4332(94)00491-9.

11. Andrews, K.W. (1965) *Journal of the International Steel Institute*. Vol 203, p721

12. Arai, Y. *et al.* (2012) Study of High-strength Low-alloy Steel OCTG with High Carbon Contents for Mildly Sour Service 'Paper No. 9051', (9051), pp. 1–12

13. Arivazhagan, B. and Vasudevan, M. (2015) 'Studies on A-TIG welding of 2.25Cr-1Mo (P22) steel', *Journal of Manufacturing Processes*. The Society of Manufacturing Engineers, 18, pp. 55–59. doi: 10.1016/j.jmapro.2014.12.003.

14. ASTM F2792 -12a (2015) Standard Terminology for Additive Manufacturing Technologies. Available at: <https://www.astm.org/DATABASE.CART/WITHDRAWN/F2792.htm>, assessed 07/11/2018

15. Avazkonandeh-Gharavol, M. H., Haddad-Sabzevar, M. and Haerian, A. (2009) 'Effect of chromium content on the microstructure and mechanical

- properties of multipass MMA, low alloy steel weld metal', *Journal of Materials Science*, 44(1), pp. 186–197. doi: 10.1007/s10853-008-3103-2
16. Babu, S. S. (2004) 'The mechanism of acicular ferrite in weld deposits', 8, pp. 267–278. doi: 10.1016/j.cossms.2004.10.001.
17. Bai, J. Y. et al. (2016) 'Effects of thermal cycles on microstructure evolution of 2219-Al during GTA-additive manufacturing', *International Journal of Advanced Manufacturing Technology*
18. Baldan, A. (2002) 'Progress in Ostwald ripening theories and their applications to nickel-base superalloys Part I : Ostwald ripening theories', 7, pp. 2171–2202.
19. Baltazar Hernandez, V.H., Nayak, S.S. and Zhou, Y. (2011) Tempering of Martensite in Dual-Phase Steels and Its Effects on Softening Behaviour. *Metallurgical and Materials Transactions A*, 42A:3115–3129
20. Barbosa, C. *et al.* (2011) 'A microstructural and fractographic study on the failure of a drive shaft', *Journal of Failure Analysis and Prevention*, 11(6), pp. 693–699. doi: 10.1007/s11668-011-9499-z
21. Barrick, E. J. and Dupont, J. N. (2020) 'Materials Science & Engineering A Microstructural characterization and toughness evaluation of 10 wt % Ni steel weld metal gas tungsten arc and gas metal arc weld fusion zones', *Materials Science & Engineering A*. Elsevier B.V., 796(July), p. 140043. doi: 10.1016/j.msea.2020.140043.
22. Baumers, M. *et al.* (2016) 'The cost of additive manufacturing: Machine productivity, economies of scale and technology-push', *Technological Forecasting and Social Change*. doi: 10.1016/j.techfore.2015.02.015.

23. Bhadeshia, H.K.D.H. and Christian, J.W. (1990) Bainite in Steels. *Metallurgical Transactions*, 21A:767–797
24. Bhadeshia, H.K.D.H. (1992) *Bainite in Steels*. The Institute of Materials, London
25. Bhadeshia H.K.D.H. and Honeycombe R.W.K. (2006) *Steels: Microstructure and Properties*. Butterworth-Heinemann
26. Bhole, S. D. *et al.* (2006) 'Effect of nickel and molybdenum additions on weld metal toughness in a submerged arc welded HSLA line-pipe steel', *Journal of Materials Processing Technology*, 173(1), pp. 92–100. doi: 10.1016/j.jmatprotec.2005.10.028.
27. Bonis, M. (2009) Weight loss corrosion with H₂S: from facts to leading parameters and mechanisms, *Corrosion/2009*, paper no. 09564, NACE International, Houston, Texas
28. Bose-Filho, W. W., Carvalho, A. L. M. and Strangwood, M. (2007) 'Effects of alloying elements on the microstructure and inclusion formation in HSLA multipass welds', *Materials Characterization*, 58(1), pp. 29–39. doi: 10.1016/j.matchar.2006.03.004.
29. Bramfitt, B. L. and Speer, J. G. (1990) 'A perspective on the morphology of bainite', *Metallurgical Transactions A*, 21(3), pp. 817–829. doi: 10.1007/BF02656565.
30. Brandl, E., Baufeld, B., Leyens, C., and Gault, R. (2010), "Additive manufactured Ti-6Al-4V using welding wire: comparison of laser and arc beam deposition and evaluation with respect to aerospace material specifications", *Physics Procedia*, vol. 5, pp. 595-606

31. Burns M, and Wangenheim C. (2019) Metal 3D Printing Applications in the Oil & Gas Industry, in SPE Middle East Oil and Gas Show and Conference. 2019, Society of Petroleum Engineers: Manama, Bahrain. p. 9.
32. Cao, Y., Zhu, S., Liang, X., Wang, W. (2011) Overlapping model of beads and curve fitting of bead section for rapid manufacturing by robotic MAG welding process. *Rob. Comput. Integr. Manuf.* 27, 641–645.
33. Castro, R.J. and De Cadenet, J. J. (1968) *Welding Metallurgy of Stainless and Heat Resisting Steels*, Cambridge University Press
34. Charles, A. et al. (2019) 'Effect of process parameters on the generated surface roughness of down-facing surfaces in selective laser melting', *Applied Sciences (Switzerland)*, 9(6), pp. 1–13. doi: 10.3390/app9061256.
35. Chen, C. *et al.* (2014) 'Inclusions and microstructure of steel weld deposits with nanosize titanium oxide addition', *Journal of Nanomaterials*, 2014. doi: 10.1155/2014/138750.
36. Chen, D., Chen, M. and Wu, C. (2015) 'Effects of phase difference on the behavior of arc and weld pool in tandem P-GMAW', *Journal of Materials Processing Technology*. Elsevier B.V., 225, pp. 45–55. doi: 10.1016/j.jmatprotec.2015.05.022
37. Choi, D. H. et al. (2012) 'Microstructures and mechanical properties of friction stir welded 2.25Cr-1Mo steel', *Materials Transactions*, 53(5), pp. 1022–1025. doi: 10.2320/matertrans. MBW201103
38. Chovet, C. and Schmitt, J. P. (2011) 'Additional recommendations for welding Cr-Mo-V steels for petrochemical applications', *Welding in the World*, 55(11–12), pp. 31–38. doi: 10.1007/BF03321540

39. Cooper, A.G. (1999) Fabrication of Ceramic Components Using Mold Shape Deposition Manufacturing, Doctor of Philosophy (PhD) Thesis, Stanford University, USA.
40. Dahat, S. et al. (2020) 'A methodology to parameterize wire + arc additive manufacturing: A case study for wall quality analysis', *Journal of Manufacturing and Materials Processing*, 4(1). Doi: 10.3390/jmmp4010014
41. De Boer, F.G., Jacono, S.F., Silver, T.M., 2000. "Gas Metal Arc Welding for Rapid Prototyping and Wear Replacement", Proc. WTIA 48th Annual Conf., WTIA, ISBN 0909539 83 9, Melbourne, Australia, Oct. 29 - Nov. 2, 2000, paper 42.
42. DebRoy, T. *et al.* (2018) 'Additive manufacturing of metallic components – Process, structure and properties', *Progress in Materials Science*. doi: 10.1016/j.pmatsci.2017.10.001
43. Deng, D. and Kiyoshima, S. (2007) 'Numerical Investigation on Welding Residual Stress in 2.25 Cr-1Mo Steel Pipes', *TRANSACTIONS of JWRI*, 36(1), pp. 73–90. Available at: <http://www.jwri.osaka-u.ac.jp/publication/trans-jwri/pdf/361-11.pdf>.
44. Deng, D. et al. (2013) 'Prediction of the residual welding stress in 2.25Cr-1Mo steel by taking into account the effect of the solid-state phase transformations', *Acta Metallurgica Sinica (English Letters)*, 26(3), pp. 333–339. doi: 10.1007/s40195-012-0163-8.
45. Dickens, P. M., Pridham, M. S., Cobb, R. C., Gibson, I., & Dixon, G. (1992). Rapid prototyping using 3-D welding. *Solid Freeform Fabrication Proceedings*, 280–290.

46. Ding, D. *et al.* (2014) 'A tool-path generation strategy for wire and arc additive manufacturing', *International Journal of Advanced Manufacturing Technology*, 73(1–4), pp. 173–183. doi: 10.1007/s00170-014-5808-5.
47. Ding, D. *et al.* (2015a) 'Wire-feed additive manufacturing of metal components: technologies, developments and future interests', *International Journal of Advanced Manufacturing Technology*, 81(1–4), pp. 465–481. doi: 10.1007/s00170-015-7077-3.
48. Ding, D. *et al.* (2015b) 'A multi-bead overlapping model for robotic wire and arc additive manufacturing (WAAM)', *Robotics and Computer-Integrated Manufacturing*. Elsevier, 31, pp. 101–110. doi: 10.1016/j.rcim.2014.08.008
49. Ding, X. *et al.* (2013) 'Numerical simulation of metal transfer process in tandem GMAW', *International Journal of Advanced Manufacturing Technology*, 69(1–4), pp. 107–112. doi: 10.1007/s00170-013-4999-5.
50. DuPont, J. N., Siefert, J. A. and Shingledecker, J. P. (2017) 'Microstructural evolution and mechanical properties of Grades 23 and 24 creep strength enhanced ferritic steels', *International Materials Reviews*. Taylor & Francis, 62(1), pp. 32–56. doi: 10.1080/09506608.2016.1207008.
51. Brandl, E. *et al.* (2010) 'Additive manufactured Ti-6Al-4V using welding wire: Comparison of laser and arc beam deposition and evaluation with respect to aerospace material specifications', *Physics Procedia*, 5(PART 2), pp. 595–606. doi: 10.1016/j.phpro.2010.08.087.
52. Ebert, W. L., & Gattu, V. K. (2020). Metal Waste Forms. *Comprehensive Nuclear Materials*, 467–482. <https://doi.org/10.1016/B978-0-12-803581-8.11776-X>

53. Elrefaey, A. *et al.* (2018) 'Evolution of microstructure and toughness in 2.25Cr-1Mo steel welds', *International Journal of Pressure Vessels and Piping*. Elsevier, 165(April 2017), pp. 20–28. doi: 10.1016/j.ijpvp.2018.05.006.
54. Esmaeely, S. N. *et al.* (2017) 'Localized corrosion of mild steel in marginally sour environments', *Corrosion*, 73(9), pp. 1098–1106. doi: 10.5006/2422.
55. Esmaeely, S. N. and Nešić, S. (2019) 'Localized Corrosion of Mild Steel in H₂S Containing Aqueous Environments—Case Studies and Common Mechanisms', *Corrosion*, 75(8), pp. 938–945. doi: 10.5006/3164
56. Fang, C. *fu et al.* (2012) 'TANDEM and GMAW Twin Wire Welding of Q690 Steel Used in Hydraulic Support', *Journal of Iron and Steel Research International*, 19(5), pp. 79–85. doi: 10.1016/S1006-706X(12)60104-6.
57. Frade, M., Enguita, J. M. and Álvarez, I. (2013) 'In-situ waviness characterization of metal plates by a lateral shearing interferometric profilometer', *Sensors (Switzerland)*, 13(4), pp. 4906–4921. doi: 10.3390/s130404906.
58. Gao, S. *et al.* (2017) Corrosion Behavior of Mild Steel in Sour Environments at Elevated Temperatures 'Paper Number: NACE (9084), pp. 1–17, Available at: <https://onepetro.org/NACECORR/proceedings-abstract/CORR17/All-CORR17/NACE-2017-9084/125381>
59. Ge, J. *et al.* (2018) 'Location-related thermal history, microstructure, and mechanical properties of arc additively manufactured 2Cr13 steel using cold metal transfer welding', *Materials Science and Engineering A*. Elsevier B.V., 715(December 2017), pp. 144–153. doi: 10.1016/j.msea.2017.12.076.

60. Ghasri-Khouzani, M. et al. (2017) 'Experimental measurement of residual stress and distortion in additively manufactured stainless-steel components with various dimensions', *Materials Science and Engineering A*. doi: 10.1016/j.msea.2017.09.108.
61. Gibson Applied Technology and Engineering (2013) 'Corrosion Testing: Methods, Results & Interpretation Corrosion Testing: Methods, Results & Interpretation', pp. 1–2. (11), Available from: http://static1.squarespace.com/static/53556018e4b0fe1121e112e6/54b683d0e4b09b2abd348a7b/54b683e2e4b09b2abd348e27/1421247458676/GAT2004_GKP-2013.09-Corrosion-Testing-Methods-Results-and-Interpretation.pdf?format=original
62. Gockel, J. et al. (2019) 'The influence of additive manufacturing processing parameters on surface roughness and fatigue life', *International Journal of Fatigue*. Elsevier, 124(March), pp. 380–388. doi: 10.1016/j.ijfatigue.2019.03.025.
63. Goecke, S. et al. (2001) 'Tandem MIG/MAG welding', *Svetsaren, a Welding Review*, 56(2–3), p. 24.
64. Gouda, M., Takahashi, M. and Ikeuchi, K. (2005) 'Microstructures of gas metal arc weld metal of 950 MPa class steel', *Science and Technology of Welding and Joining*, 10(3), pp. 369–377. doi: 10.1179/174329305X40714.
65. Gray L.G.S, et al., (1990) Effect of pH and Temperature on the Mechanism of Carbon Steel Corrosion by Aqueous Carbon Dioxide. *Corrosion/90*, Pages: 1 – 26, Paper No. 40 (Houston, TX: NACE International).

66. Griffiths, C. A. et al. (2016) 'Effect of Build Parameters on Processing Efficiency and Material Performance in Fused Deposition Modelling', *Procedia CIRP*. The Author(s), 49, pp. 28–32. doi: 10.1016/j.procir.2015.07.024.
67. Groetelaars, P. J., de Morais, C. O. and Scotti, A. (2009) 'Influence of the arc length on metal transfer in the single potential double-wire MIG/MAG process', *Welding International*, 23(2), pp. 112–119. doi: 10.1080/095071110802349643
68. Grong, O. & Matlock, D. K. (1986) Microstructural development in mild and low-alloy steel weld metals, *International Metals Reviews*, 31:1, 27-48, DOI: [10.1179/imtr.1986.31.1.27](https://doi.org/10.1179/imtr.1986.31.1.27)
69. Grover, H. S., Chawla, V. and Brar, G. S. (2017) 'Comparing mechanical and corrosion behaviour of TIG & FSW weldments of AA5083-H321', *Indian Journal of Science and Technology*, 10(45), pp. 1–10. doi: 10.17485/ijst/2017/v10i45/113537.
70. Gu, J. et al. (2018) 'Design and cracking susceptibility of additively manufactured Al-Cu-Mg alloys with tandem wires and pulsed arc', *Journal of Materials Processing Technology*. Elsevier, 262(February), pp. 210–220. doi: 10.1016/j.jmatprotec.2018.06.030
71. Haden, C. V. et al. (2017) 'Wire and arc additive manufactured steel: Tensile and wear properties', *Additive Manufacturing*. doi: 10.1016/j.addma.2017.05.010.
72. Haerian, A. (2009) 'Effect of copper content on the microstructure and mechanical properties of multi-pass MMA, low alloy steel weld metal deposits', *Materials and Design*. doi: 10.1016/j.matdes.2008.09.023

73. Hans-Olof et al, Andrén, H. O., Cai, G. and Svensson, L. E. (1995) 'Microstructure of heat resistant chromium steel weld metals', *Applied Surface Science*, 87–88(C), pp. 200–206. doi: 10.1016/0169-4332(94)00491-9
74. Hascoet, J.Y., Karunakaran, K.P. and Marya, S. (2014) 'Additive Manufacturing Viewed from Material Science: State of the Art & Fundamentals', *Materials Science Forum*, 783-786, pp. 2347-2352. doi: 10.4028/www.scientific.net/MSF.783-786.2347
75. Hemmasian Etefagh, A. et al. (2019) 'Corrosion behavior of additively manufactured Ti-6Al-4V parts and the effect of post annealing', *Additive Manufacturing*. Elsevier, 28(October 2018), pp. 252–258. doi: 10.1016/j.addma.2019.05.011
76. Hensing, D.M., Ames, A.L. and Kuhlmann, J.L. (2000) "Motion planning for a direct metal deposition rapid prototyping system", *Proc. IEEE International Conference on Robotics and Automation, ICRA '00*, IEEE, ISSN 1050-4729, vol. 4, 2000, pp.3095-3100.
77. Herzog, D. et al. (2016) 'Additive manufacturing of metals', *Acta Materialia*. doi: 10.1016/j.actamat.2016.07.019.
78. Hirtler, M. et al. (2020) 'A Study On The Mechanical Properties Of Hybrid Parts Manufactured By Forging And Wire Arc Additive Manufacturing', *Procedia Manufacturing*. doi: 10.1016/j.promfg.2020.04.136.
79. Hollomon, J.H. and Jaffe, L.D. (1945) Time-temperature Relations in Tempering Steel. *Metallurgical Transactions*, 162:223–249.
80. Hong, T. et al. (2000) 'Modeling of inclusion growth and dissolution in the weld pool', *Metallurgical and Materials Transactions B: Process Metallurgy*

- and Materials Processing Science*, 31(1), pp. 161–169. doi: 10.1007/s11663-000-0141-9.
81. Hu, S. *et al.* (2018) 'The effect of welded joint properties on the surface characteristics of laser-welded 2205 duplex stainless steel', *Advances in Mechanical Engineering*, 10(9), pp. 1–11. doi: 10.1177/1687814018797449.
82. Huang, P. F., Yao, M., Bai, S. J., & Lu, Z. Y. (2012). Study on Arc Stability Mechanism in High-Speed Tandem GMA Welding. *Advanced Materials Research*, 562–564, 785–788. <https://doi.org/10.4028/www.scientific.net/amr.562-564.785>
83. Hunnik, E. V., Pots, B.F.M. and Hendriksen E. L.J.A. (1996) The Formation of Protective FeCO₃ Corrosion Product Layers in CO₂ Corrosion. *Corrosion/96, NACE Conference Papers (No.6)*.
84. Huang, G. *et al.* (2018) 'Effects of small ni addition on the microstructure and toughness of coarse-grained heat-affected zone of high-strength low-alloy steel', *Metals*, 8(9). doi: 10.3390/met8090718.
85. Iannuzzi, M., Barnoush, A. and Johnsen, R. (2017) 'Materials and corrosion trends in offshore and subsea oil and gas production', *npj Materials Degradation*. Springer US, 1(1). doi: 10.1038/s41529-017-0003-4.
86. ISO 15156-1(2020) Petroleum and natural gas industries — Materials for use in H₂S-containing environments in oil and gas production — Part 1: General principles for selection of cracking-resistant materials. Available at: <https://www.iso.org/obp/ui/#iso:std:iso:15156:-3:ed-4:v1:en>
87. Jacono, S. F. (1999) Quality of gas metal arc welds for rapid prototyping and wear replacement. University of Wollongong

88. Jaiswal, P., Patel, J. and Rai, R. (2018) 'Build orientation optimization for additive manufacturing of functionally graded material objects', *International Journal of Advanced Manufacturing Technology*. The International Journal of Advanced Manufacturing Technology, 96(1–4), pp. 223–235. doi: 10.1007/s00170-018-1586-9.
89. Jarvis, A. R. (1992) 'The Effect of Nickel Content on the Environmental Assisted Cracking (EAC) Behaviour of Low Alloy Steels in Sour Environments--A Review', 49, pp. 271–307.
90. Javadi, Y. et al. (2017) 'Measurement of residual stresses induced by sequential weld buttering and cladding operations involving a 2.25Cr-1Mo substrate material', *International Journal of Pressure Vessels and Piping*. doi: 10.1016/j.ijpvp.2017.06.003
91. Jianbo S. (2016) 'Effect of Chromium on Corrosion Behaviour of P110 Steels in CO₂-H₂S Environment with High Pressure and High Temperature'. doi: 10.3390/ma9030200
92. Jorge, J. C. F., Souza, L. F. G. and Rebello, J. M. A. (2001) 'The effect of chromium on the microstructure/toughness relationship of C-Mn weld metal deposits', *Materials Characterization*, 47(3–4), pp. 195–205. doi: 10.1016/S1044-5803(01)00168-1
93. Kalyankar, V. D. and Chudasama, G. (2018) 'Effect of post weld heat treatment on mechanical properties of pressure vessel steels', *Materials Today: Proceedings*. Elsevier Ltd, 5(11), pp. 24675–24684. doi: 10.1016/j.matpr.2018.10.265.
94. Kamble, A. G. and Rao, R. V. (2013) 'Experimental investigation on the effects of process parameters of GMAW and transient thermal analysis of

- AISI321 steel', *Advances in Manufacturing*, 1(4), pp. 362–377. doi: 10.1007/s40436-013-0041-2.
95. Kang, B. Y., Kim, H. J. and Hwang, S. K. (2000). Effect of Mn and Ni on the variation of the microstructure and mechanical properties of low-carbon weld metals. *ISIJ International*, 40(12), 1237–1245. <https://doi.org/10.2355/isijinternational.40.1237>
96. Karunakaran, K., et al. (2012). Rapid manufacturing of metallic objects. *Rapid Prototyping Journal*, 18(4), 264–280. <http://doi.org/10.1108/13552541211231644>
97. Kazanas, P. et al. (2012) 'Fabrication of geometrical features using wire and arc additive manufacture', *Proceedings of the Institution of Mechanical Engineers, Part B: Journal of Engineering Manufacture*, 226(6), pp. 1042–1051. doi: 10.1177/09544405412437126.
98. Kermani, M.B. and Morshed A. (2003) Carbon Dioxide Corrosion in Oil and Gas Production—A Compendium. *CORROSION* 59 (8): 659–683. <https://doi.org/10.5006/1.3277596>
99. Kermani, B., Martin, J. and Esaklul, K. (2006) 'Materials design strategy: Effects of H₂S/CO₂ corrosion on materials selection', *NACE - International Corrosion Conference Series*, (06121), pp. 061211–0612115
100. Klingbeil, N. W. et al. (2002), Residual stress-induced warping in direct metal solid freeform fabrication, *International Journal of Mechanical Sciences*, 44(1), p. 57-77.
101. Koseki, T. (2005) 'A review on inclusion-assisted microstructure control in C-Mn and low-alloy steel welds', *Welding in the World*, 49(5–6), pp. 22–28. doi: 10.1007/BF03263406.

102. Kovacevic, R. (1999) 'Rapid Prototyping Technique Based on 3D Welding', Proc. 1999 NSF Design & Manufacturing Grantees Conference, Long Beach, California, USA, January 5-8, 1999. Accessed online: http://www.seas.smu.edu/me/kovacevic/papers/nsf_99_grantees_2.html
103. Kovacs, W. *et al.* (2017) 'Additive manufacturing for sour service, an experimental investigation', *NACE - International Corrosion Conference Series*, 2(9667), pp. 1287–1301.
104. Krauss, G. (1980) *Principles of Heat Treatment of Steel*. American Society for Metals
105. Kulkarni, P. and Dutta, D. (1999) "Deposition Strategies and Resulting Part Stiffnesses in Fused Deposition Modelling", *Journal of Manufacturing Science and Engineering, Transactions of the ASME*, ISSN 1087-1357, 121(1), Feb. 1999, pp.93-103.
106. Lalehpour, A. and Barari, A. (2018) 'A more accurate analytical formulation of surface roughness in layer-based additive manufacturing to enhance the product's precision', *International Journal of Advanced Manufacturing Technology*. *The International Journal of Advanced Manufacturing Technology*, 96(9–12), pp. 3793–3804. doi: 10.1007/s00170-017-1448-x.
107. lé, R. M., Rebello, J. M. A. and Charlier, J. (1996) 'A metallographic technique for detecting martensite-austenite constituents in the weld heat-affected zone of a micro-alloyed steel', *Materials Characterization*, 37(2–3), pp. 89–93. doi: 10.1016/S1044-5803(96)00069-1.
108. LePera, F. S. (1979) 'Improved etching technique for the determination of percent martensite in high-strength dual-phase steels', *Metallography*, 12(3), pp. 263–268. doi: 10.1016/0026-0800(79)90041-7.

109. Lesnewich, A. (1958), Control of melting rate and metal transfer in gas-shielded metal-arc welding – Part 1 – Control of electrode melting rate, *Welding Journal*, 37(8), p. 343s353s.
110. Li, K. H. and Zhang, Y.M. (2008) Consumable double-electrode GMAW-part 1: the process. *Welding Journal* 87: 11s-17s.
111. Li, Y. *et al.* (2018) 'GMAW-based additive manufacturing of inclined multi-layer multi-bead parts with flat-position deposition', *Journal of Materials Processing Technology*. Elsevier, 262(92), pp. 359–371. doi: 10.1016/j.jmatprotec.2018.07.010.
112. Lima, W. F. *et al.* (2017) 'Microstructure evolution and creep properties of 2.25Cr-1Mo ferrite-pearlite and ferrite-bainite steels after exposure to elevated temperatures', *Materials Research*, 20(2), pp. 418–422. doi: 10.1590/1980-5373-MR-2016-0596.
113. Lincoln electric (2020) Multi-wire SAW deposition system: accessed on 07/08/2020, available @ <https://www.lincolnelectric.com/en-gb/company/newsroom/Pages/pipe-mill-welding-seminar-oct-2014.aspx>
114. Liu, X. *et al.* (2020) 'Effect of forged substrate geometry on temperature and stress field in additive manufacturing', *Journal of Manufacturing Processes*. doi: 10.1016/j.jmapro.2020.01.054.
115. Lockett, H. *et al.* (2017) 'Design for wire + Arc additive manufacture: Design rules and build orientation selection', *Journal of Engineering Design*, 28(7–9), pp. 568–598. doi: 10.1080/09544828.2017.1365826.
116. Łomozik, Mirosław and Edmund, Tasak (2006). Physical simulation and numerical modelling of X10CrMoVNb 9.10 (P91) steel repair welding.

Conference: Materials for advanced power engineering: Proceedings of the 8th Liege Conference. At: Liege, Belgium. Vol (1417-1426)

117. Lundin, C. D., Kruse, B.J. and Pendley, M.R. (1982), Welding Research Council Bulletin 277. United Engineering Centre, New York
118. Mahesh, M. et al. (2004) Benchmarking for comparative evaluation of RP systems and processes. *Rapid Prototype. J.* 10 (2), 123–135.
119. Martina, F. *et al.* (2012) 'Investigation of the benefits of plasma deposition for the additive layer manufacture of Ti-6Al-4V', *Journal of Materials Processing Technology*. Elsevier B.V., 212(6), pp. 1377–1386. doi: 10.1016/j.jmatprotec.2012.02.002.
120. Martina, F. *et al.* (2019) 'Tandem metal inert gas process for high productivity wire arc additive manufacturing in stainless steel', *Additive Manufacturing*. Elsevier, 25(July 2018), pp. 545–550. doi: 10.1016/j.addma.2018.11.022.
121. Mistry, J. P. (2016) 'Effect of Process Parameters on Bead Geometry and Shape Relationship of Gas Metal Arc Weldments', *International Journal of Advanced Research in Mechanical Engineering & Technology (IJARMET) Vol.*, 2(2), pp. 24–27.
122. Montgomery, D.C. (2017) Design and Analysis of Experiments. 9th Edition. Wiley. ISBN: 978-1-119-32093-7
123. Motta, M. F. et al. (2007) 'A study on out-of-phase current pulses of the double wire MIG/MAG process with insulated potentials on coating applications - Part I', *Journal of the Brazilian Society of Mechanical Sciences and Engineering*, 29(2), pp. 202–206. doi: 10.1590/S1678-58782007000200010.

124. Motta, M. F. et al. (2020) 'Creating in-situ alloys by welding - new perspectives for advanced materials and applications', *Journal of Materials Research and Technology*. Korea Institute of Oriental Medicine, 9(3), pp. 6950–6956. doi: 10.1016/j.jmrt.2020.03.109.
125. Mughal, M. P. et al. (2005), Deformation modelling in layered manufacturing of metallic parts using gas metal arc welding: Effect of process parameters, *Modelling and Simulation in Materials Science and Engineering*, 13(7), p. 1187-1204.
126. Na, H., Lee, S. and Kang, C. (2018) 'Effect of micro-segregation on impact toughness of 2.25Cr-1Mo steel after post weld heat treatment', *Metals*, 8(6), pp. 1–12. doi: 10.3390/met8060373.
127. NACE TM0169/G31-12a: Standard guide on Laboratory Immersion Corrosion
128. Nescic S. and Lee K.L.J, (2002) A Mechanistic Model of Iron Carbonate Film Growth and the Effect on CO₂ Corrosion of Mild Steel. Corrosion/02, Paper No. 237
129. Ning, A. et al., 2019. Influence of Tempering Time on the Behavior of Large Carbides' Coarsening in AISI H13 Steel. *Metals*, 9(12), p.1283. Available at: <http://dx.doi.org/10.3390/met9121283>
130. Olsen, D.L. and North, T.H. (1992) (eds), *Ferrous Alloy Weldments*, Trans Tech Publications
131. Om, H. and Pandey, S. (2013) 'Effect of heat input on dilution and heat affected zone in submerged arc welding process', *Sadhana - Academy Proceedings in Engineering Sciences*, 38(6), pp. 1369–1391. doi: 10.1007/s12046-013-0182-9.

132. OneSubsea (2020) Horizontal-subsea-tree-system, Available from: <https://www.onesubsea.slb.com/subsea-production-systems/subsea-tree-systems/horizontal-subsea-tree-system>, Accessed: 02/06/20
133. Ortolani, M. and Novelli, P. (2013) Sour resistant high strength seamless pipes for risers, Proceedings of the ASME 2013 32nd International Conference on Ocean, Offshore and Arctic Engineering. 'OMAE2013-10252', pp. 1–5.
134. Palani, P. K. and Murugan, N. (2006), Selection of parameters of pulsed current gas metal arc welding, *Journal of Materials Processing Technology*, 172(1), p. 1-10
135. Pamnani, R. *et al.* (2016) 'Investigations on the impact toughness of HSLA steel arc welded joints', *Journal of Manufacturing Processes*. The Society of Manufacturing Engineers, 21, pp. 75–86. doi: 10.1016/j.jmapro.2015.11.007.
136. Pandey, C. *et al.* (2019) 'Softening mechanism of P91 steel weldments using heat treatments', *Archives of Civil and Mechanical Engineering*. Politechnika Wroc&Istrok;awska, 19(2), pp. 297–310. doi: 10.1016/j.acme.2018.10.005.
137. Pandey, P. M., Reddy, N. V. and Dhande, S. G. (2003) 'Improvement of surface finish by staircase machining in fused deposition modeling', *Journal of Materials Processing Technology*, 132(1–3), pp. 323–331. doi: 10.1016/S0924-0136(02)00953-6.
138. Peddle, B. E., & Pickles, C. A. (2001). Carbide development in the heat affected zone of tempered and post-weld heat treated 2.25Cr-1Mo

- steel weldments. *Canadian Metallurgical Quarterly*, 40(1), 105–126.
<https://doi.org/10.1179/cmq.2001.40.1.105>
139. Peddle, B.E., Pickles, C.A., *Journal of Material Engineering and Performance*. Vol 9, Iss5.
140. Poprawe, R. *et al.* (2015) 'SLM Production Systems: Recent Developments in Process Development, Machine Concepts and Component Design', (November), pp. 49–65. doi: 10.1007/978-3-319-12304-2_5.
141. Praveen, P., Yarlagadda, P. K. D. V. and Kang, M. J. (2005), Advancements in pulse gas metal arc welding, *Journal of Materials Processing Technology*, 164-165, p. 1113-1119.
142. Queguineur, A. *et al.* (2018) '*Evaluation of wire arc additive manufacturing for large-sized components in naval applications*', *Welding in the World*. *Welding in the World*, 62(2), pp. 259–266. doi: 10.1007/s40194-017-0536-8.
143. Queguineur, A. *et al.* (2020) '*Evaluation of tandem controlled short-circuit GMAW for improved deposition in additive manufacture of large Nickel Aluminium Bronze naval components*', *Welding in the World*. *Welding in the World*, 64(8), pp. 1389–1395. doi: 10.1007/s40194-020-00925-z.
144. Ramaswami, K. (1997) *Process Planning for Shape Deposition Manufacturing*, PhD. Department of Mechanical Engineering, Stanford University, USA. Accessed online: http://www-rpl.stanford.edu/files/thesis/thesis_kramaswami.pdf.
145. Ribeiro, F. (1998b). 3D printing with metals. *Computing & Control Engineering Journal*, 9(1), 31. <http://doi.org/10.1049/cce:19980108>

146. Ribeiro, R. A. et al. (2015) 'Predicting weld bead geometry in the novel CW-GMAW process', *Welding Journal*, 94(9), pp. 301s-311s.
147. Rodriguez, N. et al. (2018) 'Wire and arc additive manufacturing: a comparison between CMT and TopTIG processes applied to stainless steel', *Welding in the World*. *Welding in the World*, 62(5), pp. 1083–1096. doi: 10.1007/s40194-018-0606-6.
148. Rodrigues, T. A. et al. (2019) 'Wire and arc additive manufacturing of HSLA steel: Effect of thermal cycles on microstructure and mechanical properties', *Additive Manufacturing*. Elsevier, 27(March), pp. 440–450. doi: 10.1016/j.addma.2019.03.029.
149. Sames, W. J. et al. (2016) 'The metallurgy and processing science of metal additive manufacturing', *International Materials Reviews*. Taylor & Francis, 61(5), pp. 315–360. doi: 10.1080/09506608.2015.1116649
150. Sanaei, N. and Fatemi, A. (2020) 'Analysis of the effect of surface roughness on fatigue performance of powder bed fusion additive manufactured metals', *Theoretical and Applied Fracture Mechanics*. Elsevier, 108(November 2019), p. 102638. doi: 10.1016/j.tafmec.2020.102638.
151. Sander, G. et al. (2018) 'Corrosion of additively manufactured alloys: A review', *Corrosion*, 74(12), pp. 1318–1350. doi: 10.5006/2926
152. Sangid, M. D. et al. (2018) 'Role of heat treatment and build orientation in the microstructure sensitive deformation characteristics of IN718 produced via SLM additive manufacturing', *Additive Manufacturing*. Elsevier B.V., 22, pp. 479–496. doi: 10.1016/j.addma.2018.04.032.

153. Sarma, R., 2000. "An Assessment of Geometric Methods in Trajectory Synthesis for Shape-Creating Manufacturing Operations", *Journal of Manufacturing Systems*, SME, Dearborn, ISSN: 0278- 6125, 19(1), 2000, pp.59-72.
154. Schlumberger (2020) Spear-shale-optimized-steel-body-pdc-drill-bit, Available from: <https://www.slb.com/drilling/bottomhole-assemblies/drill-bits/pdc-bits/spear-shale-optimized-steel-body-pdc-drill-bit>, Accessed: 02/06/20
155. Schnitzer, R. *et al.* (2017) 'Influence of alloying elements on the mechanical properties of high-strength weld metal', *Science and Technology of Welding and Joining*, 22(6), pp. 536–543. doi: 10.1080/13621718.2016.1274095
156. S  ferian, D. and Bishop, E.E. (1962) (translation), *The Metallurgy of Welding*. Chapman and Hall, London
157. Seow, C. E. *et al.* (2019) 'Wire + Arc Additively Manufactured Inconel 718: Effect of post-deposition heat treatments on microstructure and tensile properties', *Materials and Design*. Elsevier Ltd, 183, p. 108157. doi: 10.1016/j.matdes.2019.108157
158. Setiyanto, N. A., Oktadinata, H. and Winarto, W. (2019) 'Effect of Nickel on the Microstructure, Hardness and Impact Toughness of SM570-TMC Weld Metals', *MATEC Web of Conferences*, 269, p. 02007. doi: 10.1051/mateccconf/201926902007.
159. Shi, J. *et al.* (2019) 'T-GMAW based novel Multi-node trajectory planning for fabricating grid stiffened panels: An efficient production technology', *Journal of Cleaner Production*. Elsevier Ltd, 238, p. 117919. doi: 10.1016/j.jclepro.2019.117919.

160. Shi, Y. and Han, Z. (2008) 'Effect of weld thermal cycle on microstructure and fracture toughness of simulated heat-affected zone for a 800 MPa grade high strength low alloy steel', *Journal of Materials Processing Technology*, 207(1–3), pp. 30–39. doi: 10.1016/j.jmatprotec.2007.12.049.
161. Shoeb, M. (2013) 'Effect of Mig Welding Input Process Parameters on Weld Bead Geometry on Hsla Steel', *International Journal of Engineering Science and Technology*, 5(1), pp. 200–212.
162. Shrestha, R., Simsiriwong, J. and Shamsaei, N. (2019) 'Fatigue behaviour of additive manufactured 316L stainless steel parts: Effects of layer orientation and surface roughness', *Additive Manufacturing*. Elsevier, 28(April), pp. 23–38. doi: 10.1016/j.addma.2019.04.011.
163. Sidney H. Avner (1974) *Introduction to physical metallurgy*, second edition; McGraw Hills Inc.
164. Siminski, M.R., De Boer, F.G. (2002b) "Weld Path Generation for Rapid Prototyping and Wear Replacement by Robotic Gas Metal Arc Welding", Proc. WTIA 50th Annual Conf., Sydney, Australia, Aug. 26-30, 2002, Welding Technology Institute of Australia, ISBN: 0 909539 98 7, paper 89.
165. Siminski, M. (2003) *Weld path optimisation for rapid prototyping and wear replacement by robotic gas metal arc welding*, PhD thesis, Faculty of Engineering, University of Wollongong. <http://ro.uow.edu.au/theses/399>
166. Simoni, F., Huxol, A. and Villmer, F. J. (2019) 'Approach Towards Surface Improvement in Additively Manufactured Tools', *IFAC-Papers*

- Online.* Elsevier Ltd, 52(10), pp. 254–259. doi: 10.1016/j.ifacol.2019.10.032.
167. Sindo Kou (2003) *Welding Metallurgy*, Second Edition, John Wiley & Sons, Inc. Hoboken, New Jersey
168. Singh, P. and Dutta, D. (2003) Multi-Direction Layered Deposition– An Overview of Process Planning Methodologies. In *Proceedings of the Solid Freeform Fabrication Symposium*: 279–288
169. Sireesha M, et. al., (2018) A review on additive manufacturing and its way into the oil and gas industry. *RSC*; 8(40):22460–8.
170. Smati, Z. (1986), Automatic pulsed MIG welding, *Metal Construction*, 18(1), p. 38R-44R.
171. Smith, S. N. and Ling, S. (2014) ‘A Parametric Study of Sour Corrosion of Carbon Steel’. Paper No.10278. *NACE Corrosion/2010*
172. Somashekara, M. A. and Suryakumar, S. (2017) ‘Studies on Dissimilar Twin-Wire Weld-Deposition for Additive Manufacturing Applications’, *Transactions of the Indian Institute of Metals*. Springer India, 70(8), pp. 2123–2135. doi: 10.1007/s12666-016-1032-3.
173. Song, H. Y., Evans, G. M. and Babu, S. S. (2014) ‘Effect of microstructural heterogeneities on scatter of toughness in multi-pass weld metal of C-Mn steels’, *Science and Technology of Welding and Joining*, 19(5), pp. 376–384. doi: 10.1179/1362171814Y.0000000194.
174. Speich, G.R. (1969) Tempering of Low-Carbon Martensite. *Metallurgical Transactions*, 245:2553–2564

175. Speich G.R. and Leslie W.C. (1972) Tempering of Steel. Metallurgical Transactions, 3(5):1043–1054
176. Spencer, J.D. and Dickens, P.M. (1995) "Production of Metal Parts Featuring Heavy Sections Using 3D Welding", Proc. First National Conf. on Rapid Prototyping and Tooling Research, Bennett, G. (ed.), ISBN 0852989822, Mechanical Engineering Publications, London, Buckinghamshire College, 6-7 November 1995, pp.127-137.
177. Spencer, J.D., Dickens, P.M. and Wykes, C.M. (1998) "Rapid Prototyping of Metal Parts by Three-Dimensional Welding", Proc. IMechE, Part B: Journal of Engineering Manufacture, ISSN 0954-4054, 212(B3), 1998, pp.175-182.
178. Sproesser, G., Pittner, A. and Rethmeier, M. (2016) 'Increasing Performance and Energy Efficiency of Gas Metal Arc Welding by a High Power Tandem Process', *Procedia CIRP*. Elsevier B.V., 40, pp. 642–647. doi: 10.1016/j.procir.2016.01.148.
179. Sridhar, N. et al. (2018) 'Corrosion-resistant alloy testing and selection for oil and gas production', Corrosion Engineering Science and Technology. Taylor & Francis, 53, pp. 75–89. doi: 10.1080/1478422X.2017.1384609
180. Strano, G. *et al.* (2013) 'Surface roughness analysis, modelling and prediction in selective laser melting', *Journal of Materials Processing Technology*. Elsevier B.V., 213(4), pp. 589–597. doi: 10.1016/j.jmatprotec.2012.11.011.
181. Subramaniam, S., White, D. R., Jones, J. E. and Lyons, D. W. (1999), Experimental approach to selection of pulsing parameters in pulsed GMAW, *Welding Journal* (Miami, Fla), 78(5), p. 166s-172s.

182. Sun, C. *et al.* (2018) 'Effect of tempering temperature on the low temperature impact toughness of 42CrMo4-V steel', *Metals*, 8(4). doi: 10.3390/met8040232
183. Sun, C. *et al.* (2021) 'Additive manufacturing for energy: A review', *Applied Energy*, 282(May 2020). doi: 10.1016/j.apenergy.2020.116041.
184. Sun, L. *et al.* (2020) 'Investigation on the process window with liner energy density for single-layer parts fabricated by wire and arc additive manufacturing', *Journal of Manufacturing Processes*. Elsevier, 56(June), pp. 898–907. doi: 10.1016/j.jmapro.2020.05.054.
185. Sun, W. and Nesic, S. (2007) 'A mechanistic model of H₂S corrosion of mild steel', *NACE - International Corrosion Conference Series*, (07655), pp. 076551–0765526.
186. Sun, W. and Nešić, S. (2009) 'A mechanistic model of uniform hydrogen sulfide/ carbon dioxide corrosion of mild steel', *Corrosion*, 65(5), pp. 291–307. doi: 10.5006/1.3319134.
187. Sun, Y. *et al.* (2012) 'Effects of nickel on low-temperature impact toughness and corrosion resistance of high-ductility ductile iron', *Materials and Design*. Elsevier Ltd, 41(June 2020), pp. 31–36. doi: 10.1016/j.matdes.2012.03.039.
188. Sun, Y., Hebert, R. J. and Aindow, M. (2018) 'Effect of heat treatments on microstructural evolution of additively manufactured and wrought 17-4PH stainless steel', *Materials and Design*. Elsevier Ltd, 156, pp. 429–440. doi: 10.1016/j.matdes.2018.07.015

189. Suryakumar, S., Karunakaran, K.P., Bernard, A., Chandrasekhar, U., Raghavender, N., Sharma, D., (2011) Weld bead modeling and process optimization in hybrid layered manufacturing. *Comput. Aided Des.* 43, 331–344.
190. Suryakumar, S and Somashekara, M A (2013) *Manufacture of Functionally Gradient Materials Using Weld-Deposition*. In: 24th International Solid Freeform Fabrication Symposium - An Additive Manufacturing Conference, SFF 2013, 12-13, August 2013, Austin, TX; United States
191. Takauchi, H., Nakanishi, T. and Nako, H. (2017) 'Welding consumables for 2.25CR-1MO-V refining reactors', *American Society of Mechanical Engineers, Pressure Vessels and Piping Division (Publication) PVP*, 7, pp. 1–10. doi: 10.1115/PVP201765640.
192. Tang, J. et al. (2010) 'The effect of H₂S concentration on the corrosion behavior of carbon steel at 90 °C', *Corrosion Science*. Elsevier Ltd, 52(6), pp. 2050–2058. doi: 10.1016/j.corsci.2010.02.004.
193. Tao, P. et al. (2010) 'Evolution and coarsening of carbides in 2.25Cr-1Mo steel weld metal during high temperature tempering', *Journal of Iron and Steel Research International*. Central Iron and Steel Research Institute, 17(5), pp. 74–78. doi: 10.1016/s1006-706x(10)60103-3
194. Thompson, M. K. et al. (2016) 'Design for Additive Manufacturing: Trends, opportunities, considerations, and constraints', *CIRP Annals - Manufacturing Technology*. doi: 10.1016/j.cirp.2016.05.004.
195. Tian, Y. et al. (2017) 'Influences of processing parameters on surface roughness of Hastelloy X produced by selective laser melting',

- Additive Manufacturing*. Elsevier B.V., 13, pp. 103–112. doi: 10.1016/j.addma.2016.10.010.
196. Tweed, J. H. and Knott J. F. (1983) Effect of reheating on microstructure and toughness of C-Mn weld metal. *Met. Sci*; 17(2):45–54
197. Ueyama, T., Ohnawa T., Yamazaki K., et al. (2005a) 'High-speed welding of steel sheets by the tandem pulsed gas metal arc welding system'. *Transactions of JWRI* 34: 11-18.
198. Ueyama, T., Ohnawa T., Tanaka M., et al. (2005b) 'Occurrence of arc interference and interruption in tandem pulsed GMA welding-study of arc stability in tandem pulsed GMA welding'. *Science and Technology of Welding and Joining* 12: 523-29.
199. Ueyama, T., Ohnawa T., Tanaka M., et al. (2005c) 'Effects of torch configuration and welding current on weld bead formation in high speed tandem pulsed gas metal arc welding of steel sheets'. *Science and Technology of Welding and Joining* 10: 750-59.
200. Vedralnam, A., Singh, G. and Kumar, A. (2018) 'Optimizing submerged arc welding using response surface methodology, regression analysis, and genetic algorithm', *Defence Technology*. Elsevier Ltd, 14(3), pp. 204–212. doi: 10.1016/j.dt.2018.01.008.
201. Vendra, L. and Achanta, A. (2020) 'Metal additive manufacturing in the oil and gas industry', *Solid Freeform Fabrication 2018: Proceedings of the 29th Annual International Solid Freeform Fabrication Symposium - An Additive Manufacturing Conference, SFF 2018*, pp. 454–460.
202. Venkateswarlu, K. et al. (2014) 'Estimation of Crystallite Size, Lattice Strain and Dislocation Density of Nanocrystalline Carbonate

- Substituted Hydroxyapatite by X-ray Peak Variance Analysis', *Procedia Materials Science*, 5, pp. 212–221. doi: 10.1016/j.mspro.2014.07.260
203. Wang H.B, et al., (2001) Characterization of Inhibitor and Corrosion Product Film using Electrochemical Impedance Spectroscopy (EIS). Corrosion (Paper No.01023)
204. Wang, W., Zhao, W. and Qu, J. (2013) 'Effect of heat treatment on microstructure and mechanical properties of 2.25Cr-1Mo steel', *Steel Research International*, 84(2), pp. 178–183. doi: 10.1002/srin.201200130
205. Wang, X. L. *et al.* (2017) 'Influence of welding pass on microstructure and toughness in the reheated zone of multi-pass weld metal of 550 MPa offshore engineering steel', *Materials Science and Engineering A*. Elsevier B.V., 702(April), pp. 196–205. doi: 10.1016/j.msea.2017.06.081
206. Wang, Z. Q. *et al.* (2018) 'Effect of Ni content on the microstructure and mechanical properties of weld metal with both-side submerged arc welding technique', *Materials Characterization*. Elsevier, 138(January), pp. 67–77. doi: 10.1016/j.matchar.2018.01.039.
207. Wen, C. et al. (2016) 'The Influence of Nickel on Corrosion Behavior of Low Alloy Steel in a Cyclic Wet-dry Condition', 11, pp. 4161–4173. doi: 10.20964/110148
208. William D. Callister and David G. Rethwisch (2011) *Materials Science and Engineering – An Introduction*, 8th Edition. John Wiley & Sons, Inc.

209. Williams, S. W. *et al.* (2016) 'Wire + Arc additive manufacturing', *Materials Science and Technology (United Kingdom)*, 32(7), pp. 641–647. doi: 10.1179/1743284715Y.0000000073.
210. Wu, K. *et al.* (2019) 'Metal transfer process and properties of double-wire double pulsed gas metal arc welding', *Journal of Manufacturing Processes*. Elsevier, 44(September 2018), pp. 367–375. doi: 10.1016/j.jmapro.2019.06.019.
211. Wu, K. *et al.* (2020) 'Investigation of double arc interaction mechanism and quantitative analysis of double arc offset in high-power double-wire DP-GMAW', *Journal of Manufacturing Processes*. Elsevier, 49(July 2019), pp. 423–437. doi: 10.1016/j.jmapro.2019.10.022.
212. Xiong, J. *et al.* (2018) 'Influences of process parameters on surface roughness of multi-layer single-pass thin-walled parts in GMAW-based additive manufacturing', *Journal of Materials Processing Technology*. Elsevier, 252(February 2017), pp. 128–136. doi: 10.1016/j.jmatprotec.2017.09.020.
213. Yacob, S. *et al.* (2015) 'The effect of welding parameters on surface quality of AA6351 aluminium alloy', *IOP Conference Series: Materials Science and Engineering*, 100(1), pp. 6–11. doi: 10.1088/1757-899X/100/1/012038.
214. Yadav, H. K. *et al.* (2017) 'Structural and Mechanical Characterization of Service Exposed 2.25Cr–1Mo Steel', *Transactions of the Indian Institute of Metals*. Springer India, 70(4), pp. 1091–1096. doi: 10.1007/s12666-016-0909-5.
215. Yan, F., Xiong, W. and Faierson, E. J. (2017) 'Grain structure control of additively manufactured metallic materials', *Materials*, 10(11), p. 1260. doi: 10.3390/ma10111260.

216. Yang, L. *et al.* (2015) 'Effect of Mn and Ni on microstructure and impact toughness of submerged arc weld metals', *Transactions of Tianjin University*, 21(6), pp. 562–566. doi: 10.1007/s12209-015-2480-2.
217. Yao, P. *et al.* (2020) 'Influence of inclination of welding torch on weld bead during pulsed-GMAW Process', *Materials*, 13(11). doi: 10.3390/ma13112652., and statistics such as design of experiments (DoE), evolutionary algorithms and computational network for modelling, control and optimisation of different welding processes.
218. You, D. *et al.* (2017) *Modeling inclusion formation during solidification of steel: A review*, *Metals*. doi: 10.3390/met7110460.
219. Yuehai Feng, Bin Zhan, Jie He, Kehong Wang, (2018) The double-wire feed and plasma arc additive manufacturing process for deposition in Cr-Ni stainless steel, *Journal of Materials Processing Tech.*, 259, pp. 206-215, <https://doi.org/10.1016/j.jmatprotec.2018.04.040>.
220. Zadi-Maad, A., Rohib, R. and Irawan, A. (2018) 'Additive manufacturing for steels: A review', *IOP Conference Series: Materials Science and Engineering*, 285(1). doi: 10.1088/1757-899X/285/1/012028.
221. Zhang, B. *et al.* (2018) 'Additive Manufacturing of Functionally Graded Material Objects: A Review', *Journal of Computing and Information Science in Engineering*, 18(4). doi: 10.1115/1.4039683.
222. Zhang, K. *et al.* (2016) 'Omae2016-54620 a Calculation Method of Ultimate Torsional Strength for Subsea', pp. 1–10.
223. Zhang, L. *et al.* (2015) 'Effect of cooling rate on microstructure and properties of microalloyed HSLA steel weld metals', *Science and*

- Technology of Welding and Joining*, 20(5), pp. 371–377. doi: 10.1179/1362171815Y.0000000026.
224. Zhang, T. *et al.* (2015) 'Effect of inclusions on microstructure and toughness of deposited metals of self-shielded flux cored wires', *Materials Science and Engineering A*. Elsevier, 628, pp. 332–339. doi: 10.1016/j.msea.2015.01.070.
225. Zhang, Y. M. *et al.* (2002) Automated system for welding-based rapid prototyping. *Mechatronics*, 12(1), 37–53. [http://doi.org/10.1016/S0957-4158\(00\)00064-7](http://doi.org/10.1016/S0957-4158(00)00064-7)
226. Zhang, Y., *et al.* (2003) Weld deposition-based rapid prototyping: a preliminary study. *J. Mater. Process. Technol.* 135, 347–357
227. Zhenyang Lu and Pengfei Huang (2011). *The Mechanism of Undercut Formation and High-Speed Welding Technology*, Arc Welding, Prof. Wladislav Sudnik (Ed.), ISBN: 978-953-307-642-3, InTech, Available from: <http://www.intechopen.com/books/arc-welding/the-mechanism-of-undercut-formation-and-high-speed-welding-technology>
228. Zhou, K. and Yao, P. (2019) '*Review of the Recent Trends of Process Monitoring and Control for Double-Wire GMAW Process*', *IEEE Access*. *IEEE*, 7, pp. 124621–124631. doi: 10.1109/ACCESS.2019.2938343.

APPENDICES

Appendix A:

A summary description of different tool path filling-in patterns and their pros and cons.

Tool-path strategy	Advantages	Disadvantages
Raster	+a	-b, -c, -d
Zigzag	+a	-b, -c, -d
Contour	+b	-a, -c
Spiral	+c	-a
Fractal space curves	+c	-a, -d
Continuous	+c	-a, -d
Hybrid	+a, +b	-c, -d
Major performance indicators of tool-path generation methods		
a. Ease of Implementation and simple algorithms		
b. Good geometrical accuracy		
c. Less tool-path passes		
d. Less tool-path elements		

Ding, D. *et al.* (2014)

Appendix B:

Experimental design matrix for the tandem-wire GMAW process, used for the high deposition rate parameter study, as well as the measured instantaneous arc characteristics and single bead responses

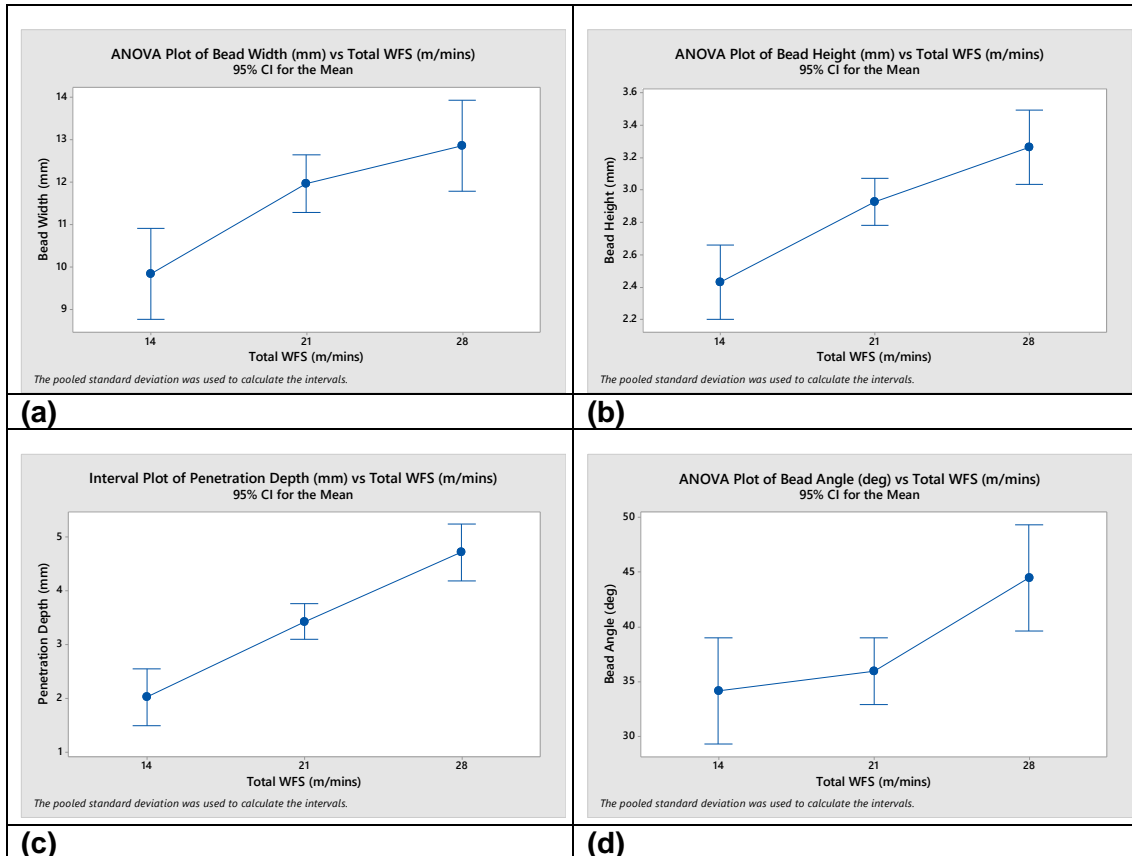
Run Order	TS (mm/s)	Temp (°C)	WFS (m/mins)	CTW D (mm)	BW (mm)	BH (mm)	BP (mm)	BA (°)	I (A) Amps	V (A) Volts	H.I (A)	I (B)	V (B) Volts	H.I (B)	H.I (A+B) KJ/m
1	13	20	21	22.5	14.2	3.6	5.0	37	267	31.1	0.64	271	31.4	0.65	1.29
2	27	20	21	22.5	10.2	2.4	2.3	33	262	27.6	0.27	251	27.2	0.25	0.52
3	13	250	21	22.5	9.5	2.1	2.0	30	254	27.9	0.55	250	27.4	0.53	1.07
4	27	250	21	22.5	10.7	3.3	2.9	33	268	31.7	0.31	265	29.8	0.29	0.61
5	20	135	14	21	9.5	2.2	1.8	28	180	24.8	0.22	171	22.7	0.19	0.42
6	20	135	28	21	12.2	3.5	5.5	40	334	31.2	0.52	323	30.9	0.50	1.02
7	20	135	14	24	8.9	2.3	1.4	33	172	19.6	0.17	172	19.1	0.16	0.33
8	20	135	28	24	12.9	3.1	4.6	33	315	30.4	0.48	303	30.0	0.45	0.93
9	13	135	21	21	15.1	3.3	5.4	34	282	31.6	0.69	283	32.7	0.71	1.40
10	27	135	21	21	10.5	2.5	2.5	22	263	28.0	0.27	259	28.2	0.27	0.54
11	13	135	21	24	15.4	3.5	4.4	33	258	30.0	0.60	254	30.7	0.60	1.20
12	27	135	21	24	8.9	3.3	2.2	48	230	32.9	0.28	226	35.3	0.30	0.58
13	20	20	14	22.5	8.9	2.3	1.5	36	172	23.9	0.21	167	22.8	0.19	0.40
14	20	250	14	22.5	14.7	3.1	3.9	28	169	23.5	0.20	167	22.7	0.19	0.39
15	20	20	28	22.5	12.8	3.4	4.4	49	326	30.8	0.50	317	30.1	0.48	0.98
16	20	250	28	22.5	11.7	2.6	3.0	54	322	30.3	0.49	314	30.2	0.48	0.96
17	13	135	14	22.5	11.6	2.8	2.7	38	186	26.8	0.38	165	22.8	0.29	0.67
18	27	135	14	22.5	8.0	2.0	1.8	34	170	23.4	0.15	170	23.9	0.15	0.30
19	13	135	28	22.5	14.7	3.5	5.5	52	321	30.1	0.74	312	30.5	0.73	1.48
20	27	135	28	22.5	11.2	3.1	3.9	41	325	30.3	0.37	314	29.9	0.35	0.71
21	20	20	21	21	10.4	3.0	3.3	48	277	30.5	0.42	275	31.1	0.43	0.85
22	20	250	21	21	11.6	2.8	2.9	31	266	27.3	0.36	259	27.3	0.35	0.72
23	20	20	21	24	10.3	3.3	3.4	59	263	30.5	0.40	260	30.9	0.40	0.80
24	20	250	21	24	12.3	2.7	2.9	30	253	28.2	0.36	245	27.9	0.34	0.70
25	20	135	21	22.5	12.4	2.8	3.1	31	259	27.6	0.36	251	27.7	0.35	0.70
26	20	135	21	22.5	11.3	3.0	3.6	38	266	30.5	0.41	265	31.0	0.41	0.82
27	20	135	21	22.5	12.1	2.7	3.1	31	257	27.7	0.36	251	27.7	0.35	0.70
28	13	20	21	22.5	14.0	3.4	5.4	46	275	31.7	0.67	271	31.5	0.66	1.33
29	27	20	21	22.5	10.0	2.5	2.2	40	260	27.5	0.27	256	27.3	0.26	0.52
30	13	250	21	22.5	15.9	3.2	4.7	29	265	30.4	0.62	256	29.6	0.58	1.20
31	27	250	21	22.5	11.0	2.4	2.6	28	268	30.0	0.30	264	30.9	0.30	0.60
32	20	135	14	21	9.4	2.3	1.9	34	177	23.7	0.21	171	22.5	0.19	0.40
33	20	135	28	21	12.7	3.1	4.8	47	331	29.6	0.49	320	29.6	0.47	0.96

34	20	135	14	24	8.5	2.6	1.2	41	173	19.7	0.17	172	19.1	0.16	0.33
35	20	135	28	24	12.3	3.5	5.1	41	318	32.0	0.51	309	31.6	0.49	1.00
36	13	135	21	21	15.4	3.3	3.6	41	264	27.4	0.56	258	26.9	0.53	1.09
37	27	135	21	21	10.1	2.6	3.0	33	267	28.3	0.28	259	27.8	0.27	0.55
38	13	135	21	24	14.3	3.7	4.7	39	260	30.9	0.62	262	31.3	0.63	1.25
39	27	135	21	24	9.9	2.4	2.3	40	250	28.0	0.26	246	28.0	0.26	0.51
40	20	20	14	22.5	9.0	2.4	1.8	35	187	26.9	0.25	165	22.8	0.19	0.44
41	20	250	14	22.5	9.7	2.1	2.2	32	169	23.4	0.20	183	26.3	0.24	0.44
42	20	20	28	22.5	12.9	3.4	4.7	42	323	30.4	0.49	317	30.7	0.49	0.98
43	20	250	28	22.5	13.4	3.1	4.9	32	323	30.3	0.49	311	30.4	0.47	0.96
44	13	135	14	22.5	11.7	2.9	2.5	38	172	24.0	0.32	159	22.6	0.28	0.59
45	27	135	14	22.5	8.3	2.0	1.6	35	166	23.3	0.14	187	26.2	0.18	0.32
46	13	135	28	22.5	16.2	4.0	6.5	70	320	31.5	0.78	314	31.8	0.77	1.54
47	27	135	28	22.5	11.3	2.9	3.7	31	323	30.7	0.37	318	30.1	0.35	0.72
48	20	20	21	21	11.6	2.9	3.4	33	267	28.1	0.37	265	28.7	0.38	0.75
49	20	250	21	21	12.6	2.8	3.9	28	275	30.2	0.42	271	30.6	0.41	0.83
50	20	20	21	24	9.7	3.1	3.2	47	264	31.0	0.41	264	31.6	0.42	0.83
51	20	250	21	24	12.3	2.5	3.2	29	252	28.2	0.35	246	27.7	0.34	0.70
52	20	135	21	22.5	11.3	3.1	3.4	50	276	32.2	0.44	267	30.9	0.41	0.86
53	20	135	21	22.5	12.7	2.6	3.5	26	256	27.6	0.35	249	27.3	0.34	0.69
54	20	135	21	22.5	13.4	3.3	4.9	29	257	27.5	0.35	253	27.7	0.35	0.70

Appendix C:

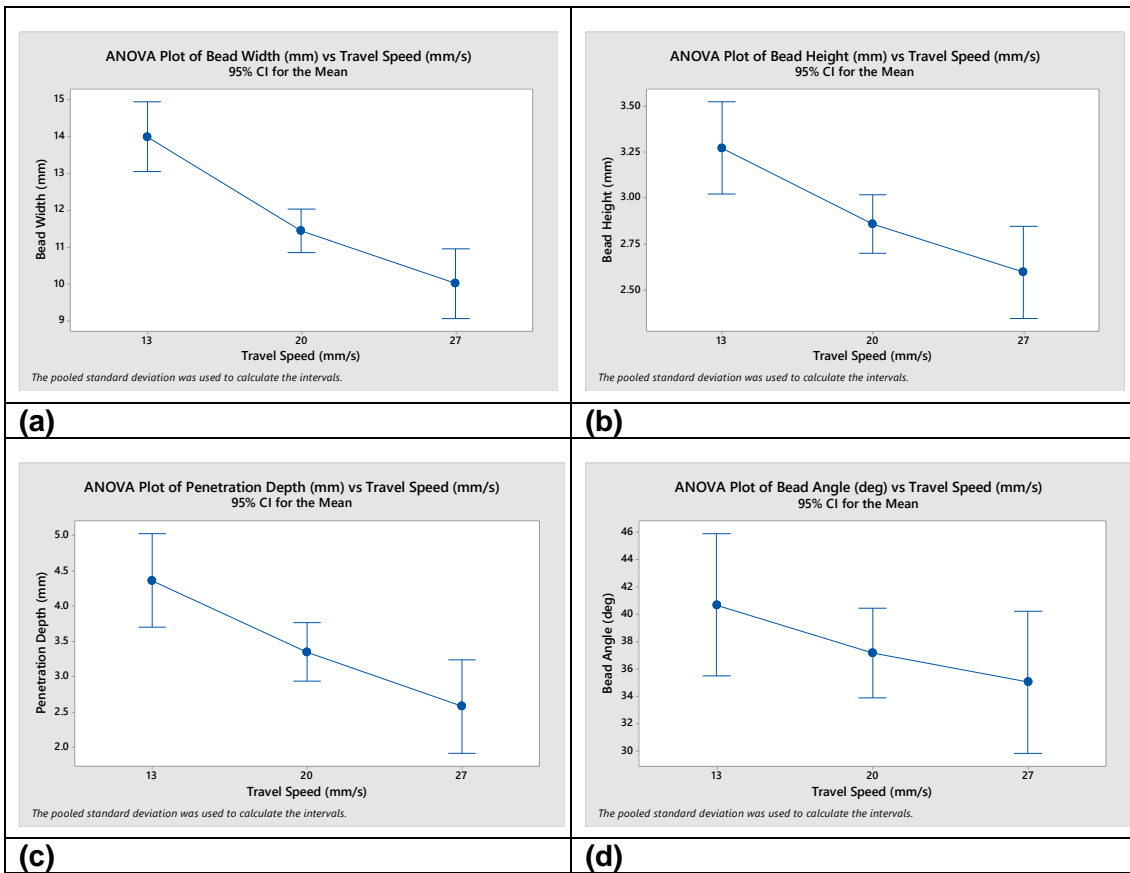
ANOVA plots and result tables of tandem GMAW parameters versus measured arc and bead responses, for high deposition rate parameter study.

(i) ANOVA plot and result table of WFS versus BW, BH, BP and BA at 95% confidence interval



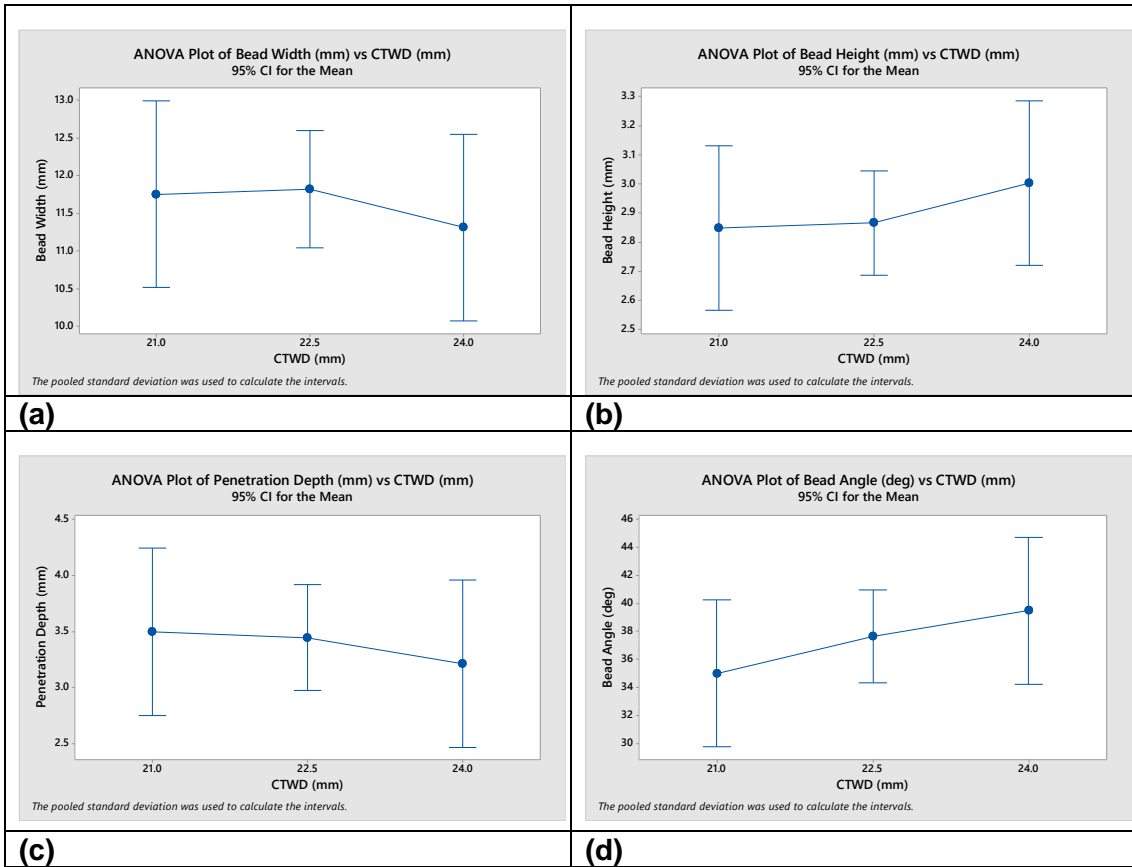
ANOVA Table (WFS)	Bead Width	Penetration	Bead Height	Bead Angle
DF	2	2	2	2
Adj. SS	59.17	43.31	4.262	781.6
Adj. MS	29.585	21.6567	2.1310	390.8
F-Value	8.64	26.41	13.5	5.68
P-Value	0.001	0.000	0.000	0.006
Total Error	233.72	85.14	12.312	4292
Pooled St. Dev.	1.85000	0.905601	0.397306	8.29646

(ii) ANOVA plot and result table of TS versus BW, BH, BP and BA at 95% confidence interval



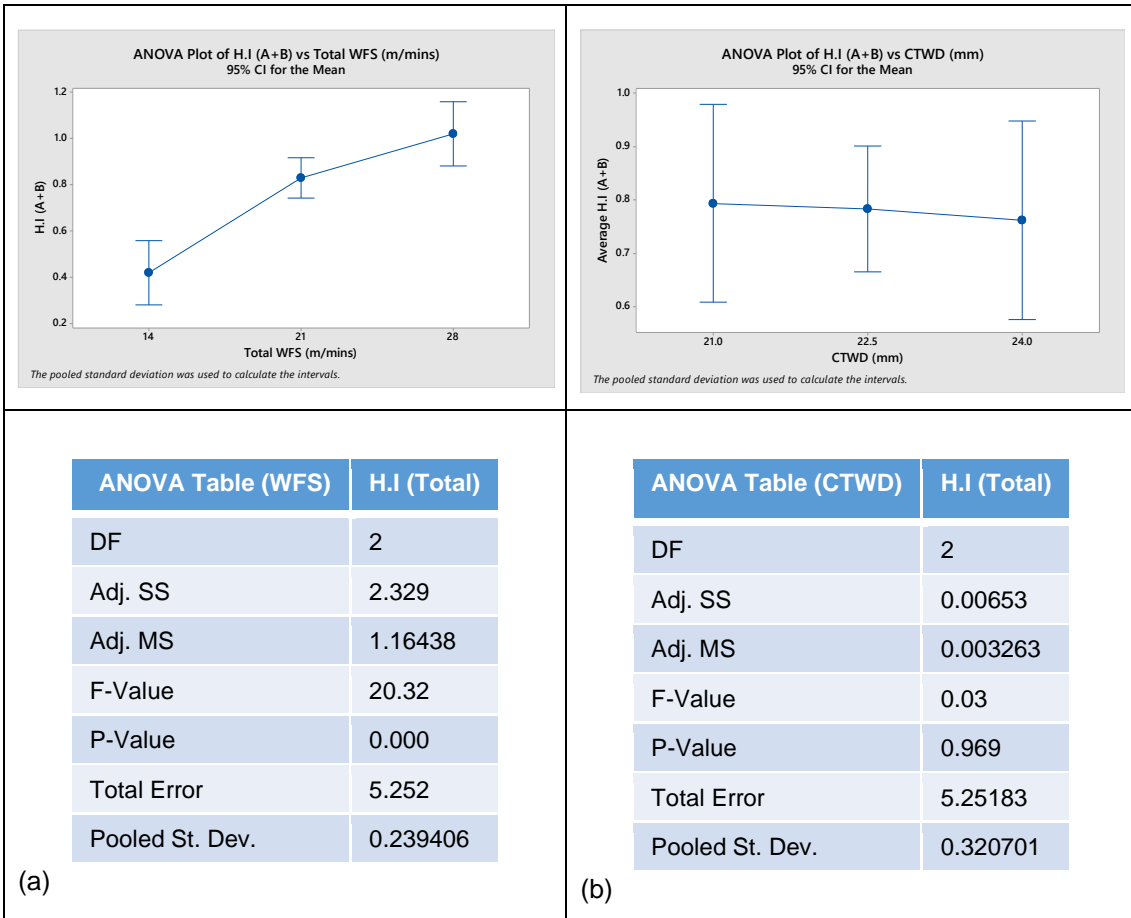
ANOVA Table (TS)	Bead Width	Bead Penetration	Bead Height	Bead Angle
DF	2	2	2	2
Adj. SS	19.10	99.13	2.799	196.8
Adj. MS	9.552	49.567	1.3995	98.42
F-Value	7.38	18.78	7.5	1.23
P-Value	0.002	0.000	0.001	0.302
Total Error	85.14	233.72	12.312	4292
Pooled St. Dev.	1.13791	1.62446	0.431901	8.96086

(iii) ANOVA plot and result table of CTWD versus BW, BH, BP and BA at 95% confidence interval

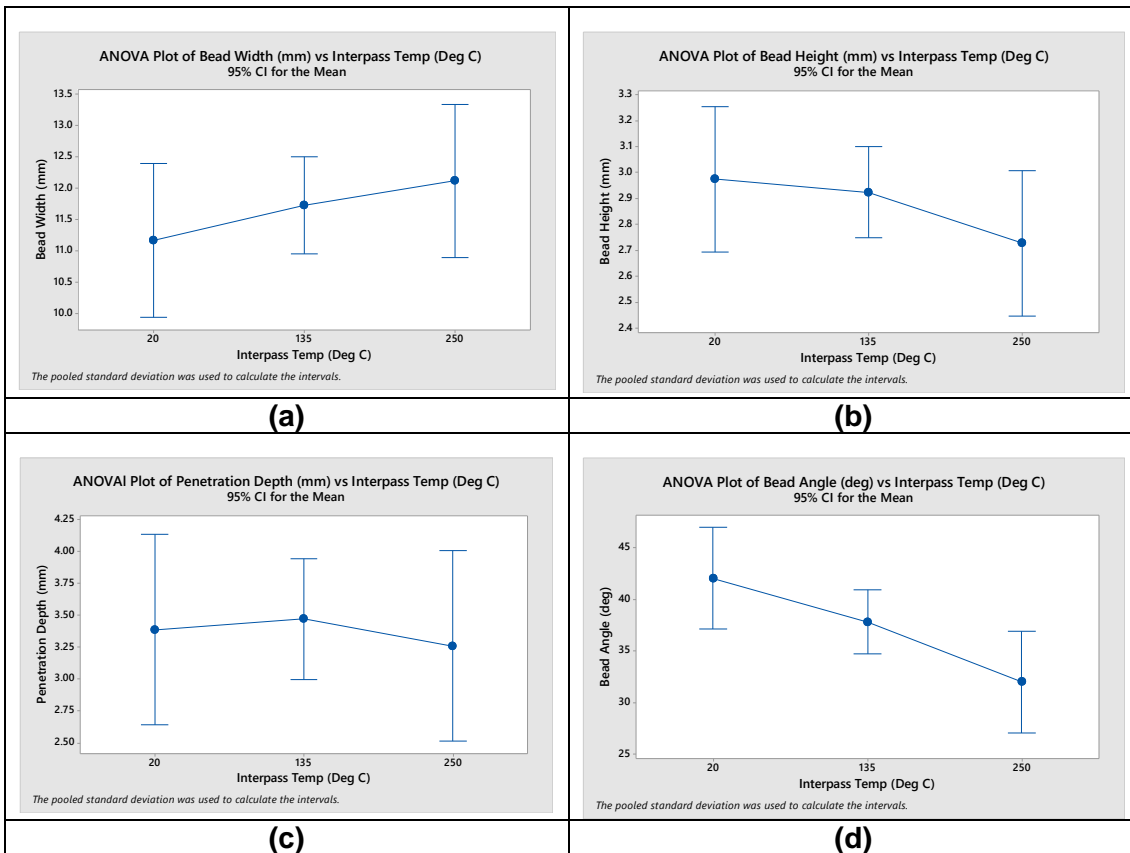


ANOVA Table (CTWD)	Bead Width	Bead Penetration	Bead Height	Bead Angle
DF	2	2	2	2
Adj. SS	2.286	0.5998	0.1933	123.1
Adj. MS	1.143	0.2999	0.09667	61.57
F-Value	0.25	0.18	0.41	0.75
P-Value	0.778	0.835	0.668	0.476
Total Error	233.717	85.1319	12.3125	4292
Pooled St. Dev.	2.13022	1.28749	0.487473	9.04115

(iv) ANOVA plot and result table of H.I versus WFS and CTWD at 95% confidence interval



(v) ANOVA plot and result table of preheat temperature versus BW, BH, BP and BA at 95% confidence interval



ANOVA Table (Preheat temp.)	Bead Width	Bead Penetration	Bead Height	Bead Angle
DF	2	2	2	2
Adj. SS	5.495	0.3851	0.4356	609.9
Adj. MS	2.748	0.1925	0.2178	304.93
F-Value	0.61	0.12	0.94	4.22
P-Value	0.545	0.891	0.399	0.020
Total Error	233.717	85.1393	12.3125	4292
Pooled St. Dev.	2.11541	1.28913	0.482577	8.49697

Appendix D:

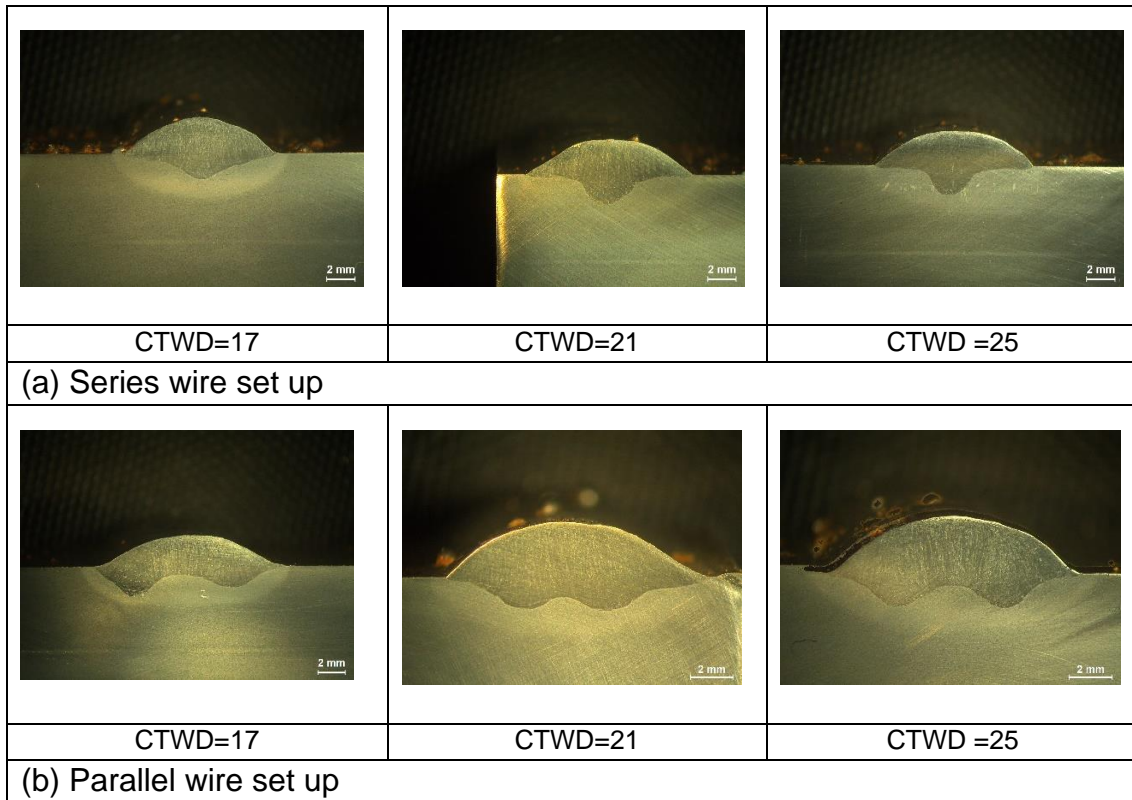
The transverse macro cross sections of the beads showing the effect of variation in WFS of lead wire (A) and trail wire (B) of tandem GMAW process, on the deposited bead geometry

Trial No	WFS(A) > WFS(B)	WFS(B) > WFS(A)
1		
2		
3		
4		
5		
6		

Transverse cross sections of tandem-GMAW single bead deposits, where wire (A) is the front wire, and (a) WFS of lead wire (A) > WFS of trail wire (B) and (b) WFS of lead wire(A) < WFS of trail wire (B)

Appendix E:

Transverse macro sections showing the effect of change in CTWD of tandem GMAW parallel and series wire orientations, on deposited bead profiles and quality.

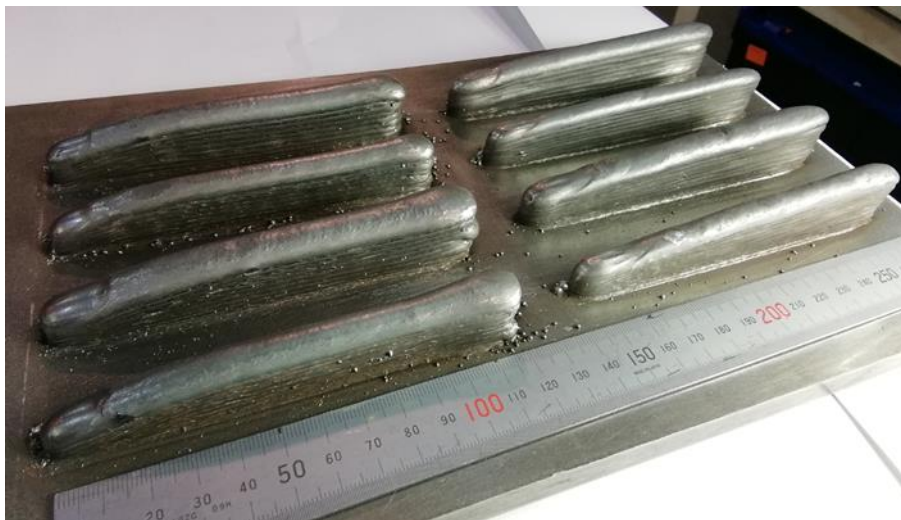


Macrograph transverse sections of weld bead produced at CTWD of 17, 21 & 25mm, and TS of 10mm/s, using Tandem-wire (a) Series configuration and (b) Parallel configuration

Appendix F:

Pre-set process parameters used to study the effect of multi-layer wall deposition parameters on the measured wall responses. Also shown are examples of the 10-layer high walls deposited during this investigation.

Deposition conditions	Wall Trial No	WFS Wire (A+B) m/mins	TS mm/s	WFS/TS	Wall Height (WH) (mm)	Avg. Layer Height (ALH) (mm)	Stdev Layer height (SdLH)	Wall Width (WW), mm	Effective Wall Width (EWW), mm	SW cal. Using width measure	MDE (%)	SW Using profiler
Tandem-wire (Series)	1	7	5	23.3	24.3	2.43	0.51	11.5	9.8	0.93	78.8	110.7
	2	7	7	16.7	21.2	2.12	0.44	9.62	8.01	0.81	79.6	125.7
	3	10	7.1	23.5	23.1	2.31	0.61	12.45	10.51	0.97	77.0	80.03
	4	10	10	16.7	20.3	2.03	0.42	10.03	8.74	0.645	81.1	88.3
Tandem-wire (Parallel)	9	7	5	23.3	23.7	2.37	0.40	12.14	10.91	0.62	84.7	60.3
	10	7	7	16.7	20.1	2.01	0.23	10.05	9.39	0.33	85.6	46.8
	11	10	7.1	23.5	22.7	2.27	0.40	12.69	11.76	0.47	84.6	57.6
	12	10	10	16.7	19.7	1.97	0.33	10.85	9.47	0.69	82.4	83.96
Single-wire GMAW	13	7	5	23.3	25.0	2.50	0.40	11.3	9.6	0.81	77.9	133.3
	14	7	7	16.7	21.6	21.6	0.30	9.1	8.2	0.48	73.3	118.7



10-layer high walls deposited during the multi-pass wall deposition investigation

Appendix G:

Detail of experimental design matrix and pre-set parameters utilised to investigate single wire GMAW parameter optimisation for depositing the skin section of a part and the measured wall responses obtained

Run Order	TS (mm/s)	WFS (m/mins)	I (Amps)	V (Volts)	H.I (kJ/mm)	CTWD (mm)	BH (mm)	BW (mm)	WFS/T S
1	11	6	171	22.8	0.354	21	1.97	7.84	9.1
2	8	7	196	23.8	0.583	21	2.55	9.71	14.6
3	12	6	173	22.8	0.329	21	1.88	7.40	8.3
4	9	6	173	22.8	0.438	21	2.21	8.39	11.1
5	9	5	148	23.2	0.382	21	2.02	7.74	9.3
6	9	4	133	22	0.325	21	1.72	7.02	7.4
7	7	5	150	23.3	0.499	21	2.25	8.90	11.9
8	8	5	150	23.2	0.435	21	2.18	7.95	10.4
9	10	7	197	23.9	0.471	21	2.31	8.87	11.7
10	7	4	133	22	0.418	21	2.12	8.18	9.5
11	6	5	152	23.1	0.585	21	2.54	9.25	13.9
12	5	4	130	22.2	0.577	21	2.50	8.74	13.3
13	10	4	130	21.8	0.283	21	1.51	6.55	6.7
14	6	4	132	22.2	0.488	21	2.31	8.53	11.1
15	11	5	150	23.1	0.315	21	1.84	7.15	7.6
16	10	5	152	23	0.350	21	1.93	7.37	8.3
17	8	6	171	22.7	0.485	21	2.33	9.07	12.5
18	7	7	195	24	0.669	21	2.88	10.58	16.7
19	6	6	171	23.2	0.661	21	2.73	10.37	16.7
20	11	4	130	21.9	0.259	21	1.40	6.39	6.1
21	10	6	174	22.6	0.393	21	2.13	8.03	10.0
22	8	4	134	22	0.369	21	1.89	7.33	8.3
23	9	7	194	24.3	0.524	21	2.45	9.40	13.0
24	7	6	170	21.1	0.542	21	2.57	9.66	14.3
25	6	7	194	24.2	0.782	21	3.11	11.11	19.4
26	11	7	194	23.8	0.420	21	2.19	8.56	10.6
27	12	7	194	24	0.388	21	2.01	8.11	9.7
28	12	5	152	23.1	0.292	21	1.72	6.79	6.9

Appendix H:

Detail of experimental design matrix and pre-set parameters utilised to investigate the tandem GMAW series wire configuration parameter optimisation, for depositing the core section of a part and the measured responses obtained

Trial	WFS (A+B) m/min s	TS (m/mins)	I(A)	I(B)	V(A)	V(B)	H.I(A)	H.I(B)	H.I (A+B) (kJ/mm)	BW (mm)	BH (mm)	BP (mm)	BA (deg)	DR (kg/hr)	WFS/T S
1	24	1.44	272	30.5	27.9	29.6	0.26	0.38	0.63	12.4	2.7	3.5	27	12.5	16.7
2	26	1.44	289	32.1	28.7	30.2	0.27	0.40	0.68	12.4	3.1	4.1	31	13.4	18.1
3	28	1.56	310	33.9	29.5	30.7	0.30	0.40	0.70	11.3	3.1	4.2	39	14.5	17.9
4	22	1.56	250	28.7	27.0	28.9	0.23	0.32	0.55	11.9	2.5	3.1	27	11.4	14.1
5	24	1.56	272	30.2	27.8	29.5	0.26	0.34	0.60	12.1	2.6	3.5	27	12.4	15.4
6	22	1.08	250	28.4	27.2	28.8	0.24	0.45	0.69	14.3	2.9	3.8	27	11.4	20.4
7	20	1.08	226	26.7	26.0	28.1	0.21	0.42	0.63	13.6	2.8	3.2	28	10.3	18.5
8	22	1.2	250	28.7	27.2	29.0	0.23	0.42	0.65	13.8	2.8	3.7	27	11.4	18.3
9	28	1.32	310	33.8	29.7	30.9	0.30	0.47	0.77	13.3	3.5	4.7	34	14.5	21.2
10	26	1.08	292	31.9	28.9	30.3	0.28	0.54	0.82	14.8	3.5	4.6	29	13.4	24.1
11	28	1.2	308	33.7	29.6	30.8	0.30	0.52	0.81	13.7	3.5	4.8	33	14.5	23.3
12	24	1.2	274	30.9	27.8	29.4	0.26	0.45	0.71	13.2	3.0	4.1	32	12.4	20.0
13	26	1.2	293	32.7	28.6	30.0	0.28	0.49	0.77	13.4	3.3	4.6	33	13.4	21.7
14	20	1.56	228	27.4	26.1	27.9	0.21	0.29	0.51	10.8	2.4	2.0	29	10.3	12.8
15	26	1.32	292	32.7	28.7	30.1	0.28	0.45	0.73	12.7	3.2	4.4	32	13.4	19.7
16	22	1.32	250	29.1	27.1	28.7	0.24	0.38	0.62	12.2	2.7	3.7	29	11.4	16.7
17	20	1.44	230	27.6	26.2	27.9	0.22	0.32	0.54	11.3	2.4	2.7	29	10.3	13.9
18	24	1.32	272	30.7	27.9	29.4	0.26	0.41	0.67	13.0	2.9	3.9	33	12.4	18.2
19	28	1.44	306	34.2	29.5	30.5	0.30	0.44	0.73	12.2	3.2	4.2	35	14.5	19.4
20	22	1.44	251	28.7	27.2	28.3	0.24	0.34	0.58	11.9	2.6	3.3	27	11.4	15.3
21	24	1.08	273	30.3	28.0	29.3	0.26	0.49	0.75	14.2	3.2	4.5	31	12.4	22.2
22	20	1.2	228	27.2	26.2	28.0	0.21	0.38	0.59	12.0	2.7	3.0	30	10.3	16.7
23	28	1.08	310	34.0	29.7	30.8	0.30	0.58	0.88	14.3	3.7	5.4	37	14.5	25.9
24	20	1.32	229	27.4	26.2	28.1	0.21	0.35	0.56	11.9	2.5	3.0	28	10.3	15.2
25	26	1.56	293	32.2	28.8	29.9	0.28	0.37	0.65	11.7	2.9	3.9	33	13.4	16.7

Appendix I:

Robotic program utilised in the manufacture of the skin and core structure

MODULE SKIN

```
VAR bool bweld:=FALSE;

PERS num skinLayerHeight := 3;

PERS num skinLayerNum := 1;

PERS num skinLen := 250;

PERS num skinWidth := 100;

VAR speeddata skinTS := [22.5,500,5000,1000];

PERS tooldata TANDEM:=[TRUE,[[[-
59.4569,140.873,494.599],[0.959426,0.020319,-
0.029137,0.279715]],,[10,[100,0,100],[1,0,0,0],0.04,0.04,0.04]];

PERS wobjdata
abb3:=[FALSE,TRUE,"",[[[228.654,742.761,295.623],[0.706442,0.000266,-
0.00028,0.707771]],,[197.347,280.792,12.2122],[0.999999,-0.000261,-
0.001454,-6.6E-05]]];

CONST robtarget Phome:=[[-36.4,-4.6,467.5],[0.01869,0.50899,0.86048,-
0.01221],[0,0,2,0],[0.41851,-0.455778,9E+09,9E+09,9E+09,9E+09]];

PERS robtarget skinPointRefY:=[[-125.5,-191.1,131.5],[0.04532,-
0.24206,0.96821,0.04386],[0,0,2,0],[0.41851,-
0.455778,9E+09,9E+09,9E+09,9E+09]];

PERS robtarget skinPointRefX:=[[-16.7,-
110.1,134.8],[0.08430,0.51907,0.85030,0.02119],[0,0,2,0],[0.41851,-
0.455778,9E+09,9E+09,9E+09,9E+09]];

VAR orient xRot := [0.0778,0.5387,0.8388,0.0114];

VAR orient yRot := [0.0454,-0.2177,0.9727,0.0657];

PROC SKINPROC()
    ConfL \Off;

    ConfJ \Off;

    MoveJ Phome,v150,fine,TANDEM\WObj:=abb3;

    IF skinLayerNum MOD 2 = 1 THEN
        ! pass 1
```

```

    MoveL
Offs(skinPointRefY,0,0,skinLayerNum*skinLayerHeight),v100,fine,TANDEM\W
Obj:=abb3;

    SetDO doWELD, 0;

    WaitTime 1.2;

    MoveL
Offs(skinPointRefY,0,skinLen,skinLayerNum*skinLayerHeight),skinTS,fine,TAN
DEM\WObj:=abb3;

    SetDo doWELD, 1;

    WaitTime 3;

    MoveJ Phome,v150,fine,TANDEM\WObj:=abb3;

    ! pass 2

    MoveL
Offs(skinPointRefY,skinWidth,0,skinLayerNum*skinLayerHeight),v100,fine,TAN
DEM\WObj:=abb3;

    SetDO doWELD, 0;

    WaitTime 1.2;

    MoveL
Offs(skinPointRefY,skinWidth,skinLen,skinLayerNum*skinLayerHeight),skinTS,f
ine,TANDEM\WObj:=abb3;

    SetDo doWELD, 1;

    WaitTime 3;

    MoveJ Phome,v150,fine,TANDEM\WObj:=abb3;

    ! pass 3

    MoveL
Offs(skinPointRefX,0,0,skinLayerNum*skinLayerHeight),v100,fine,TANDEM\W
Obj:=abb3;

    SetDO doWELD, 0;

    WaitTime 1.2;

    MoveL
Offs(skinPointRefX,skinWidth,0,skinLayerNum*skinLayerHeight),skinTS,fine,TA
NDEM\WObj:=abb3;

    SetDo doWELD, 1;

    WaitTime 3;

```

```

MoveJ Phome,v150,fine,TANDEM\WObj:=abb3;
! pass 4
MoveL
Offs(skinPointRefX,0,skinLen,skinLayerNum*skinLayerHeight),v100,fine,TANDEM\WObj:=abb3;
SetDO doWELD, 0;
WaitTime 1.2;
MoveL
Offs(skinPointRefX,skinWidth,skinLen,skinLayerNum*skinLayerHeight),skinTS,fine,TANDEM\WObj:=abb3;
SetDo doWELD, 1;
WaitTime 3;
MoveJ Phome,v150,fine,TANDEM\WObj:=abb3;
ENDIF
IF skinLayerNum MOD 2 = 0 THEN
! pass 1
MoveL
Offs(skinPointRefY,0,skinLen,skinLayerNum*skinLayerHeight),v100,fine,TANDEM\WObj:=abb3;
SetDO doWELD, 0;
WaitTime 1.2;
MoveL
Offs(skinPointRefY,0,0,skinLayerNum*skinLayerHeight),skinTS,fine,TANDEM\WObj:=abb3;
SetDo doWELD, 1;
WaitTime 3;
MoveJ Phome,v150,fine,TANDEM\WObj:=abb3;
! pass 2
MoveL
Offs(skinPointRefY,skinWidth,skinLen,skinLayerNum*skinLayerHeight),v100,fine,TANDEM\WObj:=abb3;
SetDO doWELD, 0;
WaitTime 1.2;

```

```

    MoveL
Offs(skinPointRefY,skinWidth,0,skinLayerNum*skinLayerHeight),skinTS,fine,TANDEM\WObj:=abb3;

    SetDo doWELD, 1;

    WaitTime 3;

    MoveJ Phome,v150,fine,TANDEM\WObj:=abb3;

    ! pass 3

    MoveL
Offs(skinPointRefX,skinWidth,0,skinLayerNum*skinLayerHeight),v100,fine,TANDEM\WObj:=abb3;

    SetDO doWELD, 0;

    WaitTime 1.2;

    MoveL
Offs(skinPointRefX,0,0,skinLayerNum*skinLayerHeight),skinTS,fine,TANDEM\WObj:=abb3;

    SetDo doWELD, 1;

    WaitTime 3;

    MoveJ Phome,v150,fine,TANDEM\WObj:=abb3;

    ! pass 4

    MoveL
Offs(skinPointRefX,skinWidth,skinLen,skinLayerNum*skinLayerHeight),v100,fine,TANDEM\WObj:=abb3;

    SetDO doWELD, 0;

    WaitTime 1.2;

    MoveL
Offs(skinPointRefX,0,skinLen,skinLayerNum*skinLayerHeight),skinTS,fine,TANDEM\WObj:=abb3;

    SetDo doWELD, 1;

    WaitTime 3;

    MoveJ Phome,v150,fine,TANDEM\WObj:=abb3;

ENDIF

ENDPROC

```

```

PROC main()
  ConfL \Off;
  ConfJ \Off;
  SKINPROC;
ENDPROC
ENDMODULE

```

MODULE CORE

```

VAR bool bweld:=FALSE;
PERS num coreLayerNum := 1;
PERS num coreLayerHeight := 3;
PERS num coreLen :=100;
PERS num interval:=7.5;
PERS num totalPassNum := 5;

VAR num currentPass := 1;
VAR speeddata coreTS := [22.5,500,5000,1000];

PERS tooldata TANDEM:=[TRUE,[[
59.4569,140.873,494.599],[0.959426,0.020319,-
0.029137,0.279715]],[[10,[100,0,100],[1,0,0,0],0.04,0.04,0.04]]];

PERS wobjdata
abb3:=[FALSE,TRUE,"",[[228.654,742.761,295.623],[0.706442,0.000266,-
0.00028,0.707771]],[[197.347,280.792,12.2122],[0.999999,-0.000261,-
0.001454,-6.6E-05]]];

CONST robtarget Phome:=[[-36.4,-4.6,467.5],[0.01869,0.50899,0.86048,-
0.01221],[0,0,2,0],[0.41851,-0.455778,9E+09,9E+09,9E+09,9E+09]];

PERS robtarget coreRefX:=[[-16.7,-
110.1,134.8],[0.08430,0.51907,0.85030,0.02119],[0,0,2,0],[0.41851,-
0.455778,9E+09,9E+09,9E+09,9E+09]];

VAR orient xRot := [0.0778,0.5387,0.8388,0.0114];
VAR orient yRot := [0.0454,-0.2177,0.9727,0.0657];

```

```

PROC COREPROC ()
    ConfL \Off;
    ConfJ \Off;
    MoveJ Phome,v150,fine,TANDEM\WObj:=abb3;
    IF coreLayerNum MOD 2 = 1 THEN
        WHILE currentPass <= totalPassNum DO
            IF currentPass MOD 2 = 1 THEN
                MoveL Offs(coreRefX,(currentPass-
1)*interval,0,coreLayerNum*coreLayerHeight),v100,fine,TANDEM\WObj:=abb3;
                SetDO doWELD, 0;
                WaitTime 1.2;
                MoveL Offs(coreRefX,(currentPass-
1)*interval,coreLen,coreLayerNum*coreLayerHeight),coreTS,fine,TANDEM\WO
bj:=abb3;
                SetDo doWELD, 1;
                WaitTime 3;
            ENDIF
            IF currentPass MOD 2 = 0 THEN
                MoveL Offs(coreRefX,(currentPass-1)*interval,
coreLen,coreLayerNum*coreLayerHeight),v100,fine,TANDEM\WObj:=abb3;
                SetDO doWELD, 0;
                WaitTime 1.2;
                MoveL Offs(coreRefX,(currentPass-
1)*interval,0,coreLayerNum*coreLayerHeight),coreTS,fine,TANDEM\WObj:=abb
3;
                SetDo doWELD, 1;
                WaitTime 3;
            ENDIF
            currentPass := currentPass + 1;
            MoveJ Phome,v150,fine,TANDEM\WObj:=abb3;

```

```

        ENDWHILE
    ENDIF

    IF coreLayerNum MOD 2 = 0 THEN
        WHILE currentPass <= totalPassNum DO
            IF currentPass MOD 2 = 1 THEN
                MoveL Offs(coreRefX,(currentPass-
1)*interval,coreLen,coreLayerNum*coreLayerHeight),v100,fine,TANDEM\WObj:
=abb3;

                SetDO doWELD, 0;
                WaitTime 1.2;
                MoveL Offs(coreRefX,(currentPass-
1)*interval,0,coreLayerNum*coreLayerHeight),coreTS,fine,TANDEM\WObj:=abb
3;

                SetDo doWELD, 1;
                WaitTime 3;
            ENDIF

            IF currentPass MOD 2 = 0 THEN
                MoveL Offs(coreRefX,(currentPass-
1)*interval,0,coreLayerNum*coreLayerHeight),v100,fine,TANDEM\WObj:=abb3;
                SetDO doWELD, 0;
                WaitTime 1.2;
                MoveL Offs(coreRefX,(currentPass-1)*interval,
coreLen,coreLayerNum*coreLayerHeight),coreTS,fine,TANDEM\WObj:=abb3;
                SetDo doWELD, 1;
                WaitTime 3;
            ENDIF

            currentPass := currentPass + 1;
            MoveJ Phome,v150,fine,TANDEM\WObj:=abb3;
        ENDWHILE
    
```

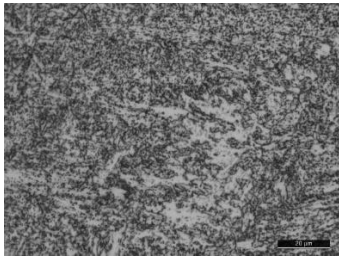
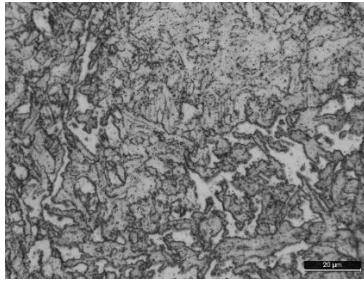
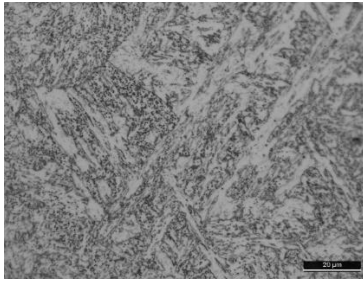
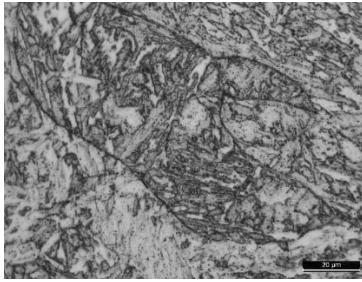
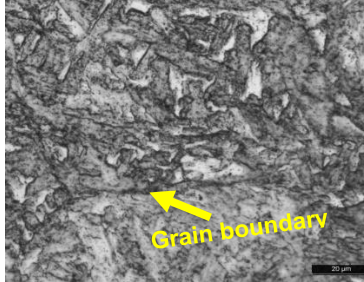
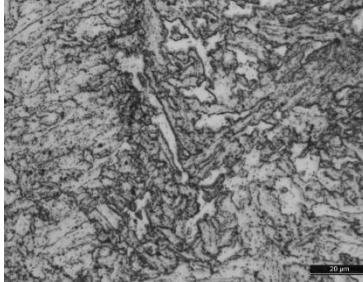
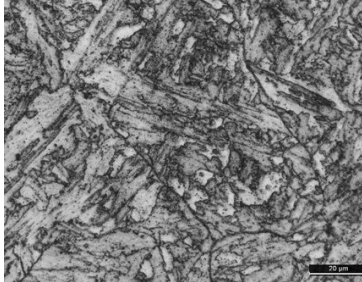


```
    ENDIF  
ENDPROC
```

```
PROC main()  
    ConfL \Off;  
    ConfJ \Off;  
    COREPROC;  
ENDPROC  
ENDMODULE
```

Appendix J:

Optical microstructures of representative ER90S-G WAAM samples, in as-deposited and heat-treated conditions, etched using 2% Nital solution. The maximum hardness values measured are also shown.

As-deposited :(360HV) Martensite+lower bainite		
		
A :670/25 (238HV):	B :690/25 (226HV)	G :670/50 (241HV)
		
H :690/50 (231HV)	I :710/50 (226HV)	F3 :670/75 (246HV)
		

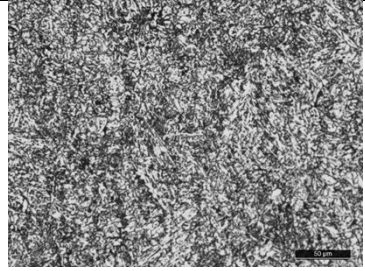
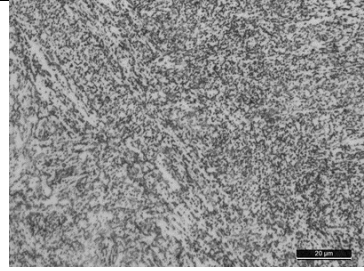
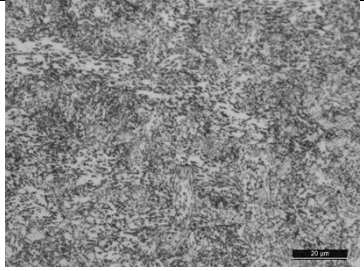
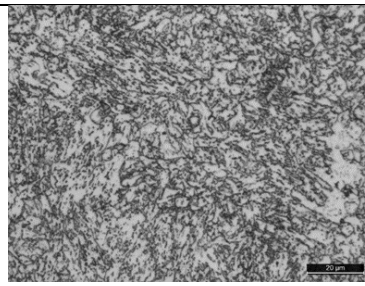
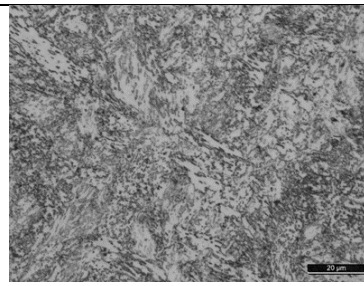
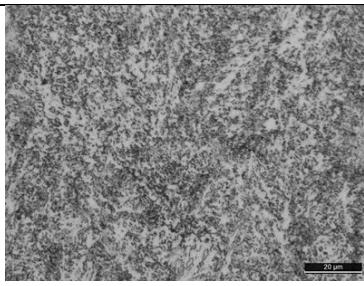
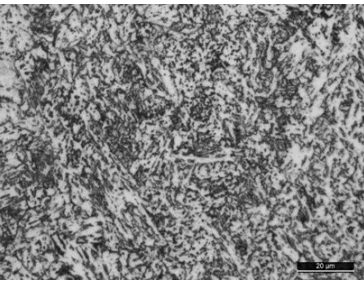
Appendix K:

Charpy impact toughness test results of representative ER90S-G WAAM samples, in as-deposited and heat-treated conditions, tested at -60°C

Height from top surface	Top 25mmn section				Middle 50mm section				Bottom 75mm section				RANGE (J)
	LD		ND		LD		ND		LD		ND		
Sample conditions PDHT: °C/(°C/hr)	J	(J) Avg.	J	(J) Avg.	J	(J) Avg.	J	(J) Avg.	J	(J) Avg.	J	(J) Avg.	
As-deposited	32,32	32	40,41	41	26,29	28	16,37	27	39,42	41	28,42	35	16 - 42
670(50)	68,93	81	86,116	101	53,68	61	52,96	74	91,106	99	13,87	50	13 – 116
690(50)	77,79	78	87,96	92	65,76	71	98,111	105	54,96	75	24,53	39	24 – 111
710(50)	83,106	95	84,100	92	93,105	99	70,92	81	28,69	49	12,19	16	12 – 106
670(75)	69,103	86	95,106	101	60,103	82	82,93	88	9,11	10	19,65	42	9 – 106

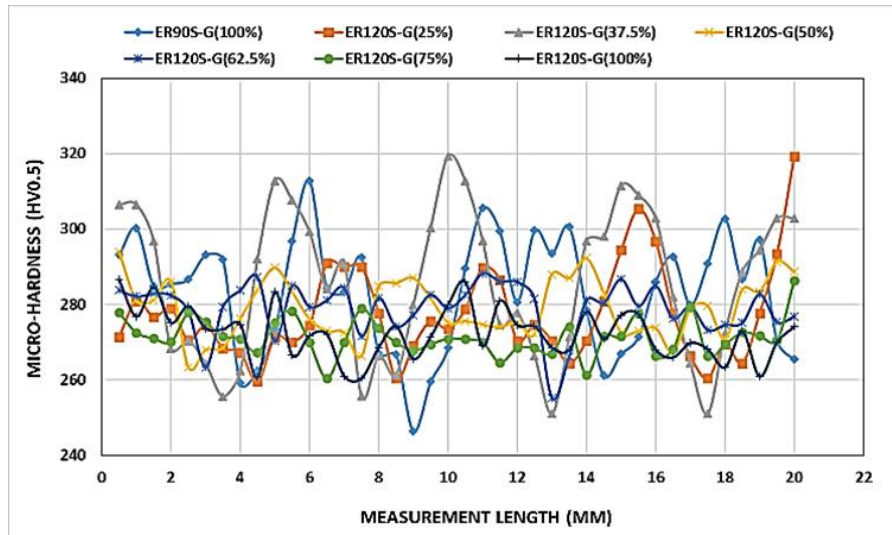
Appendix L:

Representative microstructures of modified WAAM weldments, produced by tandem GMAW mixing of ER120S-G and ER90S-G compositions, and etched using 2% Nital. The mixed compositions are presented as a proportion of ER120S-G composition, while the balance is ER90S-G

ER90S-G (100%) (HV-344 Max): 0.03 wt.% Ni	ER120S-G (25%) (HV-319 Max): 0.48 wt.% Ni	ER120S-G (37.5%) (HV- 319 Max): 0.73wt.% Ni
		
ER120S-G (50%) (HV-319 Max): 0.90 wt.% Ni	ER120S-G (62.5%) (HV- 300 Max): 1.23wt.% Ni	ER120S-G (75%) (HV-290 Max): 1.38 wt.% Ni
		
ER120S-G (100%) (HV-302 Max): 1.83 wt. % Ni		
		

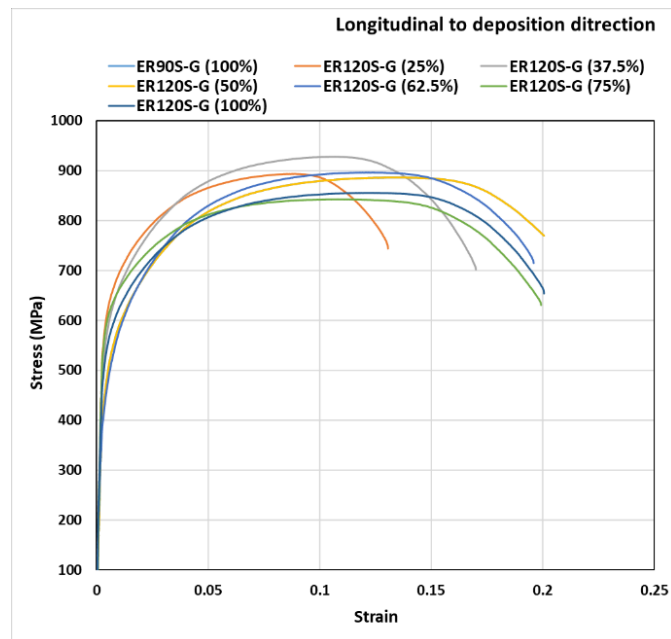
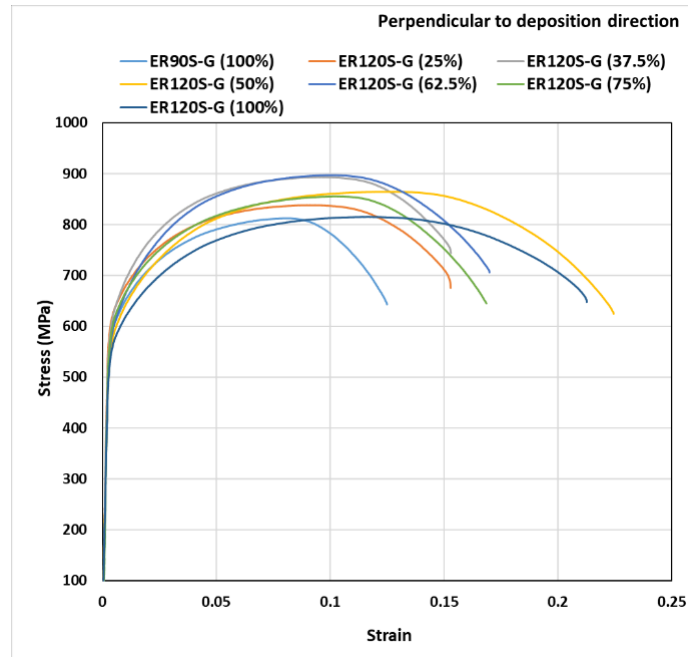
Appendix M:

Scatter plots of micro-hardness of modified WAAM weldments, produced from tandem GMAW mixing of ER120S-G and ER90S-G compositions, Scatter plot of microhardness test, as a function of proportion of ER120S-G composition and the balance is ER90S-G



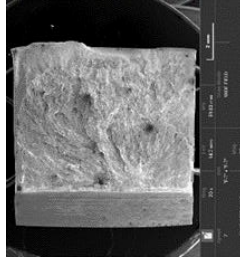
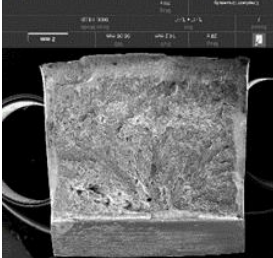
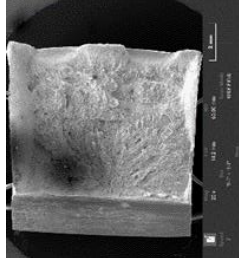
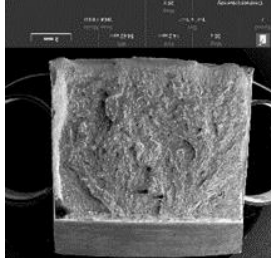
Appendix N:

Stress-strain diagrams of modified WAAM weldments, produced by tandem GMAW mixing of ER120S-G and ER90S-G compositions, measured in the perpendicular and longitudinal deposition directions, as a function of proportion of ER120S-G composition and the balance is ER90S-G



Appendix O:

Charpy fracture surface morphologies of modified WAAM specimens, produced by tandem GMAW mixing of ER120S-G and ER90S-G compositions, tested at -30°C, as a function of proportion of ER120S-G composition and the balance is ER90S-G

ER120S-G (37.5%) – 30J	ER120S-G (25%) – 30J	ER120S-G (75%) – 46J	ER120S-G (62.5%) – 29J
			
ER120S-G (50%) – 43J	ER120S-G (100%) – 37J	ER90S-G (100%) – 37J	
